الجمهورية الجزائرية الديمقراطية الشعبية
République Algérienne Démocratique et Populaire
وزارة التعليم العالي والبحث العلمي
Ministère de l'enseignement supérieur et de la recherche scientifique

Université Mohamed Khider - Biskra
Faculté des Sciences et de la Technologie
Département de Génie Civil et Hydraulique
Référence : ……

جامعة محمد خيضر - بسكرة
كلية العلوم والتكنولوجيا
قسم الهندسة المدنية والري
المرجع:.....

Thèse présentée en vue de l'obtention du diplôme de

Doctorat LMD en Génie Civil

Option : Modélisation numérique en génie civil

Modeling of Functionally Graded structures behavior

Modélisation du comportement des structures en Matériaux Fonctionnellement Gradués (FGM)

Présentée par

Amira SADGUI

Soutenue publiquement le : 06 Juillet 2022

Devant le jury composé de :

Mr. Lamine BELOUNAR	Professeur	Président	Université de Biskra
Mr. Abdelouahab TATI	Professeur	Rapporteur	Université de Biskra
Mr. Lakhdar SEDIRA	Professeur	Examinateur	Université de Biskra
Mr. Kamel MEFTAH	Professeur	Examinateur	Université de Batna2

‘’ To my dear parents, Brother, Sisters and my little prince anis.’’

Acknowledgements

First and foremost, Alhamdulillah to the Almighty *Allah* for giving me the strength and the ability to understand, learn and complete this thesis. Thank you *Allah* for everything.

I would not have been possible to write this doctoral thesis without the help and support of the kind people around me, to only some of whom it is possible to give a particular mention here.

Above all, I would like to thank my parents for their care, support and great patience at all times. Brother and sisters have given me their unequivocal support throughout, as always, for which my mere expression of thanks likewise does not suffice.

This thesis would not have been possible without the advice, help, support and patience of my supervisor, Professor Abdelouahab TATI, who has the attitude and substance of a genius. He has continuously motivated me with his wise and intelligent advice since I started working under his supervision. The good advice, support and friendship of Doctor Souhia BOUADJADJA, have been invaluable on both academic and personal levels, for which I am extremely grateful.

I would like to sincerely thank all the jury members, Mr. Lamine BELOUNAR, Professor at the University of Biskra, Mr. Lakhdar SEDIRA, Professor at the University of Biskra and Mr. Kamel MEFTAH, Professor at the University of Batna 2, for accepting to review my work.

I want to acknowledge all the professors and staff of Mohamed Khider University, who helped me or encouraged me. I also extend my sincere thanks to my friends for their moral encouragement and support.

Finally, I would also like to express my gratitude to one and all who directly or indirectly have lent their helping hands in this work.

Amira SADGUI

Abstract

A new class of composite materials known as "Functionally Graded Materials" (FGMs), has been designed by Japanese scientists to compensate for certain defects that occur in traditional laminated composites, such as stress concentration and delamination. FGMs are made from a mixture of metals and ceramics distinguished by a gradual change in composition and microstructure through the thickness, resulting in a smooth and continuous variation in material properties. FGMs have been widely used in many structural applications that differ from their first application as a thermal barrier for aerospace structures. The development of the use of FGMs in structures requires a good understanding of their mechanical behavior in order to provide an optimum profile to designers.

The main aim of the present work is to contribute to the modeling of static, stability and dynamic behaviors of plates made of FGMs. First, a four-node rectangular finite element, with five degrees of freedom per node, based on First-order shear deformation theory (FSDT), has been adapted for static, mechanical buckling and free vibration analysis of FG single layer and sandwich plates. The FSDT provides a sufficiently accurate description of response for thin to moderately thick plates. However, it predicts constant transverse shear stresses across the thickness and a shear correction factor is needed. To overcome problems related to FSDT, a novel trigonometric shear deformation model with five unknowns has been proposed for the analysis of FG plates behavior. The model accounts for the sinusoidal variation of the transverse shear strains across the thickness and satisfies the shear stress-free boundary conditions on the top and bottom surfaces of the plate. A four-node rectangular finite element based on the proposed new model (R4SSDT), has been formulated to analyze the static, stability and dynamic behavior of FG single layer plates. For the two formulated finite elements, assumed natural shear strain and the physical neutral surface position procedures have been taken into consideration. The performance and accuracy of the developed elements have been evaluated through validation tests. The effects of various parameters on the behavior of FG plate have been also studied.

Keywords: Functionally graded materials, Plates, Static, Stability, dynamic behavior, Trigonometric model, Finite element method, Assumed natural shear strain technique, Neutral axis.

ملخص

تم تصميم فئة جديدة من المواد المركبة تُعرف باسم "المواد المتدرجة وظيفيًا (FGMs) "، من قبل علماء المواد اليابانيين للتعويض عن بعض العيوب التي تحدث في المواد المركبة التقليدية، مثل تركيز الإجهاد والتفكيك (انفصال طبقات المركب). تُصنع المواد المتدرجة وظيفيًا من مزيج من المعادن والسيراميك، تتميز بتغير تدريجي في التركيب والبنية المجهرية من خلال السمك، مما يؤدي إلى تباين سلس ومستمر في خصائص المواد. تم استخدام المواد المتدرجة وظيفيًا على نطاق واسع في العديد من التطبيقات الهيكلية التي تختلف عن تطبيقها الأول كحاجز حراري لهياكل الفضاء. يتطلب تطوير استخدام المواد المتدرجة وظيفيًا في الهياكل فهماً جيداً لسلوكها الميكانيكي من أجل توفير ملف تعريف مثالي للمصممين.

الهدف الرئيسي من هذا العمل هو المساهمة في نمذجة السلوك الستاتيكي، المستقر والديناميكي للصفائح المصنوعة من المواد المتدرجة وظيفيًا. أولاً، تم تكييف عنصر محدود مستطيل الشكل بأربعة عقد وخمس درجات حرية لكل عقدة، مبني على نظرية تشوه القص من الدرجة الأولى(FSDT)، لتحليل السلوك الستاتيكي، الالتواء الميكانيكي والاهتزاز الحر للصفائح المتدرجة وظيفيًا، أحادية الطبقة والسندويتش. توفر نظرية تشوه القص من الدرجة الأولى وصفًا دقيقًا بدرجة كافية لاستجابة الصفائح الرقيقة إلى متوسطة السمك. ومع ذلك، فإنها تتنبأ بإجهادات قص ثابتة عبر السمك وهناك حاجة إلى معامل تصحيح القص. للتغلب على المشاكل المتعلقة بـFSDT ، تم اقتراح نموذج جديد لتشوه القص، مثلثي وبخمسة مجاهيل فقط، لتحليل سلوك الصفائح المتدرجة وظيفيًا. يراعي النموذج المقترح، التباين الجيبي لانفعالات القص العرضي عبر السمك ويلبي شروط انعدام اجهادات القص على الأسطح العلوية والسفلية للصفيحة. تمت صياغة عنصر محدود مستطيل الشكل رباعي العقد استنادا على النموذج الجديد المقترح ، لتحليل السلوك الستاتيكي، المستقر والديناميكي للصفائح المتدرجة وظيفيًا أحادية الطبقة. بالنسبة للعنصرين المحدودين اللذين تمت صياغتهما، فقد تم استخدام تقنية انفعال القص الطبيعي المفترض وأخذ موضع السطح الطبيعي المحايد في الاعتبار. تم تقييم أداء ودقة العناصر المطورة من خلال اختبارات التحقق. كما تمت دراسة تأثير العوامل المختلفة على سلوك الصفائح المتدرجة وظيفيًا.

الكلمات المفتاحية: المواد المتدرجة وظيفيًا، صفائح، السلوك الستاتيكي، السلوك المستقر، السلوك الديناميكي، نظرية تشوه القص المثلثية، طريقة العناصر المحدودة، تقنية انفعال القص الطبيعي المفترض، المحور المحايد.

List of Publications and Communications

International Publicalions

- **A. Sadgui**, A. Tati (2021). A novel trigonometric shear deformation theory for the buckling and free vibration analysis of functionally graded plates. Mechanics of Advanced Materials and Structures, 1-16.
- A. Tati, **A. Sadgui**, S. Bouadjadja. Numerical investigation of natural frequency of antisymmetric angle-ply laminated composite plates subjected to mechanical in-plane stress. Journal of Vibration Engineering & Technologies (JVET), ***under review***.

International Communications

- **A. Sadgui**, A. Tati, S. Bouadjadja. First-order shear deformation theory model for the bending analysis of functionally graded isotropic and sandwich plates. The First International Conference on Materials, Environment, Mechanical and Industrial Systems (ICMEMIS'19), 29-30 June 2019, Djalfa-Algeria.

- **A. Sadgui**, A. Tati. Buckling analysis of functionally graded sandwich plates under uniaxial and biaxial compression load. Fifth International Conference on Energy, Materials, Applied Energetics and Pollution (ICEMAEP'19), 22-24 October 2019, Constantine-Algeria.

- **A. Sadgui**, A. Tati, S. Bouadjadja. Bending and free vibration analysis of functionally graded sandwich plates. Congrès Algérien de Mécanique (CAM), 23-26 February 2020, Ghardaia-Algeria.

- **A. Sadgui**, A. Tati. Modelling of structure made of functionally graded materials. Algerian American foundation (AAF) summer university, 28 July to 3 August 2019, Batna-Algeria.

Contents

List of Figures

List of Tables

List of Symbols and Abbreviations

Symbols

$[A]$, $[A^s]$, $[D]$	Membrane, Shear and Bending matrix, respectively
A_{ij}, D_{ij} , A^s_{ij}	Reduced elastic matrices coefficients
$[B_m]$,$[B_b]$	Membrane and bending strain-displacement relationship matrices
$[B_s]$	shear strain-displacement relationship matrix
$[\bar{B}_s]$	Assumed natural shear strain-displacement relation matrix
C	Distance between the neutral plane and the midplane of the plate
E	Young's modulus
E_m, E_c	Young's modulus of metal and ceramic, respectively
$f(x, y)$	distributed transverse load
$f(z)$	Shear function
$\{F_e\}$	Nodal load vector
G	Effective shear
h	Thickness of plate
h_0, h_1, h_2, h_3	Vertical positions of the bottom surface, the two interfaces between layers, and the top surface of sandwich plate.
I_0, I_2	Moments of inertia
K	Bulk modulus
k_s	Transverse shear correction factor
$\{k\}$	Curvatures vector.
$[K_e]$	elementary stiffness matrix
$[k_e^{g0}]$	Geometric stiffness matrix
L, l	Length and width of the plate
M_x, M_y, M_{xy}	Moment resultants
$[m]$	Inertia matrix

$[M]$	Mass matrix
N_{cri}	Critical buckling load
$N_i(x,y)$	Bilinear Lagrange shape functions associated with node *i*
N_x, N_y, N_{xy}	Normal stress resultants
$\left[\bar{N}_0\right]$	Stress matrix resulting from mechanical loading
$[N(x,y)]$	Shape function matrix
p	Power-law index
P, P_i	Material property, material property of the constituent ***i***
$\{q\}$	Displacement vector of the element
$P_\delta(y)$, $Q_\delta(x)$	Interpolation functions
Q_{ij}	Elasticity stiffness coefficients
S_{xz}, S_{yz}	Transverse shear stress resultants
t	Time
T	Kinetic energy
U	The strain potential energy
u, v	In-plane displacements vector components
u_0, v_0	In-plane displacements on the mid-plane of the plate
V, V_i	Volume fraction, volume fraction of the constituent ***i***
V_c	Volume fraction of ceramic
w	Transverse displacement
W	The external forces work
w_0	Out-of-plane displacement on the mid-plane of the plate
α	Dilatation Coefficients of thermal expansion
β	Enhancement factor
δ	Position of the sampling point
$\delta_\alpha(x,y)$	Displacement or rotation of a given point M(x, y) within the element
δ_α^i	displacement vector
ε_z	Transverse normal strain
$\{\varepsilon^l\}$	Linear strain vector
$\{\varepsilon^0\}$	Membrane strain vector
$\{\varepsilon^{nl}\}$	Nonlinear strain vector.

$\{\gamma_z^0\}$	Shear strain vector
$\bar{\gamma}_{xz}^{0(A)}$, $\bar{\gamma}_{yz}^{0(A)}$	Natural assumed transverse shear strains
λ	Loading factor
ν	Poisson's ratio
ψ_z	Stretching contributions of the displacement in the transverse direction
π	The total potential energy
ρ	Mass density
ρ_m, ρ_c	Mass density of metal and ceramic, respectively
σ_x, σ_y	Normal stresses
σ_z	Transverse normal stress
φ_x, φ_y	transverse normal rotations about the *y* and *x* axes, respectively
Ω	surface of the plate.
ω	Natural frequency
τ_{xy}	In-plane shear stress
τ_{xz}, τ_{yz}	Transverse shear stresses

Abbreviations

2D Two-dimensional

3D Three-dimensional

AM Additive Manufacturing

ANS Assumed natural shear strain

CAD Computer-aided design

CPT The Classical Plate theory

CUF Carrera's Unified Formulation

CVD Chemical Vapor Deposition

DOF Degrees of freedom

DQM Differential quadrature method

ESDPT Exponential shear deformation theory

FEM Finite element method

FGM Functionally Graded Materials

FSDT First Order Shear Deformation Theory

FSM Finite strip method

GSDT Generalized shear deformation plate theory

HSDPT Hyperbolic shear deformation plate theory

HSDTs Higher-Order Shear Deformation Theories

IBAD Ion Beam Assisted Deposition

IGA Isogeometric analysis approach

LRVE Local Representative Volume Elements

PM Powder Metallurgy

PVD Physical Vapor Deposition

R4FSDT Four-node rectangular element based on first order shear deformation theory

R4SSDT Four-node rectangular element based on trigonometric shear deformation theory

RPIM Radial point interpolation method

RPT Refined Plate Theory

SCF Shear Correction Factor

SCSDT Second-order shear deformation theories

SDL Sinusoidally distributed load

SHS Self- Propagating High-temperature Synthesis

SSDT Sinusoidal shear deformation theory

TSDT Third order shear deformation theories

UDL Uniformly distributed load

General introduction

Scientific progress in the field of materials technology and the continuous development of modern industries have given rise to the continual demand for ever more advanced materials with the necessary properties and qualities. The need for advanced materials with specific properties has led to the gradual transformation of materials from their basic (monolithic) state into composites.

A composite material is a class of advanced material, made up of two or more materials of different nature, whose combination confers to the whole superior performances to those of the components taken separately. It consists of a matrix in which particles or fibers called "reinforcement" are embedded. Thus, properties such as stiffness, fatigue resistance, corrosion resistance, wear resistance, weight reduction and many others are improved. However, a major problem with conventional composite materials, which are usually made of layers (i.e., laminated composites), is the discontinuity of properties and stresses at the interfaces. This discontinuity leads to high stress concentrations, matrix cracking and a serious delamination problem due to the abrupt composition transition, especially in a high temperature environment.

One way to overcome these adverse effects is to use the Functionally Graded Materials (FGMs) in which material properties vary continuously. This is achieved by gradually changing the volume fraction of the constituent materials, usually in the thickness direction only. FGM eliminates the sharp interfaces that exist in composite materials and cause failures. It replaces this sharp interface with a gradient interface which produces smooth transition from one material to another. One unique characteristic of FGM is the ability to tailor a material for specific application.

FGMs occur in nature as bones, teeth etc., nature designed these materials to meet their expected service requirements. This idea is emulated from nature to solve engineering problem the same way artificial neural network is used to emulate human brain. FGMs were initially designed in the early 1980s by Japanese scientists, as thermal barrier materials for aerospace structural applications and fusion reactors. Nowadays, they have found application in various branches of engineering as structural elements such as plates, beams, shells, etc, for example, in aerospace structures, power generation industries, machine parts, etc. In recent years, these new classes of materials have gained considerable attention that motivates the importance of a deep understanding of their behavior.

FGMs possess complex behaviors that require sophisticated numerical tools for their analysis. The finite element method has established itself in recent years as a powerful and efficient method, which allows it to be widely used in the analysis of the complex behavior of this type of materials.

In general, the behavior of structural elements made of FGMs, for instance plates, can be described by three-dimensional (3D) or two-dimensional (2D) theories. The 3D approach is more accurate, however, it is difficult to implement. Therefore, the 2D approach is widely used due to its simplicity and low computational cost. For decades, the classical and first-order shear deformation theories have been used for the analysis of FG structure components behaviors. Although these theories give relatively accurate results, they show their shortcomings when evaluating the transverse shear stresses and require shear correction factors. With higher-order shear deformation theories (HSDTs), more comprehensive shear stress/strain through the plate thickness are obtained and shear stress-free boundary condition is satisfied at top and bottom surfaces as the displacement field takes into account higher order terms, and no shear correction factors are needed. It should be emphasized that the results derived from HSDTs are more accurate than those of FSDT.

Thesis objectives

The main objective of the present work is to contribute to the modeling of the static, stability and dynamic behavior of plates made of functionally graded materials, by developing finite elements that are able to describe in the most accurate way such behaviors. This work is divided into two main parts. In the first part, a finite element based on first-order shear deformation theory has been adapted to the analysis of FG single layer and sandwich plates. The element is geometrically simple and has only four nodes and five degrees of freedom per node. In the second part of this work, a novel trigonometric model has been proposed for the analysis of FG plates behaviors. Based on this new model, a four node rectangular finite element with five degrees of freedom per node, has been formulated, ensuring a better compromise between accuracy and low cost. Furthermore, another objective of this work is to study the effect of different parameters on the behavior of FG plate, such as the power-law index, side-to-thickness ratio, boundary conditions, the aspect ratio, etc.

Thesis organization

This doctoral research work is divided into three parts:

Part one entitled **‘’literature review’’** contains Chapters 1 and 2

Chapter 1 provides an overview of functionally graded materials, their characteristics, development history, fabrication techniques, application areas, and various micromechanical models and gradation laws used to describe their effective properties. Some naturally existing FGMs have been also presented.

In **Chapter 2,** the most commonly used plate theories for the analysis and modeling of FG plates have been briefly described. A review of various investigations carried out in the existing literature on static, vibration, and buckling analyses of FG plates has been also presented.

Part two entitled **''Adaptation of a first-order shear deformation finite element model for the analysis of FG plates behavior''** includes Chapters 3 and 4

In **Chapter 3,** a four-node rectangular finite element (R4FSDT) with five degrees of freedom per node, based on FSDT, previously developed for the analysis of angle-ply laminated composite, has been adapted to FG plates analysis. The element has been used to analyze the different behaviors (static, dynamic and buckling) of FG single layer and sandwich plates. The material properties of the plates have been assumed to change continuously through the thickness, depending on the volume fraction of the constituent materials based on the power-law function. The von Karman strain tensor has been used to account for the second order effect (Buckling). The concept of the neutral surface position has been introduced to simplify the problem and to avoid the membrane–bending coupling. The total potential energy principal, Hamilton's principle and Lagrangian equation have been used for the derivation of the stiffness, geometrical and mass matrices. The assumed natural shear strain technique has been introduced to ensure the effectiveness of the element against the shear locking phenomenon.

Chapter 4 is devoted to the validation of the R4FSDT element, developed in the third chapter, in static, stability and dynamic analysis of FG single layer and sandwich plates. The obtained results in terms of deflection, stresses, critical buckling loads and natural frequencies have been compared to those determined analytically and those obtained using finite element models available in the literature. In addition, the effects of some parameters such as power-law index, side-to-thickness ratio, shear correction factor on the static, buckling and free vibration responses of FG single layer and sandwich plate have been shown.

Part three entitled **''Development of a new finite element model based on new trigonometric shear deformation theory for the analysis of FG plates''** includes Chapters 5 and 6

Chapter 5 presents a new trigonometric model for the analysis of FG plates behaviors. The model accounts for a sinusoidal variation of the transverse shear strains across the thickness and satisfies the shear stress-free boundary conditions on the top and bottom surfaces of the plate, without the need of shear correction factor.

The development of a four node rectangular finite element (R4SSDT) with five degrees of freedom per node, based on the proposed model has been also presented in this chapter. The developed finite element has been intended for the analysis of static, buckling and dynamic behaviors of FG single layer plates, considering that the material properties of the FG plates change continuously through the thickness, depending on the volume fraction of the constituent materials based on the power-law function. The von Karman strain tensor has been used to take into account the second order effect. Total potential energy and Hamilton' principles and Lagrangian equation have been used to formulate the stiffness, geometric and mass matrices. The assumed natural shear strain technique has been employed to prevent any potential shear locking phenomenon. Moreover, the concept of the neutral plane has been introduced to avoid the membrane–bending coupling.

Chapter 6 presents the static, mechanical buckling and free vibration analysis results obtained using the finite element (R4SSDT), developed in chapter 5. The comparison of these results with those reported in the available literature shows the performance and the accuracy of the proposed formulation. The effect of some parameters such as power-law index, side-to-thickness ratio...etc, on the variation of deflection, normal and shear stresses, natural frequencies, as well as the critical loads of FG single layer plates has been also investigated.

Finally, the work ends with a general conclusion summarizing the problematic, objectives and obtained results, followed by some perspectives.

Part I
Literature Review

Chapter 1

Functionally Graded Materials: An overview

1.1 Introduction

Material development is the key driver of the world we live in, as all areas of human endeavor depend on material development for their performance. The evolution of materials, from monolithic to alloy and the development of composites, is based on the limitation of one class of materials that necessitates the development of other classes. Most applications require materials with conflicting properties that may not be possible to achieve in a monolithic material. Furthermore, the alloying of different materials is limited by the thermodynamic behavior of the constituent and the limitation imposed by the degree to which one material can be mixed with others. Functionally Graded Material (FGM) is the one that can meet the demands of these applications. This material is an advanced composite material that can survive in a harsh working environment, without losing its properties, and without fail during service.

An FGM is characterized by a compositional gradient of one material into another, making it completely different from conventional composite materials. The necessity of this material was born out of the failure of conventional composites, resulting from their inability to withstand harsh working conditions. The failure of traditional composite materials was due to the distinct, or well-defined, interface that exists between composite materials layers. The interface causes a high concentration of stresses which favors the initiation of cracks and their eventual propagation which leads to the ultimate failure of the composite. This process is known as "delamination". This interface is systematically eliminated in FGMs, due to the gradual change in the volume fractions of their components and, consequently, their properties in a specific direction.

The actual concept of FGM was acquired from nature and used to solve engineering problems in the same way that nature has used such materials based on their application requirement and areas of application.

FGM was initially developed for a thermal barrier application, now, the application of this important advanced material has been increased and used to solve a number of problems in engineering. Aerospace, automobile, and biomedical applications are some of the areas that are benefitting from this novel material.

1.2 Definitions and concept of FGM

Functionally Graded Materials, or ‘‘gradient materials’’ (FGMs), represent a novel, advanced generation of composite materials and have been designed to achieve superior levels of performance [1].

The term “Functionally Graded Materials” contains two important words: “functionally” and “graded.” The word “functionally” modifies “graded.” These refer to not only simple functional materials but also to graded materials [2].

FGMs are a class of composite materials that can be tailored for specific properties, functions and applications. Such materials exhibit a gradual change in either compositions/constituents or microstructures (e.g., grain size, texture, porosity, etc.) in specific directions, resulting in corresponding changes in material properties [3], i.e., they are inhomogeneous at the macroscopic and microscopic levels. [4]. In contrast, conventional composite materials are either homogeneous mixtures involving a compromise between the properties of the constituent materials, or two different materials joined together as in the case of laminated composites. Figure 1.1 [5], presents the schematic diagram of (a) the FGM and (b) the conventional laminate composite material.

FGMs do not contain distinct (well-distinguished) boundaries or interfaces between their different regions as in the case of conventional composite materials. Therefore, FGMs possess good chances of reducing mechanical and thermal stress concentration in many structural elements, which can be developed for specific applications.

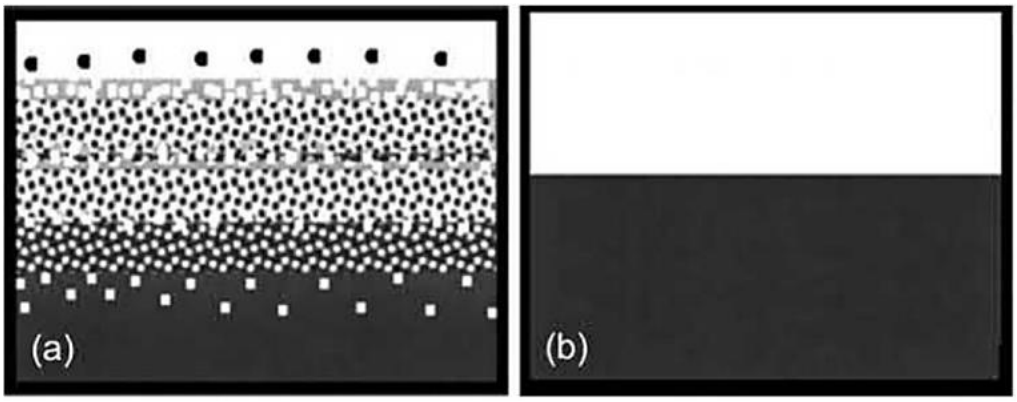

Figure 1.1 Schematic diagram of (a) FGM and (b) conventional laminate composite material [5].

FGMs were first used in Japan in 1984 during a space plane project for thermal barrier application, where their concept was first proposed [6]. The concept of these materials was proposed to reduce the thermal stresses in the conventional laminate composite materials developed for reusable rocket engines [7].

A group of researchers at the (National Aerospace Laboratory, STA, Sendai) were faced with the problem of developing a material that could withstand a high temperature difference. The application required that one side of the composite materials be subjected to a temperature of about 2000 K (1726,85°C) and this temperature should not be transmitted to the other part of the composite. In other words, the body of the plane needs a composite material that will be exposed to a temperature gradient of approximately 1000 K, between the inside and the outside of the spaceplane, as shown in Figure 1.2 [1, 5, 8, 10]. Conventional laminated composite materials that were tried for this project kept failing due to the delamination (i.e., separation of the laminated composite materials from where the two constituent materials were joined). The failure was a result of the distinct interface between the constituent materials, which is a site of high stress concentration factor (Figure 1.3 [11]), and the site where failure is usually initiated. The researchers knew that if the interface between the two materials that form the composite could be eliminated, then the problem would be solved. **The researchers changed this sharp interface into a gradient interface by gradually introducing the second material into the first material instead of 100% of**

one material and 100% of the second together. In this way, the sharp interface was eliminated, and a novel material called FGM was developed [9].

In summary, FGM's concept is to replace the sudden change in composition that occurs at the interface between different materials, with a compositionally graded phase, in order to reduce stress concentrations in the structure.

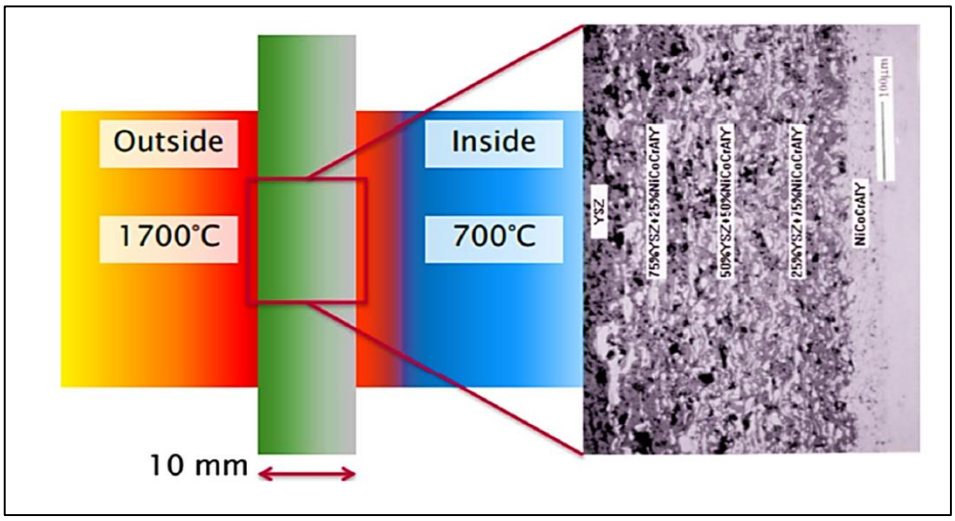

Figure 1.2 First example for metallic FGM in Japan [10].

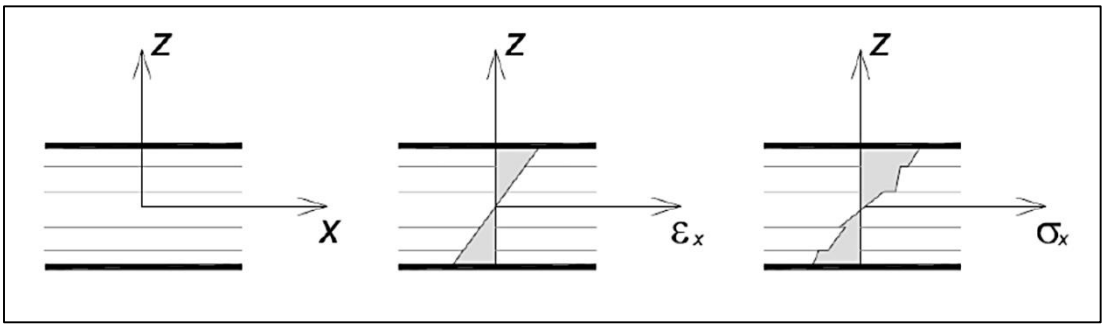

Figure 1.3 Variation of strains and stresses through the thickness of a laminate plate [11].

An FGM is usually made up of several materials with different properties. The overall properties of FGM are unique and different from any of the individual constituents. In some cases, there may be an FGM comprised of the same material but with different microstructures. Pores also are important components of FGMs, in which a gradual increase in pore distribution from the interior to the surface can confer many properties such as mechanical shock resistance, thermal insulation, catalytic efficiency, and the relaxation of thermal stress [3].

FGMs can be classified into continuous and discontinuous graded materials, as schematically shown in Figures 1.4 (a) and (b) [12], respectively. In continuous FGMs, the material ingredients and /or microstructure change continuously with positions, no clear zones or separation cut lines can be observed inside the material to distinguish the properties of each zone, whereas, in discontinuous FGMs, the microstructure and/or material composition change in a step-wise manner, resulting in a multilayered structure with an interface lying between discrete layers [3, 12]. Similarly, material properties can be varied from one surface to another, either continuously or discontinuously as shown in Figures 1.5 (a) and (b) [10], respectively. It is worthy of mention that the material ingredients may vary spatially throughout the entire material volume, or only at a specific location in the material such as the interface, a joint, or a surface as shown in Figure 1.6 [3, 13, 14].

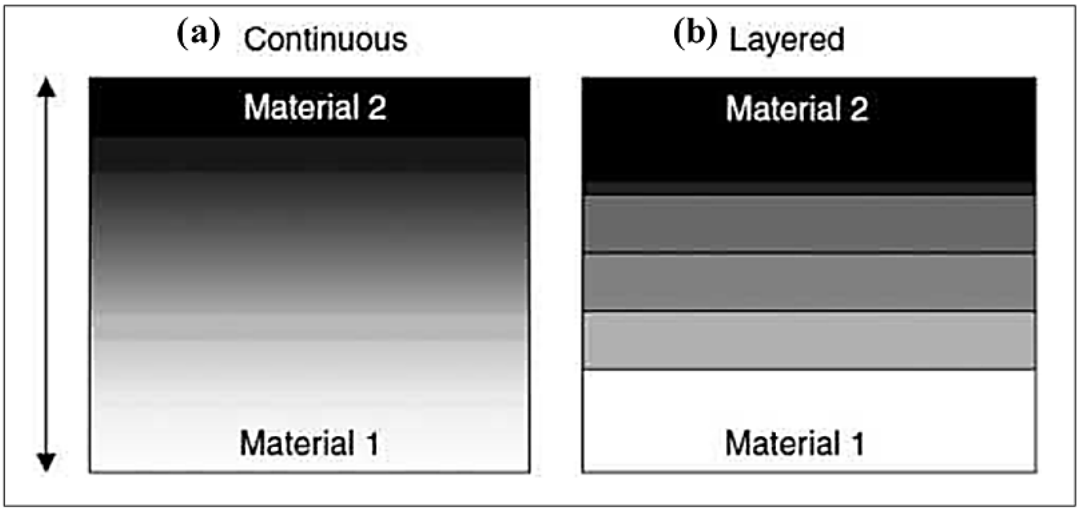

Figure 1.4 Types of FGMs (a) continuous FGM, and (b) discontinuous FGM [12].

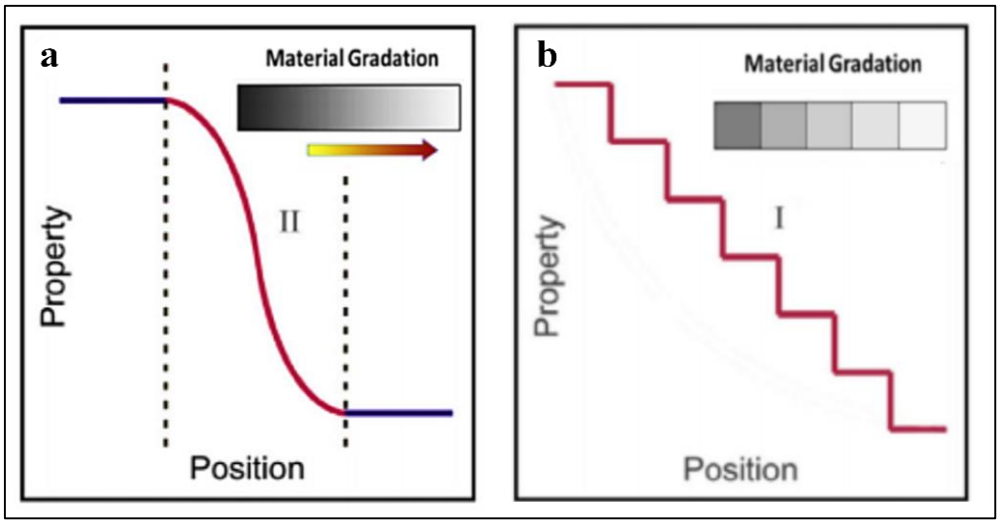

Figure 1.5 Variation of properties (a) Continuous and (b) discontinuous [10].

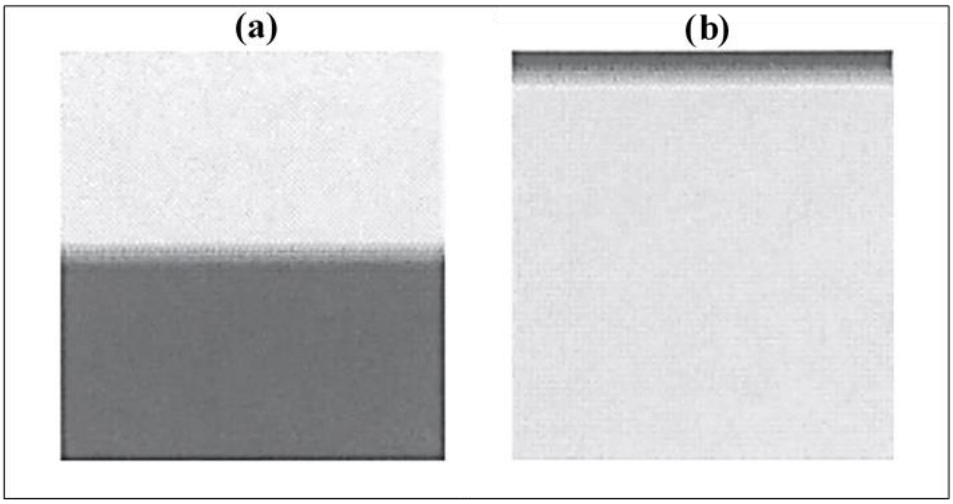

Figure 1.6 Graded structures (a) at the joint, and (b) Surface [3].

Commonly used FGMs are continuously graded in one specific direction. But in all types of FGMs, a smooth transition in thermomechanical properties is ensured, thereby mitigating problems due to delamination and cracking. FGMs are typically manufactured from isotropic components such as metals and ceramics. A continuous gradient microstructure with metal-ceramic constituents is schematically represented in Figure1.7 [15]. In general, metal-ceramic FGMs are used in high-temperature applications where the ceramic part of FGMs can withstand high-temperature environments due to their better thermal resistance characteristics; meanwhile, the metal part provides stronger mechanical performance and reduces the possibility of catastrophic fracture. The transition phase provides thermal protection as well as eliminates interface problems.

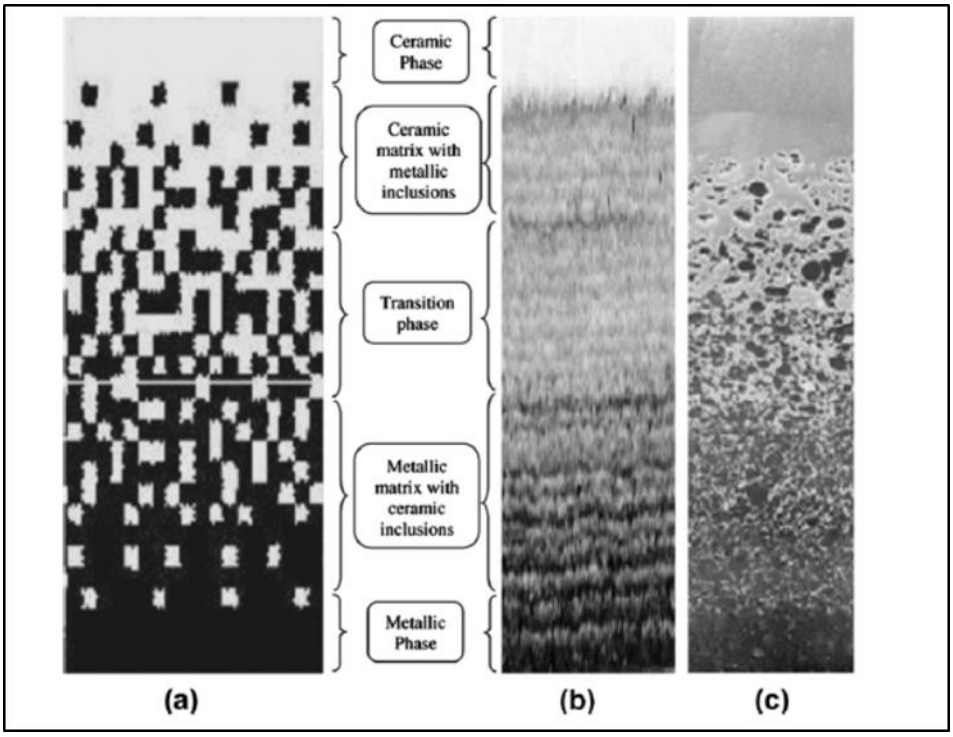

Figure 1.7 Schematic of continuously graded microstructure with metal-ceramic constituents (a) Smoothly graded microstructure (b) Enlarged view and (c) Ceramic–Metal FGM [15].

From the foregoing, it is possible to extract many advantages offered by functionally graded materials, we intend to emphasize them here in some lines.

- ✓ Because of their gradient interfaces, FGMs can help minimize thermal-mechanical stress concentrations, hence preventing delamination at crack-sensitive regions and improving the durability of loadbearing structures.

- ✓ Porosity-graded FGM helps in absorbing the shock from one face to the other, provides thermal insulation, aids the catalytic efficiency; and also helps to relax the electrical and the thermal stresses.

- ✓ FGM can act as an interface layer that connects two incompatible materials so as to enhance the bond strength, reduce the crack driving force developed within the material, provide multi-functionality namely, the ability to control deformation, wear corrosion, dynamic response, etc. FGM coatings reduce the internal residual stresses.

- ✓ Metal- ceramic FGM eliminates the abrupt transition between coefficients of thermal expansion, offers thermal/corrosion protection, and provides load-carrying capability.

1.3 Brief background on the research and development of FGMs

Though the concept of FGMs has been introduced in the early 1980s by Japanese researchers, the general idea for theoretical applications of graded structure composite and polymeric materials was suggested as a concept for the first time in 1972, by Bever and Duwez [16], and Shen and Bever [17]. However, their works had only limited impact, probably due to a lack of suitable production methods and technologies for FGMs at that time.

In the year 1986, the official terming as ‘’Functionally Gradient Materials’’, FGM, was done. As a consequence of a discussion at the Third International Symposium on FGMs held in Lausanne in 1994, the full name was changed in 1995 to ‘’Functionally Graded Materials’’ because it is more accurate both descriptively and grammatically [3, 18].

In 1987, a five-year (1987 – 1992) research project was initiated. entitled “Research on the basic Technology for the development of FGM for relaxation of thermal stress” (FGM PART1). The program aimed to develop FGMs for high-temperature uses with the objective

of using them for the hypersonic spaceplane. At the end of this project, samples of 300mm square shell and 50mm diameter hemispherical bowls for SiC-C FGM nose cones were prepared. [19].

In 1990, the first international conference on FGM (FGM 1990) was held in Sendai, Japan which was followed by regular conferences held every two years [3]. In 1992, FGMs were selected as one of the10 most advanced technologies in Japan [1].

Another 5-year (1993- 1998) project, a consequence of FGM (PART 1), has been launched in 1993 as "Research on energy conversion materials with functional gradient structures" (FGM part 2). This project focused to enhance energy conversion efficiency using FG structure technology. [6, 19, 20].

In 2001, an international workshop presenting the recent trend and forecast has been conducted under the chairmanship of Prof. Naotake Ooyama. Various topics like modeling and simulation, automatic manufacturing systems for FGM, residual stress measurement, ultrasonic imaging, and the biocompatibility of FG implant materials have been presented. Since then regular research programs, international symposiums, and workshops have been held across the world [18]. As the latest update to this, the 16th international conference on FGM (FGM 2022) will be held On August 7-10, 2022 in Hartford, USA.

1.4 Functionally graded materials in nature

Although the concept of FGMs and the ability to manufacture them, appears to be an advanced engineering invention, the concept is not new. It is basically bio-inspired [15, 21]. Scientists and engineers have always drawn inspiration from nature to solve scientific and technological problems. One example is the artificial neural network, which mimics the neural network of the human brain and how it processes information, and has been used to solve many engineering problems.

Most materials found in nature are based on FGMs, as nature has produced them based on the functionality required from these materials, as well as the working environment to which they are subjected. There are a lot of natural FGMs that have inspired scientists and engineers to design materials that are used to solve engineering and medical problems [22]. Bamboo is an example of nature’s FGMs that possess continuously graded properties and is characterized by non-uniform distribution of constituent material and varying microstructure

[23]. Another important natural FGM is wood, which is composed of cellulose and lignin, with the lignin forming the matrix while the cellulose is dispersed in varying degrees across the entire material [24].

Some tissues and organs in the human body are also naturally existing FGMs, including human skin, teeth, and bone. Human skin has a complex multi-layered structural system that consists of the epidermis, the dermis, and the hypodermis [25]. Each layer has different properties and also performs different functions. Human teeth have an outer part made with high wear-resistant material that is referred to as enamel, while the internal core is made up of dentine. The transition from the enamel to dentine is provided by an intermediate FGM layer, where the composition gradually changes from one material to the other. The bone tissue contains the cancellous (spongy bone) with changes in pore density and distribution [5]. Figure 1.8 shows certain naturally occurring functionally graded materials [21].

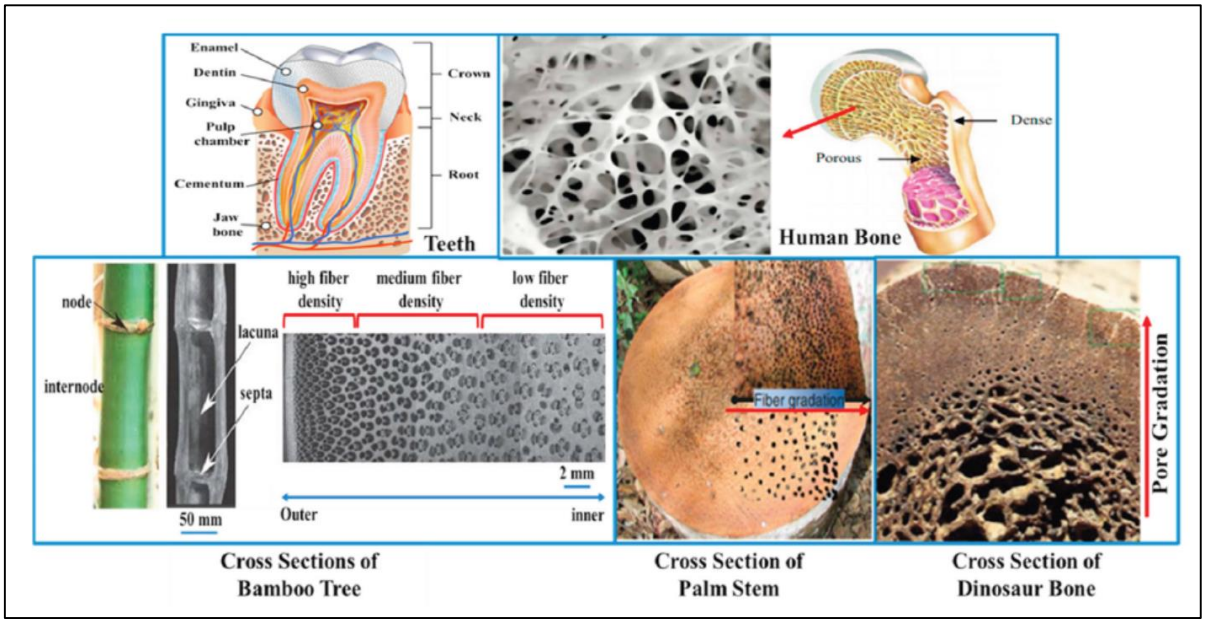

Figure 1.8 Some examples of naturally existing FGMs [21].

1.5 Fabrication techniques of FGMs

The fabrication process is one of the most important fields in FGM research, where a large part of the research work on FGMs has been devoted to processing. FGMs could be in the form of thin coatings that are applied to the surface of the material to improve the surface properties of such materials, or it could be in form of bulk material, in which the material properties are changing across the whole volume of the material. Several techniques have been introduced to fabricate FGMs depending on the requirement, either for surface coatings or bulk FGM.

Surface coatings are thin FGMs typically deposited by several vapor deposition techniques [26]. As well, surface coatings can also be prepared using techniques such as plasma spraying [27], electrodeposition [28], electrophoretic [29], Ion Beam Assisted Deposition (IBAD) [30] and Self- Propagating High-temperature Synthesis (SHS) [31], etc.

Bulk FGMs could be fabricated by the Powder Metallurgy (PM) method [32], the centrifugal casting method [33], the slip casting method [34], and the tape casting method [35], etc. Among the advanced available methods, additive manufacturing [36] is one of the promising processes for bulk and thin coating.

The fabrication process of an FGM can usually be divided into two steps. The initial one is the building up of the spatially inhomogeneous structure called ***Gradation***. The second is the transformation of this structure into a bulk material called ***Consolidation***. In detail, the gradation process can be categorized into constitutive, homogenizing, and segregating processes. The stepwise build-up of the graded structure from precursor materials is the ***constitutive*** process. ***Homogenizing*** is a process of converting sharp interfaces between two materials into a gradient by material support. ***Segregation*** starts with a macroscopically homogeneous material, which is converted into graded material by material transport caused by an external field (i.e. gravitational, electrical field, etc). Normally sintering and solidification follow the gradation process [37].

The existing and most updated fabrication techniques of FGMs are discussed in the following sections.

1.5.1 Vapor deposition technique

The vapor deposition technique is one of the most important techniques to produce a graded thin film (from nm to sub-mm) by the constructive process. The vapor deposition method describes a process by which materials are condensed into a solid material during the vapor cycle [38]. There are multiple versions of the vapor deposition techniques. Examples of these techniques are Chemical Vapor Deposition (CVD), Physical Vapor Deposition (PVD), and sputter deposition, among others. These vapor deposition techniques are used to ensure slim surface covering and a high-quality microstructure finish. However, these techniques produce harmful gases by-products [39]. Therefore, precaution and safety measures need to be undertaken if the Vapor Deposition Technique is chosen as a manufacturing method. Figures 1.9 [40] and 1.10 [21] illustrate the schematic diagram of CVD and PVD processes, respectively.

1.5.2 Power metallurgy (PM)

The powder metallurgy (PM) [41] process is an old manufacturing process for making engineering parts, which is also now used to produce FGMs through three basic steps, namely: weighing and mixing of powder according to the predesigned spatial distribution as dictated by the functional requirement, stacking and ramming of the premixed-powders, and finally sintering, as illustrated in Fig 1.11 [42]. PM technique gives rise to a stepwise structure. If a continuous structure is desired, then the centrifugal method is used.

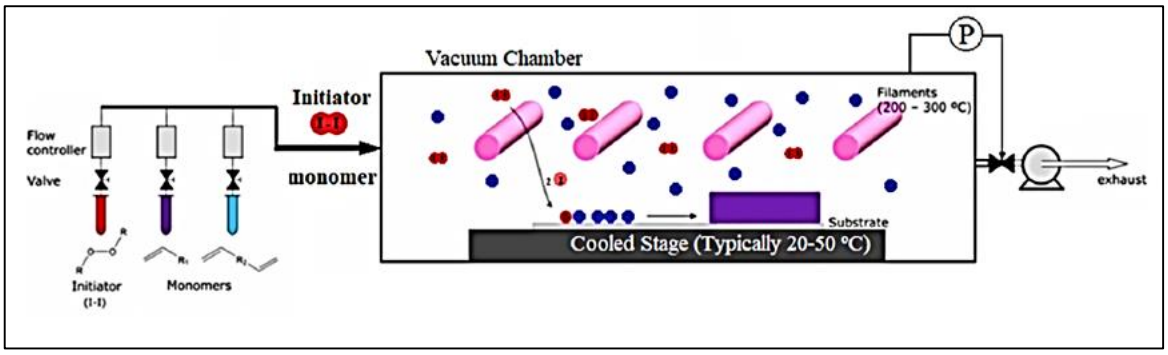

Figure 1.9 Chemical Vapor Deposition (CVD) process [40].

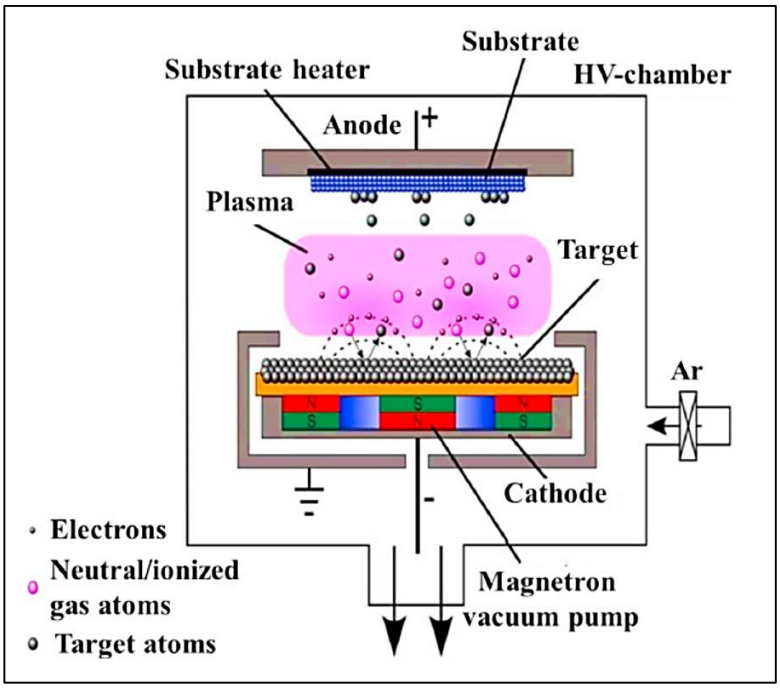

Figure 1.10 Physical Vapor Deposition (PVD) process [21] .

1.5.3 Centrifugal casting method

The centrifugal casting method is performed by pouring a molten material containing another reinforcing material, either in a molten state or solid, into a mold inside a rotating die to produce a functionally graded material [43]. A centrifugal force is created by rotating the die which helps to draw the molten material towards the mold and create separation in the suspended solid powder material and the melting of the two materials, as a result of the different densities of the two materials, and hence the creation of a FGM [33]. The graded distribution of the FGM formed by the centrifugal casting method would be significantly influenced by the processing parameters, such as the difference in density between the reinforcing powder particles and the molten material, the particle size and the particle size distribution of the powder, the viscosity of the molten material, and the solidification time. The apparatus for the centrifugal method and motion of solid particles under the centrifugal force are shown in Figure 1.12 [42].

The main advantage of using the centrifugal casting method for the production of FGMs is that a continuous gradient can be produced. The main disadvantages of the centrifugal casting method include the following:

- It can only be used to produce a cylindrical section, such as a tube, bushing, and cylindrical or tubular castings that are simple in shape.
- The gradation is limited by the centrifugal force and the density difference of the constituent materials.

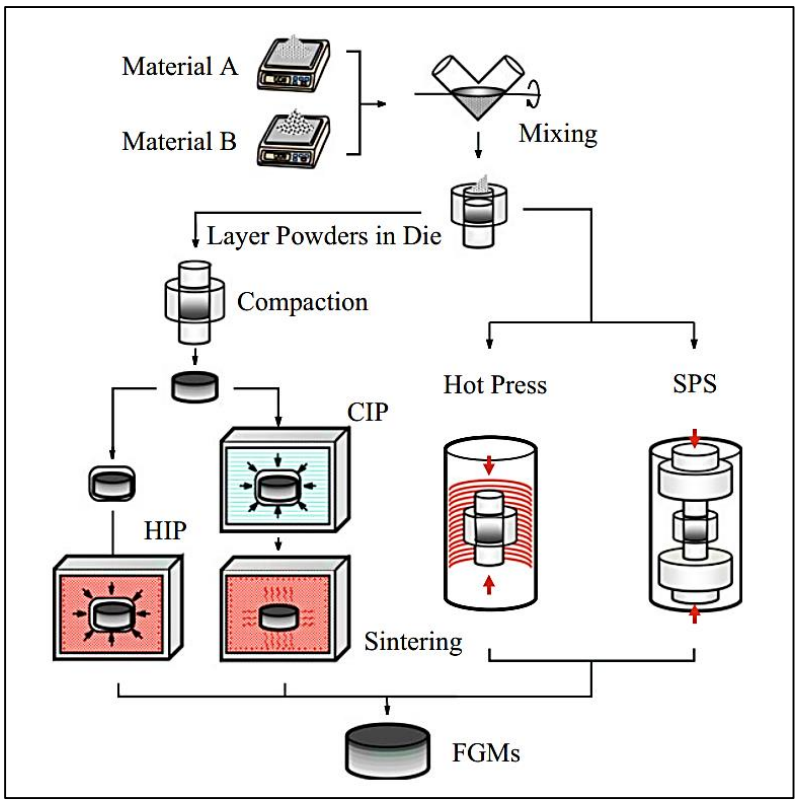

Figure 1.11 Fabrication process of the FGMs by powder Metallurgy [42].

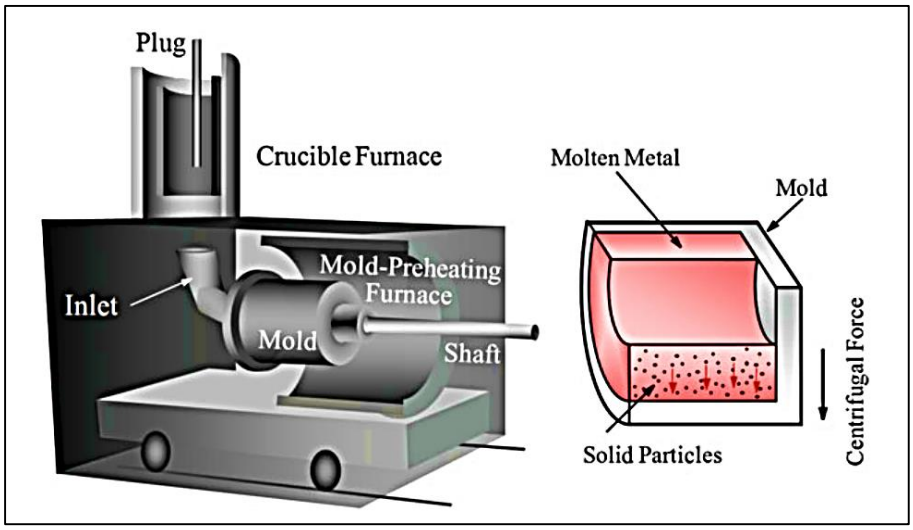

Figure 1.12 The apparatus for the centrifugal method and motion of solid particles under the centrifugal force [42].

1.5.4 Additive manufacturing (AM) method

Additive manufacturing (AM), also known as 3D printing, is an advanced manufacturing method that can be used to fabricate three-dimensional (3D) components or parts by laying one layer of material upon the other using computer-aided design (CAD) data [44]. By this process, it is possible to produce complex shapes and customized products. AM provides freedom to the designer to make the design as per his own specification with the least consideration of design for manufacturing and assembly, thereby higher production speed and maximum material utilization can be achieved.

AM has been proposed as an effective approach to fabricate FGMs with optimized stress profiles and excellent formability [45]. Laser-based methods, stereolithography method, materials jetting process, and fusion deposition simulation [14, 21] can be categorized widely as additive manufacturing methods for production FGMs with discrete gradients. Figure 1.13 illustrates the representative diagram of additive manufacturing [21].

A considerable in-depth understanding of the various FGM's fabrication process, large research investments by industries, and mass production resulted in increasing applications of functionally graded materials in comparison to conventional materials. Some of the areas of application of FGMs are presented in the next section.

1.6 Applications of FGMs

Nowadays, in view of the flexibility of producing composite materials as per application requirements and functional suitability, the scope of FGM utilization is exceptionally wide. Figure 1.14 summarized the different application areas of FGMs. FGM offers great promise in applications with harsh operating conditions or very sensitive applications [40]. Some of these applications, such as aerospace, automotive, biomedical, defense, energy, marine industry, civil engineering and sports are presented in the following subsections.

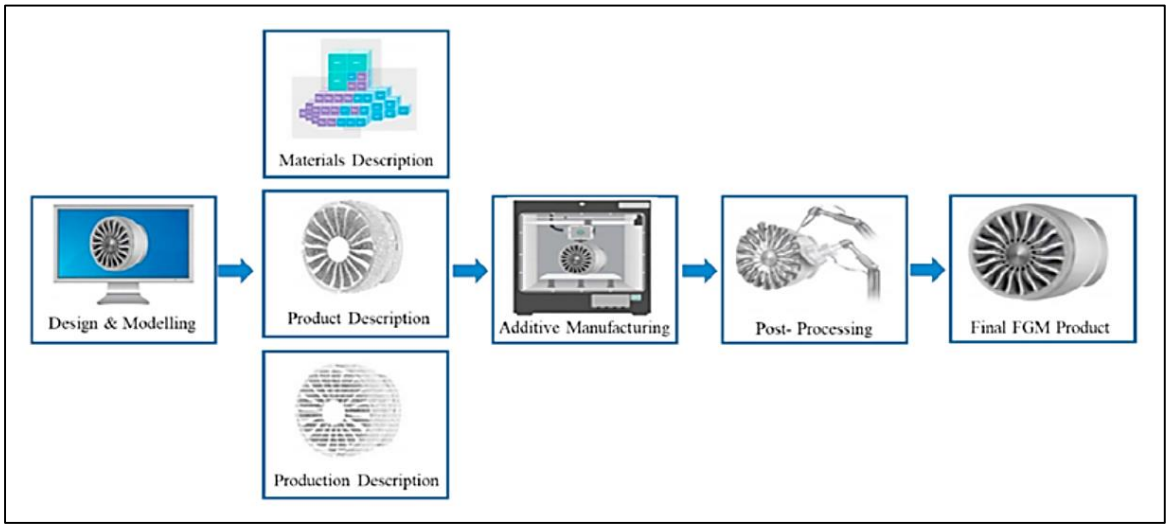

Figure 1.13 Representative diagram of additive manufacturing [21].

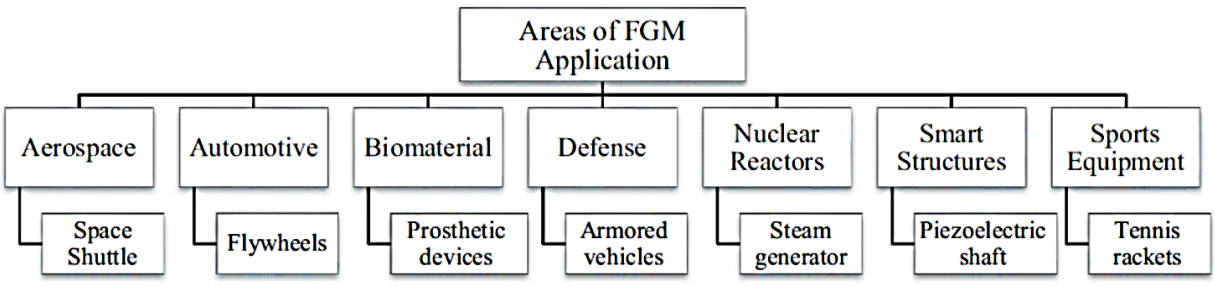

Figure 1.14 FGMs fields of application and some examples [40].

1.6.1 Aerospace applications

FGMs were first used in spacecraft for reducing thermal stresses between outside and inside surfaces. Over the years, the use of such materials extended to various aerospace applications. Most aircraft and spacecraft components are now made of FGMs such as rocket nozzle, heat exchange panels, solar panels, turbine wheels, space plane nose, combustion chamber protective layer, body components, rocket engine components, reflectors, camera housing, caps, and the leading edge of missiles and space shuttle, etc., [46, 47] as shown in Figure 1.15 [21]. FGMs are also used to make a thermal barrier as a wall of a plane (spaceplane frame), to resist the heat generated at the outer surface of the plane due to air friction.

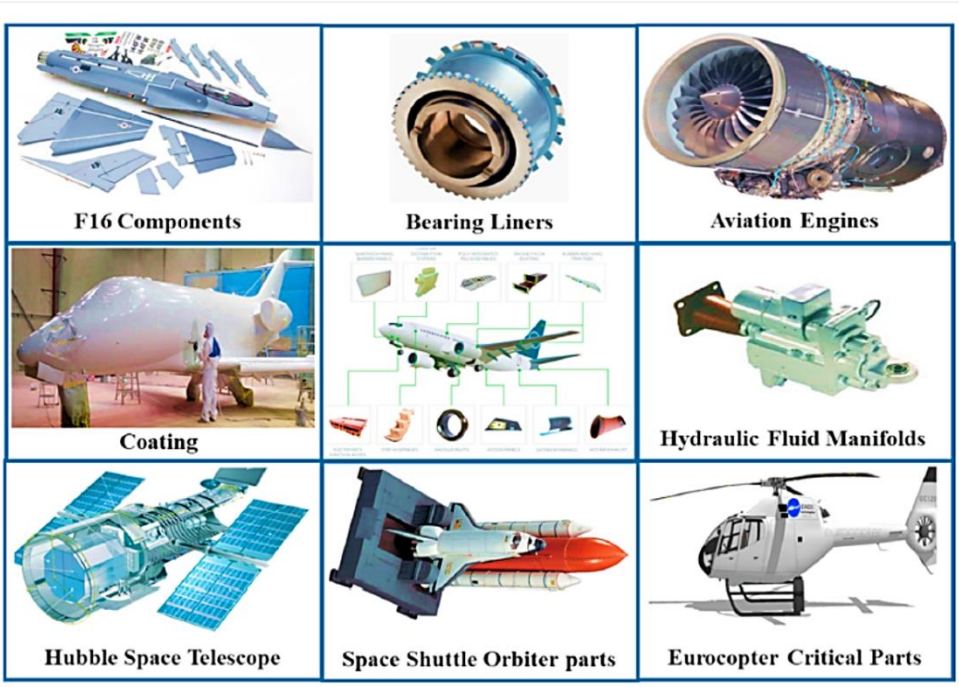

Figure 1.15 FGMs parts in Aerospace applications [21].

1.6.2 Automotive applications

Due to the high cost [48], the use of FGMs is limited in automotive applications. Where, they are only used in the critical parts of the car such as diesel engine pistons and cylinder liners, combustion chambers, racing car brakes, driveshaft's, and flywheels, as shown in Figure 1.16. FGMs can be also used in automotive body coatings [21].

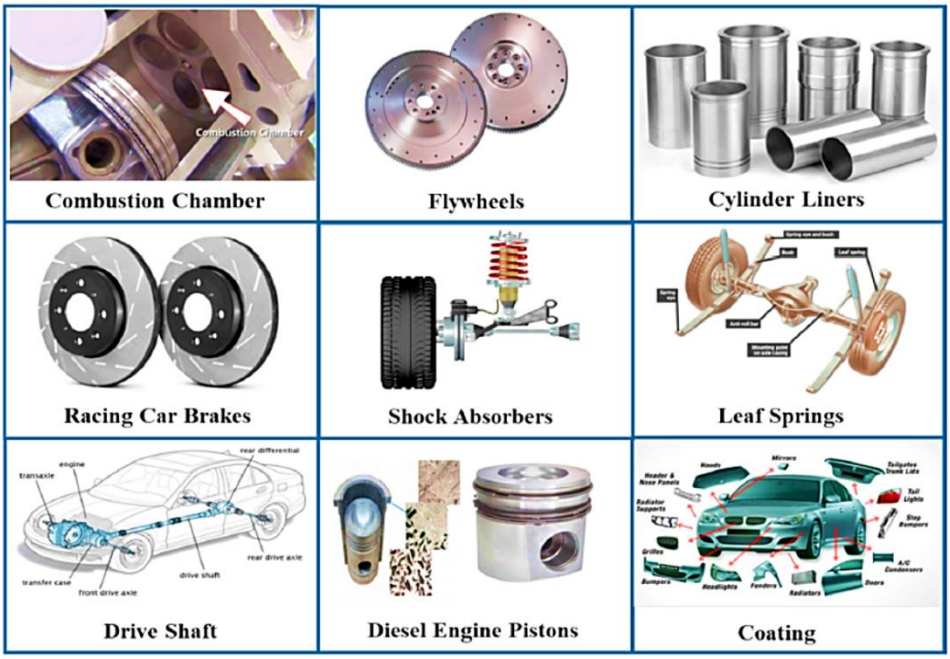

Figure 1.16 FGMs parts in automotive applications [21].

1.6.3 Biomedical applications

Human tissues, such as bones and teeth, are natural FGMs. These tissues may at times suffer from damage that cannot be treated, necessitating their replacement. To replace these tissues, a compatible material that can fulfill the function of the original bio-tissue is required. The ideal candidate for this application is functionally graded materials. FGMs have found a wide range of applications in the dental [49] and orthopedic fields for tooth and bone replacement [50]. Figure 1.17 presents a schematic view of the FGM dental implant with graded material composition [51].

1.6.4 Defense applications

The ability to inhibit crack propagation is one of the most important characteristics of functionally graded materials that makes them useful in defense applications, as a penetration resistant material used for armor plates and bullet-proof vests [52]. Another important application of FGMs is in bulletproof vehicle bodies.

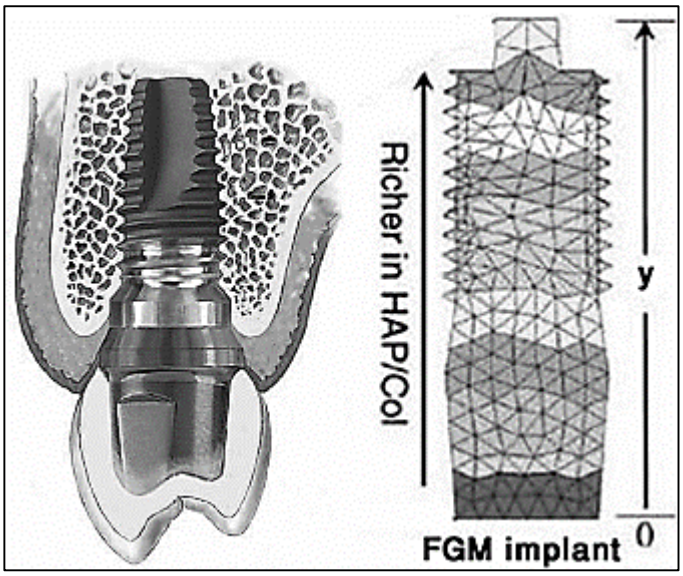

Figure 1.17 Schematic view of the FGM dental implant with graded material composition [51].

1.6.5 Energy applications

FGMs are used in the energy sector to achieve good thermal barrier and protective coatings on turbine blades in gas turbine engines. FGMs are also useful in thermoelectric generators, energy conversion devices, solar cells, sensors, etc [53, 54].

1.6.6 Electrical/electronic applications

Functionally graded materials are used in the electrical and electronics industry in many ways, including field stress relaxation in the electrode and field-spacer interface, in diodes, in semiconductors, for insulators, and in the production of sensors. The thermal-shielding elements in microelectronics are also made from carbon nanotube functionally graded materials [55].

1.6.7 Marine applications

FGMs also have applications in the marine and submarine industry, including propeller shafts, diving cylinders, sonar domes, composite piping systems, and cylindrical pressure hulls. [55, 56]

1.6.8 Opto-electronics applications

FGMs are used in optoelectronic devices because of the refractive index gradients that can be achieved. Examples include lasers, magnetic storage media, sensors, fibers, solar cells, computer circuit boards, and semiconductor applications [56].

1.6.9 Civil engineering applications

Functional gradation of concrete elements makes it possible to align the internal composition of structural components with specific structural and thermal performance requirements. This alignment is made possible by continuously altering the characteristics of the material, including its porosity, strength, or rigidity, in up to three spatial dimensions. This principle can be applied to minimize the mass of the element and to create multifunctional properties. Minimizing porosity improves the structural characteristics of the concrete whereas maximizing porosity enhances its heat insulation properties. Figure 1.18 shows the curves of hardened concrete characteristics depending on a gradual increase in porosity [57].

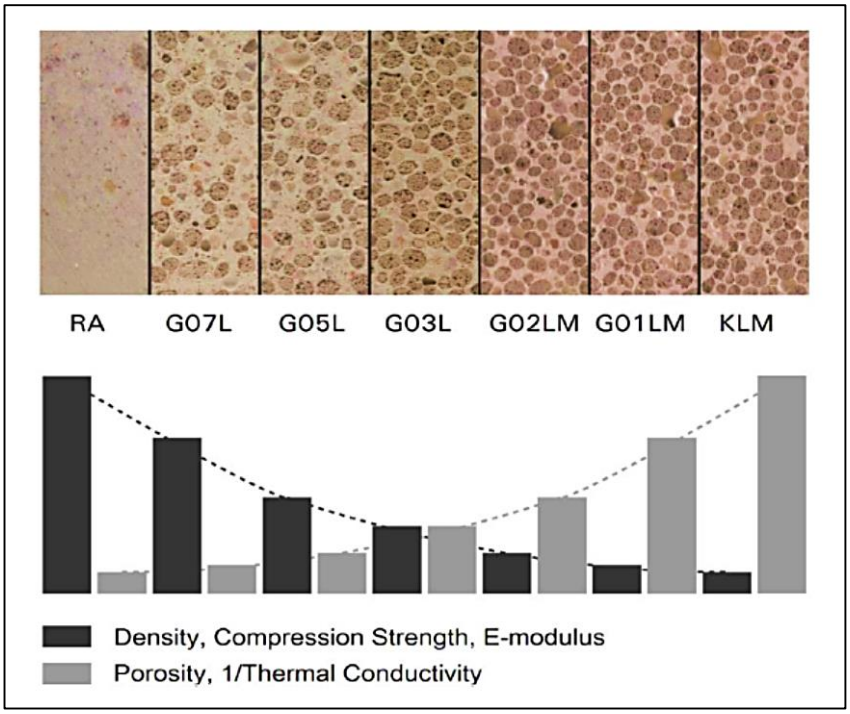

Figure 1.18 Curves of hardened concrete characteristics depending on a gradual increase in porosity [57].

1.6.10 Sport applications

FGMs, in particular those manufactured via AM techniques, are used for sports equipment such as golf clubs, skis, tennis rackets, etc. This is mainly attributed to the graded characteristics obtained and thus the reduction in weight and friction, improved durability, higher strength to weight ratio, hardness, wear resistance, and several other desirable attributes [56].

1.6.11 Other miscellaneous applications

Other uses of FGMs are in cutting tool inserts coating, in the heat exchanger, in tribology, in the making of fire retardant doors, in defense pad making to inhibit crack propagation, etc.

The scope of application of functionally graded materials is expected to expand further if the cost of production of these materials is reduced in the future.

1.7 Modeling of the effective material properties of FGMs

1.7.1 Micromechanical models (homogenization)

Most of the FGMs are manufactured by two phases of materials with different properties. The volume fraction of each phase gradually varies in the gradation direction and the effective properties of FGMs viz. elastic moduli, shear moduli, density, etc. change along this direction.

One of the main tasks of the mechanics of materials is predicting the behavior of materials. This requires the estimation of the effective (overall) properties of the two-phase composition, commonly known as homogenization. Usually, precise information on the size, shape, and distribution of the phases is not available, thus, the effective material properties of graded microstructures must be estimated based on the volume fraction distribution and the approximate shape of the dispersed phase. A variety of micromechanical models have been developed over the years to infer the effective properties of macroscopically homogeneous composites. These models can be extended to determine the effective material properties of FGMs over the entire range of volume fractions [58,59].

From the open literature, some of the micromechanical models used for modeling FGMs could be remarked, as the rules of mixtures. (Voigt [60] and Reuss [61]) are the simplest of them. Hashin–Shtrikman bounds [62, 63], also called the composite sphere assemblage model, determined the upper and lower bounds of the effective material properties by applying the variational principle. The Mori–Tanaka scheme [64] and the self-consistent scheme [65] estimated the effective material properties using the average local stress and strain fields of the constituents of the composite. The three-phase model [66], is also referred to as the generalized self-consistent method because it follows the original self-consistent method. As well Wakashima–Tsukamoto [67], Halpin–Tsai [68], Tamura [69], and cubic local representative volume elements(LRVE) [70] models, are also employed to achieve the effective material properties of FGMs. All these models have been discussed in detail in references [58], [59], [71-74] and a comparison of the estimated properties obtained from these models has been performed.

It is visible from the available studies that most of the research into FGMs uses the Mori-Tanaka and the rule of mixture (Voigt model) to evaluate the effective material properties. These two models are briefly described in the following sections.

1.7.1.1 The Mori–Tanaka scheme

The Mori–Tanaka (1973) model (Tanaka, 1997) is used for estimating the effective moduli of the material. It accounts approximately for the interaction among neighboring inclusions and is generally applicable to regions of the graded microstructure that have a well-defined continuous matrix and a discontinuous particulate phase as depicted in Figure 1.19 [15]. This method assumes that the matrix phase, denoted by the subscript 1, is reinforced by spherical particles of a particulate phase, denoted by the subscript 2.

Mori and Tanaka [64] derived a method to calculate the average internal stress in the matrix of the material. It was reformulated by Benveniste [75] for use in the computation of the effective properties of composite materials. According to Mori-Tanaka model, the effective shear (G) and bulk moduli (K) can be stated in the form [74]

$$G = G_1 + \frac{V}{\frac{1}{G_2 - G_1} + \frac{6(K_1 + 2G_1)(1-V)}{5G_1(3K_1 + 4G_1)}} \tag{1.1}$$

$$K = K_1 + \frac{V}{\frac{1}{K_2 - K_1} + \frac{3(1-V)}{(3K_1 + 4G_1)}} \tag{1.2}$$

Where ***V*** denotes the volume fraction of particles. With the help of shear and bulk moduli, the effective Young's modulus (E) and Poisson's ratio (ν) are then expressed as

$$E = \frac{9GK}{G + 3K} \tag{1.3}$$

$$\nu = \frac{3K - 2G}{2(3K + G)} \tag{1.4}$$

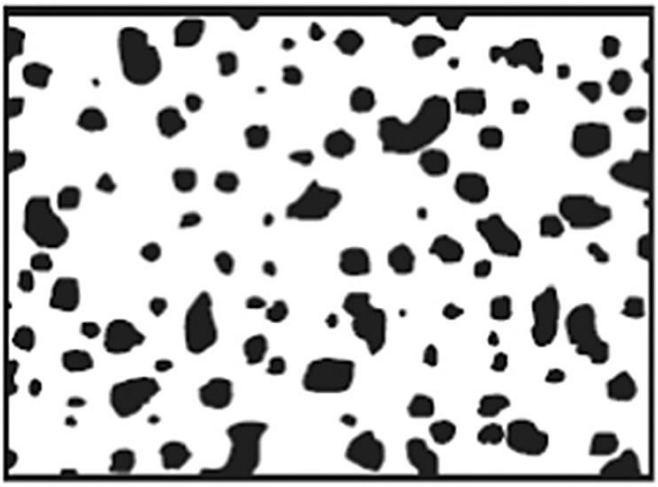

Figure 1.19 Two-phase material with particulate microstructure [15].

1.7.1.2 The rule of the mixture (Voigt Model)

Voigt model, originally introduced by Voigt in 1889 [60], is a well-known model of homogenization and usually used to predict the effective elastic properties for the different kinds of composite materials. The Voigt idea was to define such properties by averaging stresses over all phases with the strain uniformity assumption [59]. For the sake of simplification, Voigt scheme is the most popular and most commonly used model for estimating the properties of FGM.

According to this rule, an arbitrary material property ***P*** of the FGM is assumed to vary smoothly along a direction (usually thickness direction), as a function of the volume fractions and properties of the constituent materials. This property can be expressed as

$$P = \sum_{i=1}^{n} P_i * V_i \tag{1.5}$$

P can represent, for example, the young's modulus (E), the Poisson's ratio (ν) and the mass density (ρ) etc. $\boldsymbol{P_i}$ and $\boldsymbol{V_i}$ are respectively the material property and volume fraction of the constituent ***i*** of FGM. The volume fractions of all the constituent materials should add up to unity, such that

$$\sum_{i=1}^{n} V_i = 1 \tag{1.6}$$

1.7.2 Gradation Laws

The variation of the desired property of an FGM across any direction can be designed according to the requirement by considering various gradation laws. Power law, Exponential and Sigmoid Laws are commonly used by researchers to describe the volume fractions, and are presented in the following sections.

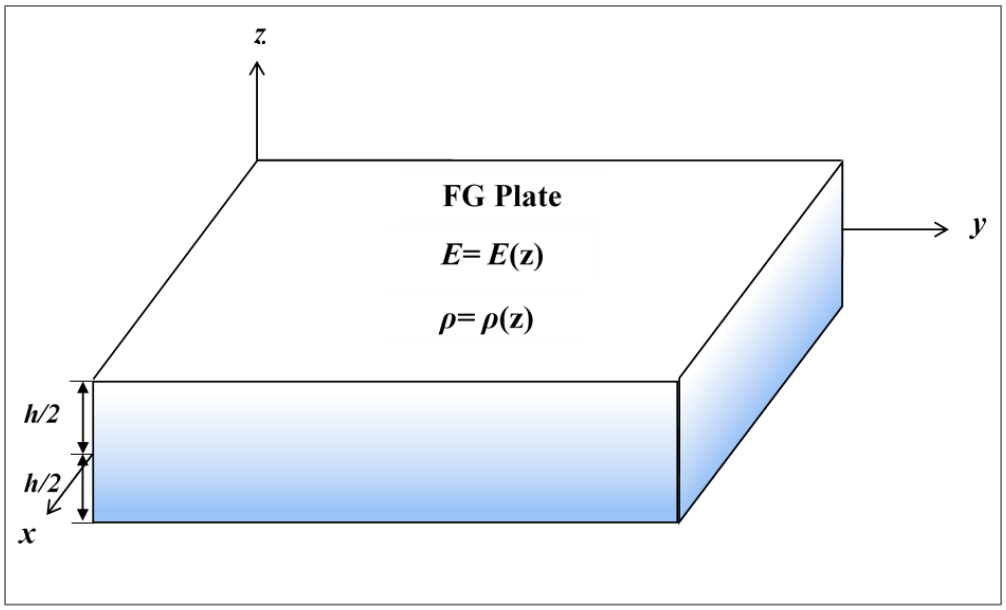

Figure 1.20 Functionally Graded Plate.

1.7.2.1 Power-law (P-FGM)

The power law for the material gradation was first introduced by Wakashima et al. [76]. Further this law is widely used by many researchers and it is more common in the stress analysis of FGM [77]. If FG plate of uniform thickness '*h*', as shown in Figure 1. 20, is used for the analysis then according to this law, the effective material property *P*(*z*)in a specific direction (along *z*), can be determined by

$$P(z) = P_2 + (P_1 - P_2)V(z) \tag{1.7}$$

P represents every effective material property (*E*, α and ρ). P_1 and P_2 are the material properties at the top-most ($z = +h/2$) and bottom-most ($z = -h/2$) surfaces of the plate, respectively. It can be seen that the material properties are dependent on the volume fraction *V* of FGM, which follows the power law as:

$$V(z) = \left(\frac{1}{2} + \frac{z}{h}\right)^p \tag{1.8}$$

where, ($0 \le p \le \infty$) is a volume fraction exponent (or power-law index).

Figure 1.21 illustrates the variation of the volume fraction in the thickness direction of the plate. It can be observed from the figure that the volume fraction decreases rapidly near the lower surface for $p<1$ and increases rapidly near the upper surface for $p> 1$.

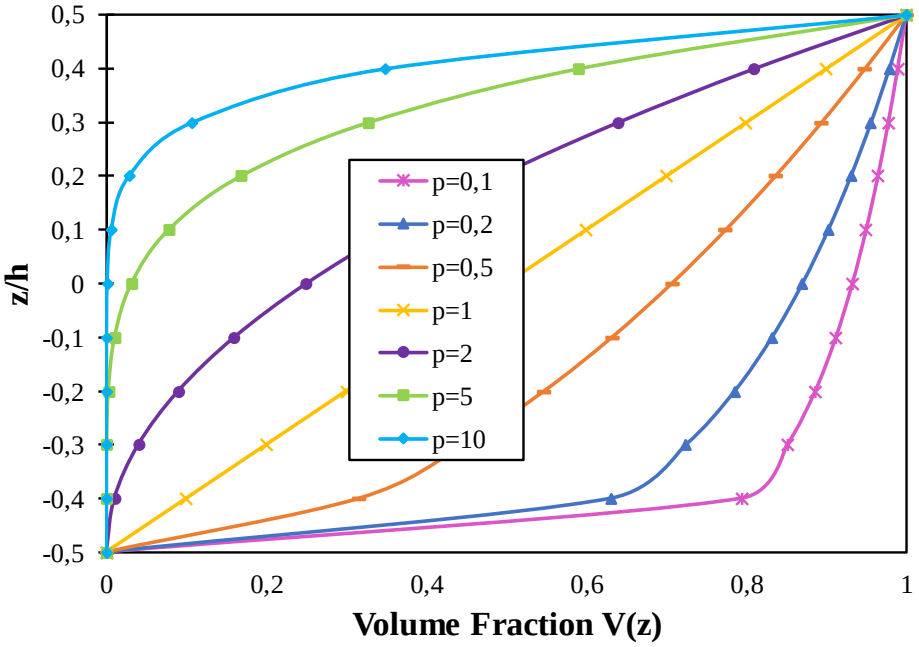

Figure 1.21 Variation of the volume fraction throughout thickness of P-FGM plate.

1.7.2.2 Sigmoid Law(S-FGM)

When a single FGM power law function is added to the multilayered composite, the stress concentrations appear in one of the interfaces in which the material is continuous but changes rapidly. Therefore, Chung and Chi [78] developed another law called the sigmoid law, which is a combination of two power law functions, to ensure the smooth distribution of stresses among all the interfaces. This law is also used to reduce the stress intensity factors in cracked structures [79]. The two power law functions are defined by:

$$V_1(z)=1-\frac{1}{2}\left(\frac{h/2-z}{h/2}\right)^p \qquad \text{For} \quad 0\le z\le h/2 \tag{1.9}$$

$$V_2(z)=\frac{1}{2}\left(\frac{h/2+z}{h/2}\right)^p \qquad \text{For } -h/2\le z\le 0 \tag{1.10}$$

By using the rule of mixture, the effective properties of the S-FGM can be calculated by

$$P(z)=P_2+(P_1-P_2)\left(1-\frac{1}{2}\left(\frac{h/2-z}{h/2}\right)^p\right) \qquad \text{For } 0\le z\le h/2 \tag{1.11}$$

$$P(z)=P_2+(P_1-P_2)\left(\frac{1}{2}\left(\frac{h/2+z}{h/2}\right)^p\right) \qquad \text{For } -h/2\le z\le 0 \tag{1.12}$$

Figure 1. 22 shows the variation of volume fraction in Eqs. (1.9) and (1.10) through the thickness of S-FGM plate.

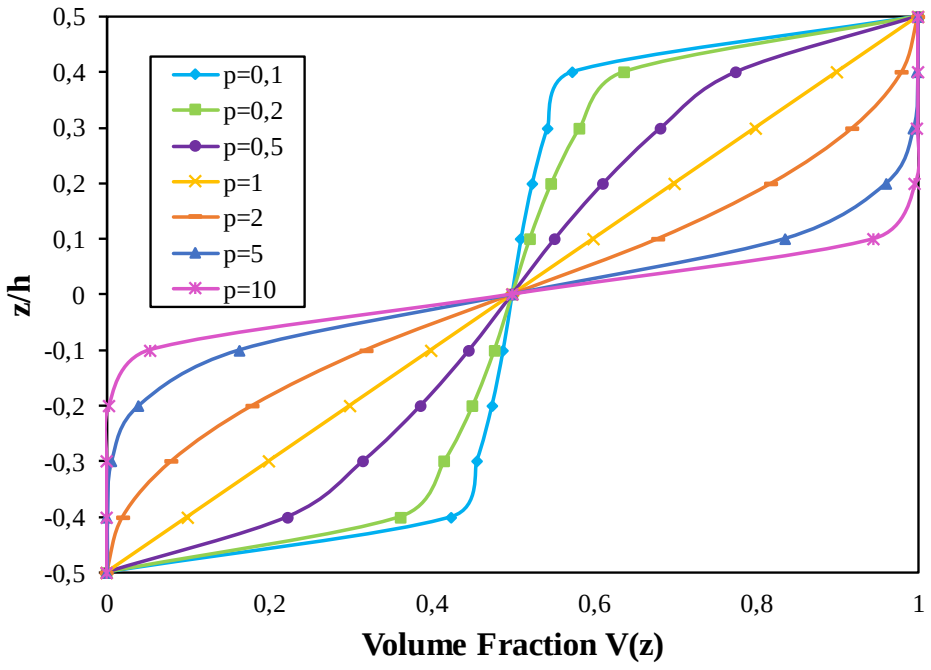

Figure 1.22 Variation of the volume fraction throughout thickness of S-FGM plate.

1.7.2.3 Exponential Law (E-FGM)

The exponential law is generally used to deal with problems related to fracture mechanism of FGM. It is given by Kim and Paulino [80] and Zhang et al. [81]. The distribution of properties of FG plates across the thickness according to the exponential law is as follows:

$$P(z) = P_2 e^{\frac{1}{h}\left(\ln\frac{P_1}{P_2}\right)\left(z+\frac{h}{2}\right)} \tag{1.13}$$

The material distribution (e.g Young's Modulus E distribution) in the thickness direction of the E-FGM plates is plotted in Figure 1.23.

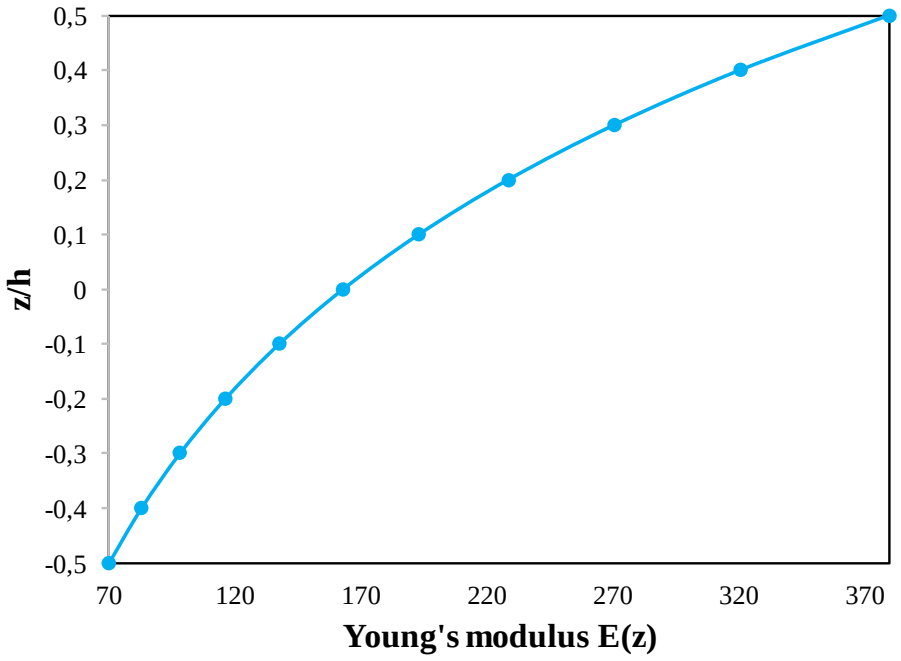

Figure 1.23 Variation of the Young's Modulus E throughout thickness of E-FGM plate.

It should be mentioned that the effective mass density ρ is obtained by the rule of mixture, regardless of the utilized micromechanical models [74]. The effect of Poisson's ratio on deformation was reported by Delale and Erdogan (1983) [82] to be much less than that of Young's modulus. Thus, the Poisson's ratio of plates is assumed to be constant.

1.8 Conclusion

Functionally Graded Materials (FGMs) have been introduced in this chapter. Japanese researchers were confronted with the problem of composite failure through delamination when trying to develop a suitable composite material for a harsh working environment in a space project. This quest to solve the problem led to the development of FGM. FGMs are differently distinguished from conventional composites. Some fundamental features of FGMs have been therefore highlighted. A brief background on the research and development of FGMs has also been presented. FGMs exist in nature, and some of them have been mentioned. FGMs are used as surface coatings (thin coatings) and as bulk material depending on the intended application. The fabrication techniques for the thin FG coating and the bulk FGM have been discussed. FGMs have evolved from the initial thermal barrier application, for which it was developed. The FGM is now used for other applications. Some of these applications have been presented. At the end of the chapter, attention is devoted to the description of micromechanics models and gradation laws employed to describe the effective properties of FGMs.

Due to the wider applicability of FGMs, it is necessary to study their behavior. Thus, to accurately predict FG structures' behavior, several theories and analytical and numerical methods are reported in the literature. The next chapter presents the various theories used for the analysis of FG structures and summarizes the studies based on the static, vibration and buckling behavior of FG structures.

Chapter 2

Modeling and Analysis of FG plates

A Review

2.1 Introduction

Functionally graded materials (FGMs) are increasingly used in the engineering field as structural elements such as plates, beams, shells, etc. In a typical FG plate, the material properties are tailored by mixing two distinct materials, for instance, ceramic and metal. FGMs are well able to reduce thermal stresses, with stand high temperature environments and prevent corrosion. In the case of FG sandwich plates, two types of sandwich are commonly used: (a) sandwich plate with FG core and two isotropic skins; (b) sandwich plate with isotropic core and two FG skins. To use them effectively, a good understanding of their bending, dynamic and buckling behaviors is necessary.

In general, the behavior of FG plates can be described by three-dimensional (3D) or two-dimensional (2D) theories. Although the first approach is more accurate it is difficult to implement, while the second is more popular due to its simplicity and low computational cost.

The most commonly used 2D plate theories are:

- The Classical Plate theory (CPT) that neglects transverse shear effects and it is only suitable for thin plates.
- The First Order Shear Deformation Theory (FSDT) which includes transverse shear effects and is dedicated to moderately thick plates.
- The Higher-Order Shear Deformation Theories (HSDTs) which are dedicated to the plates of more important thickness.

These models are based on assumptions about strains or stresses through the thickness of the plate, which allow the reduction of a 3D problem to a 2D problem.

Since they were widely used in the modeling of FG plates, the above-named theories are briefly described in this chapter. In addition, a review of the studies reported on the static, vibration and buckling analyses of FG plates is presented.

2.2 Different plate theories for FG plates modeling and analysis

A plate is defined as a solid body, bounded by two parallel flat surfaces called faces whose lateral dimensions (i.e., width and length in case of rectangular plates or the diameter in case of circular plates) are large compared to the distance between the flat surfaces called thickness of the plate.

Plates can be classified into two groups: thin plates and thick plates. A plate is said to be thin when the ratio of the thickness to the length of a side is less than 1/20 [11].

2.2.1 Classical plate theory (CPT)

The Classical plate theory, the oldest and the simplest theory was developed in 1888 by Love [83] using assumptions proposed by Kirchhoff in 1850 [84]. It is also called "Kirchhoff plate theory", "Kirchhoff-Love plate theory" or "Thin plate theory". It is actually an extension of the "Euler–Bernoulli beam theory" to thin plates.

The fundamental assumptions of CPT are:

- Plane sections initially normal to the midsurface remain plane and normal to the midsurface after deformation, Figure 2.1 [85]. Analogous to beams, this assumption implies that the effect of transverse shear strains is negligible. The deformation of the plate is thus associated principally with bending strains. Consequently, the transverse normal strain, ε_z, resulting from transverse loading can be neglected.
- The transverse normal stress, σ_z, is small compared to the other stress components of the plate and, therefore, can be neglected.

For a vast majority of thin plate problems, the CPT yields accurate results that do not differ significantly from those obtained using the 3D theory of elasticity. Under the above-mentioned assumptions, the displacement field of the CPT can be written in the following form: [85, 86]

$$\begin{aligned} u\,(x,\,y,\,z) &= u_0(x,\,y) - zw_{,x} \\ v\,(x,\,y,\,z) &= v_0(x,\,y) - zw_{,y} \\ w\,(x,\,y,\,z) &= w_0(x,\,y) \end{aligned} \tag{2.1}$$

where u_0, v_0 and w_0 are the displacement components along the x, y and z-axes at the midplane (z=0). $w_{,x}$ and $w_{,y}$ are the rotations due to bending in both directions.

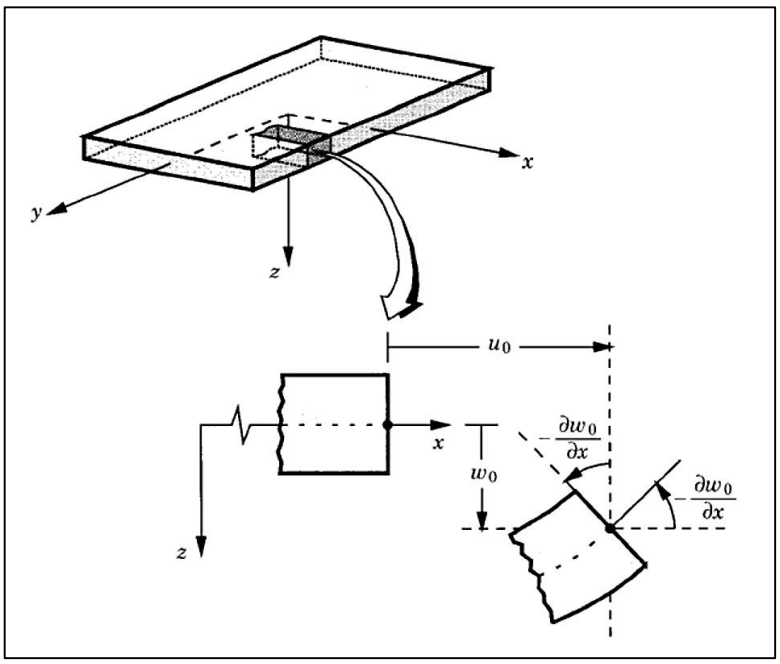

Figure 2.1 Undeformed and deformed geometry of a plate under the Kirchhoff hypotheses. [85].

Since the effect of transverse shear is not taken into account in this theory, the results for thick plates (especially plates made of advanced composites) will be inaccurate. For this purpose, the first- order shear deformation theory has been developed.

2.2.2 First-order shear deformation theory (FSDT)

The First-order shear deformation theory, also referred to as the Mindlin-Reissner theory (Reissner, 1945 [87]; Mindlin, 1951 [88]) or the Mindlin plate theory, extended the classical plate theory by taking into account the transverse shear strains effect. According to this theory, the transverse straight lines before deformation remain straight after deformation but they are not necessarily normal to the mid-plane after deformation, Figure 2.2 [85]. As a

result, transverse shear strains are constant through the thickness. Also, this theory assumes that the transverse normal stress, σ_z, is zero.

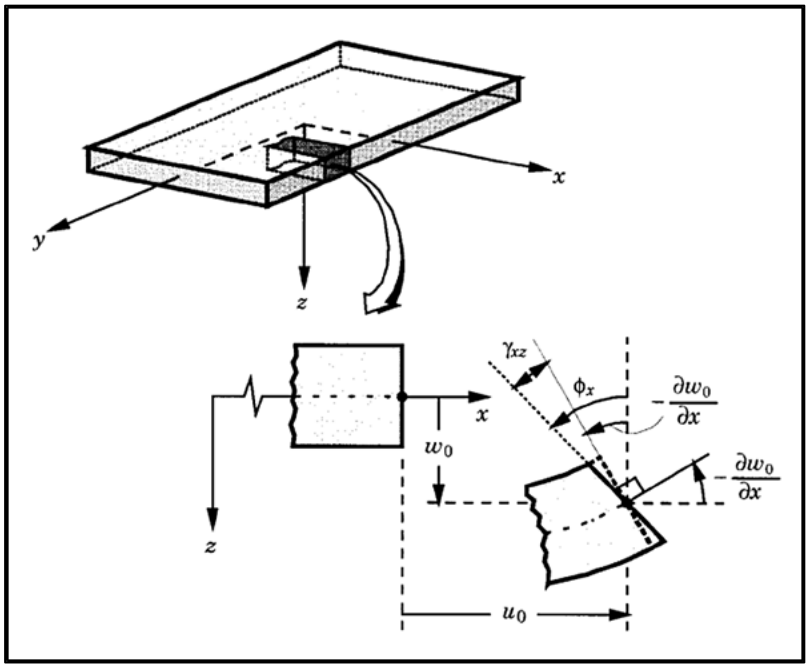

Figure 2.2 Undeformed and deformed geometry of a plate under the assumptions of the FSDT [85].

The displacement field of the FSDT can be written as follows [85, 86]

$$\begin{aligned} u\,(x,\,y,\,z) &= u_0(x,\,y) + z\phi_x(x,y) \\ v\,(x,\,y,\,z) &= v_0(x,\,y) + z\phi_y(x,y) \\ w\,(x,\,y,\,z) &= w_0(x,\,y) \end{aligned} \tag{2.2}$$

where u_0, v_0 and w_0 denote the displacement of a point on the plane $z = 0$. ϕ_x, ϕ_y are the rotations about the y and x axes, respectively.

Since the transverse shear strains are constant through the thickness of the plate, it follows that the transverse shear stress will also be constant. In general, shear stress varies parabolically through the plate thickness, and therefore a **shear correction factor** is required in the FSDT for the compensation of the actual parabolic variation of shear stress and satisfying the shear stress-free boundary conditions on the plate surfaces (i.e., the shear stress must be equal to zero at the top and bottom plate surfaces).

2.2.2.1 Shear Correction Factor (SCF)

The shear correction factor adjusts the transverse shear stiffness and thereby, the accuracy of results of the FSDT will depend significantly on the SCF [89]. In order to improve the FSDT, numerous studies have been conducted by many researchers using different approaches to calculate the SCFs for homogeneous and composite plates. The first concept of the SCF for isotropic homogeneous plates was presented by Reissner [87], where he proposed a value of 5/6 by using a calculation method based on static equilibrium and energy equivalence considerations. Mindlin [88] was the first to predict the correction factor based on dynamic analysis, where he proposed a value of $\pi^2/12$ by equating the approximate first antisymmetric thickness-shear vibration frequency to the exact solution. When the FSDT is applied to composite plates, the difficulty in accurately evaluating the SCFs presents their shortcomings. For sandwich plates, Yu [90] gave an accurate analysis for the SCF based on the comparison of the fundamental frequencies obtained by the theory of elasticity solution and by the FSDT model of the structure. It was shown that for a typical sandwich plate the value of this factor approaches unity. Chow [91] adopted a procedure based on the comparison of the shear strain energies to obtain the SCF of orthotropic symmetric laminate. This procedure has been extended by Whitney [92] to orthotropic nonsymmetrical laminates, and the accuracy of the method was demonstrated by comparing the static bending solution for various laminated plates against solutions obtained by satisfying the exact theory of elasticity in each ply as well as the continuity conditions of the interface. Also, Whitney [93] derived an expression for the SCF by considering cylindrical bending about the length and the width of the plate, and discrete values of SCFs were presented for symmetric/anti-symmetric laminate plates and sandwich plates. The author discussed the variation of the SCF due to variation in number of layers of the laminate, and it was shown that the SCF does not approach the classical value for homogeneous plates as the number of layers is increased. Predictor-corrector procedures have been proposed by Noor et al. [94, 95] to correct the SCFs by using the iteration process. The SCFs obtained from this method depend on boundary conditions, plate geometry, and loading conditions, and, hence, they cannot be directly applied for other plate configurations.

For many applications of FGMs in plate structures, the SCF is assumed to be constant 5/6. This value is not appropriate for FG plate analyses due to continuous variation of material properties [96]. Efraim and Eisenberger [97] proposed a formula for SCF in terms of Poisson's ratio and volume fractions of both gradients in an FG plate. Furthermore, Nguyen

et al. [98] obtained the SCFs for the FGM by comparing the strain energies of the average shear stresses with those obtained from the equilibrium. They assumed a cylindrical bending around the y axis and suppressed the effect of the weak terms on the shear stresses. The authors showed that the SCF for FG plates are not the same as for homogeneous plates. In fact, they showed that the SCF is as a function of the ratio between elastic modulus of constituents and of the distribution of materials through the models. Also, Nguyen et al. [99] identified the SCFs for the FSDT models made of FGMs through an energy equivalence method. A new formula for the SCFs, used in the Mindlin plate theory, is obtained for FG plates by Hosseini-Hashemi et al. [100]. In their work, a well-known commercially available finite element (FE) method package was used for the extraction of the frequency parameters. The authors obtained the SCF by making the frequency parameter of the analytic solution based on the FSDT identical to that acquired by the FE method.

2.2.3 Higher-order shear deformation theories (HSDTs)

To overcome the limitations of the CPT and the FSDT (i.e., to get the realistic variation of the transverse shear strains and stresses through the thickness of the plate and to avoid the use of SCFs), several high-order shear deformation theories have been developed [101-107]. These models are based on the assumption of nonlinear stress variation through the thickness and are capable of representing the section warping in the deformed configuration, Figure 2.3 [85].

The most developed HSDTs are based on the Taylor series expansion of the displacement fields to approximate the 3D theory [108]. The displacement is therefore assumed to be in the following form:

$$u_i(x,y,z) = u_i(x,y) + z\phi_i^{(1)}(x,y) + z^2\phi_i^{(2)}(x,y) + ... + z^j\phi_i^{(j)}(x,y) \tag{2.3}$$

Where i = 1,2,3, and j defines the order used in the theory.

The Reissner-Mindlin first-order theory corresponds to the Taylor series up to the order j =1 and $\phi_3^{(1)}$=0. In the case where a first order model does not allow to approach a given problem properly, it will be necessary to move to a higher order model (2nd order, 3rd order, or even more), in the series expansion of the displacements.

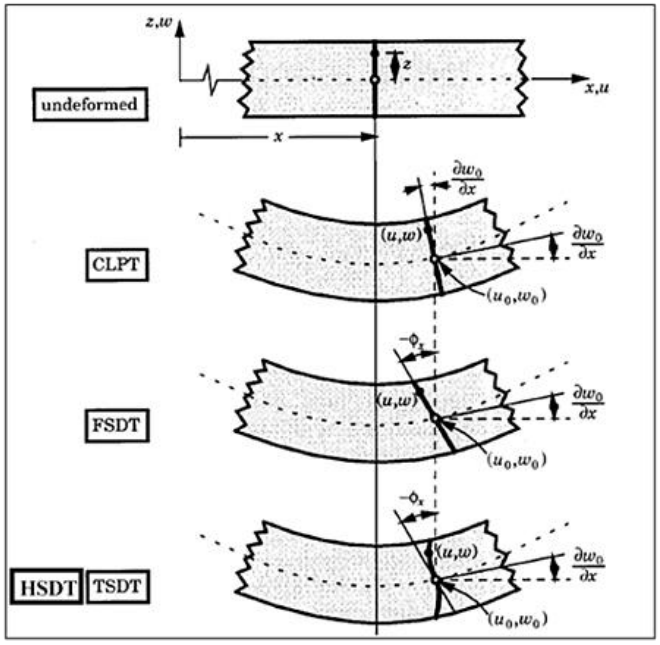

Figure 2.3 Undeformed and deformed geometry of a plate according to the CPT, FSDT and HSDT [85].

The second-order shear deformation theories (SCSDT) [109] yield slightly better results than the FSDT, but suffer from the same drawbacks as the latter (i.e., need correction factors). The displacement field of these theories can typically be described as:

$$\begin{aligned} u(x,y,z) &= u_0(x,y) + z\phi_x(x,y) + z^2\psi_x(x,y) \\ v(x,y,z) &= v_0(x,y) + z\phi_y(x,y) + z^2\psi_y(x,y) \\ w(x,y,z) &= w_0(x,y) + z\phi_z(x,y) + z^2\psi_z(x,y) \end{aligned} \tag{2.4}$$

where the parameters ψ_x, ψ_y and ψ_z are the second order functions.

Several Third order shear deformation theories (TSDT) (Parabolic shear deformation theory) have been proposed by many researchers [104-106]. The Reddy's TSDT displacement field [106] is given by:

$$\begin{aligned} u(x,y,z) &= u_0(x,y) + z\phi_x(x,y) + z^2\psi_x(x,y) + z^3\zeta_x(x,y) \\ v(x,y,z) &= v_0(x,y) + z\phi_y(x,y) + z^2\psi_y(x,y) + z^3\zeta_y(x,y) \\ w(x,y,z) &= w_0(x,y) \end{aligned} \tag{2.5}$$

where the parameters $\psi_x, \psi_y, \zeta_x, \zeta_x$ are the high order functions.

With increasing order of expansion, the number of additional parameters increases, which are often difficult to interpret. Some Simplifications have been made to reduce the displacement parameters. These simplifications consist in shortening the last terms of the Taylor series by introducing a ‘’shear function’’. Following these simplifications, the form of the displacement field is proposed as follows

$$\begin{aligned} u(x,y,z) &= u_0(x,y) - z\frac{\partial w_0}{\partial x} + f(z)\theta_x(x,y) \\ v(x,y,z) &= v_0(x,y) - z\frac{\partial w_0}{\partial y} + f(z)\theta_y(x,y) \\ w(x,y,z) &= w_0(x,y) \end{aligned} \tag{2.6}$$

Where $f(z)$ is the shear function which determines the distribution of the transverse shear strains and stresses across the plate thickness h, and $\theta_x = \frac{\partial w_0}{\partial x} + \phi_x$, $\theta_y = \frac{\partial w_0}{\partial y} + \phi_y$, with ϕ_x, ϕ_y denote the rotations about the y and x axes, respectively.

According to the equation (2.6), the displacement field of CPT is obtained by setting $f(z) = 0$, and that of the FSDT is obtained by setting $f(z) = z$. Moreover, the TSDT displacement field of Reddy [85, 106] is obtained by taking the following function

$$f(z) = z - \frac{4z^3}{3h^2} \tag{2.7}$$

This theory accommodates a parabolic distribution of transverse shear stress and satisfies the shear stress-free surface conditions on the top and bottom surfaces of the plate, thus, it provides a good approximation of the transverse shear stresses compared to the three-dimensional elasticity solution.

A different HSDT has been proposed by Touratier [110], based on a sinusoidal trigonometric function, called **The sinusoidal shear deformation theory (SSDT)**. This theory is a seminal example of the family of trigonometric HSDT and is implemented by setting

$$f(z) = \frac{h}{\pi}\sin\left(\frac{\pi z}{h}\right) \tag{2.8}$$

A Hyperbolic shear deformation plate theory (HSDPT) has been proposed by Soldatos [111], is obtained by taking

$$f(z) = h\sinh\left(\frac{z}{h}\right) - z\cosh\frac{1}{2} \tag{2.9}$$

The exponential shear deformation theory (ESDPT) developed by Karama et al. [112] is obtained by taking

$$f(z) = ze^{-2(z/h)^2} \tag{2.10}$$

Although the HSDTs do not require an SCF, their equations of motion are more complicated than those of the FSDT. Therefore, Shimpi [113] developed a simple plate theory called the Refined Plate Theory (RPT) by separating the transverse displacement into bending and shear parts. The most interesting feature of Shimpi's theory is that it has fewer unknowns (four unknowns) and governing equations than the FSDT. In addition, this theory does not require an SCF and gives a parabolic distribution of shear through the thickness of the plate. Also, it presents many similarities with the CPT as regards the equations of motion, the boundary conditions, and stress resultant expressions. The displacement field of the RPT is presented as follows.

$$\begin{aligned} u(x,y,z) &= u_0(x,y) - z\frac{\partial w_b(x,y)}{\partial x} + f(z)\frac{\partial w_s(x,y)}{\partial x} \\ v(x,y,z) &= v_0(x,y) - z\frac{\partial w_b(x,y)}{\partial y} + f(z)\frac{\partial w_s(x,y)}{\partial y} \\ w(x,y,z) &= w_b(x,y) + w_s(x,y) \end{aligned} \tag{2.11}$$

Where w_b and w_s are the bending and shear components of transverse displacement, respectively

It should be noted that the above-mentioned plate theories discard the thickness stretching effect (i.e., $\varepsilon_z = 0$) due to assuming a constant transverse displacement through the thickness. This effect plays a significant role in moderately thick and thick plates and should be taken into consideration. **Quasi-3D theories** are HSDTs that account for a higher-order variation of both in-plane and transverse displacements through the thickness, and hence both the shear

deformation effect and the thickness stretching effect are considered [114]. The displacement field of the quasi-3D theory is given by

$$\begin{aligned} u(x,y,z) &= u_0(x,y) - z\frac{\partial w_0}{\partial x} + f(z)\varphi_x(x,y) \\ v(x,y,z) &= v_0(x,y) - z\frac{\partial w_0}{\partial y} + f(z)\varphi_y(x,y) \\ w(x,y,z) &= w_0(x,y) + g(z)\varphi_z(x,y) \end{aligned} \tag{2.12}$$

Whereu_0, v_0, w_0, φ_x, φ_y and φ_z are six unknown displacements of the midplane of the plate And g(z) and f (z) are shear functions with

$$g(z) = \frac{df(z)}{dz} \tag{2.13}$$

All the previously mentioned theories have been extensively used by numerous researchers to accurately predict the behavior of FG plates. The following section summarizes the studies based on the static, vibration, and buckling behavior of FG plates.

2.3 Research studies reported on FG plates

Due to their inherent structural efficiency, there has been a great deal of interest in the analysis of structures made of FGMs. In this section, we have attempted to provide a review of the work done to date for the analysis of FG plates. The review is mainly focused on the static, vibration, and buckling analysis of FG single layer and sandwich plates. The objective here is to show the extent of the research field in the context of FGMs and that there is still much to be done in this research area.

2.3.1 Static analysis of FG plate

The understanding of the static behavior of FG plates is one of the most important issues for the design of these types of structures. Therefore, several investigators devoted themselves to the study of the static behavior of FG single layer and sandwich plates by using a variety of plate theories along with different analytical and numerical methods. Some of the papers selected from the literature are presented in this section.

Reddy and Cheng [115] analyzed the 3D thermomechanical deformations of simply supported FG rectangular plates using an asymptotic method. The effective material properties of the plates have been estimated using the Mori–Tanaka scheme. The temperature, displacements, and stresses of the plate are computed for different volume fractions of the constituents. Vel and Batra [116] presented an exact solution for 3D deformations of a simply supported FG thick plate. The effective material properties are estimated by either the Mori–Tanaka or the self-consistent schemes. The results are presented in terms of temperature, displacements, and stresses at several locations for mechanical and thermal loads. Pan [117] extended Pagano's solution [118] to derive a 3D exact solution for FG rectangular composite laminate with simply supported boundary conditions under a surface load. The laminate layers have been made of FGMs with mechanical characteristics varying exponentially through the thickness direction of the plate. The results are presented in terms of displacements and stresses and it was clearly shown that the tensile stress at the top or the compressive stress at the bottom inhomogeneous plate can be reduced by bonding a suitable FGM layer to it. Elishakof and Gentilini [119] employed the Ritz energy method based on the 3D elasticity theory to predict displacements and stresses of all-around clamped FG plates subjected to a uniformly distributed normal load on the top surface. Kashtalyan [120] and Woodward and Kashtalyan [121] derived exact solutions for the 3D static bending analysis of simply supported FG plates subjected to transverse loading. The Young's modulus and shear modulus of the plate vary exponentially through the thickness, and the Poisson's ratio is assumed to be constant. Moreover, Kashtalyan and Menshykova [122] carried out a 3D static bending analysis of simply-supported sandwich panels with an FG core under transverse loadings. The Young's modulus of the core is assumed to vary exponentially through the thickness, and the Poisson's ratio is assumed to be constant. This work has been extended by Woodward and Kashtalyan [123] to simply-supported sandwich panels subjected to distributed and concentrated loadings. Not long ago, Gholami et al. [124] presented a 3D elasticity solution for the bending analysis of anisotropic FG Plates. The differential quadrature method (DQM) has been applied to determine flexural characteristics of the anisotropic FG plate. The obtained results from the DQM approach have been compared with those of the FE method.

3D analytical solutions for FG plates are very useful since they provide benchmark results to assess the accuracy of various 2D plate theories and FE formulations. However, their solution methods involve mathematical complexities and are very difficult and tedious to

solve. Many 2D theories have been proposed for the static analysis of FG plates. Among all the plate theories, the CPT is the simplest theory for the analysis of plates. Since the CPT yields accurate results only for thin plates, few researchers employed this theory to analyze the static behavior of thin FG plates. One can refer to the work performed by Chi and Chung [78,125], where the bending analysis of FG plates under transverse load has been carried out using the CPT. The material properties of the FG plates are assumed to vary continuously throughout the thickness of the plate, according to the volume fraction of the constituent materials based on the power law, exponential, or sigmoid functions. The theoretical results have been checked by FE analysis. In the work by Amirpour et al. [126] the bending analysis of thin, through-the-length, FG plate has been performed using the CPT. The analytical results have been compared with FE simulation using graded solid elements.

To overcome the limitation of the CPT, the FSDT has been employed for the analysis of the FG plates. The model of the FSDT plate is the simplest plate model that accounts for the transverse shear strains, which are assumed constant through the plate thickness. Praveen and Reddy [127] analyzed the nonlinear static and dynamic responses of FG plates using the FE method and the FSDT with von Karman assumptions. Della Croce and Venini [128] developed a hierarchic family of finite elements for the bending analysis of FG plates under mechanical and thermal loadings using the FSDT and a variational formulation. Singha et al. [129] investigated the nonlinear behaviors of FG plates under transverse distributed load using a high precision plate bending FE. The formulation has been developed based on the FSDT, considering the physical neutral surface position concept. The SCFs have been introduced and the equilibrium equations have been used for transverse shear stresses and transverse normal stress components determination. Thai and Choi [130] presented a simplified FSDT with four unknowns for the bending and free vibration analysis of FG single layer and sandwich plates with FG core and isotropic skins by splitting the transverse displacement into the bending and shear parts. Thai et al. [131] presented analytical solutions for bending, buckling and free vibration analysis of FG single layer and sandwich plates with FG skins under various boundary conditions using a new FSDT. The authors reformulated the conventional FSDT to a simpler form by making a further assumption, in which the number of unknowns is reduced to four. The use of SCF is no longer necessary in this theory since the transverse shear stresses are directly computed from the transverse shear forces by using equilibrium equations. Furthermore, Mantari and Granados [132] used a new FSDT with only four unknowns for the static analysis of FG sandwich plates considering integral terms in the

displacement field instead of derivative terms. Bellifa et al [133] presented an analytical solution for bending and free vibration of FG plates using a new FSDT with just four unknowns based on the exact position of the neutral surface. A few years ago, Srividhya et al. [134] developed a C^0 continuous four-node isoparametric element based on FSDT to investigate the effect of material homogenization scheme on the flexural response of FG plate. For estimating the effective properties of the plate, the rule of mixtures and the Mori-Tanaka schemes, have been used. Recently, Joshi and Kar [135] analyzed the bending behavior of bi-dimensional FG plate subjected to uniform loading, using the FSDT and FE method. The material properties are varied gradually in longitudinal and transverse directions. According to the open literature, the FSDT has been widely used to model both thin and thick plates owing to its high efficiency and simplicity. However, its accuracy depends on the appropriate value of the shear correction factor [98, 99].

To avoid the use of SCFs, several HSDTs have been proposed and applied to FG plates. Reddy [136] presented both analytical and FE formulations based on his TSDT. The formulations account for the thermo-mechanical coupling, time dependency and von Karman-type geometric non-linearity. Ferreira et al. [137] studied the static characteristics of FG plates using the TSDT and a meshless method based on the multiquadrics radial basis function. The effective properties of the composite have been derived either by the rule of mixtures or by the Mori–Tanaka scheme. Saidi et al. [138] presented an analytical approach based on the TSDT for bending-stretching analysis of thick FG rectangular plates. Gulshan Taj et al. [139] also utilized Reddy's TSDT to analyze the static behavior of FG plates by applying the FE method. The Results have been obtained by employing a C^0 continuous isoparametric Lagrangian FE with seven degrees of freedom for each node. Mori-Tanaka scheme has been used to represent the material property of the FG plate at any point. For extracting mechanical response of static bending and natural frequencies of FG plates with different configurations (rectangular, circle, L-shape FG plates) in high temperature environments, Bui et al. [140] developed a displacement-based FE formulation associated with a novel TSDT without any requirement of SCFs. The new TSDT is based on rigorous kinematic of displacements, deriving from an elasticity formulation rather than the hypothesis of displacements.

The bending response of simply supported FG sandwich ceramic–metal panels has been investigated by Zenkour [141]. The sandwich plates made of isotropic and homogeneous ceramic core and FG skins have been studied, assuming the power law variation of ceramic

and metal constituents through the thickness. The formulations have been done by the CPT, FSDT, and an SSDT. Further, the same author [142], presented the static response of FG plates using a generalized shear deformation plate theory (GSDT). The effective material properties have been considered to vary according to the power-law through thickness. The thermoelastic bending response of FG sandwich plates has been also studied by Zenkour and Alghamdi [143] using the SSDT. Again, Zenkour and Alghamdi [144] analyzed the bending response of sandwich plates made of FG skins and isotropic core subjected to sinusoidally distributed thermo-mechanical loads using the SSDT. Once more, Zenkour [145] employed the SSDT to solve the bending problem of FG plates with the derivation of the bending relationships between the SSDT and CPT quantities.

Using an HPSDT, Mahi et al. [146] carried out bending and free vibration analysis of isotropic, functionally graded, sandwich, and laminated composite plates. Mantari et al. [147] combined exponential and trigonometric functions to develop an HSDT for the bending analysis of FG plates. The static response of exponentially graded plates (i.e., The mechanical properties of the plates are assumed to vary exponentially in the thickness direction) has been analyzed by Mantari and Guedes Soares [148] using a new HSDT with a tangential function. Again, Mantari and Guedes Soares [149] presented a generalized HSDT and its FE formulation for the bending analysis of advanced composite plates such as FG plates. The authors combined exponential and hyperbolic functions to develop the HSDT. The generalized FE code is based on a continuous isoparametric Lagrangian FE with seven degrees of freedom per node. Additionally, the same authors [150], studied the static response of FG plate using a new HSDT. The displacement of the middle surface is expanded as a combination of exponential and polynomial functions of the thickness coordinate. However, the transverse displacement is supposed to be constant through the thickness. A tangential-exponential HSDT has been proposed by Mantari et al. [151] for the bending analysis of FG plates. Further, Mantari et al. [152] studied the static response for FG single and sandwich plates using five different and non-existent displacement fields of the non-polynomial form (sinusoidal, tangential, exponential, hyperbolic, and modified sinusoidal) via Carrera's Unified Formulation (CUF) [153]. Lately, Belkhodja et al. [154] analyzed the bending, free vibration, and buckling mechanical behaviors of square and rectangular FG plates using an exponential-trigonometric HSDT.

Matsunaga [155] presented a 2D-HSDT to calculate the displacements and stresses of simply supported FG plates under thermal and mechanical loading, using several sets of

governing equations of truncated approximate theories. Using HSDT with 11 unknowns and FE models, Talha and Singh [156] studied the static response and free vibration analysis of FG plates. Natarajan and Manickam [157] employed a C^0 8-noded quadrilateral plate element based on HSDT with 13 unknowns to study the static deflection and the free vibration analysis of FG sandwich plates. The deflection and stresses of simply supported FG plates under a uniformly distributed load have been analyzed by Tu et al. [158] using a new eight-unknown HSDT based on a full twelve-unknown HSDT by satisfying the condition of zero transverse stresses on the upper and lower surfaces of the FG plates.

Generally, most HSDTs are highly computationally cost due to involving in many unknowns. To reduce the computational cost, HSDTs with four unknowns have been developed for FG plates. Mechab et al. [159] used a two-variable RPT to study the bending behavior of FG plates. This theory involves just four unknowns and satisfies the equilibrium conditions at the plate's top and bottom surfaces, with no need for any SCF. Navier method has been applied to obtain solutions for simply supported FG plate subjected to sinusoidal loading. Abdelaziz et al. [160] extended a two-variable RPT developed by Shimpi and Patel [161] to the static response of FG sandwich plates. Also, Mechab et al. [162] presented analytical solutions of static and dynamic analysis of FG plates using Four-variable RPT with a new hyperbolic shear function. Thai and Choi [163] presented a FE formulation of various four unknown shear deformation theories for bending and vibration analyses of FG plates. Thai and Kim [164] presented analytical solutions for the bending and free vibration analysis of simply supported FG plates using four unknowns HSDT. Li et al. [165] investigated the thermomechanical bending behavior of a new type of FG sandwich plates which consist of FG face sheets and FG core, using a four-variable RPT. Analytical solutions are obtained to predict the deflections and stresses of simply supported FG sandwich plates. In order to compare the static, free vibration and buckling of in-plane and through thickness FG plates, Farzam and Hassani [166] used a new hyperbolic RPT based on physical neutral surface position and isogeometric analysis (IGA) approach.

Carrera et al. [167] evaluated the effect of thickness stretching in plate/shell structures made of FGMs, in the thickness directions. This effect plays a significant role in moderately thick and thick plates and should be taken into consideration. Several studies have been conducted considering the stretching effect, for instance, Mantari and Soares [168] presented a generalized hybrid quasi-3D shear deformation theory for the bending analysis of FG

plates. Many 6 DOF hybrid (polynomial and/or non-polynomial) HSDTs, including the stretching effect, can be derived by using this generalized formulation. Neves et al. [169-171] used quasi-3D higher order theories with nine unknowns and meshless method to analyze the static, free vibration and buckling behavior of FG isotropic and sandwich plates considering sinusoidal [169], hyperbolic [170], and cubic [171] variations for in-plane displacements and a parabolic variation for transverse displacement. Thai and Kim [172] presented a simple quasi-3D sinusoidal shear deformation theory with only five unknowns for the bending analysis of FG plates. This theory accounts for both shear deformation and thickness stretching effects considering a sinusoidal variation of all displacements through the thickness. Bessaim et al. [173] developed a five-variable HPSDT for the bending and free vibration analysis of sandwich plates with FG isotropic face sheets. The theory accounts for the stretching and shear deformation effects without requiring an SCF. Zenkour developed a refined trigonometric HSDT with four unknowns for the bending analysis of FG isotropic [174] and sandwich [175] plates. The effects of transverse shear strains as well as the transverse normal strain have been taken into account. Hourai et al. [176] developed a five unknowns HSDT with a sinusoidal distribution through the thickness of in-plane displacements to investigate the thermoelastic bending of FG sandwich plates. The theory accounts for the stretching and shear deformation effects without the use of SCF. Belabed et al. [177] developed a new higher order shear and normal deformation theory with only five unknowns for bending and free vibration FG plates. The theory accounts for both shear deformation and thickness stretching effects by a hyperbolic variation of all displacements across the thickness, and satisfies the stress-free boundary conditions on the upper and lower surfaces of the plate without any SCF requirement. For the bending and free vibration analysis of FG plates, Hebali et al. [178] developed a new quasi-3D hyperbolic shear deformation theory with only five unknown displacement functions considering the stretching effect. Amirpour et al. [179] develop an SSDT with five unknowns for the bending analysis of FG plates with property variation throughout the length. The theory accounts for stretching and shear deformation effects without requiring an SCF. The analytical solutions have been verified against FE numerical solutions. Zenkour and Alghanmi [180] studied the bending of an FG plate with two reverse simply supported edges, using a refined quasi-3D shear and normal deformation theory with a third-order shape function. The proposed theory used only four unknowns and satisfied the free transverse shear stresses condition on the upper and lower surfaces of the plate, and therefore no SCFs are needed. Recently, Khiloun et al. [181]

presented a new quasi-3D HPSDT with four unknowns for bending and free vibration of FG plates. The theory accounts for the stretching and shear deformation effects without requiring a SCF.

It can be observed from the above mentioned works that many papers have been also dedicated to the vibration analysis of FG plates [127], [130], [131], [133], [146], [154], [156], [157], [162-164], [166], [169-171], [173], [177], [178] and [181]. Further studies on the vibration analysis of FG single layer and sandwich plates are presented in the next section.

2.3.2 Vibration analysis of FG plate

The vibration responses of FG plates have been studied extensively. Several studies about finding the 3D exact solutions for FG plates vibration analysis have been carried out. Vel and Batra. [182] presented a 3D exact solution for the vibration of FG rectangular plates. Also, Uymaz and Aydogdu [183] presented 3D solutions for the vibration of arbitrary boundary conditions of FG rectangular plates using the Ritz method with Chebyshev displacement functions. For FG sandwich rectangular plates with simply supported and clamped edges, the free vibration response has been studies based on the 3D theory of linear elasticity by Li et al. [184]. Natural frequencies of two types of FG sandwich plates, i. e., the sandwich plate with FG skins and an isotropic core and the sandwich plate with isotropic skins and an FG core, have been obtained using the Ritz method with Chebyshev polynomials. Moreover, Reddy and Kant [185] presented an analytical solution for 3D free vibration analysis of exponentially simply supported FG plates, using the power series method. Jin et al. [186] presented a new 3D exact solution for the free vibrations of arbitrarily thick FG rectangular plates with general boundary conditions. Two years ago, Singh and Kumari [187] presented a 3D elasticity based analytical solution for free vibration analysis of in-plane FG Levy-type rectangular plates.

Using the CPT, the free vibration response of FG plates has been investigated by Abrate [188]. The author indicated that FG plates behave like homogeneous plates. Zhang and Zhou [189] used the physical neutral surface concept and classical nonlinear von Karman plate theory for the vibration analysis of thin FG plates. Bending, buckling, and nonlinear bending behaviors analysis have been also carried out. Liu and Chen [190] used the CPT to study the free vibration of in-plane FG rectangular plates. Yin et al. [191] performed a free vibration

analysis of thin FG plates using CPT and physical neutral surface. Ramu and Mohanty [192] proposed a FE approach for modal analysis of rectangular FG plates based on the CPT. Recently, Loja and Barbosa [193] studied the free vibration and dynamic instability behaviors of in-plane FG plates based on the CPT, using Rayleigh-Ritz and Bolotin's methods. The influence of in-plane volume fraction distributions on the free vibrations and dynamic instability of thin plates has been also studied.

FSDT coupled with the FE method has been used by Batra and Jin [194] to perform the free vibrations of a FG anisotropic rectangular plate. Efraim and Eisenberger [97] presented an exact solution using the exact element method and the dynamic stiffness method for the vibration analysis of thick annular plates with variable thickness based on the FSDT. Later, Hosseini-Hashemi et al. [100] presented analytical solutions based on the FSDT for free vibration of moderately thick rectangular plates on elastic foundations. In this study, a new formula of the SCF for FG plates has been obtained. Zhao et al. [195] also used the FSDT and the element-free kp-Ritz method for the vibration analysis of FG plates with arbitrary boundary conditions. Mantari and Granados [196] used a novel FSDT with only four unknowns for the free vibration analysis of FG single-layered and sandwich plates. Bernardo et al. [197] studied the free vibration and static responses of FG plates by considering different numerical techniques based on the FSDT.

Abrate [198] studied the free vibration, buckling and static deflection of FG plates using the CPT, the FSDT, and the TSDT. Examples have been presented for thick as well as thin plates, for rectangular plates with different aspect ratios as well as circular and skew plates and many combinations of boundary conditions. The author showed that the natural frequencies, buckling loads and static deflections of FG plates can be obtained from the corresponding results for isotropic plates so that direct analysis of FG plates is not necessary. To calculate the natural frequencies of FG plates, Ferreira et al. [199] used the FSDT, the TSDT, and meshfree method. The Mori–Tanaka technique has been used to homogenize material properties. Kim and Reddy [200] presented analytical solutions using a couple of stress methods based on TSDT for the vibration analysis of FG plates. Bending and buckling responses have been also investigated.

Based on the SSDT, Zenkour [201] carried out the free vibration analysis of thick FG plates considering the effects of rotatory inertia. Using a 2D HSDT, Matsunaga [202] calculated the natural frequencies and buckling stresses of FG plates. Xiang et al. [203]

proposed an n-order shear deformation theory for free vibration of FG and composite sandwich plates. A High order shear and normal deformation theory with 12 unknowns has been used by Jha et al. [204] for the calculation of natural frequencies of FG plates Navier's solution technique employing the double Fourier series has been used to give an analytical solution. Also, Sheikholeslami and Saidi [205] used the high-order shear and normal deformable plate theory of Batra and Vidoli [206] to investigate the free vibration of simply supported FG rectangular plates resting on a two-parameter elastic foundation. Based on a new exponential function, Mantari et al [207] proposed an HSDT for the vibration analysis of FG plates resting on elastic foundations. Ankit Gupta et al. [208] investigated the free vibration of simply supported FG square plates resting on elastic foundations. The authors used the theory proposed by Talha and Singh [156] with a C^0 continuous isoparametric FE with 13 degrees of freedom per node. Mahmoudi. et al. [209] presented an analytical solution based on HPSDT for vibration behavior analysis of FG porous plates resting on elastic foundations. Zaoui et al. [210] devised a new 2D and Quasi-3D HSDT for analyzing the free vibration response of FG plates on elastic foundations.

A four-variable RPT has been applied by Hadji et al. [211] for the free vibration analysis of FG sandwich rectangular plates. Benachour et al. [212] presented the free vibration analysis of FG plates with arbitrary gradient based on a four-variable RPT using Navier's solution technique and Ritz method. The obtained results have compared well with those obtained using FSDT and TSDT. To analyze the vibrational behavior of FG plates, Thai et al. [213] developed an efficient shear deformation theory, which has a strong similarity with the CPT in many aspects and involves only four unknowns. Benferhat et al. [214] studied the free vibration analysis of an FG simply-supported plate resting on elastic foundations, using new four unknowns RPT, based on the neutral surface concept. The isogeometric analysis combined with an RPT has been employed by Xue et al. [215] to investigate the free vibration responses of in-plane FG plates. Merdaci et al. [216] presented a free vibration analysis of simply supported plate FG porous using four unknowns HSDT. Tabatabaei and Fattahi [217] recently developed a FE approach for modal analysis of square FG plates using the ABACUS software.

2.3.3 Buckling analysis of FG plates

Buckling behavior is one of the critical design factors for plates subjected to compressions. There have been extensive investigations carried out for the buckling analysis of FG isotropic and sandwich plates to predict the critical buckling loads under various boundary and loading conditions. Among the primary investigations is the work of Birman [218], who presented a solution to the buckling problem of hybrid composite plates with stiffer FG fibers. Feldman and Aboudi [219] studied the elastic bifurcation buckling of FG plates under in-plane compressive loading. To analyze the problem, the authors employed a method based on a combination of micromechanical and structural approaches.

Based on the CPT, Javaheri and Eslami [220, 221] studied the mechanical and thermal buckling behavior of thin FG plates. Authors [221] developed an analytical model to predict the critical buckling temperature of FG plates under the uniform, linear and non-linear thermal loads. Further to these studies, Shariat et al. [222, 223] investigated the mechanical and thermal buckling behavior of rectangular FG plates with geometrical imperfections. The equilibrium, stability, and compatibility equations of an imperfect FG plate have been derived using the CPT. Mahdavian [224] adopted the CPT to carry out the buckling analysis of simply-supported FG rectangular plates under non-uniform in-plane compressive loading. Mohammadi et al. [225] presented the Levy solution using the principle of minimum potential energy for the buckling analysis of thin FG plates based on the CPT subjected to different mechanical loads under various boundary conditions. Ramu and Mohanty [226] used the FE method and the CPT to study the buckling behavior of simply supported, rectangular FG plates under uniaxial and biaxial compression loads. The authors concluded that the critical buckling load of the rectangular plate under uniaxial compression is greater than the biaxial compression. Can et al. [227] also used the FE method to analyze the stability of thin FG plates under various boundary conditions.

The FSDT has been employed by Lanhe [228] for the thermal buckling analysis of a simply supported moderately thick rectangular FG plate under uniform and nonlinear temperature rise. Zhao et al. [229] investigated the mechanical and thermal buckling behavior of FG plates using the FSDT and the element-free *kp*-Ritz method. FG sandwich plate buckling analysis has been carried out by Yaghoobi and Yaghoobi [230] using an analytical approach based on the FSDT, considering various boundary conditions under thermal, mechanical and thermomechanical loadings. The thermal buckling behaviors of FG plates

have been investigated by Lee et al. [231] based on the neutral surface concept using the FE method and the FSDT. In this study, the material properties of the plates are temperature dependent; the location of the neutral surface depends also on the temperature change. Shahbaztabar and Arteshyar [232] used the FDST and the differential quadrature element method (DQEM) to investigate the buckling characteristics of FG plate fully or partially resting on elastic foundation and subjected to uniaxial and biaxial in-plane loadings. By Shariat and Eslami [233] a closed form solution based on the TSDT has been presented for the mechanical and thermal buckling of thick FG plates. Furthermore, Foroughi and Azhari [234] used a TSDT and the B-spline finite strip method (FSM) to analyze the mechanical buckling and free vibration of thick FG plates resting on elastic foundations. A novel and effective approach based on IGA and TSDT has been applied by Yin et al. [235] for free vibration and buckling analysis of FG plates with in-plane material inhomogeneity. An accurate computational approach based on the FE method and a new TSDT has been developed by Van Do et al. [236] to analyze the buckling and bending behaviors of the bi-directional FG plates. This approach does not require any special treatments of the shear-locking effect, and the SCFs are not required as well. Moita et al. [237] used the FE model to compare between linear and nonlinear mechanical and thermo-mechanical buckling of rectangular FG plates. The model is based on Reddy's TSDT, implemented in a nonconforming flat triangular plate/shell element with 24 degrees of freedom.

SSDT has been used by Zenkour [238] to study the buckling and free vibration of simply-supported FG sandwich plates. The obtained results were validated by comparing them with those obtained using CPT, FSDT, and TSDT. The critical buckling load obtained using non-symmetric FG sandwich plates was found to be higher than those of symmetric plates. Also, Zenkour and Mashat [239] used the SSDT to obtain the buckling response of FG plates under different types of thermal loads (uniform, linear and non-linear thermal loads). Zenkour and Sobhy [240] studied the critical buckling temperature for FG sandwich plates. They used the SSDT to deduce the stability equations.

Based on the HSDT, a Levy-type solution for buckling analysis of thick FG rectangular plates has been presented by Boghadi and Saidi [241]. Results show that the critical buckling load has an inverse relation to the aspect ratio, whereas buckling load increases as the thickness of the FG plate increases. Neves et al. [242] used a hyperbolic sine shear deformation theory for the linear buckling analysis of FG sandwich plates. The buckling governing equations and boundary conditions were derived using Carrera's Unified

Formulation (CUF) and further interpolated by collocation with radial basis functions. In another research study, an HSDT has been developed and applied by Reddy et al. [243] to calculate the mechanical buckling load of the rectangular FG plate without enforcing zero transverse shear stresses on the top and bottom surfaces of the plate. A new eight-unknown HSDT based on full twelve-unknown HSDT has been proposed by Thinh et al. [244] to study the buckling and free vibration of FG plates. Van Do et al. [245] used an improved mesh-free radial point interpolation method (RPIM) and HSDT to investigate the buckling behavior of the FG sandwich plate under uniform, linear and nonlinear temperature rises. Zenkour and Aljadani [246] examined the mechanical buckling analysis of simply supported, rectangular FG plates by employing a refined higher-order shear and normal deformation theory and Navier's technique. Nouri et al. [247] applied a CUF in conjunction with the FSM on the mechanical buckling and static analysis of the FG plate. Recently, Tati [248] used a four-node FE with five degrees of freedom per node based on a simple HSDT to investigate the buckling behavior of FG rectangular plates under mechanical and thermal loading. The proposed model accounts for a quadratic variation of the transverse shear strains across the thickness and satisfies the zero traction boundary conditions on the top and bottom surfaces of the plate without the use of SCF. The assumed natural shear strain (ANS) technique has been introduced to elevate the shear locking phenomenon. Farrokh et al. [249] studied the buckling instability of FG plates under mechanical loads as well as uniform, linear, and nonlinear temperature rise. The authors used an HSDT considering the CUF. They have concluded that the plate theory order, as well as the convective heat transfer boundary conditions, affects significantly critical instability loads. A new refined HPSDT having four unknowns has been developed by El Meiche et al. [250] for the buckling and free vibration analyses of FG sandwich plates. The obtained results have been validated by comparing with those obtained using CPT, FSDT, TSDT, SSDT, and 3D elasticity theory. Fekrar et al. [251] also used a new RPT with four unknowns to study the mechanical buckling of hybrid FG plates. The authors employed the principle of minimum total potential energy to derive governing equations and the Navier method to obtain the closed-form solution. Later, Thai and Choi [252] extended the RPT proposed by Shimpi [113] to the buckling analysis of FG plates subjected to in-plane loading. The accuracy of the obtained results was demonstrated by comparing them with those of CPT, FSDT and TSDT. Bateni et al. [253] did a comprehensive study on the stability of FG plates by employing a four-variable RPT and came to know the significance of in-plane boundary conditions for buckling analysis. Further,

Thai et al. [254] presented a new simple four-unknown shear and normal deformations theory and IGA for buckling, static and dynamic analyses of FG isotropic and sandwich plates. The mixture rule or the Mori-Tanaka technique has been used to homogenize the material properties. Several examples with different geometries, stiffness ratios, the value of power index, and boundary conditions have been illustrated.

2.4 Conclusion

In this chapter, the most commonly used plate theories, for the modeling and analysis of FG plates have been introduced. The earliest and simplest available theory is called the classical plate theory (CPT). However, this theory neglects the transverse shear deformation effects and hence predicts only the behavior of thin plates effectively. First-order shear deformation theory (FSDT) assumes a constant transverse displacement field across the plate's thickness. The models based on this theory predict constant transverse shear stresses across the thickness. Actually, the transverse shear stresses are parabolic through the thickness in nature. To define the transverse stresses accurately, a shear correction factor is required. The shear correction factor depends upon various factors such as end conditions, material properties, thickness scheme, etc. In the case of high-order shear deformation theories (HSDTs), the in-plane displacement field is expanded as a higher-order variation concerning the thickness coordinate.

A review of various investigations carried out in the existing literature on static, vibration, and buckling analysis of FG plates has been also presented in this chapter. Several theories and different analytical and numerical methods have been used to describe the behavior of FG plates.

Following this review, it can be seen that the studies carried out by finite elements on the topic are even less numerous compared to those carried out analytically. The motivation behind this thesis is to study the static, vibratory, and buckling behaviors of single layer and sandwich FG plates using the finite element method based on different plate theories.

Part II

Adaptation of a first-order shear deformation finite element model for the analysis of FG plates behavior

Chapter 3

Adaptation of a rectangular finite element (R4FSDT) for static, free vibration and buckling analysis of FG single layer and sandwich plates

3.1 Introduction

In this chapter, an FSDT-based four-node rectangular finite element (R4FSDT) with five degrees of freedom per node, previously developed for the free vibration of thermally stressed angle-ply laminated composite [255], has been adapted for static, free vibration and buckling analysis of FG single layer and sandwich plates. The material properties of the considered plates have been assumed to change continuously through the thickness according to a power-law function in terms of volume fractions of the constituents. Since the properties of FG plates are asymmetric with respect to mid-plane, the membrane and bending equations are coupled. Therefore, the concept of the neutral surface position has been introduced to simplify the problem and to avoid the membrane–bending coupling. The total potential energy and Hamilton's principles and Lagrangian equation have been used for the derivation of stiffness, geometrical and mass matrices. To take into account the effect of second order (Buckling), the von Karman strain tensor has been used. The assumed natural shear strain technique has been introduced to ensure the efficiency of the element against the shear locking phenomenon.

3.2 Functionally graded plates

Consider a rectangular plate of plan-form dimensions L and l and uniform thickness h. The coordinate system is taken such that the x–y plane ($z = 0$) coincides with the midplane of the plate ($z \in [-h/2, h/2]$).

Two types of FG plates are studied: (A) FG single layer plates; (B) sandwich plates with FG skins and isotropic core.

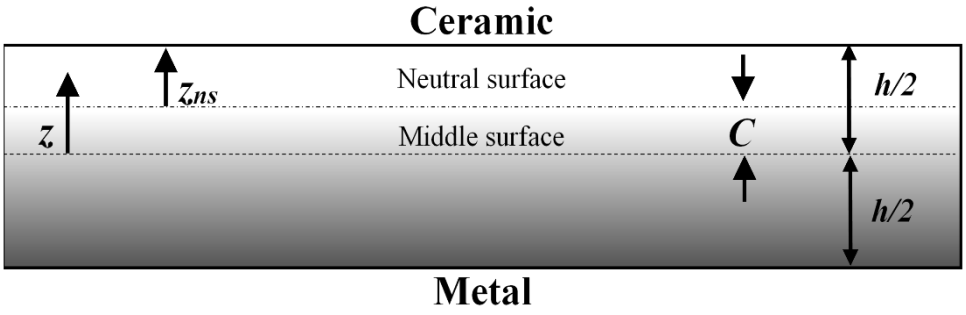

Figure 3.1 Geometry of the functionally graded single layer plate.

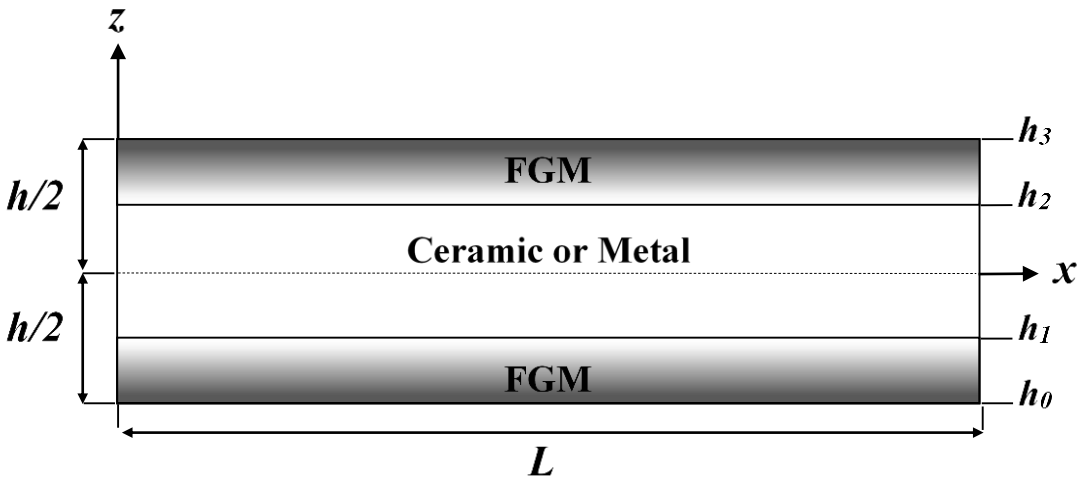

Figure 3.2 Geometry of sandwich plate with FG skins and homogeneous ceramic or metallic core.

3.2.1 FG single layer plate

This plate is graded from metal ($z = -h/2$) to ceramic ($z = h/2$) as shown in Figure 3.1. The effective material properties of the plate,including Young's modulus E and mass density ρ are assumed to vary continusely through the thickness with a power law distribution. According to Voigt's rule of mixtures, Young's modulus $E(z)$ and mass density $\rho(z)$ are given by

$$E(z) = E_m + (E_c - E_m)V_c(z) \tag{3.1}$$

$$\rho(z) = \rho_m + (\rho_c - \rho_m)V_c(z) \tag{3.2}$$

with

$$V_c(z) = \left(\frac{z}{h} + \frac{1}{2}\right)^p, \qquad z \in \left[-\frac{h}{2}, \frac{h}{2}\right] \tag{3.3}$$

where the subscripts m and c represent the metallic and ceramic constituents, respectively; $V_c(z)$ is the volume fraction of the ceramic phase and p is the power-law index that determines the volume fraction gradation, which takes values greater than or equal to zero ($p \geq 0$). The value of (p =0) represents a fully ceramic plate, whereas (p=∞) indicates a fully metallic plate.

For simplicity, Poisson's ratio of the plate is assumed to be constant for that the effect of Poisson's ratio on the deformation is much less than that of Young's modulus.

The variation of the volume fraction of ceramic $V_c(z)$ through-the-thickness of the plate has been presented in Figure (1.21).

3.2.2 Sandwich plate with FG skins and isotropic core

The sandwich plate is composed of three layers: two FG skins and one homogeneous ceramic or metallic core layer. The homogeneous metallic core is commonly employed because of the light weight and high bending stiffness in the structural design. The homogeneous ceramic core is also employed in other fields such as control or in the thermal environments.

The material constituents of the bottom skin varies from a metal-rich surface ($z = h_0$) to a ceramic-rich surface ($z = h_1$) while the top skin varies from a ceramic-rich surface ($z = h_2$) to a metal-rich surface ($z = h_3$), or vice versa, as illustrated in Figure 3.2.

The volume fraction of the ceramic and metal phase V_i (z) (i =c, m) are obtained as

$$\begin{aligned} V_i(z) &= \left(\frac{z-h_0}{h_1-h_0}\right)^p, && z \in \left[h_0, h_1\right] && \left(\text{Bottom layer}\right) \\ V_i(z) &= 1, && z \in \left[h_1, h_2\right] && \left(\text{Ceramic or Metallic core}\right) \\ V_i(z) &= \left(\frac{z-h_3}{h_2-h_3}\right)^p, && z \in \left[h_2, h_3\right] && \left(\text{Top layer}\right) \end{aligned} \tag{3.4}$$

Where h_0= -h/2, h_1, h_2, and h_3= h/2 are the vertical positions of the bottom surface, the two interfaces between layers, and the top surface.

For the brevity, the ratio of the thickness of each layer from bottom to top is denoted by the combination of three numbers, i.e. (1-0-1), (1-1-1), (1-2-1) and (2-1-2).

- The (1-0-1) FG sandwich plate: In this case the plate is symmetric and made of only two equal-thickness FG layers, i.e. there is no core layer. Thus, $h_1 = h_2 = 0$.

- The (2-1-2) FG sandwich plate: The plate is also symmetric and the thickness of the core is half the skin thickness. So, one takes h_1 = -h/10, h_2 = h/10.

- The (1-1-1) FG sandwich plate: Here, the plate is symmetric and made of three equal-thickness layers. In this case, we have, h_1 = -h/6, h_2 = h/6.

- The (1-2-1) FG sandwich plate: Here the plate is symmetric, in which the core thickness equals the sum of skins thickness. So, h_1 = -h/4, h_2 = h/4.

Figure 3.3 shows the through-the-thickness variation of the volume fraction V_i(z) of ceramic and metal for various values of the power-law index p.

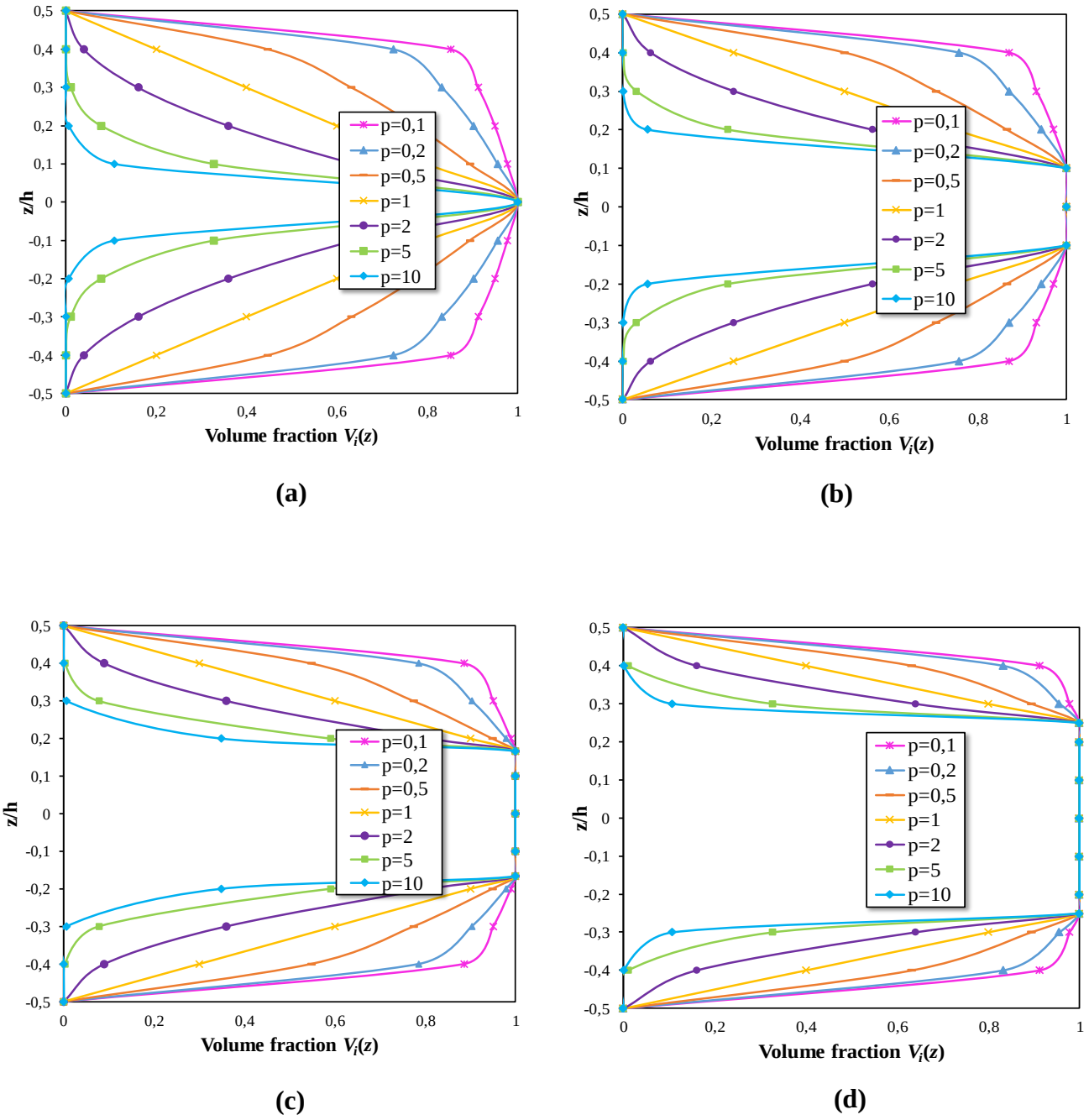

Figure 3.3 The through-the-thickness variation of the volume fraction V_i(z) versus the power-law index *p* for different sandwich plates. (a) The (1-0-1) FG sandwich plate. (b) The (2-1-2) FG sandwich plate. (c) The (1-1-1) FG sandwich plate. (d) The (1-2-1) FG sandwich plate.

3.3 Mathematical formulation

3.3.1 Displacement field

According to the first-order shear deformation theory, the displacement components vector *u*, *v* and *w* in *x*, *y* and *z* directions, respectively, of a point of coordinates (*x*, *y*, *z*) within the FG plate, are given by

$$\begin{aligned} u\,(x,\,y,\,z,t) &= u_0(x,\,y,t) + z\varphi_x(x,y,t) \\ v\,(x,\,y,\,z,t) &= v_0(x,\,y,t) + z\varphi_y(x,y,t) \\ w\,(x,\,y,\,z,t) &= w_0(x,\,y,t) \end{aligned} \tag{3.5}$$

where *t* is the time; u_0, v_0, and w_0 are the in-plane and out-of-plane displacements on the mid-plane of the plate, φ_x and φ_y represent the transverse normal rotations about the *y* and *x* axes, respectively.

3.3.2 kinematics

Using the Von-Karman nonlinear strain-displacement relationship, the strain vector components are given by

$$\begin{aligned} \varepsilon_x &= \frac{\partial u}{\partial x} + \frac{1}{2}\left(\frac{\partial w}{\partial x}\right)^2 = \frac{\partial u_0}{\partial x} + z\frac{\partial \varphi_x}{\partial x} + \frac{1}{2}\left(\frac{\partial w}{\partial x}\right)^2 = \varepsilon_x^0 + zk_x + \varepsilon_x^{nl} \\ \varepsilon_y &= \frac{\partial v}{\partial y} + \frac{1}{2}\left(\frac{\partial w}{\partial y}\right)^2 = \frac{\partial v_0}{\partial y} + z\frac{\partial \varphi_y}{\partial y} + \frac{1}{2}\left(\frac{\partial w}{\partial y}\right)^2 = \varepsilon_y^0 + zk_y + \varepsilon_y^{nl} \\ \gamma_{xy} &= \frac{\partial u}{\partial y} + \frac{\partial v}{\partial x} + \frac{\partial w}{\partial x}\frac{\partial w}{\partial y} = \frac{\partial u_0}{\partial y} + \frac{\partial v_0}{\partial x} + z\left(\frac{\partial \varphi_x}{\partial y} + \frac{\partial \varphi_y}{\partial x}\right) + \frac{\partial w}{\partial x}\frac{\partial w}{\partial y} = \gamma_{xy}^0 + zk_{xy} + \gamma_{xy}^{nl} \\ \gamma_{xz} &= \frac{\partial u}{\partial z} + \frac{\partial w}{\partial x} = \varphi_x + \frac{\partial w}{\partial x} \\ \gamma_{yz} &= \frac{\partial v}{\partial z} + \frac{\partial w}{\partial y} = \varphi_y + \frac{\partial w}{\partial y} \end{aligned} \tag{3.6}$$

Equation (3.6) can be rewritten as follows

$$\begin{aligned} &\{\varepsilon\} = \{\varepsilon^l\} + \{\varepsilon^{nl}\}, \qquad \{\varepsilon^l\} = \{\varepsilon^0\} + z\{k\} \\ &\{\gamma_z\} = \begin{Bmatrix} \gamma_{xz}^0 \\ \gamma_{yz}^0 \end{Bmatrix} \end{aligned} \tag{3.7}$$

Where

$$\left\{\varepsilon^0\right\}=\begin{Bmatrix}\varepsilon_x^0\\ \varepsilon_y^0\\ \gamma_{xy}^0\end{Bmatrix}=\begin{Bmatrix}\dfrac{\partial u_0}{\partial x}\\ \dfrac{\partial v_0}{\partial y}\\ \dfrac{\partial u_0}{\partial y}+\dfrac{\partial v_0}{\partial x}\end{Bmatrix} \tag{3.8}$$

$$\left\{k\right\}=\begin{Bmatrix}k_x\\ k_y\\ k_{xy}\end{Bmatrix}=\begin{Bmatrix}\dfrac{\partial \varphi_x}{\partial x}\\ \dfrac{\partial \varphi_y}{\partial y}\\ \dfrac{\partial \varphi_x}{\partial y}+\dfrac{\partial \varphi_y}{\partial x}\end{Bmatrix} \tag{3.9}$$

$$\left\{\varepsilon^{nl}\right\}=\begin{Bmatrix}\varepsilon_x^{nl}\\ \varepsilon_y^{nl}\\ \gamma_{xy}^{nl}\end{Bmatrix}=\begin{Bmatrix}\dfrac{1}{2}\left(\dfrac{\partial w_0}{\partial x}\right)^2\\ \dfrac{1}{2}\left(\dfrac{\partial w_0}{\partial y}\right)^2\\ \dfrac{\partial w_0}{\partial x}\dfrac{\partial w_0}{\partial y}\end{Bmatrix} \tag{3.10}$$

$$\left\{\gamma_z^0\right\}=\begin{Bmatrix}\gamma_{xz}^0\\ \gamma_{yz}^0\end{Bmatrix}=\begin{Bmatrix}\varphi_x+\dfrac{\partial w_0}{\partial x}\\ \varphi_y+\dfrac{\partial w_0}{\partial y}\end{Bmatrix} \tag{3.11}$$

$\left\{\varepsilon^l\right\}$: linear strain vector

$\left\{\varepsilon^0\right\}$: membrane strain vector.

$\left\{k\right\}$: curvatures vector.

$\left\{\varepsilon^{nl}\right\}$: nonlinear strain vector.

$\left\{\gamma_z^0\right\}$: shear strain vector.

3.3.3 Constitutive equations

The stress- strain relationships of an elastic FG plate can be written as

$$\begin{Bmatrix}\sigma_x\\ \sigma_y\\ \tau_{xy}\end{Bmatrix}=\begin{bmatrix}Q_{11} & Q_{12} & 0\\ Q_{12} & Q_{22} & 0\\ 0 & 0 & Q_{66}\end{bmatrix}\begin{Bmatrix}\varepsilon_x^l\\ \varepsilon_y^l\\ \gamma_{xy}^l\end{Bmatrix} \quad \text{or} \quad \{\sigma\}=[Q]\{\varepsilon^l\} \tag{3.12}$$

and

$$\begin{Bmatrix}\tau_{xz}\\ \tau_{yz}\end{Bmatrix}=\begin{bmatrix}k_sQ_{44} & 0\\ 0 & k_sQ_{55}\end{bmatrix}\begin{Bmatrix}\gamma_{xz}\\ \gamma_{yz}\end{Bmatrix} \quad \text{or} \quad \{\tau_z\}=\left[Q^s\right]\{\gamma_z\} \tag{3.13}$$

Where Q_{ij} are the elasticity stiffness coefficients given by

$$Q_{11}=Q_{22}=\frac{E(z)}{1-\nu^2} \tag{3.14}$$

$$Q_{12}=\nu\frac{E(z)}{1-\nu^2} \tag{3.15}$$

$$Q_{44}=Q_{55}=Q_{66}=\frac{E(z)}{2(1+\nu)} \tag{3.16}$$

k_s denotes the transverse shear correction coefficient.

3.3.4 Force and moment resultants

The asymmetry of material properties of FG plates with respect to midplane give rise to membrane–bending coupling effect in plates. Consequently, to avoid the complexity of membrane–bending coupling effect, the force and the moment resultants are calculated with respect to the physical neutral plane that does not coincide with the midplane of the plate as shown in Figure 3.1[248, 256].

$$z_{np}=z-C \tag{3.17}$$

C is the distance between the neutral plane and the midplane of the plate.

The position of the physical neutral plane can be determined by choosing C such that the membrane force due to bending at the level of ($z = C$) must be zero [256].

$$\int_{-h/2}^{h/2} \sigma_x dz_{np} = \int_{-h/2}^{h/2} \left[Q_{11}(z-C)\frac{d\varphi_x}{dx} + Q_{12}(z-C)\frac{d\varphi_y}{dy} \right] = 0 \tag{3.18}$$

Substituting Eqs (3.14) and (3.15) into Eq (3.18),

$$\int_{-h/2}^{h/2} \left[\frac{E(z)}{1-\nu^2}(z-C)\frac{d\varphi_x}{dx} + \frac{\nu E(z)}{1-\nu^2}(z-C)\frac{d\varphi_y}{dy} \right] = 0 \tag{3.19}$$

By simplifying Eq (3.19), we obtain

$$\frac{1}{1-\nu^2}\left(\frac{d\varphi_x}{dx} + \nu\frac{d\varphi_y}{dy} \right) \int_{-h/2}^{h/2} E(z)(z-C)dz = 0 \tag{3.20}$$

Then,

$$\int_{-h/2}^{h/2} E(z)(z-C)dz = 0, \quad \int_{-h/2}^{h/2} E(z)zdz - C\int_{-h/2}^{h/2} E(z)dz = 0 \tag{3.21}$$

So, the position of the neutral surface can be determined as [189]

$$C = \frac{\int_{-h/2}^{h/2} E(z)zdz}{\int_{-h/2}^{h/2} E(z)dz} \tag{3.22}$$

The forces and moments can be obtained by integrating the corresponding stresses over the thickness as follows

$$\{N\} = \begin{Bmatrix} N_x \\ N_y \\ N_{xy} \end{Bmatrix} = \int_{-h/2}^{h/2} \begin{Bmatrix} \sigma_x \\ \sigma_y \\ \tau_{xy} \end{Bmatrix} dz \tag{3.23}$$

$$\{M\} = \begin{Bmatrix} M_x \\ M_y \\ M_{xy} \end{Bmatrix} = \int_{-h/2}^{h/2} \begin{Bmatrix} \sigma_x \\ \sigma_y \\ \tau_{xy} \end{Bmatrix} (z-C)dz \tag{3.24}$$

$$\{S\} = \begin{Bmatrix} S_{xz} \\ S_{yz} \end{Bmatrix} = \int_{-h/2}^{h/2} \begin{Bmatrix} \tau_{xz} \\ \tau_{yz} \end{Bmatrix} dz \tag{3.25}$$

The relation between the stress resultants and the strains can be expressed by

$$\begin{Bmatrix} N \\ M \\ S \end{Bmatrix} = \begin{bmatrix} [A] & 0 & 0 \\ 0 & [D] & 0 \\ 0 & 0 & [A^s] \end{bmatrix} \begin{Bmatrix} \varepsilon^0 \\ k \\ \gamma_z \end{Bmatrix} \tag{3.26}$$

Equation (3.26) can be also rewritten as following

$$\begin{aligned} \{N\} &= [A]\{\varepsilon^0\} \\ \{M\} &= [D]\{k\} \\ \{S\} &= [A^s]\{\gamma_z\} \end{aligned} \tag{3.27}$$

Where $[A]$,$[D]$ and $[A^s]$ are the extensional, bending and shear reduced elastic matrix, respectively, and are given by

$$[A] = \begin{bmatrix} A_{11} & A_{12} & 0 \\ A_{12} & A_{22} & 0 \\ 0 & 0 & A_{66} \end{bmatrix}$$

$$[D] = \begin{bmatrix} D_{11} & D_{12} & 0 \\ D_{12} & D_{22} & 0 \\ 0 & 0 & D_{66} \end{bmatrix} \tag{3.28}$$

$$[A^s] = \begin{bmatrix} A^s_{44} & 0 \\ 0 & A^s_{55} \end{bmatrix}$$

In which A_{ij}, D_{ij} and A^s_{ij} are the reduced elastic matrices coefficients, defined by

$$\begin{aligned} (A_{ij}, D_{ij}) &= \int_{-h/2}^{h/2} (1, (z-C)^2) Q_{ij}(z) dz \qquad (i, j = 1, 2, 6) \\ (A^s_{ij}) &= k_s \int_{-h/2}^{h/2} Q^s{}_{ij}(z) dz \qquad (i, j = 4, 5) \end{aligned} \tag{3.29}$$

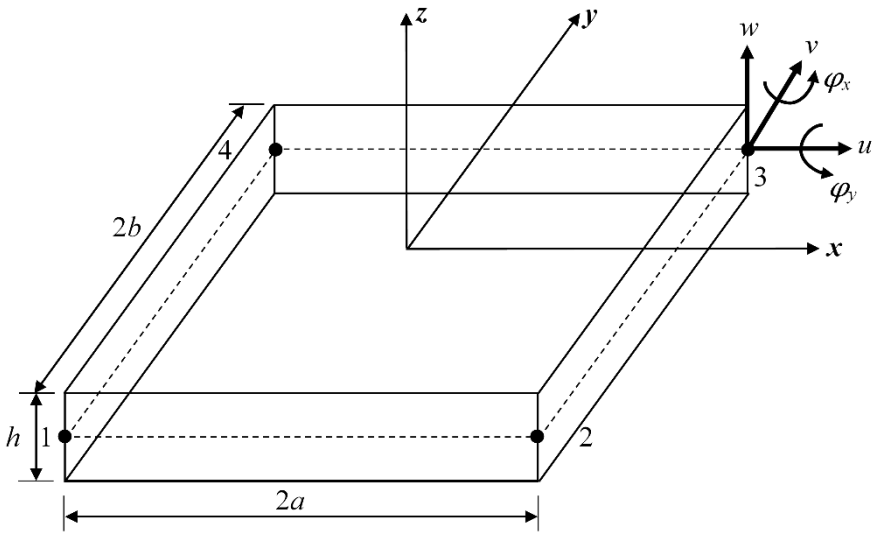

Figure 3.4 Geometry and corresponding nodal variables of the present element.

3.4 Finite element formulation

3.4.1 Element description

A rectangular, four-node finite element based on the first-order shear deformation theory (R4FSDT), with five degrees of freedom per node is used to perform the static, free vibration and buckling analysis of FG single layer and sandwich plates. Figure 3.4 shows the geometry and corresponding nodal variables of the finite element.

3.4.2 Displacement interpolation and shape functions

The displacement field vector of the present finite element can be defined as

$$\delta_\alpha(x,y)=\sum_{i=1}^{4}N_i(x,y)\delta_\alpha^i \qquad (\alpha=1,2,3,4,5) \tag{3.30}$$

Where $\delta_\alpha(x,y)$ is the displacement or rotation of a given point M(x, y) within the element. δ_α^i and $N_i(x,y)$ are the displacement vector and the bilinear Lagrange shape functions associated with node i, respectively.

Where $\delta^i = u_0^i, v_0^i, w_0^i, \varphi_x^i$ and φ_y^i $\quad (i=1,2,3,4)$

The bilinear Lagrange shape functions have the following expressions

$$\begin{aligned} N_1(x,y) &= \frac{1}{4ab}(a-x)(b-y) \\ N_2(x,y) &= \frac{1}{4ab}(a+x)(b-y) \\ N_3(x,y) &= \frac{1}{4ab}(a+x)(b+y) \\ N_4(x,y) &= \frac{1}{4ab}(a-x)(b+y) \end{aligned} \tag{3.31}$$

3.4.3 Strain-displacement relationship matrices

Using the shape functions, the strain-displacement relationship of Eqs (3.8)-(3.11) can be rewritten as follows

$$\left\{\varepsilon^0\right\} = \left[B_m\right]\{q\} \tag{3.32}$$

$$\{k\} = \left[B_b\right]\{q\} \tag{3.33}$$

$$\left\{\gamma_z^0\right\} = \left[B_s\right]\{q\} \tag{3.34}$$

$$\begin{Bmatrix} \dfrac{\partial w}{\partial x} \\ \dfrac{\partial w}{\partial y} \end{Bmatrix} = \left[G\right]\{q\} \tag{3.35}$$

Where $\left[B_m\right]$, $\left[B_b\right]$ are (3×20) matrices, and the subscripts *m* and *b* denote the membrane and the bending strains, respectively. $\left[B_s\right]$ and $\left[G\right]$ are (2×20) matrices, and the subscripts *s* denotes the shear strain. These matrices can be obtained from the derivation of the shape functions of Eq (3.31) as below

$$\left[B_m\right] = \begin{bmatrix} \dfrac{\partial N_i}{\partial x} & 0 & 0 & 0 & 0 \\ 0 & \dfrac{\partial N_i}{\partial y} & 0 & 0 & 0 \\ \dfrac{\partial N_i}{\partial y} & \dfrac{\partial N_i}{\partial x} & 0 & 0 & 0 \end{bmatrix} \qquad (i = 1,2,3,4) \tag{3.36}$$

$$[B_b]=\begin{bmatrix} 0 & 0 & 0 & \dfrac{\partial N_i}{\partial x} & 0 \\ 0 & 0 & 0 & 0 & \dfrac{\partial N_i}{\partial y} \\ 0 & 0 & 0 & \dfrac{\partial N_i}{\partial y} & \dfrac{\partial N_i}{\partial x} \end{bmatrix} \qquad (i=1,2,3,4) \tag{3.37}$$

$$[B_s]=\begin{bmatrix} 0 & 0 & \dfrac{\partial N_i}{\partial x} & N_i & 0 \\ 0 & 0 & \dfrac{\partial N_i}{\partial y} & 0 & N_i \end{bmatrix} \qquad (i=1,2,3,4) \tag{3.38}$$

$$[G]=\begin{bmatrix} 0 & 0 & \dfrac{\partial N_i}{\partial x} & 0 & 0 \\ 0 & 0 & \dfrac{\partial N_i}{\partial y} & 0 & 0 \end{bmatrix} \qquad (i=1,2,3,4) \tag{3.39}$$

$\{q\}$ is the displacement vector (20×1) of the element which given by

$$\{q\}^T=\{u_i, v_i, w_i, \varphi_{xi}, \varphi_{yi}\} \qquad (i=1,2,3,4) \tag{3.40}$$

3.4.4 Assumed natural strain technique

The FSDT coupled with the FEM to analyze mechanical behaviors of FG plates has been successfully utilized. However, it is well-known that the FSDT based FEM approaches using low-order standard shape functions (Lagrangian-based, finite elements) without special treatments inherently produce inaccurate shear strains when dealing with thin plates, due to the shear locking phenomenon. To overcome this problem, Dvorkin and Bathe [257] and Huang and Hinton [258] proposed the so-called ‘’Assumed Natural Strain (ANS) technique’’ as a solution to eliminate (or at least alleviate) the shear locking phenomena.

Here, the ANS is employed to alleviate the shear locking phenomenon. The assumed strains are derived by using the interpolation functions based on Lagrangian polynomial and the strain values at the sampling points where the locking does not exist [259].

For natural assumed transverse shear strains $\bar{\gamma}_{xz}^{0(A)}$ and $\bar{\gamma}_{yz}^{0(A)}$, the following sampling points [255, 256] are employed as shown in Figure 3.5.

$$\bar{\gamma}_{xz}^{0(A)} \to (0,b)_A : (0,-b)_C, \qquad \bar{\gamma}_{yz}^{0(A)} \to (a,0)_B : (-a,0)_D \tag{3.41}$$

Using Eq (3.41), the assumed natural strains can be defined in the following form

$$\bar{\gamma}_{xz}^{0(A)} = \sum_{\delta=1}^{2} P_\delta(y)\bar{\gamma}_{xz}^{\delta}, \qquad \bar{\gamma}_{yz}^{0(A)} = \sum_{\delta=1}^{2} Q_\delta(x)\bar{\gamma}_{yz}^{\delta} \tag{3.42}$$

Where δ is the position of the sampling point and the interpolation functions P and Q are given by

$$\begin{aligned} P_1(y) &= \frac{1}{2b}(b+y), \qquad P_2(y) = \frac{1}{2b}(b-y) \\ Q_1(x) &= \frac{1}{2a}(a+x), \qquad Q_2(x) = \frac{1}{2a}(a-x) \end{aligned} \tag{3.43}$$

The transverse shear strain–displacement relationship produced by the assumed strain method can be rewritten in the following matrix form

$$\left\{\bar{\gamma}_z^0\right\} = \begin{Bmatrix} \bar{\gamma}_{xz}^0 \\ \bar{\gamma}_{yz}^0 \end{Bmatrix} = \left[\bar{B}_s\right]\{q\} \tag{3.44}$$

Where $\left[\bar{B}_s\right]$ is a (2×20) matrix, denotes the assumed natural shear strain-displacement relation matrix given by

$$\left[\bar{B}_s\right] = \begin{bmatrix} 0 & 0 & P_1(y) & \dfrac{\partial N_i}{\partial x}(0,b) & P_1(y)\,N_i(0,b) & 0 \\ 0 & 0 & Q_1(x) & \dfrac{\partial N_i}{\partial y}(a,0) & 0 & Q_1(x)\,N_i(a,0) \end{bmatrix} + \begin{bmatrix} 0 & 0 & P_2(y) & \dfrac{\partial N_i}{\partial x}(0,-b) & P_2(y)\,N_i(0,-b) & 0 \\ 0 & 0 & Q_2(x) & \dfrac{\partial N_i}{\partial y}(-a,0) & 0 & Q_2(x)\,N_i(-a,0) \end{bmatrix} \quad (i=1,2,3,4) \tag{3.45}$$

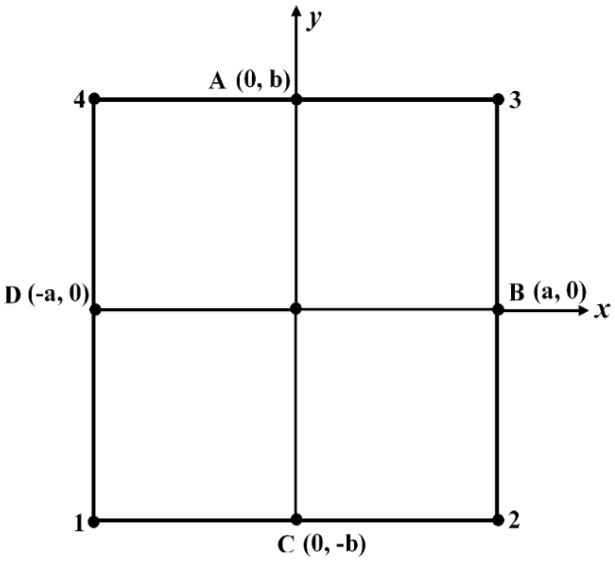

Figure 3.5 Positions of sampling points.

3.4.5 Derivation of the elementary matrices

The total potential energy principle has been used to derive the elementary stiffness and geometrical matrices of the element.

The total potential energy of an FG plate can be given as follows

$$\pi = U + W \tag{3.46}$$

Where U and W are respectively the strain potential energy and the external forces work.

By introducing the assumed natural shear strain of Eq (3.44), The strain potential energy of the plate is defined as

$$\begin{aligned} U &= \frac{1}{2}\int_{\Omega}\int_{-\frac{h}{2}}^{\frac{h}{2}}\left(\left\{\varepsilon^{l}\right\}^{T}\{\sigma\}+\left\{\bar{\gamma}_{z}^{0}\right\}^{T}\{\tau_{z}\}\right)d\Omega \\ &= \frac{1}{2}\int_{\Omega}\int_{-\frac{h}{2}}^{\frac{h}{2}}\left(\left\{\varepsilon^{0}\right\}^{T}\{\sigma\}+z\{k\}^{T}\{\sigma\}+\left\{\bar{\gamma}_{z}^{0}\right\}^{T}\{\tau_{z}\}\right)dzd\Omega \end{aligned} \tag{3.47}$$

And

$$U = \frac{1}{2}\int_{\Omega}\left(\left\{\varepsilon^0\right\}^T\{N\} + \{k\}^T\{M\} + \left\{\bar{\gamma}_z^0\right\}^T\{S\}\right)d\Omega \tag{3.48}$$

Ω is the surface of the plate.

Using Eq (3.27), Eq (3.48) my be written as

$$U = \frac{1}{2}\int_{\Omega}\left(\left\{\varepsilon^0\right\}^T[A]\left\{\varepsilon^0\right\} + \{k\}^T[D]\{k\} + \left\{\bar{\gamma}_z^0\right\}^T\left[A^s\right]\left\{\bar{\gamma}_z^0\right\}\right)d\Omega \tag{3.49}$$

Substituting the strain-displacement relationship from Eqs (3.32), (3.33) and (3.44) in the above equation, we obtain

$$\begin{aligned} U = \frac{1}{2}\int_{\Omega}\Big(&\left(\{q\}^T[B_m]^T[A][B_m]\{q\}\right) + \left(\{q\}^T[B_b]^T[D][B_b]\{q\}\right) \\ &+ \left(\{q\}^T\left[\bar{B}_s\right]^T\left[A^s\right]\left[\bar{B}_s\right]\{q\}\right)\Big)d\Omega \end{aligned} \tag{3.50}$$

3.4.5.1 Static analysis

The external work done by the distributed transverse load $f(x, y)$ applied to the plate can be expressed as

$$W = -\int_{\Omega} f(x,y)w_0(x,y)d\Omega \tag{3.51}$$

Using Eqs (3.50), (3.51), the total potential energy can be written as

$$\begin{aligned} \pi = &\frac{1}{2}\int_{-b}^{b}\int_{-a}^{a}\left(\{q\}^T\left([B_m]^T[A][B_m] + [B_b]^T[D][B_b] + \left[\bar{B}_s\right]^T\left[A^s\right]\left[\bar{B}_s\right]\right)\{q\}\right)dxdy \\ &- \int_{-b}^{b}\int_{-a}^{a} f(x,y)\{q\}^T[N(x,y)]^T dxdy \end{aligned} \tag{3.52}$$

The cancellation of the first variation of the total potential energy $\delta\pi = 0$, with respect to the nodal values $\{q\}$, leads to the following equilibrium equation

$$[K_e]\{q\} = \{F_e\} \tag{3.53}$$

Where $[K_e]$ is the elementary stiffness matrix defined by

$$[K_e] = \int_{-b}^{b}\int_{-a}^{a}\left(\underbrace{[B_m]^T[A][B_m]}_{membrane} + \underbrace{[B_b]^T[D][B_b]}_{bending} + \underbrace{[\bar{B}_s]^T[A^s][\bar{B}_s]}_{shear}\right)dxdy \tag{3.54}$$

and $\{F_e\}$ is the nodal load vector,

$$\{F_e\} = \int_{-b}^{b}\int_{-a}^{a} f(x,y)[N(x,y)]^T dxdy \tag{3.55}$$

Where $[N(x,y)]$ given by

$$[N(x,y)] = [0 \quad 0 \quad N_i \quad 0 \quad 0] \qquad (i = 1,2,3,4) \tag{3.56}$$

3.4.5.2 Mechanical buckling analysis

The strain energy of the FG plate subjected to in-plane forces due to mechanical loading is given by

$$U = \frac{1}{2}\int_{\Omega}\left(\{\varepsilon^0\}^T\{N\} + \{k\}^T\{M\} + \{\bar{\gamma}_z^0\}^T\{S\}\right)d\Omega + \int_{\Omega}\{\varepsilon^{nl}\}\{N\}\,d\Omega \tag{3.57}$$

Using Eq (3.35), we obtain

$$\begin{aligned} U = \frac{1}{2}\int_{\Omega}\Big(&\left(\{q\}^T[B_m]^T[A][B_m]\{q\}\right) + \left(\{q\}^T[B_b]^T[D][B_b]\{q\}\right) \\ &+ \left(\{q\}^T[\bar{B}_s]^T[A^s][\bar{B}_s]\{q\}\right)\Big)d\Omega + \int_{\Omega}\frac{1}{2}\{q\}^T[G]^T[\bar{N}][G]\{q\}\,d\Omega \end{aligned} \tag{3.58}$$

Where $[\bar{N}] = \begin{bmatrix} N_x & N_{xy} \\ N_{xy} & N_y \end{bmatrix}$ is the stress matrix resulting from mechanical loading.

The cancellation of the second variation of the total potential energy with respect to the nodal values $\{q\}$, allows to obtain the following eigenvalue problem

$$\left([k_e] + [k_e^g]\right)\{q\} = 0 \tag{3.59}$$

$\left[k_e^g\right]$ is the geometric stiffness matrix, given by

$$\left[k_e^g\right] = \int_{-b}^{b}\int_{-a}^{a} [G]^T [\bar{N}][G] dxdy \tag{3.60}$$

By introducing the loading factor λ, the stress resultant matrix can be expressed as $[\bar{N}] = \lambda\left[\bar{N}_0\right]$, then the geometric stiffness matrix can be written as follows

$$\left[k_e^{g0}\right] = \int_{-b}^{b}\int_{-a}^{a} [G]^T \left[\bar{N}_0\right][G] dxdy \tag{3.61}$$

Where $\left[\bar{N}_0\right]$ is the stress resultant matrix due to the applied mechanical load.

The eigenvalue problem used to evaluate the critical buckling load can be given by

$$\det\left(\left[k_e\right] + \lambda\left[k_e^{g0}\right]\right) = 0 \tag{3.62}$$

Finally, the critical buckling load is given as follows

$$N_{cri} = \lambda_{cri}\bar{N}_0 \tag{3.63}$$

3.4.5.3 Free vibration analysis

In the free vibration analysis of plates,the kinetic energy of the FG plates is given by

$$T = \frac{1}{2}\int_{\Omega}\int_{-\frac{h}{2}}^{\frac{h}{2}} \rho(z)\left((\dot{u})^2 + (\dot{v})^2 + (\dot{w})^2\right) dzd\Omega \tag{3.64}$$

Where $\rho(z)$ is the mass density calculated by law in Eq (3.2). $(\dot{\cdot})$ is the first derivative with respect to time.

The variation of the kinetic energy with respect to time is obtained as follows.

$$\delta T = \int_{\Omega} \int_{-\frac{h}{2}}^{\frac{h}{2}} \rho(z)(\ddot{u}\delta u + \ddot{v}\delta v + \ddot{w}\delta w) dz d\Omega \tag{3.65}$$

Where $(\ddot{\cdot})$ is a second derivative with respect to time.

By carrying out the integration in thickness, equation (3.65) can be written as follows

$$\delta T = \int_{\Omega} \left(I_0(\ddot{u}_0\delta u_0 + \ddot{v}_0\delta v_0 + \ddot{w}_0\delta w_0) + I_2(\ddot{\varphi}_x\delta\varphi_x + \ddot{\varphi}_y\delta\varphi_y) \right) d\Omega \tag{3.66}$$

Where (I_0, I_2) are moments of inertia defined by

$$(I_0, I_2) = \int_{\frac{-h}{2}}^{\frac{h}{2}} \rho(z)\left(1, (z-c)^2\right) dz \tag{3.67}$$

Lagrangian of the system is given by

$$L = U - T \tag{3.68}$$

In the case of free vibration, the Hamilton's principal is given by

$$\delta \int_0^t L dt = \delta \int_0^t U - T dt = 0 \tag{3.69}$$

Where *t* denotes the time.

Using the Lagrangian equation, given by

$$\frac{d}{dt}\left(\frac{\partial L}{\partial q}\right) - \frac{\partial L}{\partial q} = 0 \tag{3.70}$$

We obtain the following motion equation

$$[k_e]\{q\} + [M]\{\ddot{q}\} = 0 \tag{3.71}$$

The substitution of $\{\ddot{q}\} = -\omega^2\{q\}$ in the above equation leads to

$$\left([k_e] - \omega^2[M]\right)\{q\} = 0 \tag{3.72}$$

Where ω is the natural frequency and $[M]$ is the mass matrix given by

$$[M] = \int_{-b}^{b}\int_{-a}^{a} \left([N(x,y)]^T [m][N(x,y)] \right) dxdy \tag{3.73}$$

Where $[m]$ is the inertia matrix and is given by

$$[m] = \begin{bmatrix} I_0 & 0 & 0 & 0 & 0 \\ 0 & I_0 & 0 & 0 & 0 \\ 0 & 0 & I_0 & 0 & 0 \\ 0 & 0 & 0 & I_2 & 0 \\ 0 & 0 & 0 & 0 & I_2 \end{bmatrix} \tag{3.74}$$

And $[N(x,y)]$ is the shape function matrix

$$[N(x,y)] = \begin{bmatrix} N_i & 0 & 0 & 0 & 0 \\ 0 & N_i & 0 & 0 & 0 \\ 0 & 0 & N_i & 0 & 0 \\ 0 & 0 & 0 & N_i & 0 \\ 0 & 0 & 0 & 0 & N_i \end{bmatrix} \quad (i = 1,2,3,4) \tag{3.75}$$

3.5 Conclusion

A Four-node rectangular finite element, based on the first-order shear deformation theory (R4FSDT), with five degrees of freedom per node, has been adapted for the static, free vibration and buckling analysis of FG plates. FG Single layer and sandwich plates with FG skins and both homogeneous ceramic core and metallic core have been considered. The material properties have been assumed to vary through the plate thickness according to a power-law distribution of the volume fraction of the constituents. To avoid the membrane-bending coupling caused by the asymmetry of the plate according to the thickness, the force and the moment resultants have been calculated with respect to the physical neutral plane which does not coincide with the midplane of the plate. Total potential energy and Hamilton' principles and Lagrangian equation have been used to formulate the stiffness, geometric and mass matrices and the assumed natural shear strain technique has been introduced to alleviate the shear locking phenomenon. The results presented in the following chapter make it possible to clearly appreciate the contribution of the present finite element (R4FSDT) by comparing them with the results reported in the literature.

Chapter 4

Application of R4FSDT-Results and discussions

4.1 Introduction

In this chapter, several numerical examples are presented and discussed to evaluate the performance of the present finite element (R4FSDT). in terms of the accuracy, convergence and stability. The static, mechanical buckling and free vibration behaviors of rectangular FG single layer and sandwich plates are considered. For verification purpose, the obtained results are compared with those reported in the literature. Effects of some parameters on the behaviors of the FG plates are investigated.

4.2 Numerical results and discussions

The static, mechanical buckling and free vibration analysis results of FG single layer and sandwich plates are presented in what follow. Here ceramic–metal functionally graded plates are considered, and their properties, including Young's modulus, Poisson's ratio and density are given in Table 4.1.

Table 4.1 Material properties used in the functionally graded plates.

Properties	**Metal**	**Ceramic**		
	Aluminium (Al)	**Alumina (Al_2O_3)**	**Zirconia-1 (ZrO_2-1)**	**Zirconia-2 (ZrO_2-2)**
***E* (GPa)**	70	380	151	200
ρ(kg/m^3)	2702	3800	3000	5700
v	0.3	0.3	0.3	0.3

4.2.1 Static analysis

This section presents the static analysis of isotropic, FG single layer and sandwich plates subjected to transverse load in the form of uniformly (UDL) and sinusoidally distributed load (SDL).

Where the UDL is expressed as

$$q(x,y)=q_0 \tag{4.1}$$

and the SDL takes the form of

$$q(x,y)=q_0\sin\frac{\pi x}{L}\sin\frac{\pi y}{l} \tag{4.2}$$

For the following examples. the boundary conditions (BCs) are as follows

Simply supported (SSSS)

$$\begin{aligned} &w_0=\varphi_y=0 \quad \text{at} \quad x=0 \quad \text{and} \quad x=L \\ &w_0=\varphi_x=0 \quad \text{at} \quad y=0 \quad \text{and} \quad y=l \end{aligned} \tag{4.3}$$

Clamped (CCCC)

$$w_0=\varphi_x=\varphi_y=0 \quad \text{at} \quad x=0,\ L \quad \text{and} \quad y=0,\ l \tag{4.4}$$

4.2.1.1 Isotropic plates analysis

First, the effectiveness of the present formulation is evaluated by studying the static behavior of isotropic square plates. Two examples have been considered.

The first example deals with a SSSS square isotropic plate subjected to UDL. The side-to-thickness-ratio is taken as (L/h=10). The Young's modulus and Poisson's ratio used for this example are: E=210 GPa and ν=0.3. A shear correction factor of k_s=5/6 is used. The results are presented in terms of deflection and stresses based on the following normalized quantities

$$\begin{aligned} &\widehat{w}=\frac{100E}{q_0hS^4}w\left(\frac{L}{2},\frac{l}{2}\right); \quad \widehat{\sigma}_x=\frac{1}{q_0S^2}\sigma_x\left(\frac{L}{2},\frac{l}{2},\frac{h}{2}\right); \quad S=\frac{L}{h}; \\ &\widehat{\sigma}_y=\frac{1}{q_0S^2}\sigma_y\left(\frac{L}{2},\frac{l}{2},\frac{h}{2}\right); \quad \widehat{\tau}_{xy}=\frac{1}{q_0S^2}\tau_{xy}\left(0,0,\frac{h}{2}\right) \end{aligned} \tag{4.5}$$

Table 4.2 Dimensionless deflection and stresses for isotropic square plate (L/h=10) subjected to UDL.

Mesh size	**8×8**	**12×12**	**16×16**	**20×20**	**24×24**	**32×32**	**Exact [260]**	**TSDT6 [260]**
$\widehat{w}$	4.646	4.657	4.661	4.663	4.664	4.665	4.639	4.625
$\widehat{\sigma}_x$	0.277	0.283	0.285	0.286	0.286	0.287	0.290	0.307
$\widehat{\sigma}_y$	0.277	0.283	0.285	0.286	0.286	0.287	0.290	0.307
$\widehat{\tau}_{xy}$	0.173	0.183	0.188	0.190	0.191	0.193	-	0.195

The results obtained for different mesh sizes are presented in the Table 4.2 along with the Trigonometric Shear Deformation Theory 6 (TSDT6) and the exact solutions from Shimpi et al. [260] and they match very well.

In the second example, a fully ceramic homogeneous square plate subjected to UDL is considered to validate the results of the proposed finite element. The material properties of the used ceramic (Alumina/Al_2O_3) are presented in Table 4.1. Four different side-to-thickness ratios h/L and two types of boundary conditions are considered. The shear correction factor is taken as k_s=5/6.

The results of dimensionless deflection obtained by the present formulation for different meshes are presented in Table 4.3 and compared with the exact values of deflection reported in reference [261].

$$\bar{w} = \frac{10h^3 E_c}{q_0 L^4} w\left(\frac{L}{2}, \frac{l}{2}\right) \tag{4.6}$$

It can be observed from Table 4.3 that the current formulation can well predict the deflection of the simply supported and clamped homogeneous square plates, which confirm the performance of the present finite element.

Table 4.3 Dimensionless deflection of SSSS and CCCC square plates.

BCs	*h*/*L*	8×8	12×12	16×16	20×20	24×24	32×32	Exact [261]
SSSS	0.1	0.4646	0.4657	0.4661	0.4663	0.4664	0.4665	0.4666
	0.2	0.5344	0.5350	0.5353	0.5354	0.5354	0.5355	0.5357
	0.3	0.6508	0.6506	0.6506	0.6505	0.6505	0.6505	0.6504
	0.35	0.7264	0.7257	0.7255	0.7254	0.7253	0.7253	0.7252
CCCC	0.1	0.1625	0.1635	0.1638	0.1640	0.1641	0.1642	0.1637
	0.2	0.2356	0.2365	0.2368	0.2369	0.2370	0.2371	0.2366
	0.3	0.3538	0.3542	0.3543	0.3543	0.3544	0.3544	0.3524
	0.35	0.4300	0.4299	0.4299	0.4299	0.4299	0.4299	0.4314

4.2.1.2 FG plates analysis

In this section, the static behavior of simply supported, square FG plates under distributed transverse load is taken up for investigation. Typical mechanical properties for metal and ceramics used in the FG plates are listed in Table 4.1. In the calculations, both FG single layer and FG sandwich plates are studied. The deflection and stresses are given in the dimensionless form given by the following formulas:

$$\begin{aligned}
&\bar{w} = \frac{10h^3 E_c}{q_0 L^4} w\left(\frac{L}{2}, \frac{l}{2}\right); \quad \bar{\sigma}_x = \frac{h}{q_0 L}\sigma_x\left(\frac{L}{2}, \frac{l}{2}, z\right); \\
&\hat{w} = \frac{10hE_0}{q_0 L^2} w\left(\frac{L}{2}, \frac{l}{2}\right); \; \hat{\sigma}_x = \frac{10h^2}{q_0 L^2}\sigma_x\left(\frac{L}{2}, \frac{l}{2}, z\right); \\
&\bar{\tau}_{xy} = \frac{h}{q_0 L}\tau_{xy}\left(0, 0, z\right). \quad E_0 = 1GPa
\end{aligned} \tag{4.7}$$

The shear correction factor for homogeneous plates is typically taken to be

$$k_s = 5/6 \tag{4.8}$$

This constant shear correction factor is not appropriate for FG plates [96] since it may be a function of material properties and the geometric dimension of a FG plate.

Efraim and Eisenberger [97] presented a shear correction factor for FG plates as

$$k_s = \frac{5}{6-(\nu_m V_m + \nu_c V_c)} \tag{4.9}$$

Where V_m. V_c and ν_m. ν_c are the volume fractions and Poisson's ratios of metal and ceramic. respectively.

In the following examples the two before mentioned shear correction factors are used.

A. FG single layer plates

In this example problem, a simply supported Al/Al_2O_3 square plate (L/h=10) subjected to both UDL and SDL, has been analyzed for various values of the power-law index p. The top surface of the FG plate is ceramic (Al_2O_3) rich and the bottom surface is pure metal (Al).

The dimensionless deflections and stresses results obtained by the present formulation are compared with those obtained from the analytical solution of Zenkour [142], finite element models based on the FDST of Srividhya et al. [134] and Singha et al. [129]. The results agree well for both UDL and SDL, as presented in Tables 4.4 and 4.5, respectively.

From Tables 4.4 and 4.5, It can be observed that the shear correction factor has a slight influence on the deflections while it has no effect on the dimensionless stresses values. In the case of dimensionless deflections, the shear correction factor k_s=5/6 produces result closer to those of Zenkour and Singh. It can also be seen from these tables that the stresses of homogeneous ceramic (p=0) and metal (p=∞) plates are congruent, thus, they are independent of Young's modulus. It can be also observed that as the power-law index increases, which means a gradual change from ceramic to metal, the dimensionless deflection $\bar{w}$ and the normal stress $\bar{\sigma}_x$ increase, while the in-plane shear stress $\bar{\tau}_{xy}$ decreases up to p=2 and then increases with another increase of p.

For further illustration of the present finite element accuracy the variation of deflections $\bar{w}$ as a function of the power-law index p for side-to thickness ratio L/h = 10 under UDL and SDL is shown in Figure 4.1. From this figure, it can be seen that the dimensionless deflection increases with the increase of the power-law index p. This is because that increasing the power law index, increases the metallic volume fraction which reduces the plate rigidity. It is also observed that the present results closely match the analytical solutions given by Zenkour [142].

Table 4.4 Dimensionless stresses and deflections of a SSSS FG square plate(L/h = 10) under UDL .

p	Mesh	k_s	8×8	12×12	16×16	20×20	24×24	Singh [129]	Srividhya [134]	Zenkour [142]
0	$\bar{w}$	**5/6**	0.4646	0.4657	0.4661	0.4663	0.4663	0.4666	0.4493	0.4665
		Eq(4.9)	0.4634	0.4646	0.4650	0.4651	0.4652			
	$\bar{\sigma}_x$**(h/2)**	**5/6**	2.7674	2.8263	2.8468	2.8563	2.8615	2.8688	2.8621	2.8932
		Eq(4.9)	2.7674	2.8263	2.8468	2.8563	2.8615			
	$\bar{\tau}_{xy}$**(-h/3)**	**5/6**	1.1532	1.2222	1.2512	1.2662	1.2750	_	1.2628	1.2850
		Eq(4.9)	1.1532	1.2222	1.2511	1.2662	1.2750			
1	$\bar{w}$	**5/6**	0.9247	0.9270	0.9278	0.9282	0.9284	0.9290	0.8994	0.9287
		Eq(4.9)	0.9228	0.9251	0.9259	0.9262	0.9264			
	$\bar{\sigma}_x$**(h/2)**	**5/6**	4.2772	4.3681	4.3999	4.4146	4.4226	4.4303	4.4236	4.4745
		Eq(4.9)	4.2772	4.3681	4.3999	4.4146	4.4226			
	$\bar{\tau}_{xy}$**(-h/3)**	**5/6**	0.9957	1.0553	1.0804	1.0934	1.1010	_	1.0905	1.1143
		Eq(4.9)	0.9957	1.0553	1.0804	1.0934	1.1010			
2	$\bar{w}$	**5/6**	1.1857	1.1886	1.1897	1.1901	1.1904	1.1952	1.1528	1.1940
		Eq(4.9)	1.1831	1.1861	1.1871	1.1876	1.1878			
	$\bar{\sigma}_x$**(h/2)**	**5/6**	4.9944	5.1005	5.1376	5.1548	5.1641	5.1689	5.1653	5.2296
		Eq(4.9)	4.9944	5.1005	5.1376	5.1548	5.1641			
	$\bar{\tau}_{xy}$**(-h/3)**	**5/6**	0.8874	0.9406	0.9629	0.9745	0.9813	_	0.9719	0.9907
		Eq(4.9)	0.8874	0.9406	0.9629	0.9745	0.9813			
4	$\bar{w}$	**5/6**	1.3710	1.3744	1.3755	1.3761	1.3764	1.3908	_	1.3890
		Eq(4.9)	1.3677	1.3711	1.3722	1.3728	1.3730			
	$\bar{\sigma}_x$**(h/2)**	**5/6**	5.6169	5.7362	5.7779	5.7972	5.8077	5.8035	_	5.8915
		Eq(4.9)	5.6169	5.7362	5.7779	5.7972	5.8077			
	$\bar{\tau}_{xy}$**(-h/3)**	**5/6**	0.9258	0.9811	1.0043	1.0164	1.0235	_	_	1.0298
		Eq(4.9)	0.9258	0.9811	1.0043	1.0164	1.0235			
5	$\bar{w}$	**5/6**	1.4144	1.4178	1.4190	1.4195	1.4198	_	1.3664	1.4356
		Eq(4.9)	1.4108	1.4142	1.4154	1.4160	1.4162			
	$\bar{\sigma}_x$**(h/2)**	**5/6**	5.8616	5.9862	6.0297	6.0499	6.0608	_	6.0622	6.1504
		Eq(4.9)	5.8616	5.9862	6.0297	6.0499	6.0608			
	$\bar{\tau}_{xy}$**(-h/3)**	**5/6**	0.9403	0.9965	1.0201	1.0324	1.0396	_	1.0296	1.0451
		Eq(4.9)	0.9403	0.9965	1.0201	1.0324	1.0395			
10	$\bar{w}$	**5/6**	1.5631	1.5668	1.5681	1.5686	1.5689	_	1.5029	1.5876
		Eq(4.9)	1.5586	1.5623	1.5636	1.5642	1.5645			
	$\bar{\sigma}_x$**(h/2)**	**5/6**	7.0277	7.1771	7.2292	7.2534	7.2665	_	7.2682	7.3689
		Eq(4.9)	7.0277	7.1771	7.2292	7.2534	7.2665			
	$\bar{\tau}_{xy}$**(-h/3)**	**5/6**	0.9637	1.0213	1.0454	1.0580	1.0653	_	1.0550	1.0694
		Eq(4.9)	0.9637	1.0213	1.0454	1.0580	1.0653			
∞	$\bar{w}$	**5/6**	2.5221	2.5282	2.5303	2.5313	2.5318	_	2.4389	2.5327
		Eq(4.9)	2.5158	2.5219	2.5240	2.5250	2.5255			
	$\bar{\sigma}_x$**(h/2)**	**5/6**	2.7674	2.8263	2.8468	2.8563	2.8615	_	2.8621	2.8932
		Eq(4.9)	2.7674	2.8263	2.8468	2.8563	2.8615			
	$\bar{\tau}_{xy}$**(-h/3)**	**5/6**	1.1532	1.2222	1.2512	1.2662	1.2750	_	1.2628	1.2850
		Eq(4.9)	1.1532	1.2222	1.2511	1.2662	1.2750			

Table 4.5 Dimensionless stresses and deflections of a SSSS FG square plate (L/h = 10) under SDL.

p	Mesh	k_s	8×8	12×12	16×16	20×20	24×24	Zenkour [142]	Srividhya [134]	Singh [129]
0	$\bar{w}$	**5/6**	0.2938	0.2951	0.2955	0.2957	0.2958	0.2960	0.2839	0.2961
		Eq(4.9)	0.2930	0.2943	0.2947	0.2949	0.2950			
	$\bar{\sigma}_x$**(h/2)**	**5/6**	1.8597	1.9235	1.9463	1.9568	1.9626	1.9955	1.9572	1.9679
		Eq(4.9)	1.8597	1.9235	1.9463	1.9568	1.9626			
	$\bar{\tau}_{xy}$**(-h/3)**	**5/6**	0.6676	0.6905	0.6987	0.7025	0.7045	0.7065	0.7026	_
		Eq(4.9)	0.6676	0.6905	0.6987	0.7025	0.7045			
1	$\bar{w}$	**5/6**	0.5844	0.5869	0.5878	0.5882	0.5885	0.5889	0.5683	0.5891
		Eq(4.9)	0.5830	0.5856	0.5865	0.5869	0.5871			
	$\bar{\sigma}_x$**(h/2)**	**5/6**	2.8743	2.9729	3.0081	3.0244	3.0333	3.0870	3.0249	3.0389
		Eq(4.9)	2.8743	2.9729	3.0081	3.0244	3.0333			
	$\bar{\tau}_{xy}$**(-h/3)**	**5/6**	0.5765	0.5963	0.6034	0.6066	0.6084	0.6110	0.6067	_
		Eq(4.9)	0.5765	0.5963	0.6034	0.6066	0.6084			
2	$\bar{w}$	**5/6**	0.7493	0.7526	0.7538	0.7543	0.7546	0.7573	0.7284	0.7582
		Eq(4.9)	0.7476	0.7509	0.7520	0.7526	0.7529			
	$\bar{\sigma}_x$**(h/2)**	**5/6**	3.3562	3.4714	3.5124	3.5315	3.5419	3.6094	3.5321	3.5456
		Eq(4.9)	3.3562	3.4714	3.5124	3.5315	3.5419			
	$\bar{\tau}_{xy}$**(-h/3)**	**5/6**	0.5138	0.5315	0.5378	0.5407	0.5423	0.5441	0.5408	_
		Eq(4.9)	0.5138	0.5315	0.5378	0.5407	0.5423			
4	$\bar{w}$	**5/6**	0.8669	0.8707	0.8720	0.8726	0.8729	0.8819	_	0.8831
		Eq(4.9)	0.8646	0.8684	0.8697	0.8703	0.8706			
	$\bar{\sigma}_x$**(h/2)**	**5/6**	3.7745	3.9041	3.9502	3.9716	3.9834	4.0693	_	3.9813
		Eq(4.9)	3.7745	3.9041	3.9502	3.9716	3.9834			
	$\bar{\tau}_{xy}$**(-h/3)**	**5/6**	0.5359	0.5543	0.5608	0.5639	0.5655	0.5667	_	_
		Eq(4.9)	0.5359	0.5543	0.5608	0.5639	0.5655			
5	$\bar{w}$	**5/6**	0.8946	0.8984	0.8997	0.9004	0.9007	0.9118	0.8636	_
		Eq(4.9)	0.8921	0.8959	0.8973	0.8979	0.8982			
	$\bar{\sigma}_x$**(h/2)**	**5/6**	3.9390	4.0742	4.1223	4.1447	4.1570	4.2488	4.1454	_
		Eq(4.9)	3.9390	4.0742	4.1223	4.1447	4.1570			
	$\bar{\tau}_{xy}$**(-h/3)**	**5/6**	0.5443	0.5630	0.5696	0.5727	0.5744	0.5755	0.5728	_
		Eq(4.9)	0.5443	0.5630	0.5696	0.5727	0.5744			
10	$\bar{w}$	**5/6**	0.9892	0.9934	0.9948	0.9954	0.9958	1.0089	0.9500	_
		Eq(4.9)	0.9861	0.9903	0.9917	0.9924	0.9928			
	$\bar{\sigma}_x$**(h/2)**	**5/6**	4.7226	4.8847	4.9424	4.9692	4.9839	5.0890	4.9701	_
		Eq(4.9)	4.7226	4.8847	4.9424	4.9692	4.9839			
	$\bar{\tau}_{xy}$**(-h/3)**	**5/6**	0.5578	0.5769	0.5837	0.5869	0.5886	0.5894	0.5870	_
		Eq(4.9)	0.5578	0.5769	0.5837	0.5869	0.5886			
∞	$\bar{w}$	**5/6**	1.5949	1.6018	1.6042	1.6053	1.6059	1.6070	1.5414	1.6072
		Eq(4.9)	1.5906	1.5975	1.5999	1.6010	1.6016			
	$\bar{\sigma}_x$**(h/2)**	**5/6**	1.8597	1.9235	1.9463	1.9568	1.9626	1.9955	1.9572	1.9679
		Eq(4.9)	1.8597	1.9235	1.9463	1.9568	1.9626			
	$\bar{\tau}_{xy}$**(-h/3)**	**5/6**	0.6676	0.6905	0.6987	0.7025	0.7045	0.7065	0.7026	_
		Eq(4.9)	0.6676	0.6905	0.6987	0.7025	0.7045			

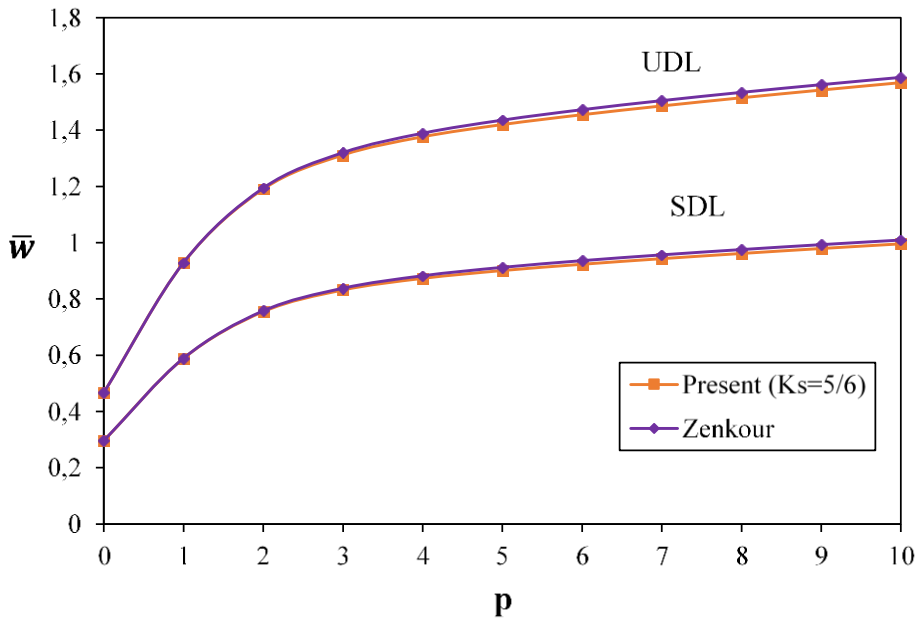

Figure 4.1 Variation of dimensionless deflections versus the power-law index under UDL and SDL, (*L*/*h*=10).

The variation of the dimensionless stresses through the thickness of a square FG plate under SDL has been studied and the results are presented in Figures 4.2 and 4.3.

The distribution of the dimensionless normal stress $\bar{\sigma}_x$ for different values of *p* through the thickness is shown in Figures 4.2. From this figure it can be noticed that the dimensionless normal stress increases with the increase of the power-law index *p* value. It can also be observed that the dimensionless normal stress is tensile at the top surface and compressive at the bottom surface. The homogeneous ceramic plate (*p*= 0) yields the maximum compressive stresses at the bottom surface and the minimum tensile stresses at the top surface of the plate.

Figures 4.3 shows that the dimensionless in-plane shear stress $\bar{\tau}_{xy}$ is tensile at the bottom surface and compressive at the top surface of the FG plates. The homogeneous ceramic plate (*p*= 0) yields the maximum tensile stresses at the bottom surface and the minimum compressive stresses at the top surface of the FG plate. Unlike the dimensionless normal stress, the dimensionless in-plane shear stress decreases with the increasing of the power-law index.

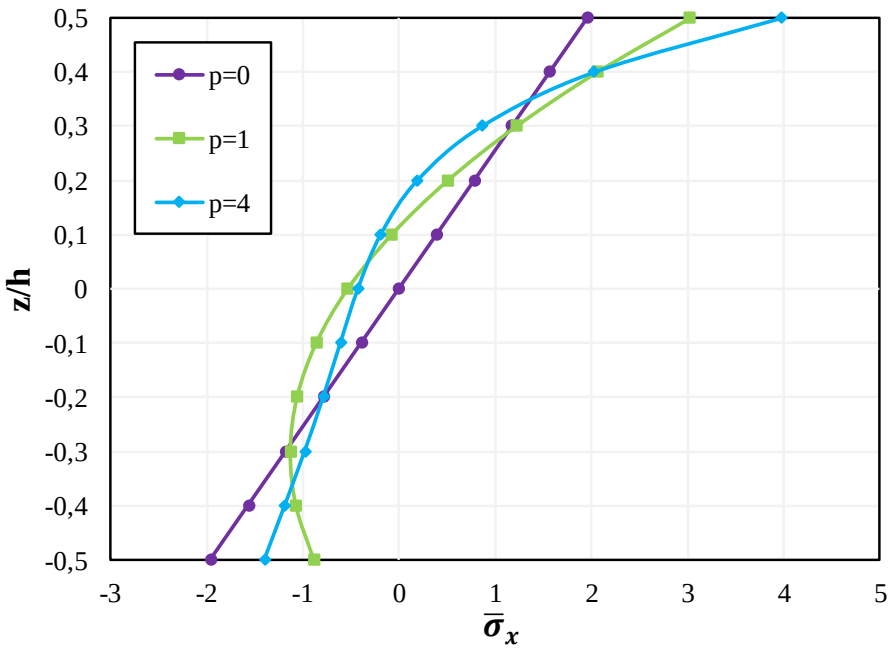

Figure 4.2 Variation of the dimensionless normal stress $\bar{\sigma}_x$ of a FG square plate under SDL for different power-law index values (L/h = 10).

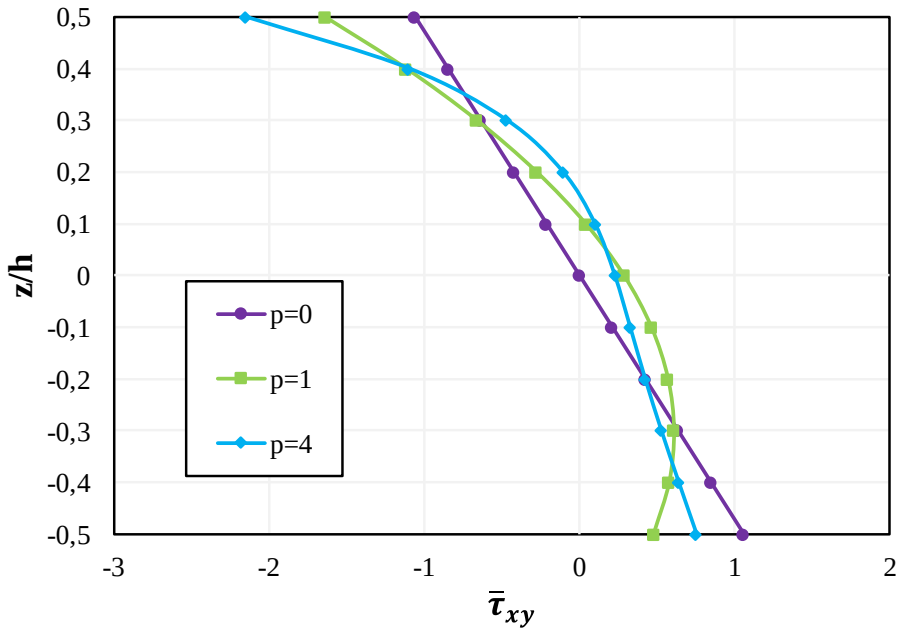

Figure 4.3 Variation of the dimensionless in-plane shear stress $\bar{\tau}_{xy}$ of a FG square plate under SDL for different power-law index values (L/h = 10).

The effect of side-to-thickness ratio *L*/*h* on the dimensionless deflection $\bar{w}$ and the normal stress $\bar{\sigma}_x$ of a simply supported, FG square plates subjected to sinusoidal load are presented in Table 4.6. The results obtained using a 20 × 20 mesh size, are compared with the quasi-3D solutions generated by Neves et al. [171]. As it can be seen, the values of deflection and normal stress obtained by the present finite element are in good agreement with those of the reference. This reiterates the fact that FSDT may be well suited to simpler geometries and moderately thick plates.

Table 4.6 Effect of side-to-thickness ratio *L*/*h* on the dimensionless deflection and normal stress of SSSS Al/Al_2O_3 square plate under SDL.

P	**Theory**	$\bar{\sigma}_x$**(h/3)**			$\bar{w}$		
		L/h=4	**L/h=10**	**L/h=100**	**L/h=4**	**L/h=10**	**L/h=100**
0	Neves [171]	0.5151	1.3124	13.1610	0.3786	0.2961	0.2803
	Present (5/6)	**0.5218**	**1.3046**	**13.0463**	**0.3789**	**0.2957**	**0.2800**
	Present (Eq(4.9))	**0.5218**	**1.3046**	**13.0463**	**0.3739**	**0.2949**	**0.2800**
0.5	Neves [171]	0.5736	1.4629	14.6720	0.5699	0.4579	0.4365
	Present (5/6)	**0.5802**	**1.4505**	**14.5057**	**0.5677**	**0.4535**	**0.4320**
	Present (Eq(4.9))	**0.5802**	**1.4505**	**14.5058**	**0.5609**	**0.4524**	**0.4320**
1	Neves [171]	0.5806	1.4874	14.944	0.7308	0.5913	0.5648
	Present (5/6)	**0.5930**	**1.4825**	**14.8258**	**0.7287**	**0.5882**	**0.5618**
	Present (Eq(4.9))	**0.5930**	**1.4825**	**14.8259**	**0.7203**	**0.5869**	**0.5618**
4	Neves [171]	0.4338	1.1592	11.7370	1.1552	0.8770	0.8241
	Present (5/6)	**0.4723**	**1.1808**	**11.8087**	**1.1120**	**0.8726**	**0.8275**
	Present (Eq(4.9))	**0.4723**	**1.1808**	**11.8087**	**1.0977**	**0.8703**	**0.8275**
10	Neves [171]	0.3112	0.8468	8.6011	1.3760	0.9952	0.9228
	Present (5/6)	**0.3529**	**0.8822**	**8.8223**	**1.3173**	**0.9954**	**0.9348**
	Present (Eq(4.9))	**0.3529**	**0.8822**	**8.8223**	**1.2981**	**0.9924**	**0.9348**

From Table 4.6, one can clearly observe that the dimensionless deflection decreases as the side-to thickness ratio (*L*/*h*) increase, while the dimensionless normal stress increases. Additionally, it is easily observable that the influence of the shear correction factor on the dimensionless deflection decreases as the side-to-thickness ratio L/h increases.

B. FG sandwich plates analysis

In this section, the deflections and stresses of a simply supported sandwich plate with FG skins and homogeneous core are presented and compared with the existing solutions to verify the accuracy of the present formulation. FG sandwich plates made of two sets of material combinations of metal and ceramic, Al/ZrO_2-1 and Al/Al_2O_3 are considered. Their material properties are given in Table 4.1.

Two cases of FG sandwich plates are studied:

- ***Sandwich plate with ceramic core*:** homogeneous core with ZrO_2-1 and FG skins with top and bottom surfaces made of Al.
- ***Sandwich plate with Metallic core*:** homogeneous core with Al and FG skins with top and bottom surfaces made of Al_2O_3.

At First, a convergence study was performed for the dimensionless deflection $\hat{w}$ and normal stress $\hat{\sigma}_x$ of a square Al/ZrO_2-1 sandwich plate under SDL considering p=2. Four configurations of sandwich plates (1-0-1, 1-2-1, 1-1-1 and 2-1-2) are considered. The results for several meshes are reported in Table 4.7. It is observed that the present results converge rapidly to those of Zenkour's FSDT [141].

Tables 4.8 and 4.9 contain the dimensionless deflection $\hat{w}$ and normal stress $\hat{\sigma}_x$ of square Al/ZrO_2-1 sandwich plates with homogeneous ceramic core. A 20 × 20 mesh is considered. The results are considered for different values of p and for different types of sandwich plates. The obtained results using the present finite element are compared with the SSDT, TSDT and FSDT results generated by Zenkour [141]. In general, a good agreement is found.

Table 4.7 Convergence of the dimensionless deflection and normal stress under SDL for p=2 and L/h=10.

Mesh size	**Sandwich plate configurations**			
	1-0-1	**2-1-2**	**1-1-1**	**1-2-1**
Dimensionless deflection $\widehat{w}$				
4×4	0.3627	0.3422	0.3232	0.2936
8×8	0.3722	0.3513	0.3318	0.3013
12×12	0.3738	0.3529	0.3332	0.3026
16×16	0.3744	0.3534	0.3338	0.3031
20×20	0.3747	0.3536	0.3340	0.3033
24×24	0.3748	0.3538	0.3341	0.3034
FSDT [141]	0.3751	0.3541	0.3344	0.3037
Dimensionless normal stress $\widehat{\sigma}_x$				
4×4	1.3821	1.3072	1.2350	1.1206
8×8	1.6668	1.5766	1.4895	1.3515
12×12	1.7240	1.6307	1.5406	1.3978
16×16	1.7444	1.6500	1.5588	1.4144
20×20	1.7539	1.6589	1.5673	1.4221
24×24	1.7591	1.6638	1.5719	1.4262
FSDT [141]	1.7709	1.6750	1.5824	1.4358

From Table 4.8, it can be seen that the shear correction factor has an effect on the dimensionless deflection $\widehat{w}$ as previously indicated. It can be observed from the table that when the shear correction factor is k_s=5/6, the deflection results by the present formulation are close to those obtained by FSDT. However, in the case of k_s (see Eq (4.9)), the present dimensionless deflection results are identical to those of TSDT and SSDT. The values of the dimensionless normal stresses $\widehat{\sigma}_x$ do not depend of the used shear correction factor, as shown in Table 4.9.

In general, the difference between several types of sandwich plates is insignificant for fully ceramic plates (p = 0). The fully ceramic plates give the smallest deflections and the largest normal stresses. As the power-law index p increases, the dimensionless deflection and normal stress increase, excepted for the case of (p = 0). These results decrease as the core thickness, with respect to the total thickness of the plate, increases (1-2-1).

Table 4.8 Dimensionless deflection of SSSS FG sandwich square plate with ceramic core under SDL (L/h= 10).

p	Theory	$\widehat{w}$			
		1-0-1	2-1-2	1-1-1	1-2-1
0	SSDT [141]	0.1961	0.1961	0.1961	0.1961
	TSDT [141]	0.1961	0.1961	0.1961	0.1961
	FSDT [141]	0.1961	0.1961	0.1961	0.1961
	Present (5/6)	**0.1958**	**0.1958**	**0.1958**	**0.1958**
	Present (Eq(4.9))	**0.1953**	**0.1953**	**0.1953**	**0.1953**
1	SSDT [141]	0.3235	0.3062	0.2919	0.2709
	TSDT [141]	0.3236	0.3063	0.2920	0.2709
	FSDT [141]	0.3248	0.3075	0.2930	0.2717
	Present (5/6)	**0.3244**	**0.3071**	**0.2926**	**0.2713**
	Present (Eq(4.9))	**0.3237**	**0.3065**	**0.2920**	**0.2707**
5	SSDT [141]	0.4091	0.3916	0.3713	0.3347
	TSDT [141]	0.4093	0.3918	0.3715	0.3348
	FSDT [141]	0.4112	0.3942	0.3736	0.3363
	Present (5/6)	**0.4107**	**0.3937**	**0.3731**	**0.3359**
	Present (Eq(4.9))	**0.4097**	**0.3929**	**0.3724**	**0.3352**
10	SSDT [141]	0.4175	0.4038	0.3849	0.3412
	TSDT [141]	0.4177	0.4041	0.3855	0.3482
	FSDT [141]	0.4192	0.4066	0.3879	0.3499
	Present (5/6)	**0.4187**	**0.4061**	**0.3874**	**0.3495**
	Present (Eq(4.9))	**0.4177**	**0.4052**	**0.3866**	**0.3488**

Figure 4.4 illustrates the variation of dimensionless deflection $\widehat{w}$ of square Al/ZrO_2-1 sandwich plates with homogeneous ceramic core versus the power-law index *p*. Side-to-thickness ratio is taken equal to *L*/*h*=10.

Figures 4.5 and 4.6 contain the plots of the dimensionless normal stress $\widehat{\sigma}_x$ through the thickness of (1-1-1) and (1-2-1) sandwich plates with homogeneous ceramic core and for *p* = 0,1,4. It is clear from those two figures that the stress profile for plate made of pure material (ceramic, *p*=0) changes linearly through the thickness. However, the normal stress variation is not linear for FG plate (*p*=1, 4). It can be seen that the normal stress is tensile at the top surface and compressive at the bottom surface. The homogeneous ceramic plate (*p*=0) yields the

maximum compressive stresses at the bottom surface and the minimum tensile stresses at the top surface of the sandwich plate.

Tables 4.10 and 4.11 list the dimensionless deflection $\hat{w}$ and normal stress $\hat{\sigma}_x$ for p = 0,0.5,1, 5, 10 and different types of square Al/Al_2O_3 sandwich plate with homogeneous metallic core. The results obtained using the present formulation are compared with those based on the Hyperbolic refined four-variable theory (HRPT) of Boucheta [262]. It can be noted that the results are in a good agreement. Contrary to the case of ceramic core, it can be observed that the dimensionless deflection and normal stress for FG plates decrease with increasing the power-law index *p*. It is also observed from Tables 4.10 and 4.11 that as the core thickness, with respect to the total thickness of the plate increases, both dimensionless deflection and normal stress increase.

Table 4.9 Dimensionless normal stress of SSSS FG sandwich square plate with ceramic core under SDL (L/h= 10).

P	**Theory**	$\hat{\sigma}_x(h/2)$			
		1-0-1	2-1-2	1-1-1	1-2-1
0	SSDT [141]	2.0545	2.0545	2.0545	2.0545
	TSDT [141]	2.0499	2.0499	2.0499	2.0499
	FSDT [141]	1.9758	1.9758	1.9758	1.9758
	Present (5/6)	**1.9568**	**1.9568**	**1.9568**	**1.9568**
	Present (Eq(4.9))	**1.9568**	**1.9568**	**1.9568**	**1.9568**
1	SSDT [141]	1.5820	1.4986	1.4289	1.3259
	TSDT [141]	1.5792	1.4959	1.4262	1.3231
	FSDT [141]	1.5325	1.4517	1.3830	1.2809
	Present (5/6)	**1.5178**	**1.4378**	**1.3698**	**1.2687**
	Present (Eq(4.9))	**1.5178**	**1.4378**	**1.3698**	**1.2687**
5	SSDT [141]	1.9957	1.9155	1.8184	1.6411
	TSDT [141]	1.9927	1.9130	1.8158	1.6381
	FSDT [141]	1.9358	1.8648	1.7699	1.5931
	Present (5/6)	**1.9172**	**1.8469**	**1.7529**	**1.5778**
	Present (Eq(4.9))	**1.9172**	**1.8469**	**1.7529**	**1.5778**
10	SSDT [141]	2.0336	1.9731	1.8815	1.6485
	TSDT [141]	2.0304	1.9713	1.8838	1.7042
	FSDT [141]	1.9678	1.9217	1.8375	1.6584
	Present (5/6)	**1.9490**	**1.9033**	**1.8199**	**1.6428**
	Present (Eq(4.9))	**1.9490**	**1.9032**	**1.8199**	**1.6428**

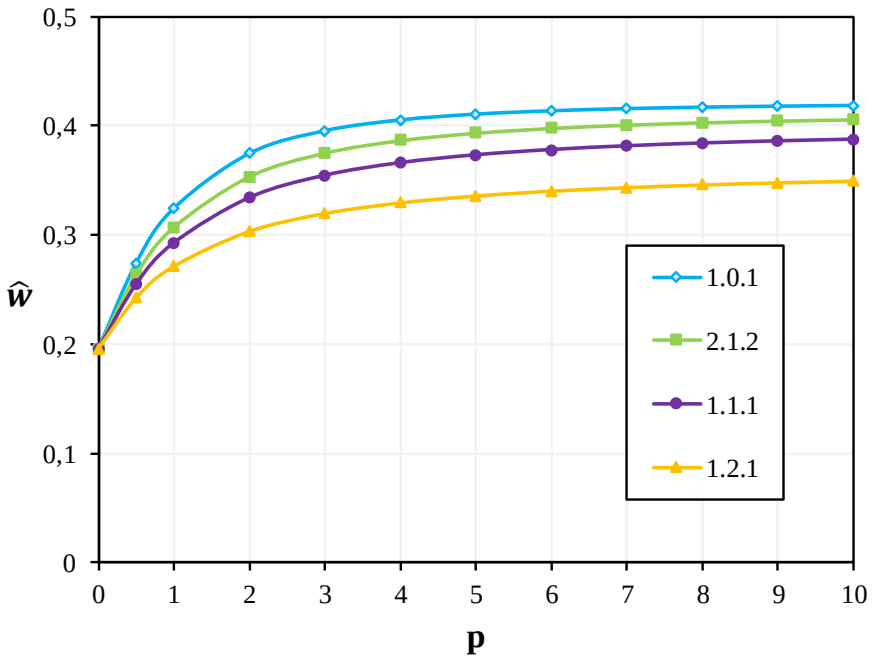

Figure 4.4 Variation of the dimensionless deflection $\hat{w}$ of Al/ZrO$_2$-1 sandwich square plates with ceramic core under SDL for different power-law index values (L/h = 10), k_s=5/6.

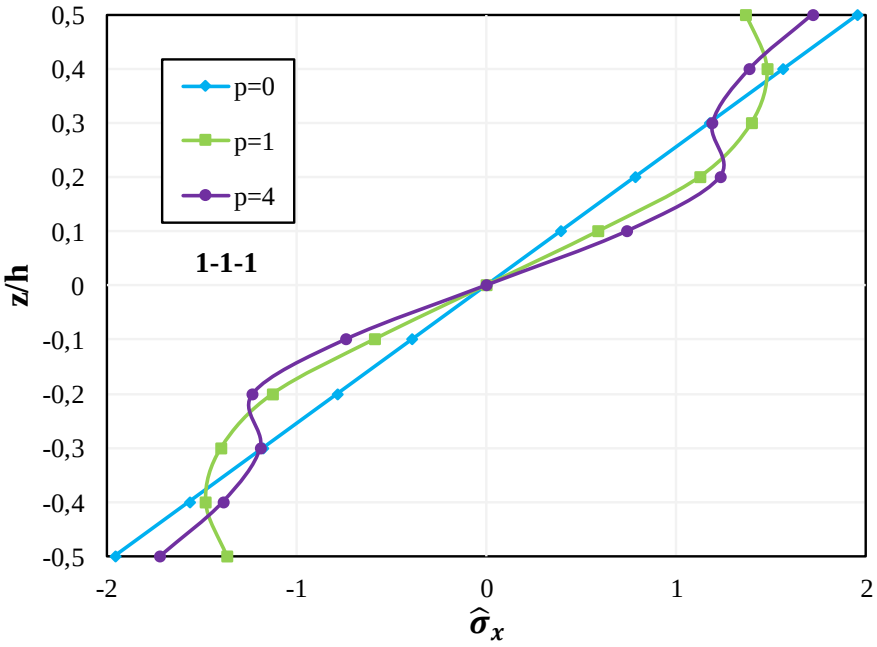

Figure 4.5 Variation of the dimensionless normal stress $\hat{\sigma}_x$ of Al/ZrO$_2$-1 sandwich square plate (1-1-1) with ceramic core under SDL for different power-law index values (L/h = 10).

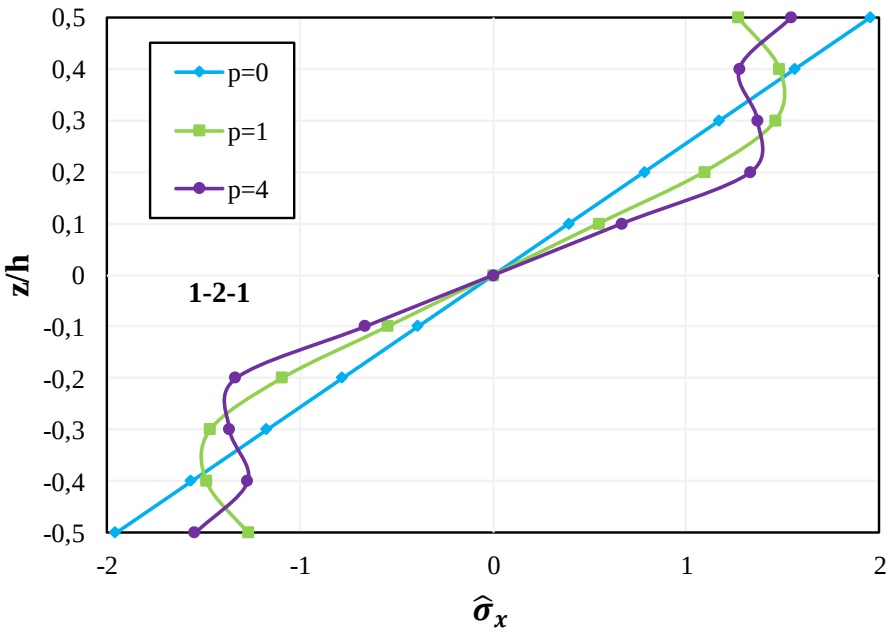

Figure 4.6 Variation of the dimensionless normal stress $\hat{\sigma}_x$ of Al/ZrO_2-1 sandwich square plate (1-2-1) with ceramic core under SDL for different power-law index values (L/h = 10).

Figure 4.7 shows the variation of dimensionless deflection $\hat{w}$ of square Al/Al_2O_3 sandwich plates with homogeneous metallic core versus the power-law index p. Side-to-thickness ratio is taken to equal L/h=10.

Figures 4.8 and 4.9 illustrate the variation of the dimensionless normal stress $\hat{\sigma}_x$ through the thickness of (1-1-1) and (1-2-1) sandwich plates with homogenous metallic core for p = 0,1,4. As shown in figures, the dimensionless axial stress of purely metallic plate (p=0) varies linearly through the thickness. However, the variation of this stress is not linear for cases of p>0. The maximum values of the normal compressive and tensile stresses are found on the lower and upper extreme surfaces of the plate respectively.

- **Effect of side-to-thickness ratio on the dimensionless deflection of FG sandwich plate with homogeneous core either ceramic or metallic**

The variation of the dimensionless deflection $\hat{w}$ of square FG sandwich plate with homogeneous core either ceramic or metallic versus side-to-thickness ratio L/h is shown in Figures 4.10 and 4.11.

Table 4.10 Dimensionless deflection of SSSS FG sandwich square plate with metallic core under SDL (L/h= 10).

p	Theory	$\widehat{w}$			
		1-0-1	**2-1-2**	**1-1-1**	**1-2-1**
0	HRPT [262]	0.4229	0.4229	0.4229	0.4229
	Present (5/6)	**0.4224**	**0.4224**	**0.4224**	**0.4224**
	Present (Eq(4.9))	**0.4213**	**0.4213**	**0.4213**	**0.4213**
0.5	HRPT [262]	0.1292	0.1404	0.1510	0.1700
	Present (5/6)	**0.1266**	**0.1367**	**0.1465**	**0.1651**
	Present (Eq(4.9))	**0.1261**	**0.1361**	**0.1460**	**0.1644**
1	HRPT [262]	0.1015	0.1103	0.1190	0.1355
	Present (5/6)	**0.0996**	**0.1070**	**0.1147**	**0.1300**
	Present (Eq(4.9))	**0.0992**	**0.1066**	**0.1142**	**0.1295**
5	HRPT [262]	0.0802	0.0843	0.0897	0.1015
	Present (5/6)	**0.0796**	**0.0826**	**0.0868**	**0.0966**
	Present (Eq(4.9))	**0.0793**	**0.0823**	**0.0864**	**0.0962**
10	HRPT [262]	0.0787	0.0819	0.0864	0.0971
	Present (5/6)	**0.0784**	**0.0805**	**0.0839**	**0.0926**
	Present (Eq(4.9))	**0.0781**	**0.0802**	**0.0836**	**0.0923**

Table 4.11 Dimensionless normal stress of SSSS FG sandwich square plate with metallic core under SDL (L/h= 10).

p	Theory	$\widehat{\sigma}_x(h/2)$			
		1-0-1	**2-1-2**	**1-1-1**	**1-2-1**
0	HRPT [262]	1.9933	1.9933	1.9933	1.9933
	Present (5/6)	**1.9568**	**1.9568**	**1.9568**	**1.9568**
	Present (Eq(4.9))	**1.9568**	**1.9568**	**1.9568**	**1.9568**
0.5	HRPT [262]	3.1927	3.4362	3.6778	4.1362
	Present (5/6)	**3.1206**	**3.3551**	**3.5902**	**4.0405**
	Present (Eq(4.9))	**3.1206**	**3.3551**	**3.5902**	**4.0405**
1	HRPT [262]	2.5155	2.6915	2.8776	3.2509
	Present (5/6)	**2.4582**	**2.6250**	**2.8041**	**3.1685**
	Present (Eq(4.9))	**2.4582**	**2.6250**	**2.8041**	**3.1685**
5	HRPT [262]	2.0273	2.0921	2.1887	2.4238
	Present (5/6)	**1.9858**	**2.0425**	**2.1317**	**2.3558**
	Present (Eq(4.9))	**1.9858**	**2.0425**	**2.1317**	**2.3558**
10	HRPT [262]	2.0015	2.0431	2.1203	2.3270
	Present (5/6)	**1.9624**	**1.9965**	**2.0664**	**2.2617**
	Present (Eq(4.9))	**1.9624**	**1.9965**	**2.0664**	**2.2617**

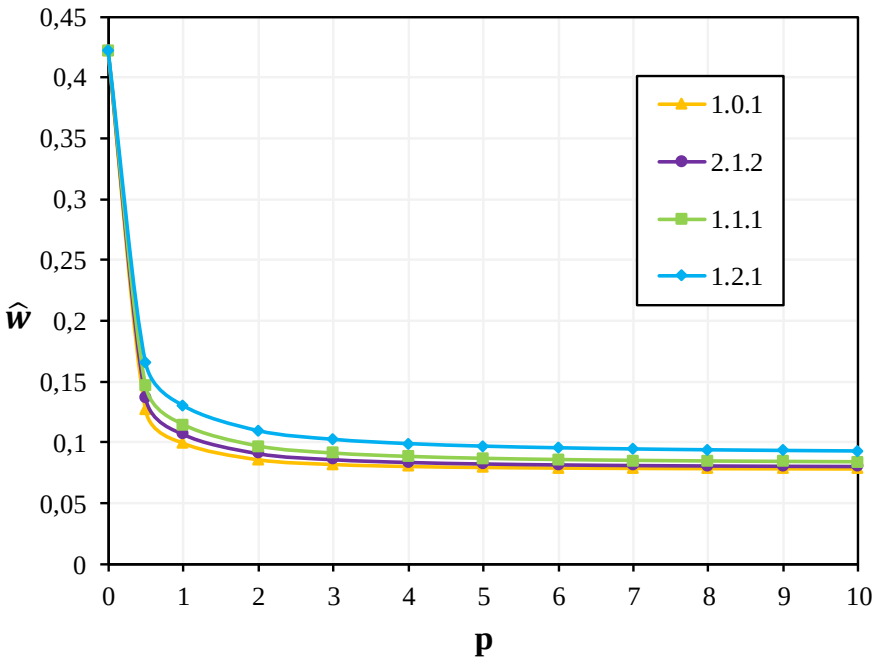

Figure 4.7 Variation of the dimensionless deflection $\widehat{w}$ of Al/Al_2O_3 sandwich square plates with metallic core under SDL for different power-law index values (L/h = 10), k_s=5/6.

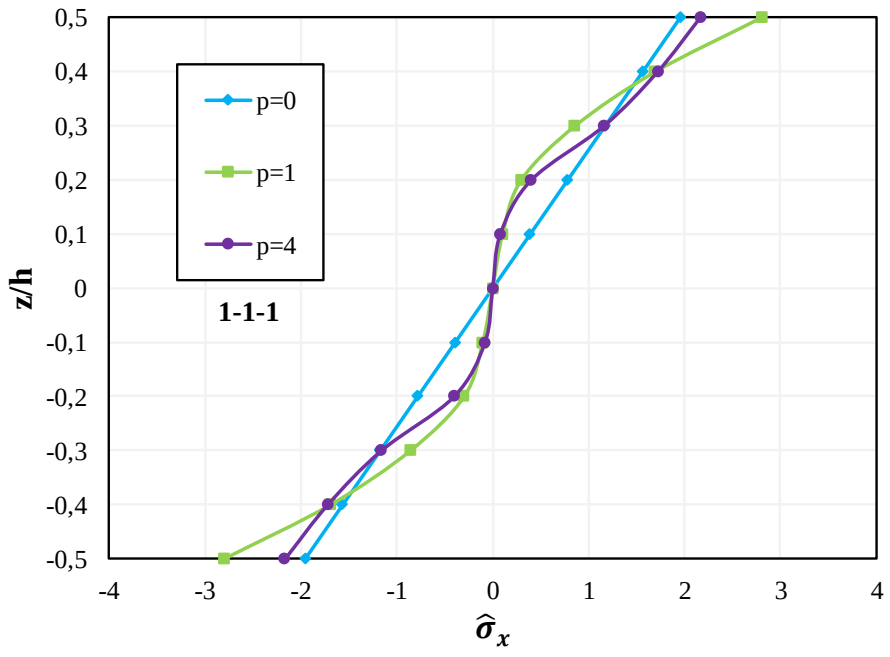

Figure 4.8 Variation of the dimensionless normal stress $\widehat{\sigma}_x$ of Al/Al_2O_3 sandwich square plate (1-1-1) with metallic core under SDL for different power-law index values (L/h = 10).

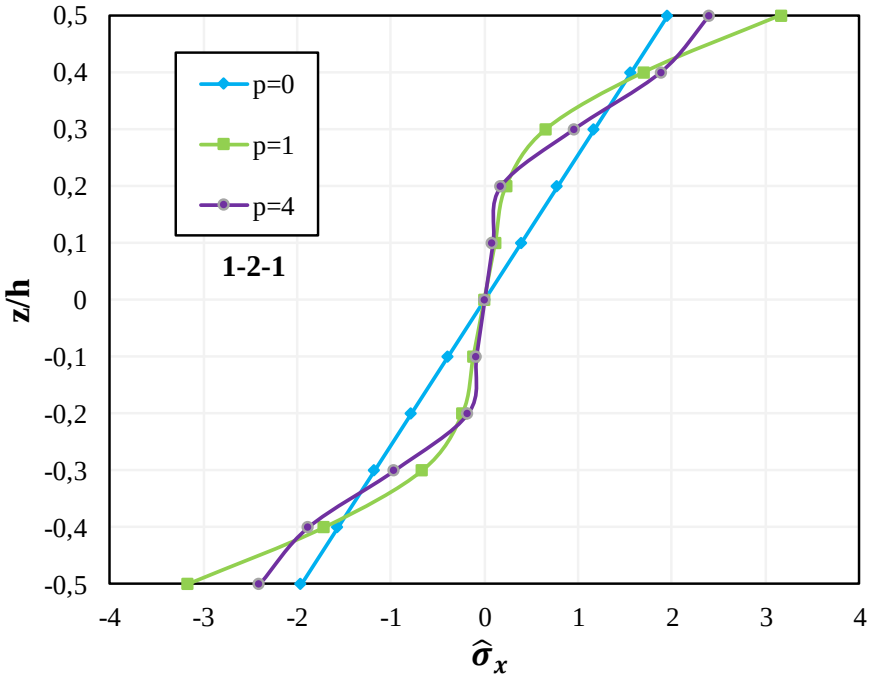

Figure 4.9 Variation of the dimensionless normal stress $\widehat{\sigma}_x$ of Al/Al_2O_3 sandwich square plate (1-2-1) with metallic core under SDL for different power-law index values (L/h = 10).

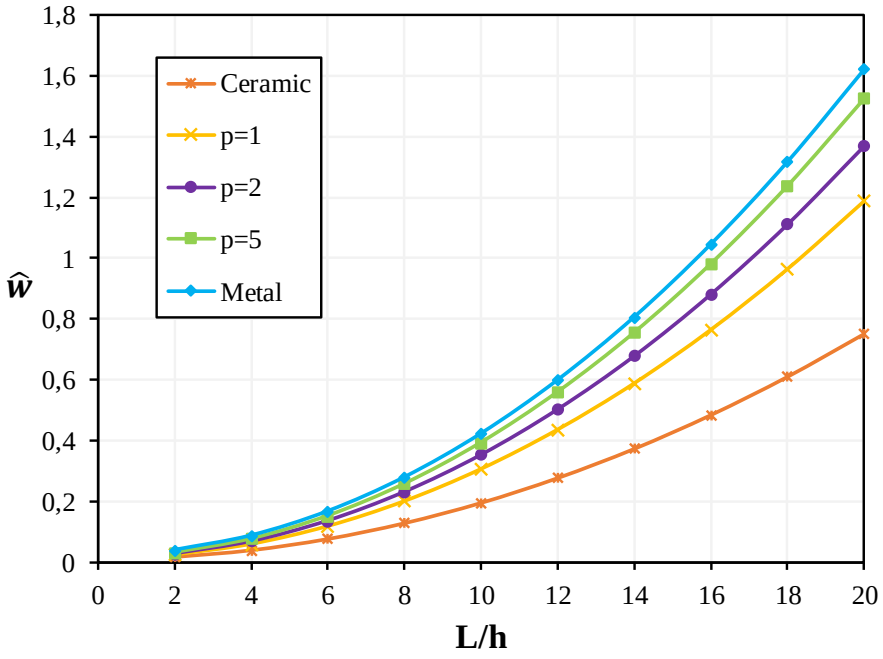

Figure 4.10 Variation of dimensionless deflection $\widehat{w}$ of (2-1-2) FG sandwich square plate with homogeneous ceramic core under SDL versus side-to-thickness ratio L/h, (k_s=5/6).

Figures 4.10 depicts the variation of dimensionless deflection of a simply supported (2-1-2) sandwich plate with homogeneous ceramic core versus side-to-thickness ratio for different values of power- law index *p*. It can be observed that the dimensionless deflection increases with the increase of L/h. it is also noticed that the dimensionless deflection of the metallic plate is the largest and that of the ceramic plate is the smallest. This is due to the fact that the metallic plate is less rigid than the ceramic plate. All plates with intermediate properties (p= 1, 2, 5) exhibit corresponding intermediate values of dimensionless deflection.

Figures 4.11 shows the variation of dimensionless deflection of a simply supported (2-1-2) sandwich plate with homogeneous metallic core versus side-to-thickness ratio. Unlike the case of homogeneous ceramic core, it can be observed that for FG plates with homogeneous metallic core, dimensionless deflection decreases as power law index *p* is increased.

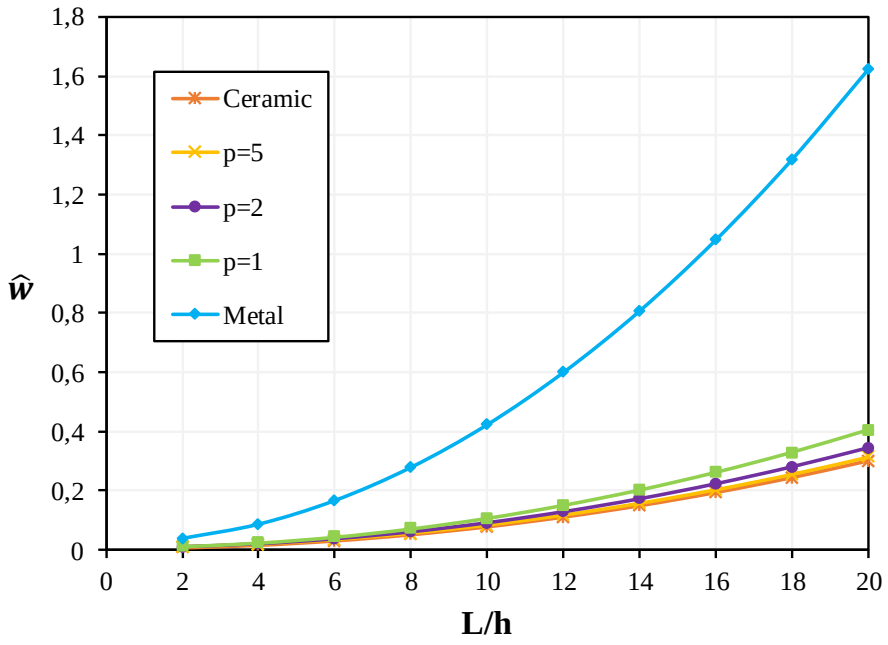

Figure 4.11 Variation of dimensionless deflection $\widehat{w}$ of (2-1-2) FG sandwich square plate with homogeneous metallic core under SDL versus side-to-thickness ratio *L*/*h*, (k_s=5/6).

4.2.2 Mechanical buckling analysis

The aim of this section is to verify the accuracy of the present finite element (R4FSDT) in predicting the critical buckling load of FG sandwich plates. Square Al/Al_2O_3 sandwich plates with homogeneous core either ceramic (Alumina, Al_2O_3) or metallic (Aluminum, Al) are considered. Young's modulus and Poisson's ratio of aluminum are E_m=70 GPa, ν_m= 0.3, respectively, and those of alumina are E_c=380 GPa, ν_c= 0.3. Three different types of in-plane loads, uniaxial compression, biaxial compression and biaxial compression and tension are considered.

For convenience, the following dimensionless critical buckling load is used

$$\widehat{N}_{cri} = N_{cri}\frac{L^2}{100E_0h^3}, \qquad E_0 = 1 \text{ GPa} \tag{4.10}$$

The plates are assumed to be simply supported at all edges, (Eq (4.3)). The shear correction factor is taken as 5/6.

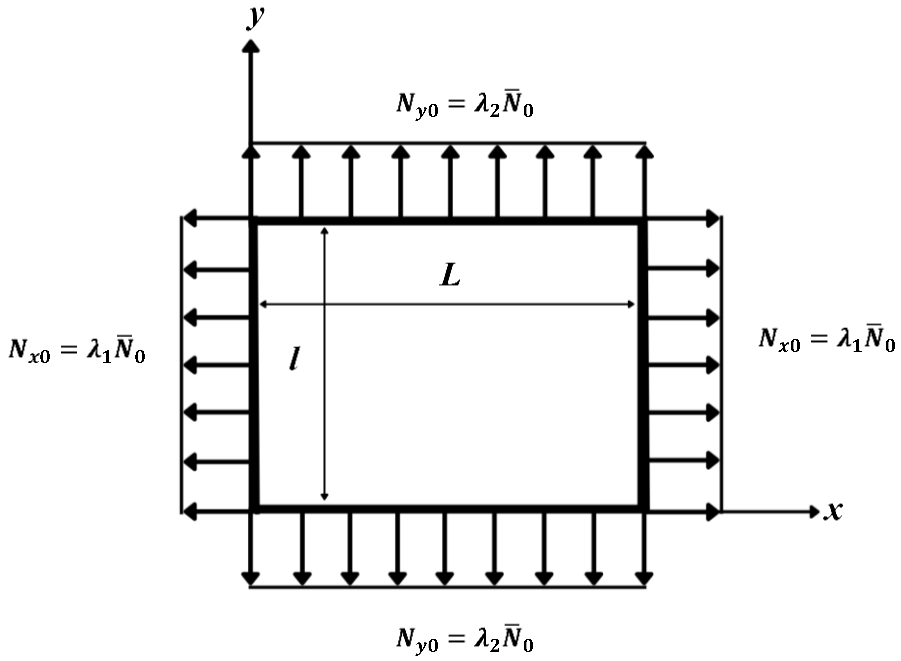

Figure 4.12 The rectangular plate subjected to in-plane loads.

4.2.2.1 Convergence of the dimensionless critical buckling load of (2-1-2) Al/Al_2O_3 sandwich plate with homogeneous ceramic core and metallic core

Table 4.12 shows the critical buckling loads $\widehat{N}_{cri}$ obtained for the square (2-1-2) Al/Al_2O_3 sandwich plate with homogeneous ceramic core and metallic core under uniaxial (λ_1= -1, λ_2 = 0), biaxial compression (λ_1= λ_2 = -1) and biaxial compression and tension (λ_1= -1, λ_2 = 1), Figure 4.12. Different mesh sizes are considered. It can be observed that the obtained results for power-law index p=5 and side-to-thickness *L*/*h*=10 compare well with those obtained using the analytical solutions with improved transverse shear stiffness based on the FSDT of Nguyen et al. [263]. These results confirm the performance of the present finite element.

Table 4.12 Convergence of the dimensionless critical buckling loads $\widehat{N}_{cri}$ of (2-1-2) Al/Al_2O_3 sandwich plate with homogeneous ceramic core and metallic core under different loading, *p*=5, *L*/*h*= 10.

Mesh	**8×8**	**12×12**	**16×16**	**20×20**	**24×24**	**32×32**	**FSDT [263]**
Uniaxial compression							
Ceramic core	3.0870	3.0509	3.0384	3.0327	3.0296	3.0265	3.0226
Metallic core	12.5021	12.3622	12.3139	12.2917	12.2796	12.2676	12.2523
Biaxial compression							
Ceramic core	1.5435	1.5254	1.5192	1.5163	1.5148	1.5132	1.5113
Metallic core	6.2510	6.1811	6.1570	6.1458	6.1398	6.1338	6.1261
Biaxial compression and tension							
Ceramic core	6.4145	6.2037	6.1350	6.1039	6.0873	6.0709	6.0501
Metallic core	24.300	23.6362	23.4095	23.3070	23.2520	23.1978	23.1287

4.2.2.2 The dimensionless critical buckling loads of square Al/Al$_2$O$_3$ sandwich plate with homogeneous ceramic core and metallic core under different loading

A moderately thick square Al/Al$_2$O$_3$ sandwich plate with the side-to-thickness ratio L/h =10 and the power-law index *p* varied from 0 to 10 is analyzed. Dimensionless critical buckling loads $\widehat{N}_{cri}$ of the square sandwich plates with homogeneous ceramic core and metallic core under uniaxial compression, biaxial compression and biaxial compression and tension are presented in Tables 4.13, 4.14 and 4.15, respectively. The obtained results using a 24×24 mesh size are compared with those generated by Nguyen et al. [263] based on the FSDT. A good agreement between the results is observed for all plate configurations and values of power-law index.

Table 4.13 Dimensionless critical buckling loads $\widehat{N}_{cri}$ of square Al/Al$_2$O$_3$ sandwich plates subjected to uniaxial compressive load (λ_1= -1, λ_2 = 0) with homogeneous ceramic core and metallic core, L/h=10.

p	**Theory**	$\widehat{N}_{cri}$			
		1-0-1	**2-1-2**	**1-1-1**	**1-2-1**
Ceramic core					
0	FSDT [263]	13.0045	13.0045	13.0045	13.0045
	Present (5/6)	**13.0340**	**13.0340**	**13.0340**	**13.0340**
0.5	FSDT [263]	7.3279	7.9056	8.4041	9.1905
	Present (5/6)	**7.3542**	**7.9314**	**8.4296**	**9.2162**
1	FSDT [263]	5.1424	5.8138	6.4389	7.4837
	Present (5/6)	**5.1542**	**5.8272**	**6.4538**	**7.5009**
5	FSDT [263]	2.6385	3.0226	3.5596	4.7147
	Present (5/6)	**2.6445**	**3.0296**	**3.5679**	**4.7257**
10	FSDT [263]	2.46906	2.7262	3.1752	4.2604
	Present (5/6)	**2.4747**	**2.7326**	**3.1826**	**4.2703**
Metallic core					
0	FSDT [263]	2.3956	2.3956	2.3956	2.3956
	Present (5/6)	**2.4010**	**2.4010**	**2.4010**	**2.4010**
0.5	FSDT [263]	8.0036	7.4133	6.9129	6.1347
	Present (5/6)	**8.0125**	**7.4226**	**6.9223**	**6.1439**
1	FSDT [263]	10.1653	9.4620	8.8256	7.7859
	Present (5/6)	**10.1880**	**9.4830**	**8.8450**	**7.8030**
5	FSDT [263]	12.7196	12.2523	11.6639	10.4751
	Present (5/6)	**12.7483**	**12.2796**	**11.6897**	**10.4982**
10	FSDT [263]	12.9143	12.5714	12.0602	10.9258
	Present (5/6)	**12.9435**	**12.5995**	**12.0870**	**10.9499**

Tables 4.13-4.15 show that the dimensionless critical buckling loads are the highest when (λ_1= -1, λ_2 = 1) and are the lowest when (λ_1= λ_2 = -1) for all power-law index values. In the case of p =0, the dimensionless critical buckling load for several kinds of sandwich plates has the same value. From these tables, it can be observed that with the increase of the power-law index, the dimensionless critical buckling loads decrease for sandwich plate with homogeneous ceramic core, and increase for sandwich plate with homogeneous metallic core. This is due to the fact that higher values of power-law index correspond to high portion of metal in comparison with the ceramic part for homogeneous ceramic core and inversely for homogeneous metallic core.

Table 4.14 Dimensionless critical buckling loads $\widehat{N}_{cri}$ of square Al/Al_2O_3 sandwich plates subjected to biaxial compressive load (λ1= λ2 = -1) with homogeneous ceramic core and metallic core, L/h=10.

p	Theory	$\widehat{N}_{cri}$			
		1-0-1	**2-1-2**	**1-1-1**	**1-2-1**
Ceramic core					
0	FSDT [263]	6.5022	6.5022	6.5022	6.5022
	Present (5/6)	**6.5170**	**6.5170**	**6.5170**	**6.5170**
0.5	FSDT [263]	3.6639	3.9528	4.2020	4.5952
	Present (5/6)	**3.6771**	**3.9657**	**4.2148**	**4.6081**
1	FSDT [263]	2.5712	2.9069	3.2195	3.7418
	Present (5/6)	**2.5771**	**2.9136**	**3.2269**	**3.7504**
5	FSDT [263]	1.3193	1.5113	1.7798	2.3574
	Present (5/6)	**1.3223**	**1.5148**	**1.7839**	**2.3629**
10	FSDT [263]	1.2345	1.3631	1.5876	2.1302
	Present (5/6)	**1.2374**	**1.3663**	**1.5913**	**2.1352**
Metallic core					
0	FSDT [263]	1.1978	1.1978	1.1978	1.1978
	Present (5/6)	**1.2005**	**1.2005**	**1.2005**	**1.2005**
0.5	FSDT [263]	4.0018	3.7066	3.4564	3.0674
	Present (5/6)	**4.0063**	**3.7113**	**3.4611**	**3.0719**
1	FSDT [263]	5.0827	4.7310	4.4128	3.8929
	Present (5/6)	**5.0940**	**4.7415**	**4.4225**	**3.9015**
5	FSDT [263]	6.3598	6.1261	5.8320	5.2376
	Present (5/6)	**6.3741**	**6.1398**	**5.8449**	**5.2491**
10	FSDT [263]	6.4571	6.2857	6.0301	5.4629
	Present (5/6)	**6.4717**	**6.2998**	**6.0435**	**5.4749**

It is also observed from the above mentioned tables that as the core thickness, with respect to the total thickness of the plate, increases, the dimensionless critical buckling loads increase for sandwich plate with homogeneous ceramic core, and decrease for sandwich plate with homogeneous metallic core.

Table 4.15 Dimensionless critical buckling loads $\widehat{N}_{cri}$ of square Al/Al_2O_3 sandwich plates subjected to biaxial compression and tension load ($\lambda1$= -1, $\lambda2$ = 1) with homogeneous ceramic core and metallic core, L/h=10.

p	**Theory**	$\widehat{N}_{cri}$			
		1-0-1	**2-1-2**	**1-1-1**	**1-2-1**
Ceramic core					
0	FSDT [263]	25.0840	25.0840	25.0840	25.0840
	Present (5/6)	**25.2251**	**25.2251**	**25.2251**	**25.2251**
0.5	FSDT [263]	14.3784	15.5078	16.4695	17.9713
	Present (5/6)	**14.4773**	**15.6103**	**16.5755**	**18.0831**
1	FSDT [263]	10.1694	11.5009	12.7216	14.7378
	Present (5/6)	**10.2302**	**11.5698**	**12.7975**	**14.8251**
5	FSDT [263]	5.2314	6.0501	7.1299	9.4086
	Present (5/6)	**5.2627**	**6.0873**	**7.1739**	**9.4661**
10	FSDT [263]	4.8580	5.4545	6.3687	8.5206
	Present (5/6)	**4.8867**	**5.4881**	**6.4081**	**8.5729**
Metallic core					
0	FSDT [263]	4.6207	4.6207	4.6207	4.6207
	Present (5/6)	**4.6467**	**4.6467**	**4.6467**	**4.6467**
0.5	FSDT [263]	15.0457	13.8664	12.8978	11.4306
	Present (5/6)	**15.1125**	**13.9288**	**12.9564**	**11.4835**
1	FSDT [263]	19.1529	17.6932	16.4292	14.4373
	Present (5/6)	**19.2545**	**17.7852**	**16.5136**	**14.5107**
5	FSDT [263]	24.2966	23.1287	21.8390	19.4317
	Present (5/6)	**24.4302**	**23.2520**	**21.9529**	**19.5306**
10	FSDT [263]	24.7766	23.8189	22.6471	20.3011
	Present (5/6)	**24.9142**	**23.9470**	**22.7661**	**20.4050**

4.2.3 Free vibration analysis

Through this section, the dynamic behavior of square FG single layer and sandwich plates are numerically studied. In order to verify the accuracy of the present finite element, convergence and comparison study is shown through some examples by comparing the results with the available results in the literature. Two sets of material combinations of metal and ceramic, Al/ZrO_2-2 and Al*/Al_2O_3 are considered, which their material properties are listed in Table 4.1. Young's modulus, Poisson's ratio and mass density of (Aluminum*/Al*) are E_m=70 GPa, ν_m=0.3 and ρ_m= 2707 kg/m^3, respectively.

For convenience, following dimensionless natural frequency parameters are used in presenting the numerical results in tabular form.

$$\bar{\beta} = \omega h\sqrt{\rho_m / E_m}, \qquad \bar{\omega} = \frac{\omega L^2}{h}\sqrt{\rho_0 / E_0}, \qquad \rho_0 = 1Kg/m^3 \ , \quad E_0 = 1\ \text{GPa} \tag{4.11}$$

The plates are simply supported (SSSS) at all four edges.

$$\begin{aligned} u_0 = w_0 = \varphi_y = 0 \quad \text{at} \quad x = 0 \quad \text{and} \quad x = L \\ v_0 = w_0 = \varphi_x = 0 \quad \text{at} \quad y = 0 \quad \text{and} \quad y = l \end{aligned} \tag{4.12}$$

4.2.3.1 FG single layer plates

This example is carried out for Al/ZrO_2-2 square plates with different values of side-to-thickness ratio L/h and power-law index p. The dimensionless fundamental frequencies $\bar{\beta}$ are obtained using the present finite element (R4FSDT), considering different mesh sizes. The value of shear correction factor is taken as k_s=5/6. The obtained results are compared with those of 3D exact solutions of Vel and Batra [182], 2D-HSDT solutions of Matsunaga [202] and FSDT-based analytical solutions of Hosseini-Hashemi et al. [264] in Table 4.16.

It can be seen from Table 4.16 that the results are in good agreement, however the present formulation results are identical to those acquired by the 2D-HSDT [202] and FSDT [264] for both thin and thick plates with various values of power law index p. Ones again, the obtained results show the rapidity and stability of the present finite element.

Table 4.16 Dimensionless fundamental frequency $\bar{\beta}$ of single layer Al/ZrO_2-2 square plates.

Mesh	***p*=0***		***p*=1**			***L*/*h*=5**		
	***L*/*h*=$\sqrt{10}$**	***L*/*h*=10**	***L*/*h*=5**	***L*/*h*=10**	***L*/*h*=20**	***p*=2**	***p*=3**	***p*=5**
8×8	0.4678	0.0587	0.2311	0.0629	0.0161	0.2298	0.2310	0.2325
12×12	0.4645	0.0581	0.2292	0.0623	0.0160	0.2279	0.2291	0.2306
16×16	0.4633	0.0579	0.2285	0.0621	0.0159	0.2272	0.2285	0.2299
20×20	0.4628	0.0578	0.2282	0.0620	0.0159	0.2269	0.2282	0.2296
24×24	0.4625	0.0578	0.2280	0.0620	0.0159	0.2267	0.2280	0.2295
32×32	0.4622	0.0578	0.2278	0.0619	0.0159	0.2266	0.2278	0.2293
3D [182]	0.4658	0.0578	0.2192	0.0596	0.0153	0.2197	0.2211	0.2225
2D-HSDT [202]	0.4658	0.0578	0.2285	0.0619	0.0158	0.2264	0.2270	0.2281
FSDT [264]	0.4618	0.0577	0.2276	0.0619	0.0158	0.2264	0.2276	0.2291

$*\bar{\beta} = \omega h\sqrt{\rho_c / E_c}$

4.2.3.2 FG sandwich plates

In the following, the natural frequency $\bar{\omega}$ of square sandwich plates with FG skins and homogeneous ceramic or metallic core is analyzed. The plates are made of a mixture of Aluminum (Al*) and Alumina (Al_2O_3). Three shear correction factors, k_s from Eq (4.9), $k_s = 5/6$ and $k_s = \pi^2/12$, are considered.

The convergence of the dimensionless natural frequency $\bar{\omega}$ of (2-1-2) Al*/Al_2O_3 square sandwich plate with homogeneous ceramic (Al_2O_3) or metallic (Al*) core is presented in Table 4.17. The results are presented for power-law index *p*=1, 10 and side-to-thickness ratio *L*/*h*=5, considering different meshes. The obtained results are compared with those obtained analytically by Thai et al. [131] based on a new FSDT with four unknowns using a shear correction factor k_s =5/6 and with the exact 3D solutions reported by Li et al. [184]

It can be seen from Table 4.17, that the shear correction factor has a slight influence on the dimensionless natural frequency $\bar{\omega}$. In the case of sandwich plate with ceramic core, the obtained results using the shear correction factor of Eq (4.9) are close to 3D solutions [184], while the results obtained using shear correction factors $k_s = 5/6$ and $k_s = \pi^2/12$ converge to those based on FSDT [131]. In the case of sandwich plate with metallic core, it is observed that whatever the shear correction factor value, the obtained results using the present formulation

are in good agreement with those of FSDT [131]. For the following calculation, a 20×20 mesh size and shear correction factor $k_s = 5/6$ are used.

Table 4.17 Convergence of the dimensionless natural frequency $\bar{\omega}$ of (2-1-2) Al*/Al_2O_3 square sandwich plate with homogeneous ceramic core and metallic core , *L*/*h*= 5.

p	k_s	8×8	12×12	16×16	20×20	24×24	FSDT [131]	3D [184]
Ceramic core								
1	**Eq (4.9)**	1.2371	1.2265	1.2228	1.2211	1.2202	1.2145	1.2292
	5/6	1.2334	1.2229	1.2192	1.2175	1.2166		
	$\pi^2/12$	1.2324	1.2219	1.2183	1.2166	1.2157		
10	**Eq (4.9)**	0.9043	0.8964	0.8937	0.8924	0.8918	0.8881	0.8923
	5/6	0.9022	0.8943	0.8916	0.8904	0.8897		
	$\pi^2/12$	0.9016	0.8938	0.8911	0.8898	0.8891		
Metallic core								
1	**Eq (4.9)**	1.5546	1.5423	1.5380	1.5360	1.5350	1.5237	1.4333
	5/6	1.5456	1.5334	1.5291	1.5272	1.5262		
	$\pi^2/12$	1.5432	1.5311	1.5269	1.5249	1.5239		
10	**Eq (4.9)**	1.7321	1.7321	1.7321	1.6583	1.6583	1.6827	1.6091
	5/6	1.7321	1.6583	1.6583	1.6583	1.6583		
	$\pi^2/12$	1.7321	1.6583	1.6583	1.6583	1.6583		

Tables 4.18 and 4.19 list the dimensionless natural frequency $\bar{\omega}$ of simply supported, Al*/Al_2O_3 square sandwich plates with homogeneous ceramic or metallic core for side-to thickness ratio *L*/*h*= 5 and *L*/*h*= 10, respectively. The obtained results for different values of power-law index *p* are compared with the 3D exact solutions given by Li et al. [184], analytical solutions based on FSDT presented by Thai et al. [131] and Nguyen et al. [263] using shear correction factor equal to $5/6$. It can be observed that a good agreement exists between the results, however, in the case of sandwich plates with metallic core the obtained results are in excellent agreement with those obtained based on FSDT.

For both side-to-thickness ratios, it can be seen that for *p*=0 the dimensionless natural frequencies of the several kinds of sandwich plates are the same. Furthermore, it is seen that as the power-law index increase the dimensionless natural frequencies decrease for sandwich plate with homogeneous ceramic core, whereas they increase for sandwich plate with homogeneous metallic core. This is because higher values of the power-law index correspond

to a high portion of metal in comparison with the ceramic part for homogeneous ceramic core and inversely for the homogeneous metallic core.

Tables 4.18 and 4.19 also show that as the core thickness, with respect to the total thickness of the plate, increases, the dimensionless natural frequencies increase for sandwich plate with homogeneous ceramic core, while they decrease for sandwich plate with homogeneous metallic core.

Table 4.18 Dimensionless natural frequency $\bar{\omega}$ of simply supported Al*/Al_2O_3 square sandwich plates with homogeneous ceramic or metallic core for $L/h = 5$.

p	Theory	$\bar{\omega}$			
		1-0-1	**2-1-2**	**1-1-1**	**1-2-1**
Ceramic core					
0	3D[184]	1.6771	1.6771	1.6771	1.6771
	FSDT [131]	1.6697	1.6697	1.6697	1.6697
	Present (5/6)	**1.6583**	**1.6583**	**1.6583**	**1.6583**
0.5	3D[184]	1.3536	1.3905	1.4218	1.4694
	FSDT [131]	1.3395	1.3764	1.4081	1.4571
	Present (5/6)	**1.3428**	**1.3798**	**1.4116**	**1.4607**
1	3D[184]	1.1749	1.2292	1.2777	1.3534
	FSDT [131]	1.1607	1.2145	1.2632	1.3403
	Present (5/6)	**1.1635**	**1.2175**	**1.2663**	**1.3435**
5	3D[184]	0.8909	0.9336	0.9980	1.1190
	FSDT [131]	0.8836	0.9256	0.9862	1.1056
	Present (5/6)	**0.8858**	**0.9279**	**0.9887**	**1.1084**
10	3D[184]	0.8683	0.8923	0.9498	1.0729
	FSDT [131]	0.8613	0.8881	0.9406	1.0596
	Present (5/6)	**0.8634**	**0.8904**	**0.9430**	**1.0622**
Metallic core					
0	3D[184]	0.8529	0.8529	0.8529	0.8529
	FSDT [131]	0.8491	0.8491	0.8491	0.8491
	Present (5/6)	**0.8511**	**0.8511**	**0.8511**	**0.8511**
0.5	3D[184]	1.3789	1.3206	1.2805	1.2258
	FSDT [131]	1.4242	1.3816	1.3423	1.2766
	Present (5/6)	**1.4275**	**1.3847**	**1.3454**	**1.2795**
1	3D[184]	1.5090	1.4333	1.3824	1.3213
	FSDT [131]	1.5626	1.5237	1.4835	1.4101
	Present (5/6)	**1.5640**	**1.5272**	**1.4868**	**1.4133**
5	3D[184]	1.6587	1.5801	1.5028	1.4267
	FSDT [131]	1.6774	1.6718	1.6491	1.5876
	Present (5/6)	**1.6583**	**1.6583**	**1.6583**	**1.5811**
10	3D[184]	1.6728	1.6091	1.5267	1.4410
	FSDT [131]	1.6778	1.6827	1.6672	1.6130
	Present (5/6)	**1.6583**	**1.6583**	**1.6583**	**1.5811**

Table 4.19 Dimensionless natural frequency $\bar{\omega}$ of simply supported Al*/Al_2O_3 square sandwich plates with homogeneous ceramic or metallic core for L/h= 10.

p	Theory	$\bar{\omega}$			
		1-0-1	**2-1-2**	**1-1-1**	**1-2-1**
Ceramic core					
0	3D[184]	1.8268	1.8268	1.8268	1.8268
	FSDT [263]	1.8244	1.8244	1.8244	1.8244
	Present (5/6)	**1.8292**	**1.8292**	**1.8292**	**1.8292**
0.5	3D[184]	1.4461	1.4861	1.5213	1.5767
	FSDT [263]	1.4408	1.4809	1.5164	1.5723
	Present (5/6)	**1.4455**	**1.4855**	**1.5210**	**1.5769**
1	3D[184]	1.2447	1.3018	1.3552	1.4414
	FSDT [263]	1.2403	1.2973	1.3507	1.4372
	Present (5/6)	**1.2436**	**1.3007**	**1.3543**	**1.4410**
5	3D[184]	0.9448	0.9810	1.0453	1.1757
	FSDT [263]	0.9426	0.9787	1.0418	1.1716
	Present (5/6)	**0.9451**	**0.9813**	**1.0446**	**1.1747**
10	3D[184]	0.9273	0.9408	0.9952	1.1247
	FSDT [263]	0.9251	0.9396	0.9926	1.1207
	Present (5/6)	**0.9275**	**0.9421**	**0.9952**	**1.1237**
Metallic core					
0	3D[184]	0.9290	0.9290	0.9290	0.9290
	FSDT [263]	0.9278	0.9278	0.9278	0.9278
	Present (5/6)	**0.9302**	**0.9302**	**0.9302**	**0.9302**
0.5	3D[184]	1.5735	1.5259	1.4846	1.4166
	FSDT [263]	1.5916	1.5503	1.5094	1.4369
	Present (5/6)	**1.5949**	**1.5536**	**1.5127**	**1.4401**
1	3D[184]	1.7223	1.6744	1.6305	1.5579
	FSDT [263]	1.7427	1.7102	1.6712	1.5936
	Present (5/6)	**1.7472**	**1.7147**	**1.6756**	**1.5977**
5	3D[184]	1.8420	1.8261	1.7896	1.7267
	FSDT [263]	1.8488	1.8617	1.8493	1.7941
	Present (5/6)	**1.8536**	**1.8665**	**1.8541**	**1.7987**
10	3D[184]	1.8402	1.8399	1.8081	1.7481
	FSDT [263]	1.8421	1.8679	1.8650	1.8204
	Present (5/6)	**1.8469**	**1.8728**	**1.8698**	**1.8250**

4.3 Conclusion

In this chapter, the present finite element (R4FSDT) has been used to investigate the static, mechanical buckling and free vibration behaviors of FG single layer and sandwich plates. numerical results in terms of deflection, stresses, critical buckling loads and natural frequencies are presented and compared with those available in the literature. All the comparisons show that the results obtained with the present element and those of the references are in good agreement, confirming the performance and accuracy of the present formulation. The effects of some parameters like power-law index p, side-to-thickness ratio L/h, etc on the behaviors of the FG plates, have been also investigated. The important conclusions that emerge from this study can be summarized as follows:

- The present results show that the developed finite element R4FSDT can well predict the static, stability and vibration responses of FG single layer and sandwich plates.
- The obtained results using the R4FSDT element reiterate that FSDT may be well suited to simpler geometries and moderately thick plates.
- The shear correction factor has a slight influence on the dimensionless deflections and natural frequency while it has no effect on the dimensionless normal stresses values. The influence of the shear correction factor on the dimensionless deflection decreases as the side-to-thickness ratio L/h increases.
- In the case of FG single layer plates, the dimensionless deflection decreases by increasing the L/h ratio whereas it increases with the increasing of power-law values.
- In the case of a sandwich plate with a ceramic core, the dimensionless deflection increases as the power-law index increases and decreases as the core thickness increases. The opposite has been observed for the homogeneous metallic core. For sandwich plate with either ceramic or metallic core the dimensionless deflection increases with the increase of side-to-thickness ratio L/h.
- The dimensionless critical buckling loads and natural frequencies decrease for sandwich plate with homogeneous ceramic core with the increase of the power-law index, whereas they increase for sandwich plate with homogeneous metallic core. The results increase for sandwich plate with homogeneous ceramic core as the core thickness, with respect to the total thickness of the plate increases, while they decrease for sandwich plate with homogeneous metallic core.

Part III

Development of a new finite element model based on new trigonometric shear deformation theory for the analysis of FG plates

Chapter 5

Development of a new rectangular finite element based on a novel trigonometric shear deformation theory (R4SSDT) for the analysis of FG single layer plates behavior

5.1 Introduction

This chapter aims to present a novel trigonometric shear deformation model with only five unknowns for the analysis of FG plates behavior. The model presents a sinusoidal variation of the transverse shear strains across the thickness and satisfies the shear stress-free boundary conditions on the top and bottom surfaces of the plate, without the need of shear correction factor. Based on the proposed model, a rectangular finite element has been developed for the static, buckling and dynamic analysis of FG single layer plates. The present finite element, has been defined by four nodes and five degree of freedom per node. The considered FG plates have been assumed to have isotropic, two constituent material distribution through the thickness, and the material properties have been assumed to vary according to a power-law distribution in terms of volume fractions of the constituents. To take into account the effect of second order, the von Karman strain tensor has been used. Total potential energy and Hamilton' principles and Lagrangian equation have been used to formulate the stiffness, geometric and mass matrices. The assumed natural shear strain technique has been employed to prevent any shear locking phenomenon. Furthermore, the concept of the neutral plane has been introduced to avoid the membrane–bending coupling.

5.2 A novel trigonometric shear deformation theory for FG plates

In this chapter, a novel trigonometric shear deformation model has been proposed. The model is an amelioration of the Reissner–Mindlin model by introducing the effect of stretching.

5.1.1 The proposed displacement field

The in-plane displacements *u*, *v* and the transverse displacement *w* for the plate are assumed as,

$$\begin{aligned} u\,(x,\,y,\,z,t) &= u_0(x,\,y,t) + z\varphi_x(x,y,t) \\ v\,(x,\,y,\,z,t) &= v_0(x,\,y,t) + z\varphi_y(x,y,t) \\ w\,(x,\,y,\,z,t) &= w_0(x,\,y,t) + \frac{h^2}{\pi^2}\left(\sin\frac{\pi z}{h}\right)^2 \psi_z(x,y,t) \end{aligned} \tag{5.1}$$

Where *u*, *v* and *w* denote the displacements of a point M (*x*, *y*, *z*) within the FG plate. u_0 and v_0 are the in-plane displacement vector components at any point of the midplane in *x* and *y* directions, respectively. w_0 (*x*, *y*) is the transverse displacement of the midplane points of the plate and ψ_z is the stretching contributions of the displacement in the transverse direction. The variable ψ_z will be eliminated on the assumption of zero shear stress at the top and the bottom surfaces of the plate and that the transverse shear strains are sinusoidally distributed through the thickness.

5.1.2 Kinematics

According to the Von Karman deformation tensor, the vector strains components are expressed as follows

$$\begin{aligned} \varepsilon_x &= \frac{\partial u}{\partial x} = \frac{\partial u_0}{\partial x} + z\frac{\partial \varphi_x}{\partial x} + \frac{1}{2}\left(\frac{\partial w_0}{\partial x}\right)^2 \\ \varepsilon_y &= \frac{\partial v}{\partial y} = \frac{\partial v_0}{\partial y} + z\frac{\partial \varphi_y}{\partial y} + \frac{1}{2}\left(\frac{\partial w_0}{\partial y}\right)^2 \\ \gamma_{xy} &= \frac{\partial u}{\partial y} + \frac{\partial v}{\partial x} = \frac{\partial u_0}{\partial y} + \frac{\partial v_0}{\partial x} + z\left(\frac{\partial \varphi_x}{\partial y} + \frac{\partial \varphi_y}{\partial x}\right) + \frac{\partial w_0}{\partial x}\frac{\partial w_0}{\partial y} \\ \gamma_{xz} &= \frac{\partial u}{\partial z} + \frac{\partial w}{\partial x} = \varphi_x + \frac{\partial w_0}{\partial x} + \frac{h^2}{\pi^2}\left(\sin\frac{\pi z}{h}\right)^2 \frac{\partial \psi_z}{\partial x} \\ \gamma_{yz} &= \frac{\partial v}{\partial z} + \frac{\partial w}{\partial y} = \varphi_y + \frac{\partial w_0}{\partial y} + \frac{h^2}{\pi^2}\left(\sin\frac{\pi z}{h}\right)^2 \frac{\partial \psi_z}{\partial y} \end{aligned} \tag{5.2}$$

To eliminate the variable $\psi_z(x,y,t)$, the condition of zero shear stress at the free top and bottom surfaces of the plate is imposed.

$$\gamma_{xz}\left(\pm\frac{h}{2}\right)=\gamma_{yz}\left(\pm\frac{h}{2}\right)=0 \tag{5.3}$$

The variable $\psi_z(x,y)$, can be expressed in term of γ_{xz}^0 and γ_{yz}^0 as follows

$$\frac{\partial\psi_z(x,y)}{\partial x}=-\frac{\pi^2}{h^2}\gamma_{xz}^0, \qquad \frac{\partial\psi_z(x,y)}{\partial y}=-\frac{\pi^2}{h^2}\gamma_{yz}^0 \tag{5.4}$$

Using Eq (5.4), the transverse shear strain components of Eq (5.2) can be expressed by

$$\begin{aligned}\gamma_{xz}&=\gamma_{xz}^0\left(1-\sin^2\frac{\pi z}{h}\right)\\ \gamma_{yz}&=\gamma_{yz}^0\left(1-\sin^2\frac{\pi z}{h}\right)\end{aligned} \tag{5.5}$$

Eq (5.5) can be rewritten as

$$\begin{aligned}\gamma_{xz}&=\gamma_{xz}^0 f_1(z)\\ \gamma_{yz}&=\gamma_{yz}^0 f_1(z)\end{aligned} \tag{5.6}$$

With $f_1(z)$ is a shear function defined by

$$f_1(z)=\left(1-\sin^2\frac{\pi z}{h}\right) \tag{5.7}$$

- **Enhancement of the shear function**

In the case of the Reissner–Mindlin theory, correction factors are introduced to take into account the supposition of constant shear deformation through the thickness of the plate. These factors are obtained by comparing the energy of shear deformation according to tridimensional elasticity theory and that of Reissner–Mindlin theory. Therefore, the shear stress for assumed isotropic material is given by

$$\begin{aligned}\tau_{xz}&=\frac{5}{6}Q_{44}\gamma_{xz}^0\\ \tau_{yz}&=\frac{5}{6}Q_{55}\gamma_{yz}^0\end{aligned} \tag{5.8}$$

Where Q_{44} and Q_{55} are the stiffness coefficients of the elasticity matrix of the material.

The shear strain energy per unit area can be expressed by

$$U_{sd}^{RM} = \frac{1}{2}\int_{-h/2}^{h/2}\left(\tau_{xz}\gamma_{xz}^{0} + \tau_{yz}\gamma_{yz}^{0}\right)dz = \frac{1}{2}\int_{-h/2}^{h/2}\left(\frac{5}{6}Q_{44}\left(\gamma_{xz}^{0}\right)^{2} + \frac{5}{6}Q_{55}\left(\gamma_{yz}^{0}\right)^{2}\right)dz \tag{5.9}$$

By integrating over the thickness, Eq (5.9) can be written as

$$U_{sd}^{RM} = \frac{1}{2}\frac{5}{6}Q_{44}h\left(\left(\gamma_{xz}^{0}\right)^{2} + \left(\gamma_{yz}^{0}\right)^{2}\right) \tag{5.10}$$

The shear strain varying through the thickness according to the following expressions

$$\gamma_{xz} = f(z)\gamma_{xz}^{0}, \qquad \gamma_{yz} = f(z)\gamma_{yz}^{0} \tag{5.11}$$

Where

$$f(z) = \beta f_1(z) \tag{5.12}$$

β denotes the enhancement factor.

The shear stresses are given by

$$\tau_{xz} = Q_{44}f(z)\gamma_{xz}^{0}, \qquad \tau_{yz} = Q_{55}f(z)\gamma_{yz}^{0} \tag{5.13}$$

The shear strain energy per unit area can be written as follows

$$U_{sd}^{SIN} = \frac{1}{2}\int_{-h/2}^{h/2}\left(\tau_{xz}\gamma_{xz} + \tau_{yz}\gamma_{yz}\right)dz = \frac{1}{2}\int_{-h/2}^{h/2}\left(Q_{44}f(z)^{2}\left(\gamma_{xz}^{0}\right)^{2} + Q_{55}f(z)^{2}\left(\gamma_{yz}^{0}\right)^{2}\right)dz \tag{5.14}$$

The integration through the thickness of Eq (5.14) leads to

$$U_{sd}^{SIN} = \frac{1}{2}Q_{44}\left(\left(\gamma_{xz}^{0}\right)^{2} + \left(\gamma_{yz}^{0}\right)^{2}\right)\frac{3}{8}\beta^{2}h \tag{5.15}$$

The equalization of the two expressions of energy in Eqs (5.10) and (5.15) allows to have

$$\frac{3}{8}\beta^{2}h = \frac{5}{6}h \tag{5.16}$$

Then

$$\beta = \frac{2\sqrt{5}}{3} \tag{5.17}$$

Finally, the enhanced shear function can be written as

$$f(z) = \frac{2\sqrt{5}}{3}\left(1 - \left(\sin\frac{\pi z}{h}\right)^2\right) \tag{5.18}$$

After the elimination of the variable $\psi_z(x,y,t)$, The displacement field of the new model is given as follows [256]

$$\begin{aligned} u\,(x,\,y,\,z,t) &= u_0(x,\,y,t) + z\varphi_x(x,y,t) \\ v\,(x,\,y,\,z,t) &= v_0(x,\,y,t) + z\varphi_y(x,y,t) \\ w\,(x,\,y,\,z,t) &= f(z)w_0(x,\,y,t) + \big(f(z)-1\big)G(x,y,t) \end{aligned} \tag{5.19}$$

Where $G(x,y,t)$ is a function defined by

$$\varphi_x(x,y,t) = \frac{\partial G(x,y,t)}{\partial x}, \qquad \varphi_y(x,y,t) = \frac{\partial G(x,y,t)}{\partial y} \tag{5.20}$$

It can be seen that the displacement field in Eq (5.19) contains only five unknowns as in Reissner–Mindlin model.

The strain field can be rewritten in matrix form as

$$\{\varepsilon\} = \begin{Bmatrix} \varepsilon_x \\ \varepsilon_y \\ \gamma_{xy} \end{Bmatrix} = \begin{Bmatrix} \varepsilon_x^l \\ \varepsilon_y^l \\ \gamma_{xy}^l \end{Bmatrix} + \begin{Bmatrix} \varepsilon_x^{nl} \\ \varepsilon_y^{nl} \\ \gamma_{xy}^{nl} \end{Bmatrix} \tag{5.21}$$

$$\{\varepsilon^l\} = \begin{Bmatrix} \varepsilon_x^l \\ \varepsilon_y^l \\ \gamma_{xy}^l \end{Bmatrix} = \begin{Bmatrix} \varepsilon_x^0 \\ \varepsilon_y^0 \\ \gamma_{xy}^0 \end{Bmatrix} + z\begin{Bmatrix} k_x \\ k_y \\ k_{xy} \end{Bmatrix} \tag{5.22}$$

$$\{\gamma_z\} = \begin{Bmatrix} \gamma_{xz} \\ \gamma_{yz} \end{Bmatrix} = f(z)\begin{Bmatrix} \gamma_{xz}^0 \\ \gamma_{yz}^0 \end{Bmatrix} \tag{5.23}$$

Where

$$\left\{\varepsilon^0\right\}=\begin{Bmatrix}\varepsilon_x^0\\ \varepsilon_y^0\\ \gamma_{xy}^0\end{Bmatrix}=\begin{Bmatrix}\dfrac{\partial u_0}{\partial x}\\ \dfrac{\partial v_0}{\partial y}\\ \dfrac{\partial u_0}{\partial y}+\dfrac{\partial v_0}{\partial x}\end{Bmatrix} \tag{5.24}$$

$$\left\{k\right\}=\begin{Bmatrix}k_x\\ k_y\\ k_{xy}\end{Bmatrix}=\begin{Bmatrix}\dfrac{\partial \varphi_x}{\partial x}\\ \dfrac{\partial \varphi_y}{\partial y}\\ \dfrac{\partial \varphi_x}{\partial y}+\dfrac{\partial \varphi_y}{\partial x}\end{Bmatrix} \tag{5.25}$$

$$\left\{\varepsilon^{nl}\right\}=\begin{Bmatrix}\varepsilon_x^{nl}\\ \varepsilon_y^{nl}\\ \gamma_{xy}^{nl}\end{Bmatrix}=\begin{Bmatrix}\dfrac{1}{2}\left(\dfrac{\partial w_0}{\partial x}\right)^2\\ \dfrac{1}{2}\left(\dfrac{\partial w_0}{\partial y}\right)^2\\ \dfrac{\partial w_0}{\partial x}\dfrac{\partial w_0}{\partial y}\end{Bmatrix} \tag{5.26}$$

$$\left\{\gamma_z^0\right\}=\begin{Bmatrix}\gamma_{xz}^0\\ \gamma_{yz}^0\end{Bmatrix}=\begin{Bmatrix}\varphi_x+\dfrac{\partial w_0}{\partial x}\\ \varphi_y+\dfrac{\partial w_0}{\partial y}\end{Bmatrix} \tag{5.27}$$

5.2.3 Constitutive equations

The same rectangular FG single layer plate studied in chapter 3 is considered here. As shown in Figure (3.1), the plate is assumed to be composed of metal and ceramic. The Young's modulus E and mass density ρ of the plate are assumed to vary depending on the thickness according to the power-law distribution and are defined in the same way as in Chapter 3

$$E(z)=E_m+\left(E_c-E_m\right)\left(\frac{z}{h}+\frac{1}{2}\right)^p \tag{5.28}$$

$$\rho(z) = \rho_m + (\rho_c - \rho_m)\left(\frac{z}{h} + \frac{1}{2}\right)^p \tag{5.29}$$

Subscripts *m*, *c* and the index *p* retains the same definitions. The Poisson's ratio ν is assumed to be constant through the thickness of the plate.

For an elastic FG plate, the constitutive relations can be given by

$$\begin{Bmatrix} \sigma_x \\ \sigma_y \\ \tau_{xz} \\ \tau_{yz} \\ \tau_{xy} \end{Bmatrix} = \frac{E(z)}{1-\nu^2} \begin{bmatrix} 1 & \nu & 0 & 0 & 0 \\ \nu & 1 & 0 & 0 & 0 \\ 0 & 0 & \frac{1-\nu}{2} & 0 & 0 \\ 0 & 0 & 0 & \frac{1-\nu}{2} & 0 \\ 0 & 0 & 0 & 0 & \frac{1-\nu}{2} \end{bmatrix} \begin{Bmatrix} \varepsilon_x^l \\ \varepsilon_y^l \\ \gamma_{xz} \\ \gamma_{yz} \\ \gamma_{xy}^l \end{Bmatrix} \tag{5.30}$$

5.2.4 Force and moment resultants

As indicated in chapter 3, to avoid the membrane-bending coupling caused by plate asymmetry, the force and the moment resultants are calculated with respect to the physical neutral plane, which does not coincide with the midplane of the plate.

The definition of the position of the neutral surface remains the same and is given as follows

$$C = \frac{\int_{-h/2}^{h/2} E(z) z dz}{\int_{-h/2}^{h/2} E(z) dz} \tag{5.31}$$

Using the constitutive equations, the force and moment results can be expressed as follows

$$(N_i, M_i) = \int_{-h/2}^{h/2} (1, (z-C))(\sigma_i)\, dz, \qquad (i = x, y, xy) \tag{5.32}$$

$$S_i = \int_{-h/2}^{h/2} f(z)(\tau_i)\, dz, \qquad (i = xz, yz) \tag{5.33}$$

The stress resultants-strains relationship can be written in matrix form as below

$$\begin{Bmatrix} N \\ M \\ S \end{Bmatrix} = \begin{bmatrix} [A] & 0 & 0 \\ 0 & [D] & 0 \\ 0 & 0 & [A^s] \end{bmatrix} \begin{Bmatrix} \varepsilon^0 \\ k \\ \gamma_z^0 \end{Bmatrix} \tag{5.34}$$

Where

$$[A] = \begin{bmatrix} A_{11} & A_{12} & 0 \\ A_{12} & A_{22} & 0 \\ 0 & 0 & A_{66} \end{bmatrix}$$

$$[D] = \begin{bmatrix} D_{11} & D_{12} & 0 \\ D_{12} & D_{22} & 0 \\ 0 & 0 & D_{66} \end{bmatrix} \tag{5.35}$$

$$[A^s] = \begin{bmatrix} A^s_{44} & 0 \\ 0 & A^s_{55} \end{bmatrix}$$

And the reduced elastic matrices coefficients A_{ij}, D_{ij} and A^s_{ij} are defined by

$$\begin{aligned} \left(A_{ij}, D_{ij}\right) &= \int_{-h/2}^{h/2} \left(1, (z-C)^2\right) Q_{ij}(z)\, dz \qquad (i, j = 1,2,6) \\ \left(A^s_{ij}\right) &= \int_{-h/2}^{h/2} Q_{ij}(z)\, f(z)^2\, dz \qquad (i, j = 4,5) \end{aligned} \tag{5.36}$$

5.2 Finite element formulation

Based on the proposed trigonometric (sinusoidal) shear deformation model, a four-node rectangular finite element, named (R4SSDT) has five degrees of freedom per node is formulated for the analysis of the static, free vibration and mechanical buckling responses of FG single layer plates.

5.3.1 Kinematic relationships

The displacements within the element are interpolated using the bilinear Lagrange shape functions that were expressed before in Eq (3.30) in Chapter 3.

The strains can be expressed in terms of nodal displacements using the matrices given in Eqs (3.36)-(3.39).

To prevent any potential shear locking phenomenon, the assumed natural shear strain technique is employed. Therefore, the $[B_s]$ matrix from Eq (3.38) is replaced by the assumed natural deformation displacement relationship matrix $[\bar{B}_s]$ given in Eq (3.45).

5.3.2 Derivation of the elementary matrices

The total potential energy principle has been used to derive the elementary stiffness and geometrical matrices of the element.

$$\pi = U + W \tag{5.37}$$

For static analysis, the equilibrium equation can be obtained by the cancellation of the first variation of the total potential energy $\delta\pi = 0$, with respect to the nodal values $\{q\}$.

$$[K_e]\{q\} = \{F_e\} \tag{5.38}$$

Where $[K_e]$ and $\{F_e\}$ are the elementary stiffness matrix and the nodal load vector, respectively.

$$[K_e] = \int_{-b}^{b}\int_{-a}^{a}\left(\underbrace{[B_m]^T[A][B_m]}_{membrane} + \underbrace{[B_b]^T[D][B_b]}_{bending} + \underbrace{[\bar{B}_s]^T[A^s][\bar{B}_s]}_{shear}\right)dxdy \tag{5.39}$$

$$\{F_e\} = \int_{-b}^{b}\int_{-a}^{a} f(x,y)[N(x,y)]^T dxdy \tag{5.40}$$

For the mechanical buckling analysis, the cancellation of the second variation of the total potential energy leads to the following eigenvalue problem

$$\left(\left[k_e\right]+\left[k_e^g\right]\right)\{q\}=0 \tag{5.41}$$

The elementry geometric stiffness matrix is given by

$$\left[k_e^g\right]=\int_{-b}^{b}\int_{-a}^{a}[G]^T\left[\bar{N}\right][G]dxdy \tag{5.42}$$

Using the loading factor λ, the stress resultant matrix can be expressed as $\left[\bar{N}\right]=\lambda\left[\bar{N}_0\right]$, then the geometrical matrix can be rewritten as

$$\left[k_e^{g0}\right]=\int_{-b}^{b}\int_{-a}^{a}[G]^T\left[\bar{N}_0\right][G]dxdy \tag{5.43}$$

To evaluate the critical buckling load The following eigenvalue problem is used

$$\det\left(\left[k_e\right]+\lambda\left[k_e^{g0}\right]\right)=0 \tag{5.44}$$

The critical buckling load is finally given as follows

$$N_{cri}=\lambda_{cri}\bar{N}_0 \tag{5.45}$$

For free vibration problem we set the external forces and the damping to zero . by applying Lagrangian equations (see, Eq (3.68) and (3.70)), the equations of motion can be expressed by

$$\left[k_e\right]\{q\}+[M]\{\ddot{q}\}=0 \tag{5.46}$$

$$\left(\left[k_e\right]-\omega^2[M]\right)\{q\}=0 \tag{5.47}$$

Where ω is the natural frequency; $[M]$ is the element mass matrix given by

$$[M]=\int_{-b}^{b}\int_{-a}^{a}\left(\left[N(x,y)\right]^T[m]\left[N(x,y)\right]\right)dxdy \tag{5.48}$$

Where $[m]$ And $\left[N(x,y)\right]$ are respectively the inertia matrix and the shape function matrix, given as in Eqs (3.74) and (3.75), respectively.

5.3 Conclusion

In this chapter, a novel trigonometric shear deformation model with five unknowns, has been proposed for the analysis of FG plates behavior. The model accounts for the sinusoidal variation of the transverse shear strains across the thickness and satisfies the shear stress-free boundary conditions on the top and bottom surfaces of the plate. A shear correction factor, therefore, is not required. On the basis of the proposed model, a four-node rectangular finite element, with five degrees of freedom per node, has been formulated for the static, free vibration and buckling analysis of FG single layer plates. The material properties have been assumed to vary through the plate thickness according to a power-law distribution of the volume fraction of the constituents. To avoid the membrane-bending coupling caused by the asymmetry of the plate according to the thickness, the force and the moment resultants have been calculated with respect to the physical neutral plane which does not coincide with the midplane of the plate. Total potential energy and Hamilton' principles and Lagrangian equation have been used for the derivation of the stiffness, geometric and mass matrices. Furthermore, the assumed natural shear strain technique has been introduced to prevent any shear locking phenomenon.

Chapter 6

Application of R4SSDT- Results and discussions

6.1 Introduction

Through this chapter, a number of numerical examples are conducted to show the performance and the accuracy of the proposed finite element model in predicting the static, mechanical buckling and free vibration responses of rectangular FG single layer plates. Numerical results in terms of deflection, stresses, critical buckling loads and frequencies are obtained and compared with the existing results in the literature. Effects of various parameters such as boundary conditions, aspect ratio, plate thickness, and material distribution across the thickness of the plate are investigated.

6.2 Numerical results and discussions

In this section, one presents the static response, the critical buckling loads and the natural frequencies of rectangular FG single layer plates using the developed finite element based on the new proposed model (R4SSDT). Two types of FG plates, one made up of Al/Al_2O_3, and the other made up of Al/ZrO_2 are considered. The material properties of these constituents are listed in Table 6.1.

Table 6.1 Material properties used in the functionally graded plates.

Properties	**Metal**	**Ceramic**	
	Aluminium (Al)	**Alumina (Al_2O_3)**	**Zirconia (ZrO_2)**
***E* (GPa)**	70	380	200
***ρ*(kg/m3)**	2702	3800	5700
v	0.3	0.3	0.3

6.2.1 Static analysis

The static behavior of a rectangular FG plate comprised of Aluminum/Alumina under distributed transverse load is taken up for investigation. The top surface of the FG plate is ceramic (Alumina) rich and the bottom surface is pure metal (Aluminum). Material properties of the aluminum and alumina are shown in Table 6.1. Transverse load $q(x,y)$ is applied on the top surface ($z = h/2$) of the plate, in the form of uniformly distributed load (UDL), $q(x,y) = q_0$, or sinusoidal loads (SSL), $q(x,y) = q_0 \sin\frac{\pi x}{L}\sin\frac{\pi y}{l}$.

For all the following examples, only simply supported boundary conditions are considered and are as follows

$$\begin{aligned} w_0 = \varphi_y = 0 \quad \text{at} \quad x = 0 \quad \text{and} \quad x = L \\ w_0 = \varphi_x = 0 \quad \text{at} \quad y = 0 \quad \text{and} \quad y = l \end{aligned} \tag{6.1}$$

For convenience, the following relations for the non-dimensional deflection and stresses are

$$\begin{aligned} &\bar{w} = \frac{10h^3E_c}{q_0L^4}w\left(\frac{L}{2},\frac{l}{2}\right); \quad \bar{\sigma}_x = \frac{h}{q_0L}\sigma_x\left(\frac{L}{2},\frac{l}{2},\frac{h}{2}\right); \\ &\bar{\sigma}_y = \frac{h}{q_0L}\sigma_y\left(\frac{L}{2},\frac{l}{2},\frac{h}{3}\right); \quad \bar{\tau}_{xy} = \frac{h}{q_0L}\tau_{xy}\left(0,0,-\frac{h}{3}\right); \\ &\bar{\tau}_{xz} = \frac{h}{q_0L}\tau_{xz}\left(0,\frac{l}{2},0\right); \quad \bar{\tau}_{yz} = \frac{h}{q_0L}\tau_{yz}\left(\frac{L}{2},0,\frac{h}{6}\right) \end{aligned} \tag{6.2}$$

6.2.1.1 FG square plate with *L*/*h*=10 subjected to uniform and sinusoidal loading

Firstly, a simply supported, moderately thick Al/Al_2O_3 square plate under UDL has been examined (L/h = 10). The plate has been subdivided into 8 × 8, 12 × 12, 16 × 16, and 20 × 20 mesh size. Table 6.2 contains the dimensionless deflection and stresses for different values of power-law index *p*. The obtained results using the present finite element (R4SSDT) are compared with those obtained using the present FSDT- based finite element (R4FSDT) with 20 × 20 mesh size, the SSDT developed by Zenkour [142], the finite element model based on the HSDT of Tati [256] and the finite element model based on the TSDT of Reddy [136].

Table 6.2 Dimensionless deflection and stresses of a SSSS Al/Al_2O_3 square plate under UDL for different power-law index values (L/h=10).

p		R4SSDT				R4FSDT	SSDT	HSDT	TSDT
		8×8	12×12	16×16	20×20	20 × 20	[142]	[256]	[136]
Ceramic	$\bar{w}$	0.4646	0.4657	0.4661	0.4663	0.4663	0.4665	0.4663	0.4665
	$\bar{\sigma}_x$	2.7674	2.8263	2.8468	2.8563	2.8563	2.8932	2.856	2.8920
	$\bar{\sigma}_y$	1.8450	1.8842	1.8979	1.9042	-	1.9103	1.904	1.9106
	$\bar{\tau}_{xy}$	1.1532	1.2222	1.2512	1.2662	1.2662	1.2850	1.266	1.2855
	$\bar{\tau}_{xz}$	0.4963	0.5314	0.5492	0.5600	-	0.5114	0.4696	0.4963
	$\bar{\tau}_{yz}$	0.3722	0.3986	0.4119	0.4200	-	0.4429	0.4174	0.4411
1	$\bar{w}$	0.9247	0.9270	0.9278	0.9282	0.9282	0.9287	0.9282	0.9421
	$\bar{\sigma}_x$	4.2772	4.3681	4.3999	4.4146	4.4146	4.4745	4.415	4.2598
	$\bar{\sigma}_y$	2.0966	2.1412	2.1567	2.1639	-	2.1692	2.164	2.2569
	$\bar{\tau}_{xy}$	0.9957	1.0553	1.0804	1.0934	1.0934	1.1143	1.093	1.1573
	$\bar{\tau}_{xz}$	0.4963	0.5314	0.5492	0.5600	-	0.5114	0.4696	0.4963
	$\bar{\tau}_{yz}$	0.4577	0.4901	0.5065	0.5165	-	0.5446	0.5133	0.5425
2	$\bar{w}$	1.1922	1.1951	1.1961	1.1966	1.1901	1.1940	1.1948	1.2228
	$\bar{\sigma}_x$	4.9944	5.1005	5.1376	5.1548	5.1548	5.2296	5.155	4.8881
	$\bar{\sigma}_y$	1.9689	2.0107	2.0253	2.0321	-	2.0338	2.032	2.1663
	$\bar{\tau}_{xy}$	0.8876	0.9407	0.9630	0.9746	0.9745	0.9907	0.9745	1.0449
	$\bar{\tau}_{xz}$	0.4763	0.5100	0.5271	0.5374	-	0.4700	0.4368	0.4538
	$\bar{\tau}_{yz}$	0.5032	0.5388	0.5568	0.5678	-	0.5734	0.5469	0.5686
4	$\bar{w}$	1.3934	1.3966	1.3976	1.3982	1.3761	1.3890	1.3916	-
	$\bar{\sigma}_x$	5.6169	5.7362	5.7779	5.7972	5.7972	5.8915	5.797	-
	$\bar{\sigma}_y$	1.6699	1.7054	1.7178	1.7236	-	1.7197	1.724	-
	$\bar{\tau}_{xy}$	0.9261	0.9814	1.0045	1.0165	1.0164	1.0298	1.016	-
	$\bar{\tau}_{xz}$	0.4480	0.4797	0.4958	0.5055	-	0.4204	0.3926	-
	$\bar{\tau}_{yz}$	0.4934	0.5283	0.5460	0.5567	-	0.5346	0.5124	-
5	$\bar{w}$	1.4419	1.4452	1.4463	1.4468	1.4195	1.4356	1.4389	1.4647
	$\bar{\sigma}_x$	5.8616	5.9862	6.0297	6.0499	6.0499	6.1504	6.050	5.7065
	$\bar{\sigma}_y$	1.5654	1.5987	1.6103	1.6157	-	1.6104	1.616	1.7144
	$\bar{\tau}_{xy}$	0.9407	0.9969	1.0204	1.0326	1.0324	1.0451	1.032	1.1016
	$\bar{\tau}_{xz}$	0.4481	0.4798	0.4959	0.5057	-	0.4177	0.3905	0.4004
	$\bar{\tau}_{yz}$	0.4674	0.5005	0.5172	0.5274	-	0.5031	0.4827	0.4950
10	$\bar{w}$	1.5945	1.5979	1.5992	1.5997	1.5686	1.5876	1.5934	1.6054
	$\bar{\sigma}_x$	7.0277	7.1771	7.2292	7.2534	7.2534	7.3689	7.253	6.9540
	$\bar{\sigma}_y$	1.2476	1.2741	1.2834	1.2877	-	1.2820	1.288	1.3350
	$\bar{\tau}_{xy}$	0.9641	1.0216	1.0457	1.0581	1.0580	1.0694	1.058	1.1119
	$\bar{\tau}_{xz}$	0.4791	0.5130	0.5302	0.5407	-	0.4552	0.4298	0.4392
	$\bar{\tau}_{yz}$	0.3853	0.4125	0.4264	0.4348	-	0.4227	0.4096	0.4180
Metal	$\bar{w}$	2.5221	2.5282	2.5303	2.5313	2.5313	2.5327	-	-
	$\bar{\sigma}_x$	2.7674	2.8263	2.8468	2.8563	2.8563	2.8932	-	-
	$\bar{\sigma}_y$	1.8450	1.8842	1.8979	1.9042	-	1.9103	-	-
	$\bar{\tau}_{xy}$	1.1532	1.2222	1.2512	1.2662	1.2662	1.2850	-	-
	$\bar{\tau}_{xz}$	0.4963	0.5314	0.5492	0.5600	-	0.5114	-	-
	$\bar{\tau}_{yz}$	0.3722	0.3986	0.4119	0.4200	-	0.4429	-	-

The bending behavior of the previous plate has also been analyzed for a SDL. The dimensionless deflection and stresses using different mesh sizes for different values of power law-index *p* are presented in Table 6.3. The obtained results are compared with those obtained using the present R4FSDT with 20 × 20 mesh size, the results reported by Zenkour [142] obtained analytically using an SSDT and those obtained using a finite element model based on HSDT of Tati [256].

As shown in Tables 6.2 and 6.3, it is clear, for all the power-law values, that the obtained results using the element R4SSDT are generally in good agreement with those reported in the before mentioned references. However, the values of the shear stress $\bar{\tau}_{xz}$ is quite greater. Also, It can be observed, that the deflection results obtained using the R4SSDT are more accurate than those of R4FSDT, while the stresses are the same. These results confirm the performance of the present finite element R4SSDT in terms of both accuracy and rate of convergence.

Tables 6.2 and 6.3 show that the stresses for a fully ceramic plate are the same as that for a fully metal plate. This is because the plate for these two cases is fully homogeneous, and the stresses do not depend on the young's modulus. It is important to observe that the dimensionless deflection $\bar{w}$ and normal stress $\bar{\sigma}_x$ increase as the power law index increases. The in-plane shear stress $\bar{\tau}_{xy}$ decreases in range of *p* from 0 to 2, then increases with increasing power-law index. The transverse stress $\bar{\tau}_{xz}$ and $\bar{\tau}_{yz}$ remain mostly unchanged in range of *p* from 0 to 1, decreases in range of *p* from 1 to 5, and then increases with the increasing of the power-law index.

Figures 6.1, 6.2 and 6.3, exhibit respectively the variation of the dimensionless normal stress $\bar{\sigma}_x$, in-plane shear stress $\bar{\tau}_{xy}$, and transverse shear stress $\bar{\tau}_{xz}$ across the thickness for different power-law index values *p*, of a simply supported FG square plate subjected to UDL. The side-to-thickness ratio *L*/*h* is taken to be 4. It can be observed that all the stresses of the fully ceramic and metal plates (homogeneous) are matched with each other because they are not depending on Young's modulus.

Table 6.3 Dimensionless deflection and stresses of a SSSS Al/Al_2O_3 square plate under SDL for different power-law index values (L/h=10).

p		R4SSDT				R4FSDT	Zenkour	Tati
		8×8	12×12	16×16	20×20	20×20	[142]	[256]
Ceramic	$\bar{w}$	0.2938	0.2951	0.2955	0.2957	0.2957	0.2960	0.2957
	$\bar{\sigma}_x$	1.8597	1.9235	1.9463	1.9568	1.9568	1.9955	1.9570
	$\bar{\sigma}_y$	1.2398	1.2824	1.2975	1.3046	-	1.3121	1.3050
	$\bar{\tau}_{xy}$	0.6940	0.7025	0.7054	0.7068	0.7025	0.7065	0.7025
	$\bar{\tau}_{xz}$	0.2703	0.2783	0.2811	0.2824	-	0.2462	0.2368
	$\bar{\tau}_{yz}$	0.2027	0.2087	0.2108	0.2118	-	0.2132	0.2105
1	$\bar{w}$	0.5844	0.5869	0.5878	0.5882	0.5882	0.5889	0.5882
	$\bar{\sigma}_x$	2.8743	2.9729	3.0081	3.0244	3.0244	3.0870	3.0240
	$\bar{\sigma}_y$	1.4089	1.4573	1.4745	1.4825	-	1.4894	1.4820
	$\bar{\tau}_{xy}$	0.5993	0.6067	0.6092	0.6104	0.6066	0.6110	0.6066
	$\bar{\tau}_{xz}$	0.2703	0.2783	0.2811	0.2824	-	0.2462	0.2368
	$\bar{\tau}_{yz}$	0.2493	0.2566	0.2592	0.2604	-	0.2622	0.2588
2	$\bar{w}$	0.7538	0.7571	0.7582	0.7587	0.7543	0.7573	0.7575
	$\bar{\sigma}_x$	3.3562	3.4714	3.5124	3.5315	3.5315	3.6094	3.5320
	$\bar{\sigma}_y$	1.3231	1.3685	1.3847	1.3922	-	1.3954	1.3920
	$\bar{\tau}_{xy}$	0.5342	0.5407	0.5430	0.5440	0.5407	0.5441	0.5406
	$\bar{\tau}_{xz}$	0.2594	0.2670	0.2697	0.2710	-	0.2265	0.2202
	$\bar{\tau}_{yz}$	0.2741	0.2821	0.2850	0.2863	-	0.2763	0.2758
4	$\bar{w}$	0.8823	0.8859	0.8872	0.8878	0.8726	0.8819	0.8832
	$\bar{\sigma}_x$	3.7745	3.9040	3.9502	3.9716	3.9716	4.0693	3.9720
	$\bar{\sigma}_y$	1.1222	1.1607	1.1744	1.1808	-	1.1783	1.1810
	$\bar{\tau}_{xy}$	0.5571	0.5639	0.5663	0.5674	0.5639	0.5667	0.5639
	$\bar{\tau}_{xz}$	0.2440	0.2512	0.2537	0.2549	-	0.2029	0.1979
	$\bar{\tau}_{yz}$	0.2688	0.2766	0.2794	0.2807	-	0.2580	0.2584
5	$\bar{w}$	0.9135	0.9172	0.9185	0.9191	0.9004	0.9118	0.9136
	$\bar{\sigma}_x$	3.9390	4.0742	4.1223	4.1447	4.1447	4.2488	4.1450
	$\bar{\sigma}_y$	1.0519	1.0880	1.1009	1.1069	-	1.1029	1.1070
	$\bar{\tau}_{xy}$	0.5658	0.5727	0.5752	0.5763	0.5727	0.5755	0.5727
	$\bar{\tau}_{xz}$	0.2441	0.2512	0.2538	0.2550	-	0.2017	0.1969
	$\bar{\tau}_{yz}$	0.2546	0.2621	0.2647	0.2659	-	0.2429	0.2434
10	$\bar{w}$	1.0108	1.0148	1.0162	1.0168	0.9954	1.0089	1.0125
	$\bar{\sigma}_x$	4.7226	4.8847	4.9424	4.9692	4.9692	5.0890	4.9690
	$\bar{\sigma}_y$	0.8384	0.8672	0.8774	0.8822	-	0.8775	0.8822
	$\bar{\tau}_{xy}$	0.5798	0.5869	0.5894	0.5905	0.5869	0.5894	0.5868
	$\bar{\tau}_{xz}$	0.2610	0.2686	0.2714	0.2726	-	0.2198	0.2167
	$\bar{\tau}_{yz}$	0.2099	0.2160	0.2182	0.2192	-	0.2041	0.2065
Metal	$\bar{w}$	1.5949	1.6018	1.6042	1.6053	1.6053	1.6070	-
	$\bar{\sigma}_x$	1.8597	1.9235	1.9463	1.9568	1.9568	1.9955	-
	$\bar{\sigma}_y$	1.2398	1.2824	1.2975	1.3046	-	1.3121	-
	$\bar{\tau}_{xy}$	0.6940	0.7025	0.7054	0.7068	0.7025	0.7065	-
	$\bar{\tau}_{xz}$	0.2703	0.2783	0.2811	0.2824	-	0.2462	-
	$\bar{\tau}_{yz}$	0.2027	0.2087	0.2108	0.2118	-	0.2132	-

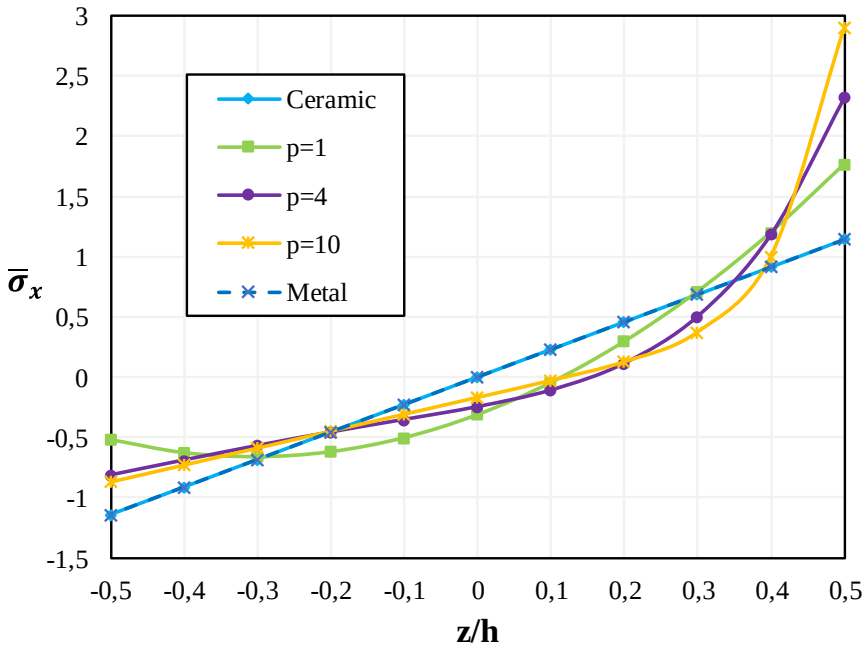

Figure 6.1 Variation of the dimensionless normal stress $\bar{\sigma}_x$ of a SSSS FG square plate under UDL for different power-law index values (L/h =4).

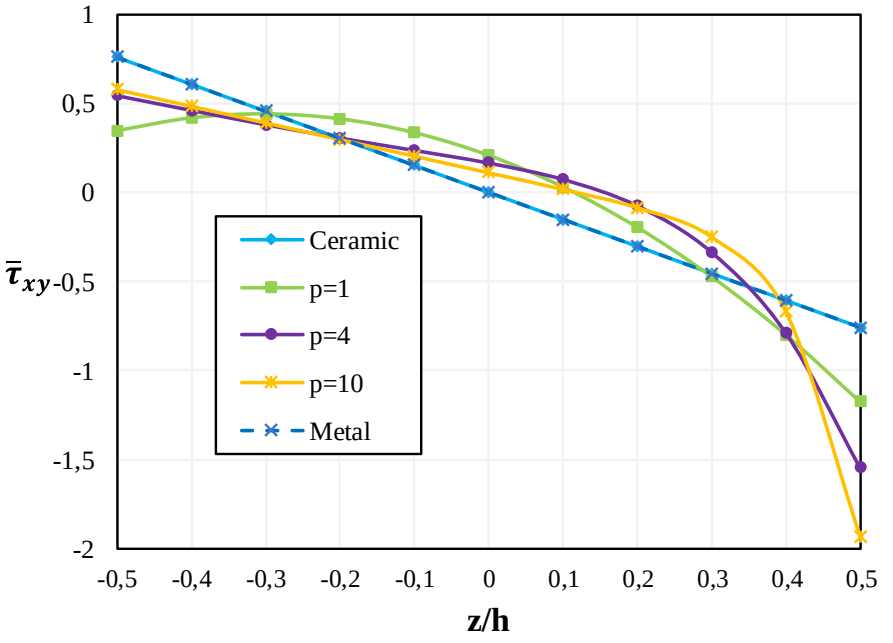

Figure 6.2 Variation of the dimensionless in-plane shear stress $\bar{\tau}_{xy}$ of a SSSS FG square plate under UDL for different power-law index values (L/h = 4).

Figure 6.1 shows that the in-plane stress $\bar{\sigma}_x$ is tensile at the upper surface while becoming compressive at the lower surface of the FG square plate and the homogeneous plate gives the maximum compressive stresses at the lower surface and the minimum tensile stresses at the upper surface of the FG square plate.

Unlike the in-plane stress, the in-plane shear stress becomes tensile at the lower surface and compress at the upper surface and the homogeneous plate gives the maximum tensile stress at the lower surface and the minimum compressive stress at the upper surface of the FG rectangular plate as shown in Figure 6.2.

As depicted in Figure 6.3, the shear stress $\bar{\tau}_{xz}$ of homogenous plates is sinusoidally distributed through the thickness. However, it is not perfectly sinusoidal in the case of FG plates.

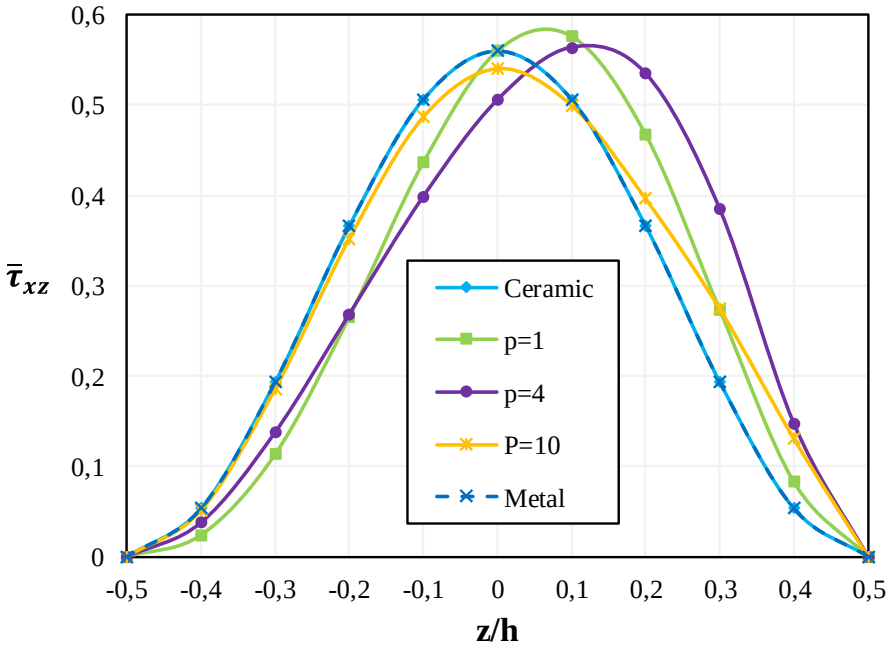

Figure 6.3 Variation of the dimensionless transverse shear stress $\bar{\tau}_{xz}$ of a SSSS FG square plate under UDL for different power-law index values (L/h = 4).

6.2.1.2 FG rectangular plate subjected to uniform loading with different side-to-thickness and aspect ratios

To investigate the effects of side-to-thickness and aspect ratios, two examples have been considered using the element R4SSDT with a 20 × 20 mesh size.

The first example is about a SSSS plate with (L/l = 1). The power-law index is taken as p = 0. The second is performed for a SSSS plate with (l = 3L) and p = 2. Tables 6.4 and 6.5 present the deflection and stresses corresponding to various side-to-thickness ratio (L/h= 4, 10, 20 and 100). Several results obtained using the present element are compared with those given by Zenkour [142], Reddy [136] and Tati [256] and a good agreement is observed.

It is seen from Tables 6.4 and 6.5, that the dimensionless deflection $\bar{w}$ decreases with the increasing of the side-to-thickness ratio L/h, while the in-plane stresses $\bar{\sigma}_x$, $\bar{\sigma}_y$ and $\bar{\tau}_{xy}$ increase. It can be also noted that although the side-to-thickness changes, the dimensionless transverse shear stresses $\bar{\tau}_{xz}$ and $\bar{\tau}_{yz}$ remain unchanged.

Figure 6.4 shows the variation of the dimensionless deflection $\bar{w}$ of a square SSSS FG plate with the L/h ratio considering different values of p. The plate is subjected to UDL. As can be seen, the dimensionless deflection decreases by increasing the L/h ratio whereas it increases with the increasing of power-law values.

Figure 6.5 illustrates the variation of dimensionless deflection $\bar{w}$ of a moderately thick FG plate versus the aspect ratio L/l. The results are presented for p values and L/h=10. It can be seen that the dimensionless deflection decreases as the aspect ratio increase.

Table 6.4 Deflections and stresses of a FG square plate (L/l = 1) under UDL, p = 0.

L/h	Theory	$\bar{w}$	$\bar{\sigma}_x$	$\bar{\sigma}_y$	$\bar{\tau}_{yz}$	$\bar{\tau}_{xz}$	$\bar{\tau}_{xy}$
4	SSDT [142]	0.5865	1.1988	0.7534	0.4307	0.4973	0.4906
	TSDT [136]	0.5868	1.1959	0.7541	0.4304	0.4842	0.4913
	HSDT [256]	0.5872	1.1425	0.7617	0.4173	0.4695	0.5070
	Present	**0.5872**	**1.1425**	**0.7617**	**0.4199**	**0.5599**	**0.5071**
10	SSDT [142]	0.4665	2.8932	1.9103	0.4429	0.5114	1.2850
	TSDT [136]	0.4666	2.8920	1.9106	0.4411	0.4963	1.2855
	HSDT [256]	0.4663	2.8560	1.9040	0.4174	0.4700	1.2660
	Present	**0.4663**	**2.8563**	**1.9042**	**0.4200**	**0.5600**	**1.2662**
100	SSDT [142]	0.4438	28.7342	19.1543	0.4472	0.5164	13.0125
	TSDT [136]	0.4438	28.7341	19.1543	0.4448	0.5004	12.9885
	HSDT [256]	0.4435	28.5600	19.0400	0.4174	0.4696	12.6500
	Present	**0.4435**	**28.5646**	**19.0431**	**0.4200**	**0.5600**	**12.6505**

Figures 6.6-6.10 represent the dimensionless in-plane normal stresses $\bar{\sigma}_x$, $\bar{\sigma}_y$, in plane shear stress $\bar{\tau}_{xy}$, and $\bar{\tau}_{xz}$, $\bar{\tau}_{yz}$ shear stresses distribution across the thickness for different values of the aspect ratio of a SSSS FG plate under UDL, respectively. In these figures, the power-law index is assumed to be p=2 and side-to-thickness ratio is equal as L/h=10.

As exhibited in Figures 6.6 and 6.7, the in-plane normal stresses $\bar{\sigma}_x$ and $\bar{\sigma}_y$ are compressive throughout the plate up to $z \simeq 0.15$ and then they become tensile. The maximum compressive stresses occur at a point on the bottom surface and the maximum tensile stresses occur, of course, at a point on the top surface of the FG plate. However, the tensile and compressive values of the in-plane shear stress $\bar{\tau}_{xy}$, as shown in Figure 6.8, are maximum at a point on the bottom and top surfaces of the FGM plate, respectively. It is clear that the minimum value of zero for all in-plane stresses occurs at $z \simeq 0.14904$ and this is irrespective of the aspect ratio.

Table 6.5 Deflections and stresses of a FG square plate (l = 3L) under UDL, p = 2.

L/h	Theory	$\bar{w}$	$\bar{\sigma}_x$	$\bar{\sigma}_y$	$\bar{\tau}_{yz}$	$\bar{\tau}_{xz}$	$\bar{\tau}_{xy}$
4	SSDT [142]	3.9900	5.3144	0.6810	0.6096	0.6796	0.5646
	TSDT [136]	4.0529	5.2759	0.6652	0.6058	0.6545	0.5898
	HSDT [256]	3.9908	5.1100	0.6878	0.5843	0.6441	0.5653
	Present	**4.0148**	**5.1244**	**0.6899**	**0.6277**	**0.8031**	**0.5728**
10	SSDT [142]	3.5235	12.9374	1.7292	0.6211	0.6910	1.4500
	TSDT [136]	3.5537	12.9234	1.6941	0.6155	0.6672	1.4898
	HSDT [256]	3.5090	12.7800	1.7200	0.5843	0.6441	1.4110
	Present	**3.5178**	**12.8111**	**1.7246**	**0.6278**	**0.8031**	**1.4307**
20	SSDT [142]	3.4567	25.7748	3.4662	0.6232	0.6947	2.9126
	TSDT [136]	3.4823	25.7703	3.3972	0.6171	0.6704	2.9844
	Present	**3.4468**	**25.6224**	**3.4491**	**0.6278**	**0.8031**	**2.8602**
100	SSDT [142]	3.4353	128.7130	17.3437	0.6238	0.6963	14.5840
	TSDT [136]	3.4594	128.7283	17.0009	0.6177	0.6718	14.9303
	HSDT [256]	3.4185	127.8000	17.1900	0.5844	0.6442	14.1000
	Present	**3.4245**	**128.1251**	**17.2475**	**0.6138**	**0.8032**	**14.2983**

As depicted in Figures 6.9 and 6.10, the transverse shear stress $\bar{\tau}_{xz}$, $\bar{\tau}_{yz}$ distributions are not perfectly sinusoidal through the thickness, and the stresses increase as the aspect ratio decreases. It is to be noted that the maximum value occurs at $z = 0.1$, not at the plate center as in the homogeneous case.

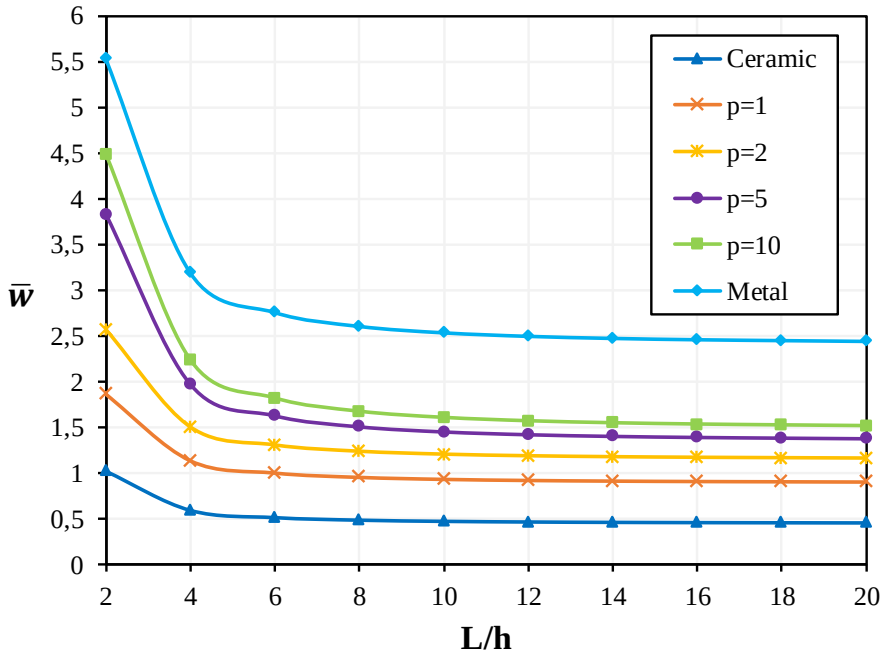

Figure 6.4 Variation of the dimensionless deflection $\bar{w}$ of a square SSSS FG plate subjected to UDL with the *L*/*h* ratio considering different values of *p*.

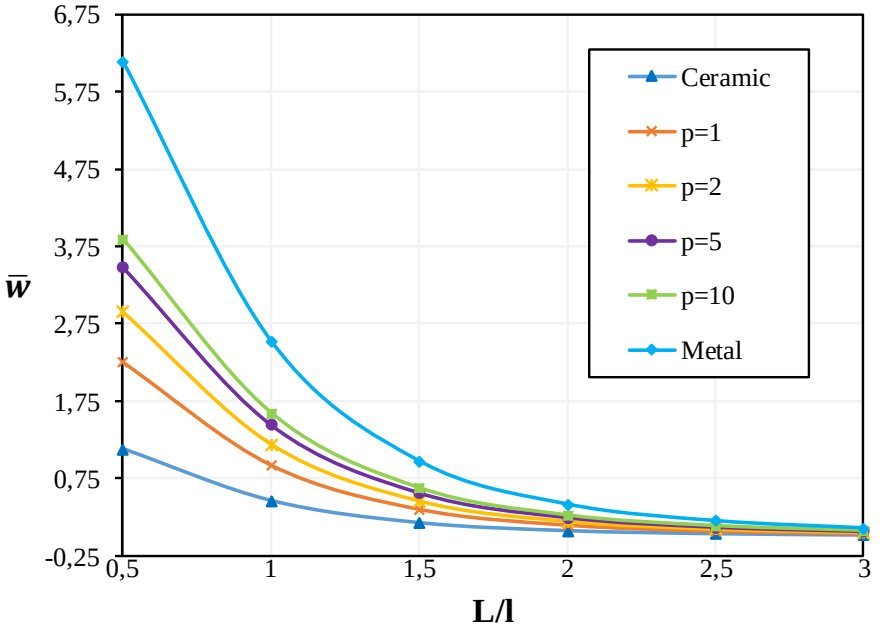

Figure 6.5 Variation of dimensionless deflection $\bar{w}$ of a SSSS moderately thick FG plate subjected to UDL versus the aspect ratio L/l.

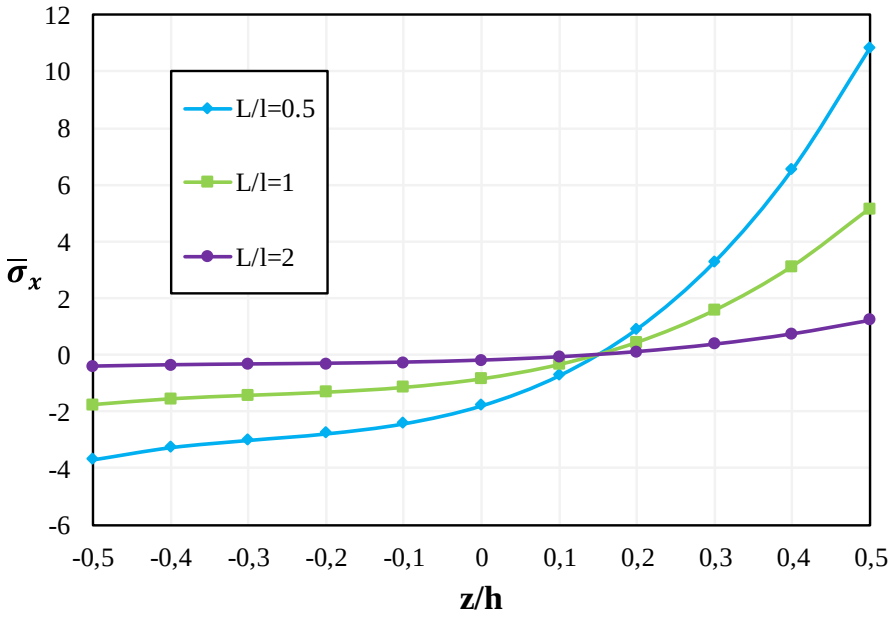

Figure 6.6 Variation of in-plane normal stress $\bar{\sigma}_x$ through-the thickness of a SSSS FG plate (L/h=10) subjected to UDL for different values of the aspect ratio, p=2.

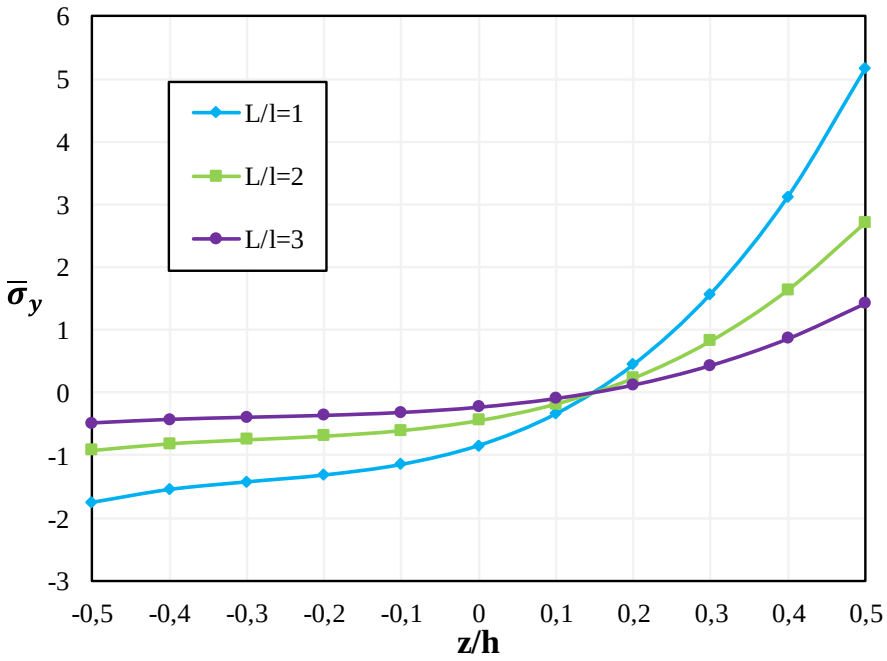

Figure 6.7 Variation of in-plane normal stress $\bar{\sigma}_y$ through-the thickness of a SSSS FG plate (L/h=10) subjected to UDL for different values of the aspect ratio, p=2.

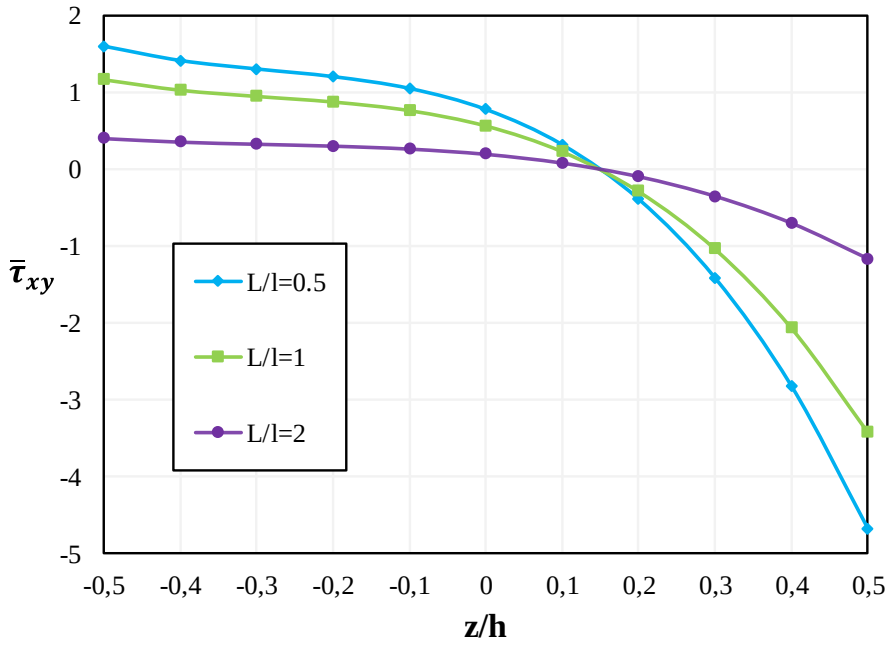

Figure 6.8 Variation of in-plane shear stress $\bar{\tau}_{xy}$ through-the thickness of a SSSS FG plate (L/h=10) subjected to UDL for different values of the aspect ratio, p=2.

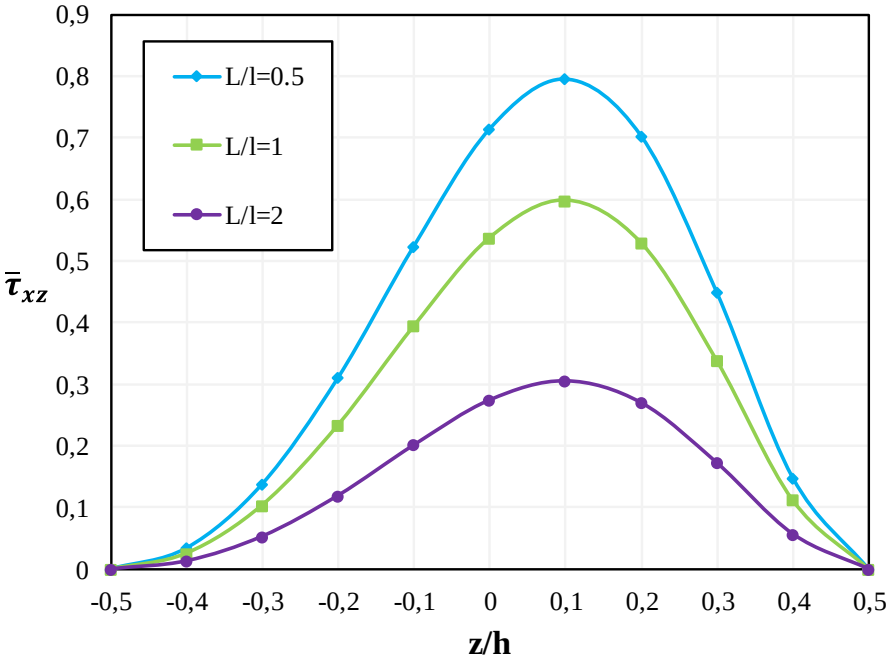

Figure 6.9 Variation of transverse shear stress $\bar{\tau}_{xz}$ through-the thickness of a SSSS FG plate (L/h=10) subjected to UDL for different values of the aspect ratio, p=2.

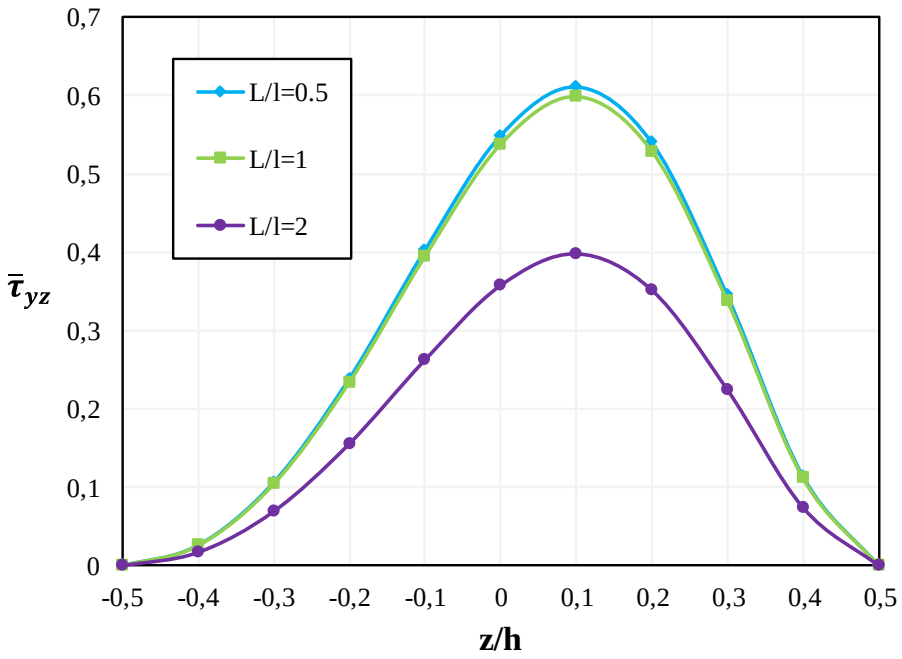

Figure 6.10 Variation of transverse shear stress $\bar{\tau}_{yz}$ through-the thickness of a SSSS FG plate (L/h=10) subjected to UDL for different values of the aspect ratio, p=2.

6.2.2 Mechanical buckling analysis

In the next examples the present element R4SSDT is used for the mechanical buckling analysis of Al/Al_2O_3 rectangular plates. Three different types of in-plane loadings, uniaxial compression (λ_1= -1, λ_2 = 0), biaxial compression (λ_1= λ_2 = -1), and biaxial compression and tension (λ_1= -1, λ_2 = 1) are considered, Figure 4.12. The effects of power-law index, side-to-thickness, aspect ratio and boundary conditions on the critical buckling load have been presented.

The dimensionless critical buckling load is presented using the following expression

$$\widehat{N}_{cri} = N_{cri}\frac{L^2}{E_m h^3} \tag{6.3}$$

The used boundary conditions are as follows

Simply supported (SSSS)

$$\begin{aligned} w_0 = \varphi_y = 0 \quad &\text{at} \quad x = 0, \quad x = L \\ w_0 = \varphi_x = 0 \quad &\text{at} \quad y = 0, \quad y = l \end{aligned} \tag{6.4}$$

Clamped (CCCC)

$$w_0 = \varphi_x = \varphi_y = 0 \qquad \text{at} \quad x = 0, L \text{ and } y = 0, l \tag{6.5}$$

Simply-Clamped (SCSC)

$$\begin{aligned} w_0 &= \varphi_y = 0 && \text{at} \quad x = 0, \quad x = L \\ w_0 &= \varphi_x = \varphi_y = 0 && \text{at} \quad \text{y} = 0, \quad \text{y} = l \end{aligned} \tag{6.6}$$

Simply and Clamped (SSSC)

$$\begin{aligned} w_0 &= \varphi_y = 0 && \text{at} \quad x = 0, \quad x = L \\ w_0 &= \varphi_x = 0 && \text{at} \quad \text{y} = 0 \\ w_0 &= \varphi_x = \varphi_y = 0 && \text{at} \quad \text{y} = l \end{aligned} \tag{6.7}$$

Clamped-Simply-Clamped (CSCC)

$$\begin{aligned} w_0 &= \varphi_x = \varphi_y = 0 && \text{at} \quad x = 0, \quad x = L \\ w_0 &= \varphi_x = 0 && \text{at} \quad \text{y} = 0 \\ w_0 &= \varphi_x = \varphi_y = 0 && \text{at} \quad \text{y} = l \end{aligned} \tag{6.8}$$

Simply and Free (SSSF)

$$\begin{aligned} w_0 &= \varphi_y = 0 && \text{at} \quad x = 0, \quad x = L \\ w_0 &= \varphi_x = 0 && \text{at} \quad \text{y} = 0 \\ \text{Free} & && \text{at} \quad \text{y} = l \end{aligned} \tag{6.9}$$

Clamped and Free (CFCC)

$$\begin{aligned} w_0 &= \varphi_x = \varphi_y = 0 && \text{at} \quad x = 0, \quad x = L \\ \text{Free} & && \text{at} \quad \text{y} = 0 \\ w_0 &= \varphi_x = \varphi_y = 0 && \text{at} \quad \text{y} = l \end{aligned} \tag{6.10}$$

Simply-Clamped-Simply-Free (SCSF)

$$\begin{aligned} w_0 &= \varphi_y = 0 && \text{at} \quad x = 0, \quad x = L \\ w_0 &= \varphi_x = \varphi_y = 0 && \text{at} \quad \text{y} = 0 \\ \text{Free} & && \text{at} \quad \text{y} = l \end{aligned} \tag{6.11}$$

6.2.2.1 FG square plate with different side-to-thickness ratio and power-law index values under different loading

In this section, the buckling behavior of a simply supported Al/Al_2O_3 square plate subjected to three different in-plane loads is analyzed. Six mesh sizes ranging from 8×8 to 32×32 elements have been used. Different side-to-thickness ratios and power-law index values have been considered. The dimensionless critical buckling loads of the FG square plate under uniaxial compression, biaxial compression and biaxial compression and tension are reported in Tables 6.6-6.8, respectively. The obtained results show the convergence and the stability of the present element. The comparison of the present results with those obtained by the HSDT-based finite element model of Tati [248], the RPT of Thai and Choi [252], the quasi-3D refined theory of Zenkour and Aljadani [246] and the HSDT of Reddy et al. [243] show the accuracy of the results obtained using the present finite element R4SSDT.

From Tables 6.6-6.8 and Figure 6.11, it can be observed that the dimensionless critical buckling load of plate subjected to uniaxial compression loading is greater than that subjected to biaxial compression and less than those subjected to biaxial compression and tension loads. This is due the fact that the application of a tension load to the plates increases their bending stiffness. It can also be seen that the dimensionless critical buckling load decreases with the increase of power-law index value while it increases with the increase of side-to-thickness ratio.

6.2.2.2 FG rectangular plate with different side-to-thickness ratio and power-law index values subjected to different loading

For this example, the dimensionless critical buckling loads $\widehat{N}_{cri}$ for simply supported, Al/Al_2O_3 rectangular plates subjected to uniaxial, biaxial compression and biaxial compression and tension are investigated. The obtained results are listed in Tables 6.9-6.11, respectively. Different values of the power-law index p with aspect ratio L/l (L/l = 0.5, 1, 1.5, 2) and side-to-thickness ratio L/h (L/h= 5, 10 and 20) are considered. The results of the proposed formulation are compared with those given by RPT of Thai and Choi [252] and the solutions of the CUF-based finite strip method (FSM) [247] and they are in good agreement. However, the obtained results are closer to those given by the RPT. As observed in the previous example, the dimensionless critical buckling load decreases with the increase of power-law index value whereas it increases with the increase of side-to-thickness ratio. Also, increasing of aspect ratio increases the critical buckling load values.

Table 6.6 Dimensionless critical buckling load $\widehat{N}_{cri}$ of SSSS Al/Al_2O_3 square plate under uniaxial compression (λ_1= -1, λ_2 = 0).

L/h	Mesh size	p=0	p=1	p=2	p=5	p=10	p=20
5	**8×8**	**16.2986**	**8.3720**	**6.3852**	**4.9731**	**4.4167**	**3.9914**
	12×12	**16.1390**	**8.2875**	**6.3222**	**4.9279**	**4.3776**	**3.9552**
	16×16	**16.0837**	**8.2583**	**6.3004**	**4.9122**	**4.3640**	**3.9427**
	20×20	**16.0583**	**8.2448**	**6.2903**	**4.9050**	**4.3578**	**3.9369**
	24×24	**16.0445**	**8.2375**	**6.2849**	**4.9011**	**4.3544**	**3.9337**
	32×32	**16.0308**	**8.2303**	**6.2795**	**4.8972**	**4.3510**	**3.9306**
	HSDT [248]	16.0582	8.2448	6.3250	5.0010	4.4178	3.9509
	RPT [252]	16.0211	8.2245	6.3432	5.0531	4.4807	4.0070
	Quazi-3D [246]	16.0210	8.2244	6.3431	5.0530	4.4806	4.0069
	HSDT [243]	16.0000	8.1460	6.2300	4.9700	4.4400	3.9800
10	**8×8**	**18.9631**	**9.5342**	**7.3910**	**6.0990**	**5.5120**	**4.9033**
	12×12	**18.7474**	**9.4248**	**7.3068**	**6.0311**	**5.4512**	**4.8488**
	16×16	**18.6729**	**9.3870**	**7.2777**	**6.0077**	**5.4301**	**4.8299**
	20×20	**18.6386**	**9.3696**	**7.2643**	**5.9969**	**5.4205**	**4.8212**
	24×24	**18.6200**	**9.3602**	**7.2570**	**5.9910**	**5.4152**	**4.8165**
	32×32	**18.6015**	**9.3508**	**7.2498**	**5.9852**	**5.4100**	**4.8119**
	HSDT [248]	18.6385	9.3696	-	6.0323	5.4435	4.8265
	RPT [252]	18.5785	9.3391	7.2630	6.0353	5.4528	4.8346
	Quazi-3D [246]	18.5785	9.3391	7.2630	6.0353	5.4528	4.8346
	HSDT [243]	18.5400	9.2990	7.2100	5.990	5.4200	4.8200
50	**8×8**	**20.0097**	**9.9772**	**7.7833**	**6.5753**	**5.9871**	**5.2900**
	12×12	**19.7696**	**9.8575**	**7.6899**	**6.4965**	**5.9154**	**5.2266**
	16×16	**19.6868**	**9.8162**	**7.6577**	**6.4693**	**5.8906**	**5.2047**
	20×20	**19.6486**	**9.7972**	**7.6428**	**6.4567**	**5.8792**	**5.1946**
	24×24	**19.6280**	**9.7868**	**7.6348**	**6.4500**	**5.8730**	**5.1892**
	32×32	**19.6075**	**9.7766**	**7.6268**	**6.4432**	**5.8669**	**5.1837**
	HSDT [248]	19.6486	9.7971	7.6433	6.4584	5.8803	5.1948
	RPT [252]	19.5814	9.7636	7.6177	6.4373	5.8614	5.1782
	Quazi-3D [246]	19.5814	9.7636	7.6176	6.4372	5.8613	5.1781
	HSDT [243]	19.5400	9.7430	7.6010	6.4200	5.8400	5.1600
100	**8×8**	**20.0435**	**9.9913**	**7.7959**	**6.5912**	**6.0031**	**5.3029**
	12×12	**19.8026**	**9.8712**	**7.7022**	**6.5120**	**5.9310**	**5.2392**
	16×16	**19.7195**	**9.8298**	**7.6699**	**6.4847**	**5.9061**	**5.2172**
	20×20	**19.6812**	**9.8107**	**7.6550**	**6.4721**	**5.8947**	**5.2071**
	24×24	**19.6605**	**9.8004**	**7.6469**	**6.4653**	**5.8884**	**5.2016**
	32×32	**19.6399**	**9.7901**	**7.6389**	**6.4585**	**5.8823**	**5.1961**
	HSDT [248]	19.6812	9.8107	7.6551	6.4724	5.8949	5.2071
	RPT [252]	19.6145	9.7775	7.6293	6.4507	5.8752	5.1897
	Quazi-3D [246]	19.6145	9.7775	7.6293	6.4507	5.8752	5.1896
	HSDT [243]	19.5700	9.7500	7.6100	6.4300	5.8600	5.1700

Table 6.7 Dimensionless critical buckling load $\widehat{N}_{cri}$ of SSSS Al/Al_2O_3 square plate under biaxial compression ($\lambda_1=\lambda_2=-1$).

L/h		p=0	p=1	p=2	p=5	p=10	p=20
5	**8×8**	**8.1493**	**4.1860**	**3.1926**	**2.4865**	**2.2084**	**1.9957**
	12×12	**8.0695**	**4.1438**	**3.1611**	**2.4639**	**2.1888**	**1.9776**
	16×16	**8.0419**	**4.1292**	**3.1502**	**2.4561**	**2.1820**	**1.9713**
	20×20	**8.0291**	**4.1224**	**3.1452**	**2.4525**	**2.1789**	**1.9684**
	24×24	**8.0222**	**4.1188**	**3.1424**	**2.4505**	**2.1772**	**1.9669**
	32×32	**8.0154**	**4.1151**	**3.1397**	**2.4486**	**2.1755**	**1.9653**
	HSDT [248]	8.0291	4.1224	3.1625	2.5005	2.2089	1.9754
	RPT [252]	8.0110	4.1120	3.1720	2.5270	2.2400	2.0040
	Quazi-3D [246]	8.0105	4.1122	3.1715	2.5265	2.2403	2.0034
	HSDT [243]	8.0010	4.0730	3.1200	2.4870	2.2210	1.9940
10	**8×8**	**9.4815**	**4.7671**	**3.6955**	**3.0495**	**2.7560**	**2.4516**
	12×12	**9.3737**	**4.7124**	**3.6534**	**3.0156**	**2.7256**	**2.4244**
	16×16	**9.3364**	**4.6935**	**3.6388**	**3.0038**	**2.7151**	**2.4150**
	20×20	**9.3193**	**4.6848**	**3.6321**	**2.9984**	**2.7102**	**2.4106**
	24×24	**9.3100**	**4.6801**	**3.6285**	**2.9955**	**2.7076**	**2.4083**
	32×32	**9.3008**	**4.6754**	**3.6249**	**2.9926**	**2.7050**	**2.4059**
	HSDT [248]	9.3193	4.6848	3.6379	3.01613	2.7217	2.4132
	RPT [252]	9.2890	4.6700	3.6320	3.0180	2.7346	2.4170
	Quazi-3D [246]	9.2892	4.6695	3.6315	3.0176	2.7264	2.4173
	HSDT [243]	9.2730	4.6500	3.6080	2.9980	2.7150	2.4100
50	**8×8**	**10.0048**	**4.9886**	**3.8916**	**3.2876**	**2.9935**	**2.6450**
	12×12	**9.8848**	**4.9287**	**3.8450**	**3.2482**	**2.9577**	**2.6133**
	16×16	**9.8434**	**4.9081**	**3.8288**	**3.2346**	**2.9453**	**2.6023**
	20×20	**9.8243**	**4.8986**	**3.8214**	**3.2284**	**2.9396**	**2.5973**
	24×24	**9.8140**	**4.8934**	**3.8174**	**3.2250**	**2.9365**	**2.5946**
	32×32	**9.8037**	**4.8883**	**3.8134**	**3.2216**	**2.9335**	**2.5919**
	HSDT [248]	9.8243	4.8986	3.8217	3.2292	2.9401	2.5974
	RPT [252]	9.7910	4.8820	3.8090	3.2190	2.9310	2.5890
	Quazi-3D [246]	9.7907	4.8818	3.8088	3.2186	2.9306	2.5890
	HSDT [243]	9.7720	4.8720	3.8010	3.2120	2.9250	2.5840
100	**8×8**	**10.0217**	**4.9956**	**3.8980**	**3.2956**	**3.0016**	**2.6514**
	12×12	**9.9013**	**4.9356**	**3.8511**	**3.2560**	**2.9655**	**2.6196**
	16×16	**9.8597**	**4.9149**	**3.8349**	**3.2423**	**2.9531**	**2.6086**
	20×20	**9.8406**	**4.9053**	**3.8275**	**3.2360**	**2.9473**	**2.6035**
	24×24	**9.8302**	**4.9002**	**3.8235**	**3.2326**	**2.9442**	**2.6008**
	32×32	**9.8199**	**4.8950**	**3.8195**	**3.2292**	**2.9411**	**2.5981**
	HSDT [248]	9.8406	4.9053	3.8275	3.2362	2.9474	2.6035
	RPT [252]	9.8070	4.8890	3.8150	3.2250	2.9380	2.5950
	Quazi-3D [246]	9.8072	4.8887	3.8146	3.2253	2.9375	2.5948
	HSDT [243]	9.7880	4.8790	3.8070	3.2190	2.9320	2.5900

Table 6.8 Dimensionless critical buckling load $\widehat{N}_{cri}$ of SSSS Al/Al_2O_3 square plate under biaxial compression and tension (λ_1= -1, λ_2 = 1).

L/h		p=0	p=1	p=2	p=5	p=10	p=20
5	**8×8**	**27.0191**	**14.3294**	**10.6646**	**7.6726**	**6.6664**	**6.1448**
	12×12	**26.5159**	**14.0361**	**10.4615**	**7.5601**	**6.5764**	**6.0554**
	16×16	**26.3495**	**13.9392**	**10.3943**	**7.5228**	**6.5466**	**6.0258**
	20×20	**26.2742**	**13.8954**	**10.3639**	**7.5060**	**6.5331**	**6.0124**
	24×24	**26.2337**	**13.8718**	**10.3475**	**7.4969**	**6.5259**	**6.0052**
	32×32	**26.1937**	**13.8485**	**10.3314**	**7.4880**	**6.5187**	**5.9981**
	RPT [252]	26.2058	13.8486	10.5589	7.9590	6.8970	6.2320
	Quazi-3D [246]	26.2057	13.8486	10.5589	7.9589	6.8970	6.2320
	HSDT [243]	26.1600	13.6200	10.2600	7.7600	6.8100	6.1800
10	**8×8**	**37.8002**	**19.2461**	**14.7776**	**11,7809**	**10.5352**	**9.4617**
	12×12	**36.6652**	**18.6519**	**14.3309**	**11.4516**	**10.2480**	**9.1978**
	16×16	**36.2936**	**18.4575**	**14.1847**	**11.3436**	**10.1537**	**9.1113**
	20×20	**36.1259**	**18.3698**	**14.1187**	**11.2948**	**10.1111**	**9.0722**
	24×24	**36.0359**	**18.3228**	**14.0833**	**11.2686**	**10.0882**	**9.0512**
	32×32	**35.9472**	**18.2764**	**14.0484**	**11.2428**	**10.0657**	**9.0305**
	RPT [252]	35.8416	18.2206	14.1073	11.4583	10.2468	9.1281
	Quazi-3D [246]	35.8416	18.2205	14.1072	11.4582	10.2468	9.1281
	HSDT [243]	35.7100	18.0400	13.9000	11.3000	10.1500	9.0700
50	**8×8**	**43.3334**	**21.6200**	**16.8581**	**14.2171**	**12.9381**	**11.4374**
	12×12	**41.7827**	**20.8454**	**16.2547**	**13.7099**	**12.4771**	**11.0294**
	16×16	**41.2785**	**20.5935**	**16.0585**	**13.5450**	**12.3272**	**10.8968**
	20×20	**41.0514**	**20.4801**	**15.9701**	**13.4707**	**12.2596**	**10.8370**
	24×24	**40.9296**	**20.4192**	**15.9227**	**13.4309**	**12.2234**	**10.8050**
	32×32	**40.8097**	**20.3593**	**15.8761**	**13.3916**	**12.1878**	**10.7734**
	RPT [252]	40.6574	20.2833	15.8219	13.3554	12.1543	10.7401
	Quazi-3D [246]	40.6573	20.2832	15.8218	13.3553	12.1542	10.7400
	HSDT [243]	40.4600	20.1790	15.7300	13.280	12.0900	10.6800
100	**8×8**	**43.5319**	**21.7033**	**16.9324**	**14.3094**	**13.0309**	**11.5124**
	12×12	**41.9652**	**20.9219**	**16.3229**	**13.7948**	**12.5624**	**11.0984**
	16×16	**41.4558**	**20.6679**	**16.1248**	**13.6275**	**12.4101**	**10.9638**
	20×20	**41.2264**	**20.5535**	**16.0356**	**13.5521**	**12.3415**	**10.9032**
	24×24	**41.1034**	**20.4921**	**15.9877**	**13.5118**	**12.3047**	**10.8707**
	32×32	**40.9823**	**20.4317**	**15.9406**	**13.4720**	**12.2684**	**10.8387**
	RPT [252]	40.8291	20.3554	15.8823	13.4250	12.2256	10.7998
	Quazi-3D [246]	40.8290	20.3553	15.8822	13.4249	12.2255	10.7998
	HSDT [243]	40.6200	20.2500	15.8000	13.3500	12.1600	10.7400

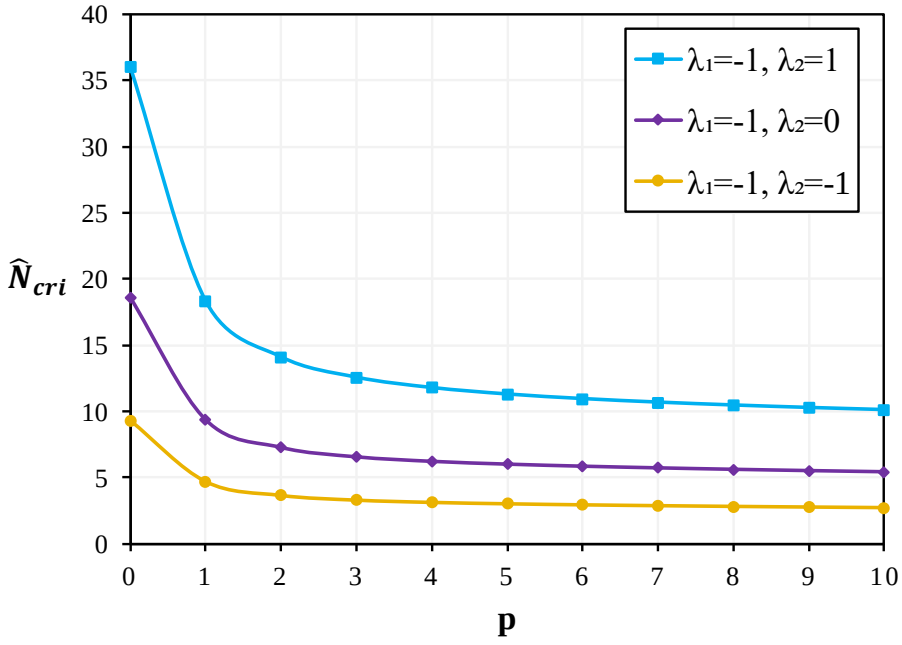

Figure 6.11 The effect of power-law index *p* on dimensionless critical buckling load $\widehat{N}_{cri}$ of SSSS square plate (*L*/*h*=10) with different types of loading.

6.2.2.3 FG square plate subjected to uniaxial compression with different *L*/*h* values

In this example, simply supported, Al/Al_2O_3 square plates under uniaxial compression ($\lambda_1 = -1$, $\lambda_2 = 0$) have been considered for different values of side-to-thickness ratio *L*/*h* and power-law index *p* = 1 and 10. The dimensionless critical buckling loads $\widehat{N}_{cri}$ have been obtained using a 24 × 24 mesh size. Table 6.12 compares the results predicted by the proposed formulation with the results of research studies in which the CPT [220], FSDT [265], HSDT [243] and high-order plate theory considering Carrera's unified formulation (CUF) [249] have been used. As it can be seen, the results obtained using the FSDT, HSDT, CUF and the present formulation diverge from those obtained using CPT for *L*/*h* =10 and converge for higher values of *L*/*h*. Good agreement between the present results and those obtained by HSDT and CUF can be observed. However, for *L*/*h* ≥ 40 the present study and CUF results are identical.

Table 6.9 Dimensionless critical buckling load $\bar{N}_{cri}$ of SSSS Al/Al_2O_3 rectangular plate subjected to uniaxial compression along the x-axis (λ_1= -1, λ_2 = 0).

L/l	*L/h*	*Theory*	*p*						
			0	**1**	**2**	**5**	**10**	**20**	**100**
0.5[a]	**5**	RPT [252]	6.7203	3.4164	2.6451	2.1484	1.9213	1.7115	1.3737
		Present	**6.7664**	**3.4404**	**2.6444**	**2.1159**	**1.8942**	**1.6995**	**1.3767**
	10	RPT [252]	7.4053	3.7111	2.8897	2.4165	2.1896	1.9387	1.5251
		CUF [247]	7.3760	3.6940	2.8720	-	2.1760	-	-
		Present	**7.4635**	**3.7405**	**2.9067**	**2.4203**	**2.1936**	**1.9463**	**1.5351**
	20	RPT [252]	7.5993	3.7930	2.9582	2.4944	2.2690	2.0054	1.5683
		CUF [247]	7.5910	3.7890	2.9530	-	2.2650	-	-
		Present	**7.6609**	**3.8238**	**2.9806**	**2.5106**	**2.2838**	**2.0197**	**1.5805**
1[b]	**5**	RPT [252]	16.0211	8.2245	6.3432	5.0531	4.4807	4.0070	3.2586
		Present	**16.0445**	**8.2375**	**6.2849**	**4.9011**	**4.3544**	**3.9337**	**3.2413**
	10	RPT [252]	18.5785	9.3391	7.2631	6.0353	5.4528	4.8346	3.8198
		CUF [247]	18.3650	9.2170	7.1520	-	5.3780	-	-
		Present	**18.6200**	**9.3602**	**7.2570**	**5.9910**	**5.4152**	**4.8165**	**3.8208**
	20	RPT [252]	19.3528	9.6675	7.5371	6.3448	5.7668	5.0988	3.9923
		CUF [247]	19.2940	9.6350	7.5070	-	5.7450	-	-
		Present	**19.3984**	**9.6903**	**7.5489**	**6.3437**	**5.7664**	**5.1028**	**3.9996**
1.5[c]	**5**	RPT [252]	28.1996	15.0344	11.4234	8.4727	7.2952	6.6106	5.6325
		Present	**28.2144**	**15.0526**	**11.1518**	**7.9118**	**6.8494**	**6.3341**	**5.5479**
	10	RPT [252]	40.7476	20.8024	16.0793	12.9501	11.5379	10.2958	8.3112
		Present	**40.9869**	**20.9291**	**16.0345**	**12.6846**	**11.3173**	**10.1852**	**8.3131**
	20	RPT [252]	45.8930	23.0286	17.9221	14.9472	13.5273	11.9843	9.4447
		Present	**46.2175**	**23.1927**	**18.0054**	**14.9373**	**13.5225**	**12.0108**	**9.4964**
2[d]	**5**	RPT [252]	37.7404	20.7491	15.5819	10.9554	9.1505	8.3988	7.4403
		Present	**37.5590**	**20.6808**	**14.9524**	**9.7017**	**8.1340**	**7.7421**	**7.2321**
	10	RPT [252]	64.0842	32.8980	25.3727	20.2123	17.9227	16.0280	13.0345
		Present	**64.5559**	**33.1501**	**25.2887**	**19.7115**	**17.5104**	**15.8208**	**13.0397**
	20	RPT [252]	74.3140	37.3564	29.0523	24.1413	21.8114	19.3385	15.2794
		Present	**74.9896**	**37.6991**	**29.2271**	**24.1244**	**21.8047**	**19.3950**	**15.3873**

[a] 288 elements [b] 576 elements

[c] 384 elements [d] 288 elements

Table 6.10 Dimensionless critical buckling load $\widehat{N}_{cri}$ of SSSS Al/Al_2O_3 rectangular plate subjected to biaxial compression ($\lambda 1$= -1, $\lambda 2$ = -1).

L/l	*L/h*	*Theory*	*p*						
			0	**1**	**2**	**5**	**10**	**20**	**100**
0.5[a]	**5**	RPT [252]	5.3762	2.7331	2.1161	1.7187	1.5370	1.3692	1.0990
		CUF [247]	5.2440	2.6530	2.0450	1.6630	1.4950	1.3330	-
		Present	**5.4177**	**2.7545**	**2.1173**	**1.6942**	**1.5167**	**1.3608**	**1.1023**
	10	RPT [252]	5.9243	2.9689	2.3117	1.9332	1.7517	1.5510	1.2200
		CUF [247]	5.9020	2.9560	2.2980	1.9200	1.7410	1.5420	-
		Present	**5.9759**	**2.9949**	**2.3274**	**1.9379**	**1.7564**	**1.5584**	**1.2291**
	20	RPT [252]	6.0794	3.0344	2.3665	1.9955	1.8152	1.6044	1.2547
		CUF [247]	6.0730	3.0310	2.3620	1.9910	1.8120	1.6020	-
		Present	**6.1339**	**3.0617**	**2.3866**	**2.0102**	**1.8286**	**1.6171**	**1.2655**
1[b]	**5**	RPT [252]	8.0105	4.1122	3.1716	2.5265	2.2403	2.0035	1.6293
		CUF [247]	7.7350	3.9420	3.0240	2.4180	2.1590	1.9320	-
		Present	**8.0222**	**4.1188**	**3.1425**	**2.4505**	**2.1772**	**1.9669**	**1.6206**
	10	RPT [252]	9.2893	4.6696	3.6315	3.0177	2.7264	2.4173	1.9099
		CUF [247]	9.1930	4.6140	3.5800	2.9740	2.6920	2.3880	-
		Present	**9.3100**	**4.6801**	**3.6285**	**2.9955**	**2.7076**	**2.4083**	**1.9104**
	20	RPT [252]	9.6764	4.8337	3.7686	3.1724	2.8834	2.5494	1.9961
		CUF [247]	9.6480	4.8180	3.7540	3.1590	2.8730	2.5410	-
		Present	**9.6992**	**4.8452**	**3.7745**	**3.1719**	**2.8832**	**2.5514**	**1.9998**
1.5[c]	**5**	RPT [252]	11.6820	6.0799	4.6637	3.6176	3.1718	2.8510	2.3600
		CUF [247]	11.1630	5.7490	4.3840	3.4270	3.0340	2.7250	-
		Present	**11.7085**	**6.0955**	**4.6015**	**3.4631**	**3.0459**	**2.7769**	**2.3418**
	10	RPT [252]	14.6084	7.3793	5.7279	4.7124	4.2384	3.7657	2.9959
		CUF [247]	14.3530	7.2300	5.5950	4.6040	4.1550	3.6930	-
		Present	**14.6700**	**7.4110**	**5.7243**	**4.6616**	**4.1958**	**3.7463**	**2.9992**
	20	RPT [252]	15.5887	7.7977	6.0761	5.1006	4.6300	4.0961	3.2135
		CUF [247]	15.5090	7.7530	6.0350	5.0650	4.6020	4.0720	-
		Present	**15.6603**	**7.8336**	**6.0962**	**5.1032**	**4.6330**	**4.1045**	**3.2256**
2[d]	**5**	RPT [252]	15.7235	8.3092	6.3353	4.7754	4.1382	3.7392	3.1534
		CUF [247]	14.9130	7.7730	5.8940	4.5000	3.9440	3.5560	-
		Present	**15.7761**	**8.3425**	**6.2227**	**4.5084**	**3.9245**	**3.6113**	**3.1211**
	10	RPT [252]	21.5050	10.9323	8.4644	6.8750	6.1481	5.4769	4.3958
		CUF [247]	21.3690	10.615	8.186	6.657	5.982	5.331	-
		Present	**21.6709**	**11.0187**	**8.4692**	**6.7766**	**6.0668**	**5.4431**	**4.4092**
	20	RPT [252]	23.6970	11.8755	9.2469	7.7327	7.0067	6.2040	4.8802
		CUF [247]	23.5120	11.7700	9.1520	7.6520	6.9430	6.1500	-
		Present	**23.9038**	**11.9797**	**9.3095**	**7.7516**	**7.0255**	**6.2336**	**4.9164**

[a] 288 elements [b] 576 elements

[c] 384 elements [d] 288 elements

Table 6.11 Dimensionless critical buckling load $\widehat{N}_{cri}$ of SSSS Al/Al_2O_3 rectangular plate subjected to biaxial compression and tension (λ_1= -1, λ_2 = 1).

L/l	*L/h*	*Theory*	*p*						
			0	**1**	**2**	**5**	**10**	**20**	**100**
0.5[a]	**5**	RPT [252]	8.9604	4.5551	3.5268	2.8646	2.5617	2.2820	1.8316
		CUF [247]	8.6840	4.3890	3.3820	2.7510	2.4730	2.2040	-
		Present	**9.0090**	**4.5807**	**3.5208**	**2.8172**	**2.5221**	**2.2628**	**1.8330**
	10	RPT [252]	9.8738	4.9481	3.8529	3.2219	2.9195	2.5850	2.0334
		CUF [247]	9.8300	4.9230	3.8270	3.1970	2.9000	2.5690	-
		Present	**9.9372**	**4.9802**	**3.8701**	**3.2225**	**2.9206**	**2.5914**	**2.0439**
	20	RPT [252]	10.1324	5.0574	3.9442	3.3259	3.0253	2.6739	2.0911
		CUF [247]	10.1200	5.0410	3.9360	3.3190	3.0200	2.6700	-
		Present	**10.2000**	**5.0912**	**3.9685**	**3.3427**	**3.0408**	**2.6890**	**2.1044**
1[b]	**5**	RPT [252]	26.2058	13.8486	10.5589	7.9590	6.8970	6.2320	5.2556
		CUF [247]	25.7960	13.3200	9.8780	7.4320	6.6750	5.9810	-
		Present	**26.2337**	**13.8718**	**10.3475**	**7.4969**	**6.5259**	**6.0052**	**5,1900**
	10	RPT [252]	35.8416	18.2206	14.1073	11.4583	10.2468	9.1281	7.3263
		CUF [247]	35.4130	17.9560	13.8350	11.2180	10.0690	8.9760	-
		Present	**36.0359**	**18.3228**	**14.0833**	**11.2686**	**10.0882**	**9.0512**	**7.3319**
	20	RPT [252]	39.4951	19.7925	15.4115	12.8878	11.6779	10.3400	8.1336
		CUF [247]	39.2880	19.6750	15.2960	12.7800	11.6050	10.2800	-
		Present	**39.7470**	**19.9207**	**15.4805**	**12.8899**	**11.6826**	**10.3657**	**8.1754**
1.5[c]	**5**	RPT [252]	29.0249	15.7823	11.9009	8.5250	7.2422	6.6008	5.7477
		CUF [247]	28.3740	15.1430	11.1580	8.2260	7.1430	6.5220	-
		Present	**29.0555**	**15.8171**	**11.5384**	**7.8142**	**6.6865**	**6.2487**	**5.6351**
	10	RPT [252]	37.9819	19.1863	14.8925	12.2523	11.0199	9.7909	7.7894
		CUF [247]	37.1410	18.7180	14.4760	11.8970	10.7290	9.5380	-
		Present	**38.0669**	**19.2306**	**14.8540**	**12.0964**	**10.8875**	**9.7211**	**7.7825**
	20	RPT [252]	40.5307	20.2740	15.7980	13.2616	12.0379	10.6500	8.3551
		CUF [247]	40.2960	20.1450	15.6810	13.1580	11.9530	10.5780	-
		Present	**40.6366**	**20.3273**	**15.8190**	**13.2421**	**12.0222**	**10.6506**	**8.3699**
2[d]	**5**	RPT [252]	26.2058	13.8486	10.5589	7.9590	6.8970	6.2320	5.2556
		CUF [247]	25.5270	13.4040	9.9970	7.5810	6.7590	6.1010	-
		Present	**26.2337**	**13.8718**	**10.3475**	**7.4969**	**6.5259**	**6.0052**	**5.1900**
	10	RPT [252]	35.8416	18.2206	14.1073	11.4583	10.2468	9.1281	7.3263
		CUF [247]	34.8690	17.6560	13.6110	11.0610	9.9370	8.8570	-
		Present	**36.0359**	**18.3228**	**14.0833**	**11.2686**	**10.0882**	**9.0512**	**7.3319**
	20	RPT [252]	39.4951	19.7925	15.4115	12.8878	11.6779	10.3400	8.1336
		CUF [247]	39.1740	19.6110	15.2490	12.7470	11.5660	10.2440	-
		Present	**39.7470**	**19.9207**	**15.4805**	**12.8899**	**11.6826**	**10.3657**	**8.1754**

[a] 288 elements [b] 576 elements

[c] 384 elements [d] 288 elements

Table 6.12 Comparison of dimensionless critical buckling load $\widehat{N}_{cri}$ of simply supported Al/Al_2O_3 plate subjected to uniaxial compression (λ_1= -1, λ_2 = 0).

L/h	***p* = 1**					***p* =10**				
	CPT [220]	FSDT [265]	HSDT [243]	CUF [249]	**Present**	CPT [220]	FSDT [265]	HSDT [243]	CUF [249]	**Present**
10	9.78	9.33	9.29	9.21	**9.36**	5.87	5.66	5.42	5.38	**5.42**
20	9.78	9.66	9.64	9.64	**9.69**	5.87	5.78	5.75	5.75	**5.77**
40	9.78	9.75	9.73	9.77	**9.78**	5.87	5.85	5.83	5.86	**5.86**
50	9.78	9.76	9.74	9.79	**9.79**	5.87	5.86	5.84	5.87	**5.87**
100	9.78	9.77	9.75	9.82	**9.80**	5.87	5.87	5.86	5.90	**5.89**

6.2.2.4 The effects of different parameters on the critical buckling load

The main objective of this example is to investigate the effects of some parameters including power-law index *p*, aspect ratio *L*/*l*, side-to-thickness ratio *L*/*h* and boundary conditions on the dimensionless critical buckling load $\widehat{N}_{cri}$ of FG plates.

Figures (6.12)-(6.14) show the variation of the dimensionless critical buckling load $\widehat{N}_{cri}$ of square plates (*L*/*h*=10) with different boundary conditions under uniaxial compression, biaxial compression, and biaxial compression and tension with respect to the power-law index *p*. It can be observed that the dimensionless critical buckling load decreases by increasing the power-law index *p*. This is because that the increase of the power-law index decreases the volume fraction of the ceramic and, consequently, the plate bending stiffness. It can be also seen from those figures that as the boundary constraints increase, the dimensionless critical buckling load increases.

Figure 6.15 depicts the variation of the dimensionless critical buckling loads $\widehat{N}_{cri}$ versus the side-to-thickness ratio *L*/*h* for square FG plate with different values of power-law index *p* subjected to uniaxial compression. It can be seen that the dimensionless critical buckling load increases by the increase of side-to-thickness ratio up to *L*/*h*=10 and then becomes almost constant for *L*/*h*>10.

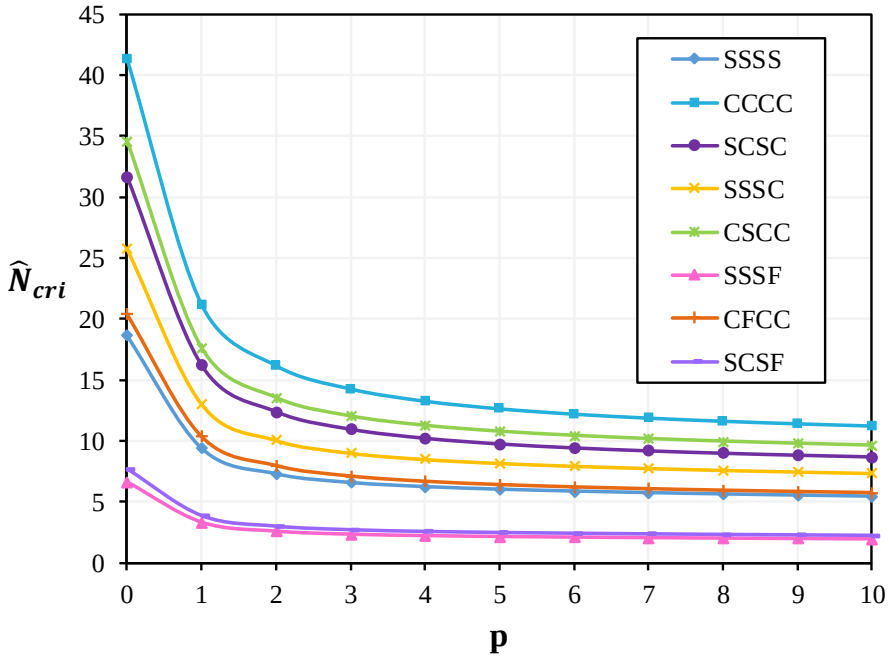

Figure 6.12 The variation of the dimensionless critical buckling load $\widehat{N}_{cri}$ of square plate (L/h=10) with different boundary conditions under uniaxial compression.

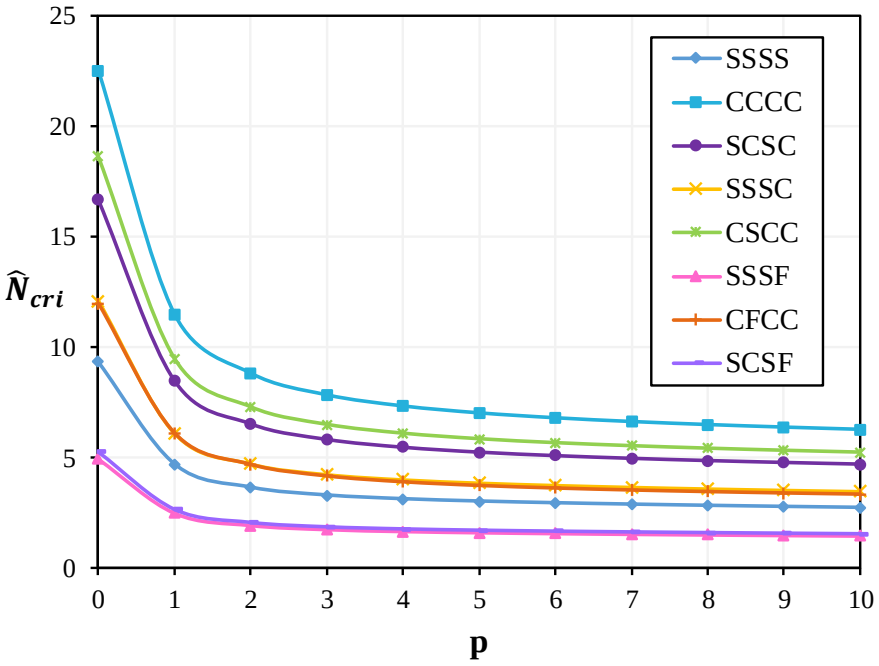

Figure 6.13 The variation of the dimensionless critical buckling load $\widehat{N}_{cri}$ of square plate (L/h=10) with different boundary conditions under biaxial compression.

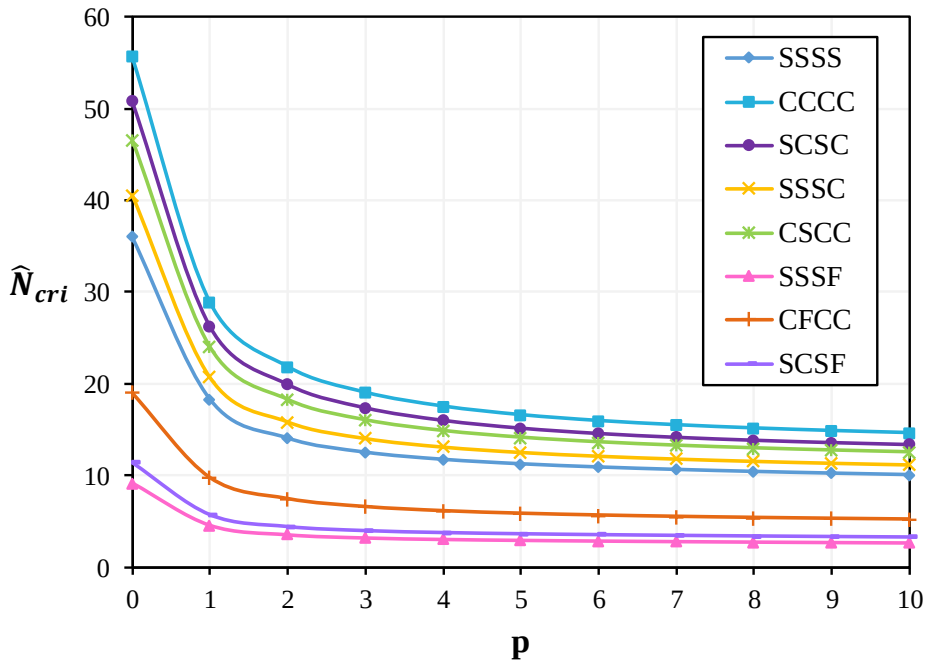

Figure 6.14 The variation of the dimensionless critical buckling load $\widehat{N}_{cri}$ of square plate (L/h=10) with different boundary conditions under biaxial compression and tension.

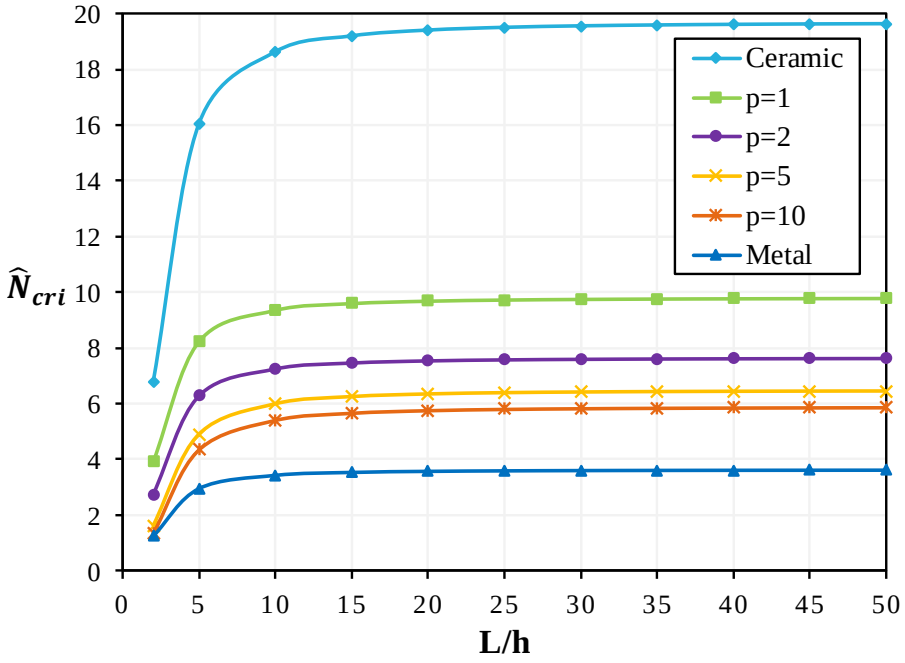

Figure 6.15 The variation of the dimensionless critical buckling loads $\widehat{N}_{cri}$ vs. the side-to-thickness ratio L/h for SSSS square plate (L/h=10) with different values of power-law index p under uniaxial compression.

The variation of the dimensionless critical buckling loads with respect to the aspect ratio l/L for simply supported rectangular plates with different values of the power-law index *p* subjected to uniaxial and biaxial loading is illustrated in Figures 6.16 and 6.17 respectively. As depicted in the two figures, the dimensionless critical buckling load decreases by increasing the aspect ratio. In the case of uniaxial compression loading it can be seen that the critical buckling modes change by the increase of the aspect ratio l/L as indicated by [252] and [247]. While, in the case of biaxial compression loading, the graph appears smooth, meaning that, whatever the aspect ratio, the plate buckles with only one mode.

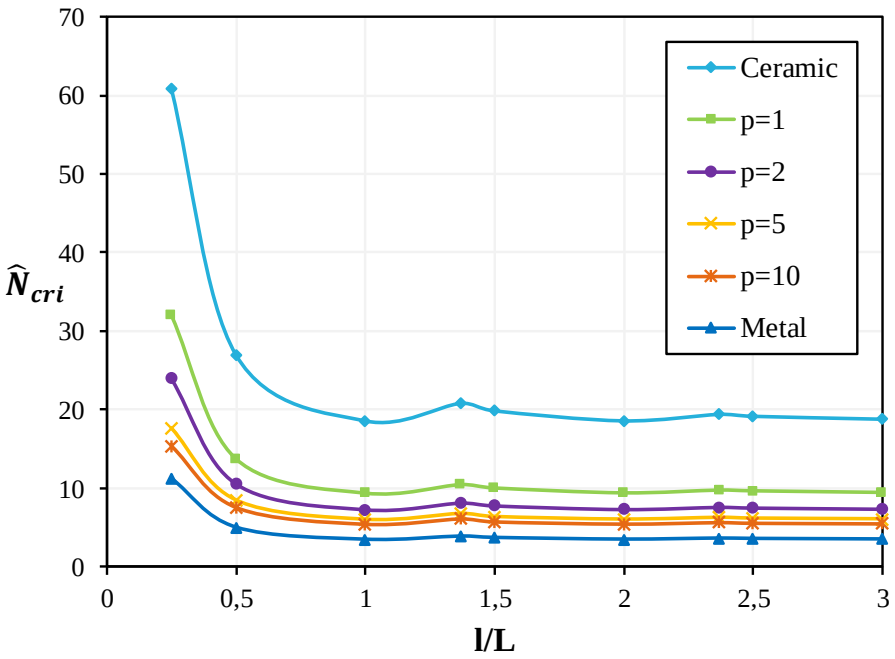

Figure 6.16 The variation of the dimensionless critical buckling loads $\widehat{N}_{cri}$ vs. the aspect ratio *l*/*L* for SSSS rectangular plate with different values of power-law index *p* under uniaxial compression.

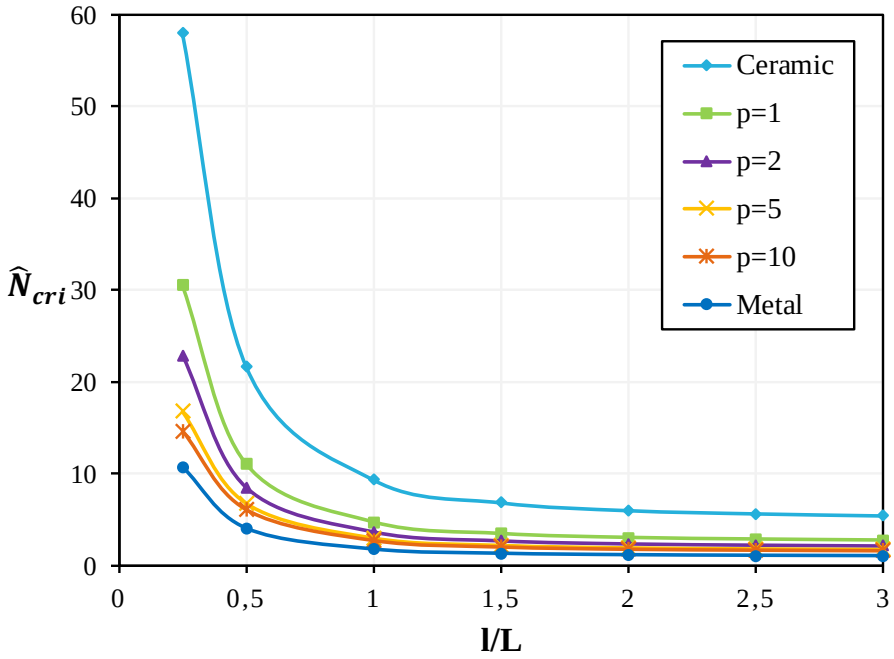

Figure 6.17 The variation of the dimensionless critical buckling loads $\widehat{N}_{cri}$ vs. the aspect ratio *l*/*L* for SSSS rectangular plate with different values of power-law index *p* under biaxial compression.

6.2.3 Free vibration analysis

In this section, the accuracy and the performance of the present finite element formulation is evaluated. Numerical examples for free vibration analysis of FG plates with various indexes that specify the material variation profile through the thickness and several values of the side-to-thickness ratio *L*/*h* and aspect ratio *L*/*l* are also presented. Typical mechanical properties for metal and ceramics used in the numerical examples are listed in Table 6.1.

For this study the following relations for presentations of dimensionless frequencies are utilized

$$\bar{\beta} = \omega h\sqrt{\rho_m / E_m}; \quad \hat{\omega} = \omega h\sqrt{\rho_c / E_c}; \quad \bar{\omega} = \omega \frac{L^2}{h}\sqrt{\rho_c / E_c}; \tag{6.12}$$

The used boundary conditions are as follows

Simply supported (SSSS)

$$\begin{aligned} u_0 = w_0 = \varphi_y = 0 \qquad & \text{at} \quad x = 0, \quad x = L \\ v_0 = w_0 = \varphi_x = 0 \qquad & \text{at} \quad y = 0, \quad y = l \end{aligned} \tag{6.13}$$

Clamped (CCCC)

$$\begin{aligned} u_0 = w_0 = \varphi_x = \varphi_y = 0 \qquad & \text{at} \quad x = 0,\ L \\ v_0 = w_0 = \varphi_x = \varphi_y = 0 \qquad & \text{at} \quad y = 0,\ l \end{aligned} \tag{6.14}$$

Simply-Clamped (SCSC)

$$\begin{aligned} u_0 = w_0 = \varphi_y = 0 \qquad & \text{at} \quad x = 0,\ L \\ v_0 = w_0 = \varphi_x = \varphi_y = 0 \qquad & \text{at} \quad y = 0,\ l \end{aligned} \tag{6.15}$$

Simply and Clamped (SSSC)

$$\begin{aligned} u_0 = w_0 = \varphi_y = 0 \qquad & \text{at} \quad x = 0, \quad x = L \\ v_0 = w_0 = \varphi_x = 0 \qquad & \text{at} \quad y = 0 \\ v_0 = w_0 = \varphi_x = \varphi_y = 0 \qquad & \text{at} \quad y = l \end{aligned} \tag{6.16}$$

Simply-Free-Simply (SFSS)

$$\begin{aligned} u_0 = w_0 = \varphi_y = 0 \qquad & \text{at} \quad x = 0, \quad x = L \\ \text{Free} \qquad & \text{at} \quad y = 0 \\ v_0 = w_0 = \varphi_x = 0 \qquad & \text{at} \quad y = l \end{aligned} \tag{6.17}$$

Simply-Free (SFSF)

$$\begin{aligned} u_0 = w_0 = \varphi_y = 0 \qquad & \text{at} \quad x = 0, \quad x = L \\ \text{Free} \qquad & \text{at} \quad y = 0, \quad y = l \end{aligned} \tag{6.18}$$

Simply-Free-Simply-Clamped (SFSC)

$$\begin{aligned} u_0 = w_0 = \varphi_y = 0 \qquad & \text{at} \quad x = 0, \quad x = L \\ \text{Free} \qquad & \text{at} \quad y = 0 \\ v_0 = w_0 = \varphi_x = \varphi_y = 0 \qquad & \text{at} \quad y = l \end{aligned} \tag{6.19}$$

6.2.3.1 Fundamental frequency $\bar{\beta}$ for simply supported Al/ ZrO_2 square plate

The aim of this example is to show the performance of the present finite element in predicting the free vibration response of a simply supported Al/ ZrO_2 square plate. The dimensionless fundamental frequencies $\bar{\beta}$ obtained using the present formulation with different meshes are presented in Table 6.13 for different values of power-law index *p* and side-to-thickness ratio *L*/*h*. The present results are compared with the exact 3D solutions of Vel and Batra [182], simplified FSDT solutions of Thai and Choi [130], HSDT solutions of Matsunaga [202] and Mantari et al [207], quasi-3D solutions of Neves et al [169] and the results obtained using the present R4FSDT. It can be noticed that the present results are in good agreement with those of the mentioned references. However, it is clear from the results presented in the table that the convergence of the present finite element results to HSDT solutions is very good.

It is also observed from Table 6.13 that for *p* equal to 0 and 1, the present results are the same as those obtained using the R4FSDT element, while for other values of *p*, a slight difference is observed.

Table 6.13 Dimensionless fundamental frequency $\bar{\beta}$ of Al/ZrO_2 square plates.

Theory	***p*=0***		**p=1**			***L*/*h*=5**		
	***L*/*h*=√10**	***L*/*h*=10**	***L*/*h*=5**	***L*/*h*=10**	***L*/*h*=20**	***p*=2**	***p*=3**	***p*=5**
3D [182]	0.4658	0.0578	0.2192	0.0596	0.0153	0.2197	0.2211	0.2225
S-FSDT [130]	0.4618	0.0577	0.2173	0.0592	0.0152	0.2189	0.2207	0.2222
2D-HSDT [202]	0.4658	0.0578	0.2285	0.0619	0.0158	0.2264	0.2270	0.2281
HSDT [207]	0.4624	0.0577	0.2277	0.0619	0.0158	0.2257	0.2263	0.2271
Quasi-3D [169]	-	-	0.2193	0.0596	0.0153	0.2198	0.2212	0.2225
R4FSDT 32×32	0.4622	0.0578	0.2278	0.0619	0.0159	0.2266	0.2278	0.2293
Present 8×8	**0.4678**	**0.0587**	**0.2311**	**0.0629**	**0.0161**	**0.2283**	**0.2283**	**0.2288**
Present 16×16	**0.4633**	**0.0579**	**0.2285**	**0.0621**	**0.0159**	**0.2258**	**0.2258**	**0.2263**
Present 24×24	**0.4625**	**0.0578**	**0.2280**	**0.0620**	**0.0159**	**0.2253**	**0.2254**	**0.2258**
Present 32×32	**0.4622**	**0.0578**	**0.2278**	**0.0619**	**0.0159**	**0.2251**	**0.2252**	**0.2257**

$*\bar{\beta} = \omega h\sqrt{\rho_c / E_c}$

6.2.3.2 Fundamental frequency $\hat{\omega}$ for simply supported Al/Al_2O_3 square plate

This example is performed for thin and thick SSSS, Al/Al_2O_3 square plates. The first two dimensionless frequencies $\hat{\omega}$ for various values of side-to-thickness ratio *L*/*h* and power-law index *p* are presented in Table 6.14. The obtained results using the element R4SSDT with a 24 × 24 mesh size are compared with solutions based on HSDT presented by Matsunaga [202] and solutions reported by Thai and Choi [130] using a simple FSDT. In general, a good agreement between the results is found. It can be observed that the solutions from this formulation are very close to those reported by Matsunaga [202] for all FG plates with various values of power-law index *p*.

Table 6.14 The first two dimensionless frequencies $\hat{\omega}$ of Al/Al_2O_3 square plates.

Mode	L/h	Theory	Power-law index p			
			0	**1**	**4**	**10**
1	**5**	FSDT [130]	0.2112	0.1631	0.1397	0.1324
		HSDT [202]	0.2121	0.1640	0.1383	0.1306
		Present	**0.2116**	**0.1634**	**0.1363**	**0.1285**
	10	FSDT [130]	0.0577	0.0442	0.0382	0.0366
		HSDT [202]	0.0578	0.0443	0.0381	0.0364
		Present	**0.0578**	**0.0443**	**0.0380**	**0.0363**
2	**5**	FSDT [130]	0.4618	0.3604	0.3049	0.2856
		HSDT [202]	0.4658	0.3644	0.3000	0.2790
		Present	**0.4642**	**0.3624**	**0.2923**	**0.2713**
	10	FSDT [130]	0.1376	0.1059	0.0911	0.0867
		HSDT [202]	0.1381	0.1063	0.0905	0.0859
		Present	**0.1385**	**0.1066**	**0.0900**	**0.0853**

6.2.3.3 Fundamental frequency $\bar{\beta}$ for simply supported Al/Al_2O_3 rectangular plates

In this example, an Al/Al_2O_3 FG plates with simply supported edges are analyzed. In Table 6.15, dimensionless fundamental frequencies $\bar{\beta}$ for different values of aspect ratio *l* / *L*, side-to-thickness *L* / *h* and power-law index *p* are calculated and compared with the 3D exact solution proposed by Jin et al. [186], HSDT results of Mantari et al. [207] and Quasi-3D solutions reported by Zaoui et al. [210]. For all cases, a good agreement is found.

Table 6.15 The dimensionless fundamental frequencies $\bar{\beta}$ of Al/Al_2O_3 plates.

l/L	L/h	p	Theory			
			3D [186]	HSDT [207]	Quazi-3D [210]	**Present**
1[a]	**10**	**0**	0.1135	0.1134	0.1137	**0.1136**
		1	0.0870	0.0868	0.0883	**0.0870**
		2	0.0789	0.0788	0.0807	**0.0788**
		5	0.0741	0.0740	0.0756	**0.0738**
	5	**0**	0.4169	0.4151	0.4178	**0.4156**
		1	0.3222	0.3205	0.3267	**0.3210**
		2	0.2905	0.2892	0.2968	**0.2883**
		5	0.2676	0.2666	0.2725	**0.2632**
	2	**0**	1.8470	1.8277	1.8583	**1.8224**
		1	1.4687	1.4460	1.4830	**1.4435**
		2	1.3095	1.2896	1.3269	**1.2675**
		5	1.1450	1.1312	1.1576	**1.0829**
2[b]	**10**	**0**	0.0719	0.0717	0.0719	**0.0722**
		1	0.0550	0.0549	0.0558	**0.0553**
		2	0.0499	0.0498	0.0511	**0.0501**
		5	0.0471	0.0470	0.0480	**0.0472**
	5	**0**	0.2713	0.2705	0.2718	**0.2721**
		1	0.2088	0.2081	0.2119	**0.2094**
		2	0.1888	0.1882	0.1930	**0.1888**
		5	0.1754	0.1750	0.1788	**0.1743**
	2	**0**	0.9570	1.2910	1.3086	**1.2943**
		1	0.7937	1.0137	1.0378	**1.0172**
		2	0.7149	0.9067	0.9322	**0.8988**
		5	0.6168	0.8064	0.8250	**0.7824**

[a] 576 elements [b] 288 elements

6.2.3.4 The effects of different parameters on the fundamental frequency $\bar{\omega}$ of an Al/Al_2O_3 square plate

In this section, the dimensionless fundamental frequencies $\bar{\omega}$ of an Al/Al_2O_3 plates are determined to show the effect of some parameters like side-to-thickness ratio, power-law index, aspect ratio and boundary conditions on the vibrational behavior of FG plates. The obtained results using the present finite element with a 24 × 24 mesh size are listed in Table 6.16 and plotted in Figures 6.18 and 6.19.

Table 6.16 presents the dimensionless fundamental frequency $\bar{\omega}$ for square FG plate with different boundary conditions for various values of power-law index *p* and side-to-thickness

ratio. Figure 6.18 depicts the variation of the dimensionless frequency $\bar{\omega}$ versus side-to-thickness ratio L/h for square FG plate with different boundary conditions and p=2.

The variation of the dimensionless frequency versus power-law index p is sown in Figure 6.19 for square FG plate (L/h=5) with different boundary conditions. It can be seen from Table 6.16 and Figure 6.18 that the increase of the side-to-thickness ratio results in an increase in the dimensionless frequency, this is probably due to the effects of shear deformation as indicated by [163]. It is also observed from Table 6.16 and Figure 6.19 that increasing the power-law index leads to a reduction of the dimensionless frequency. This is due to the fact that increasing the power-law index increases the volume fraction of metal which reduce the FG plate bending stiffness.

Table 6.16 Dimensionless fundamental frequency $\bar{\omega}$ of Al/Al_2O_3 square plates.

L/h	***p***	**Boundary conditions**						
		CCCC	**SCSC**	**SSSC**	**SSSS**	**SFSC**	**SFSS**	**SFSF**
5	**0**	8.0511	6.7836	5.9747	5.2889	3.4447	3.2437	2.7242
	1	6.3451	5.3189	4.6459	4.0845	2.6558	2.4952	2.0931
	2	5.6174	4.7243	4.1514	3.6683	2.3897	2.2493	1.8896
	5	4.8888	4.1616	3.7281	3.3496	2.1957	2.0785	1.7532
	10	4.6219	3.9498	3.5572	3.2111	2.1089	1.9995	1.6881
10	**0**	9.8818	8.0981	6.7919	5.7799	3.7152	3.4494	2.8636
	1	7.6376	6.2442	5.2170	4.4273	2.8456	2.6396	2.1901
	2	6.8712	5.6277	4.7155	4.0103	2.5785	2.3936	1.9872
	5	6.2861	5.1801	4.3848	3.7576	2.4185	2.2510	1.8721
	10	6.0243	4.9735	4.2230	3.6273	2.3353	2.1752	1.8099
20	**0**	10.6329	8.6000	7.0711	5.9311	3.8061	3.5147	2.9050
	1	8.1466	6.5836	5.4068	4.5313	2.9084	2.6849	2.2186
	2	7.3840	5.9712	4.9082	4.1162	2.6418	2.4394	2.0162
	5	6.9241	5.6123	4.6287	3.8908	2.4966	2.3074	1.9084
	10	6.6830	5.4208	4.4754	3.7648	2.4154	2.2330	1.8473
50	**0**	10.8873	8.7628	7.1577	5.9760	3.8382	3.5371	2.9181
	1	8.3155	6.6919	5.4650	4.5621	2.9304	2.7003	2.2276
	2	7.5573	6.0824	4.9680	4.1477	2.6641	2.4550	2.0254
	5	7.1527	5.7693	4.7069	3.9313	2.5246	2.3269	1.9201
	10	6.9229	5.5751	4.5572	3.8068	2.4444	2.2532	1.8593
100	**0**	10.9257	8.7870	7.1703	5.9824	3.8436	3.5408	2.9201
	1	8.3408	6.7078	5.4734	4.5665	2.9339	2.7027	2.2289
	2	7.5834	6.0989	4.9767	4.1522	2.6677	2.4576	2.0268
	5	7.1880	5.7815	4.7185	3.9372	2.5294	2.3303	1.9219
	10	6.9602	5.5985	4.5693	3.8128	2.4495	2.2567	1.8612

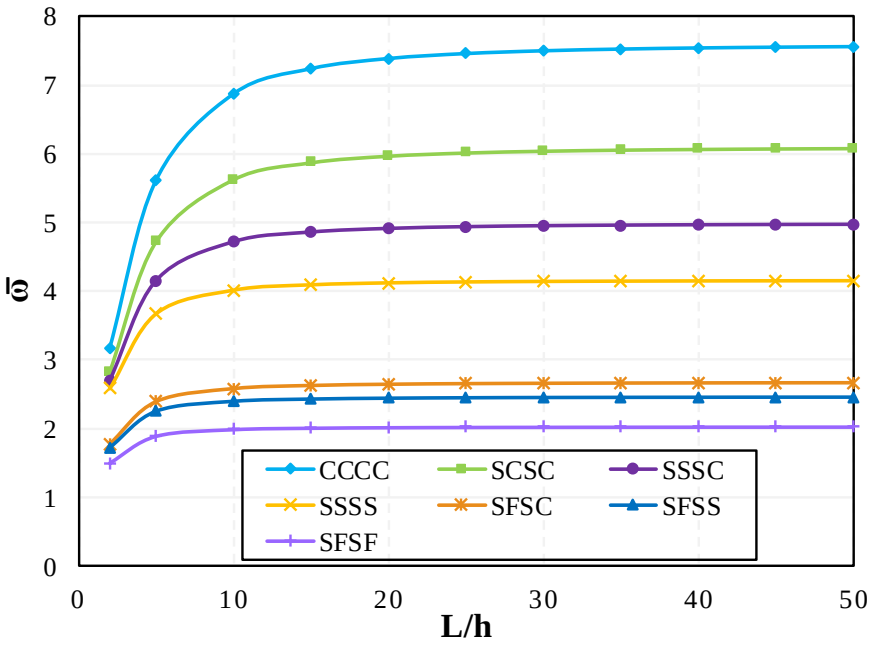

Figure 6.18 The effect of side-to-thickness ratio L/h on the dimensionless frequency $\bar{\omega}$ for FG square plate with different boundary conditions and p=2.

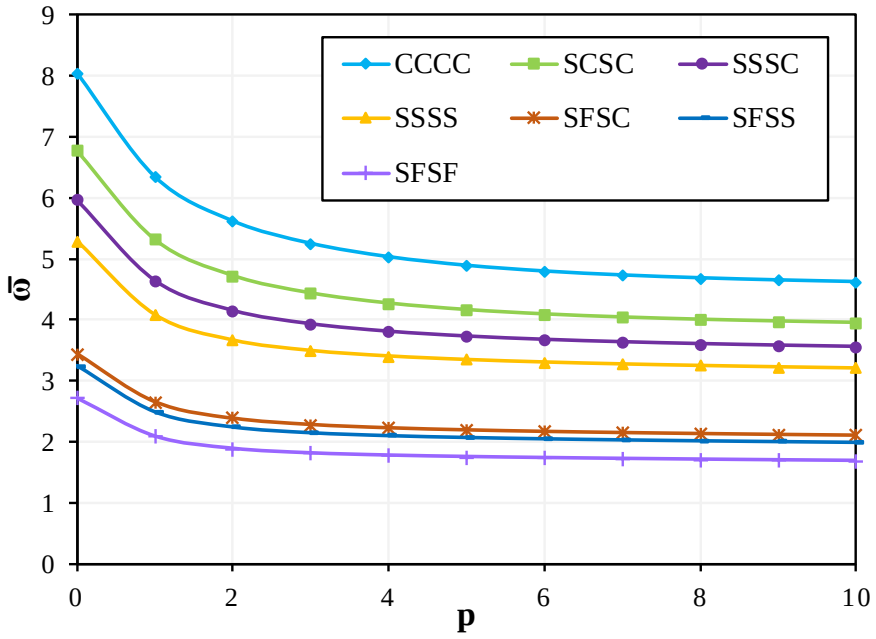

Figure 6.19 The effect of power-law index p on the dimensionless frequency $\bar{\omega}$ for square FG plate (L/h=5) with different boundary conditions.

It can be also noticed from the above mentioned table and figures that the dimensionless frequency increases with the increasing constraints at the edges of plates. This behavior is due to the fact that higher constraints at the edges increase the bending stiffness of the plate, resulting in higher vibrational responses.

Figure 6.20 shows the variation of the dimensionless fundamental frequency $\bar{\omega}$ for SSSS rectangular FG plate (L/h=5) with different values of the power-law index p with respect to the aspect ratio l/L. From this figure, it can be seen that with a particular power-law index p, the dimensionless fundamental frequency decreases as aspect ratio l/L increases.

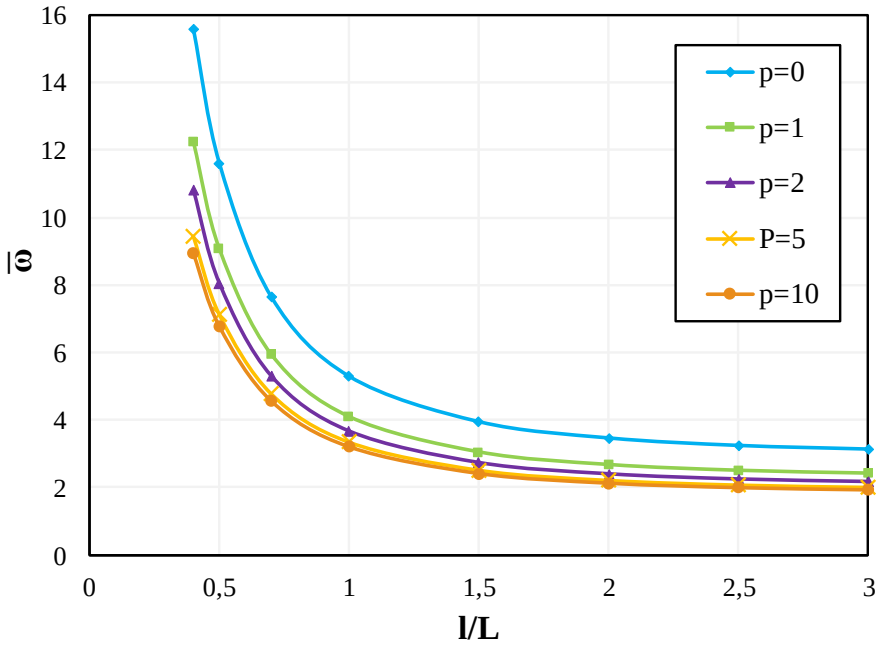

Figure 6.20 The effect of aspect ratio l/L on the dimensionless frequency $\bar{\omega}$ for SSSS FG rectangular plate (L/h=5).

6.3 Conclusion

By using the present finite element (R4SSDT), numerical results of the static, mechanical buckling and free vibration analysis of FG single layer plates have been presented in this chapter. The obtained results in terms of deflection, stresses, critical loads and frequencies were in good agreement with those available in the literature which confirms the performance of the present element. The effects of some parameters like as power-law index, boundary conditions, aspect and side-to-thickness ratios on the behaviors of the FG plates, have been also investigated and discussed in detail. Some of the important observations can be concluded from this work in the following points

- The present results show that the developed finite element R4SSDT can well predict the static, stability and vibration responses of FG single layer plates.
- The dimensionless deflection decreases by increasing the side-to-thickness ratio whereas it increases with the increasing of power-law values.
- The dimensionless critical buckling loads and frequencies increase as the side-to thickness ratio and the boundary constraints increase and they decrease as the power-law index and aspect ratio increase.
- The dimensionless critical buckling load of plate subjected to uniaxial compression loading is greater than that subjected to bi-axial compression and less than those subjected to bi-axial compression and tension loads.
- The critical buckling modes change by the increase of the aspect ratio l/L in the case of uniaxial compression loading. While, in the case of biaxial compression loading the plate buckles with only one mode whatever the aspect ratio.

General conclusion

Despite their advantages, conventional composite materials suffer from discontinuity of material properties at the interfaces of the layers and constituents of the composite. As a result, the stress fields in these regions create interface problems and stress concentrations, especially in a high temperature environment. As well, large plastic deformation of the interface may trigger the initiation and propagation of cracks that lead to ultimate failure of the composite. These problems can be decreased by gradually changing the volume fraction of constituent materials and tailoring the material for the desired application, as in Functionally Graded Materials (FGMs).

FGMs are advanced composites with varying composition, microstructure and properties, usually in the thickness direction. They represent a rapidly evolving field in science and engineering with many practical applications. Research needs in this area are particularly numerous and varied, FGMs promise significant potential benefits that justify the need for significant efforts. The design and development of these materials requires the development of analysis tools adapted to their geometric and material specificities.

Application of 3D analysis, in general, is quite cumbersome while dealing with complex loading and boundary conditions. Hence, the analysis of FG plates are carried out numerically as well as analytically using 2D plate theories. Classical Plate Theory (CPT) is the simplest model which is suitable for thin plates where the transverse shear effects are neglected. For improving the limitations of CPT, the first-order shear deformation theory (FSDT) was proposed. FSDT is suitable for moderately thick to thin plates. Herein, the FSDT shear stresses need to be justified by shear correction factors (SCFs) to tune for the shear energy. As known, the choice of SCFs is a problem dependent. To avoid this difficulty, higher- order shear deformation theories were developed. In the HSDT, the transverse shear stresses are more

correctly approximated throughout the thickness and consequently no shear correction factors are needed.

The principal objective of this work is to contribute to the modeling of the static, stability and dynamic behaviors of plates made of functionally graded materials, by developing finite elements capable of accurately describing such behaviors. First, an FSDT-based finite element has been adapted to the analysis of FG single layer and sandwich plates. The element is geometrically simple and has only four nodes and five degrees of freedom per node. Secondly, a new trigonometric model has been proposed for the analysis of FG plates behaviors. On the basis of this new model, a four-node rectangular finite element with five degrees of freedom per node, has been developed, providing a better compromise between accuracy and low cost. Furthermore, the effects of different parameters on the static, buckling and free vibration responses of FG plates, including the power-law index, side-to-thickness ratio, etc have been investigated.

In the first part of the thesis, an overview on FGMs have been presented. The most commonly used plate theories for the analysis and modeling of FG plates have been briefly described in chapter two. A review of various research in the existing literature on static, vibration, and buckling analysis of FG plates has been also presented. It has been seen that the studies carried out by finite elements on the topic are even less numerous compared to those carried out analytically.

In the second part, a four-node rectangular finite element (R4FSDT) with five degrees of freedom per node, based on FSDT, previously developed for the analysis of angle-ply laminated composite, has been adapted for the analysis of various behaviors of FG plates. The von Karman strain tensor has been used to account for the second order effect (Buckling). The concept of the neutral surface position has been introduced to simplify the problem and to avoid the membrane–bending coupling. The total potential energy and Hamilton's principles and Lagrangian equation have been used for the derivation of stiffness, geometrical and mass matrices. The assumed natural shear strain technique has been introduced to ensure the effectiveness of the element against the shear locking phenomenon. The performance and reliability of the developed element (R4FSDT) have been evaluated through a series of applications in static, buckling and free vibration of FG single layer and sandwich plates with different loading cases, geometry, etc.

In the third part, a new trigonometric model with five unknowns has been proposed for the analysis of FG plates behaviors. The model accounts for a sinusoidal variation of the transverse shear strains across the thickness and satisfies the shear stress-free boundary conditions on the top and bottom surfaces of the plate with no requirement for a shear correction factor. Based on this model a new finite element R4SSDT has been formulated in the same manner as the first element R4FSDT. The developed finite element has been used to analyze the static, buckling and dynamic behaviors of FG single layer plates. For the purpose of validation of the element, the obtained results in terms of deflection, normal and shear stresses, critical loads and natural frequencies have been compared with those existing in the available literature. All the comparisons show that the results obtained with the present element and those of the references are in good agreement, confirming the performance and accuracy of the present formulation. Furthermore, for the sake of comparison, the present results obtained using the R4SSDT have been also compared with those obtained using the R4FSDT.It has been seen, that the R4SSDT results are more accurate than those of R4FSDT.

In addition, the effects of some parameters such as power-law index, side-to-thickness ratio, etc on the static, buckling and free vibration responses of FG plates has been also shown.

In the following, some of the important observations can be concluded from this work:

- The present results show that the developed finite elements R4FSDT and R4SSDT can well predict the static, stability and vibration responses of FG single layer and sandwich plates.
- The obtained results using the R4FSDT reiterate that FSDT may be well suited to simpler geometries and moderately thick plates.
- The shear correction factor has a slight influence on the dimensionless deflections and natural frequency while it has no effect on the dimensionless normal stresses values. The shear correction factor has almost no effect on the dimensionless deflection in case of thin plates.
- In the case of FG single layer plates, the dimensionless deflection decreases by increasing the side-to-thickness ratio whereas it increases with the increasing of power-law values.
- In the case of a sandwich plate with a ceramic core, the dimensionless deflection increases as the power-law index increases and decreases as the core thickness increases. The opposite has been observed for the homogeneous metallic core.

- For sandwich plate with either ceramic or metallic core the dimensionless deflection increases with the increase of side-to-thickness ratio L/h.
- The dimensionless critical buckling loads and natural frequencies decrease for sandwich plate with homogeneous ceramic core with the increase of the power-law index, whereas they increase for sandwich plate with homogeneous metallic core.
- The dimensionless critical buckling loads and natural frequencies increase for sandwich plate with homogeneous ceramic core as the core thickness, with respect to the total thickness of the plate increases, while they decrease for sandwich plate with homogeneous metallic core.
- The dimensionless critical buckling loads and frequencies of FG single layer plate increase as the side-to thickness ratio and the boundary constraints increase and they decrease as the power-law index and aspect ratio increase.
- The dimensionless critical buckling load of plate subjected to uniaxial compression loading is greater than that subjected to bi-axial compression and less than those subjected to bi-axial compression and tension loads.
- The critical buckling modes change by the increase of the aspect ratio l/L in the case of uniaxial compression loading. While, in the case of biaxial compression loading the plate buckles with only one mode whatever the aspect ratio.

Perspectives

In perspective, it is planned to apply the R4SSDT element for the analysis of thermal buckling response of FG plates and to analyze the static, dynamic and stability behaviors of FG sandwich plates.

It is also planned to use the trigonometric model for the analysis of various forms of thin and thick FG structures behaviors.

Finally, this doctoral research work is part of the contribution of **LGEM** and **MN2I2S** laboratories in the development of new theories, finite elements for the analysis of FG structures behaviors.

Bibliography

[1] F. Ebrahimi, Advances in Functionally Graded Materials and Structures. (INTECH Open, Croatia, 2016).

[2] S. Somiya (2013). Handbook of advanced ceramics: materials, applications, processing, and properties. Academic press.

[3] Y. Miyamoto, W. A. Kaysser, B. H. Rabin, A. Kawasaki, R. G. Ford (Eds.), Functionally Graded Materials: design, processing and applications. (Springer US, Boston (MA), 1999).

[4] Y. Watanabe, H. Sato (2011). Review fabrication of functionally graded materials under a centrifugal force. In Nanocomposites with unique properties and applications in medicine and industry, 133-150.

[5] R. M. Mahamood, E. T. Akinlabi (2017). Introduction to functionally graded materials. In Functionally Graded Materials, 1-8. Springer, Cham.

[6] Koizumi, M. F. G. M. (1997). FGM activities in Japan. Composites Part B: Engineering, 28(1-2), 1-4.

[7] Koizumi, M., Niino, M.: Overview of FGM research in Japan. MRS Bull. 20(1995), 19–24(1995)

[8] G. E. Knoppers, J. W. Gunnink, J. Van Den Hout, W. Van Vliet, (2005). The reality of functionally graded material products. In Intelligent Production Machines and Systems: First I* PROMS Virtual Conference, 467-474. Elsevier, Amsterdam.

[9] R. Mahamood, TC Jen, S. Akinlabi, S. Hassan, M. Shatalov, E. Murashkin, E. Akinlabi. (2021) Functionally Graded Materials: An Introduction. In Functionally Graded Materials (FGMs) Fabrication, Properties, Applications, and Advancements, 1-10. CRC Press.

[10] B. Saleh, J. Jiang, A. Ma, D. Song, D. Yang, Q. Xu (2020). Review on the influence of different reinforcements on the microstructure and wear behavior of functionally graded aluminum matrix composites by centrifugal casting. Metals and Materials International, 26(7), 933-960.

[11] I. E. Elishakoff, D. Pentaras, C. Gentilini (2015). Mechanics of functionally graded material structures. World Scientific.

[12] S. K. Sarangi (2021). Modeling and Analysis of Smart Functionally Graded Structures. In Functionally Graded Materials (FGMs), 139-168. CRC Press.

[13] Z. Liu, M. A. Meyers, Z. Zhang, R. O. Ritchie (2017). Functional gradients and heterogeneities in biological materials: Design principles, functions, and bioinspired applications. Progress in Materials Science, 88, 467-498.

[14] C. Zhang, F. Chen, Z. Huang, M. Jia, G. Chen, Y. Ye, ..., E. J. Lavernia (2019). Additive manufacturing of functionally graded materials: A review. Materials Science and Engineering: A, 764, 138209.

[15] D. K. Jha, T. Kant, R. K. Singh (2013). A critical review of recent research on functionally graded plates. Composite Structures, 96, 833-849.

[16] M. B. Bever, P. E. Duwez (1970). On Gradient Composites. Preliminary Reports, Memoranda and Technical Notes of the ARPA Materials Summer Conference, 117–140.

[17] M. Shen, M.B. Bever (1972). Gradients in polymeric materials. J. Mater. Sci, 7 (7), 741-746.

[18] P. G. Koppad, M. R. Ramesh, S. Joladarashi, S. T. Aruna, N. C. Reddy, C. Siddaraju (2021). Gaseous Phase Processing Techniques for Functionally Graded Materials. In Functionally Graded Materials (FGMs): Fabrication, Properties, Applications, and Advancements, 49-71. CRC Press.

[19] K. Ichikawa (Ed.). (2001). Functionally graded materials in the 21st century: a workshop on trends and forecasts. Springer Science & Business Media.

[20] N. Zhang, T. Khan, H. Guo, S. Shi, W. Zhong, W. Zhang (2019). Functionally graded materials: an overview of stability, buckling, and free vibration analysis. Advances in Materials Science and Engineering.

[21] B. Saleh, J. Jiang, R. Fathi, T. Al-hababi, Q. Xu, L. Wang, ..., A. Ma (2020). 30 Years of functionally graded materials: An overview of manufacturing methods, Applications and Future Challenges. Composites Part B: Engineering, 108376.

[22] M. Sato, A. Inoue, H. Shima (2017) Bamboo-inspired optimal design for functionally graded hollow cylinders. PLoS ONE 12, 1–14.

[23] A.K. Ray, S.K. Das, S. Mondal, P. Ramachandrarao (2004). Microstructural characterization of bamboo. J. Mater. Sci, 39(3), 1055–1060.

[24] D. Hon, W. Shiraishi (2001). Cellulose Chemistry, 2nd ed. Marcel Dekker, New York.

[25] P.F. Wilkinson, R. Millington (2009). Skin (Digitally Printed Version ed.). Cambridge University Press, Cambridge, 49–50.

[26] R. M. Mahamood, E. T. Akinlabi, M. Shukla, S. Pityana (2012). Functionally Graded Material, An Overview. Proceedings of the World Congress on Engineering, III, London, U.K.

[27] V. Cannillo, L. Lusvarghi, T. Manfredini, M. Montorsi, C. Siligardi, A. Sola (2007). Glass-alumina functionally graded materials produced by plasma spraying. In Key Engineering Materials, 333, 227-230. Trans Tech Publications Ltd.

[28] S. A. Lajevardi, T. Shahrabi, J. A. Szpunar (2013). Synthesis of functionally graded nano Al2O3–Ni composite coating by pulse electrodeposition. Applied Surface Science, 279, 180-188.

[29] S. Put, J. Vleugels, O. Van der Biest (2001). Functionally graded WC–Co materials produced by electrophoretic deposition. Scripta materialia, 45(10), 1139-1145.

[30] G.S. Was, J.W. Jones, C. E. Kalnas, L.J. Parfitt, M. Goldiner (1994). Role of ion beam assisted deposition in the synthesis and fracture of metal-ceramic multilayers. Surf Coat Technol, 65(1-3): 77-83.

[31] A. L. Dumont, J. P. Bonnet, T. Chartier, J. M. Ferreira (2001). MoSi2/Al2O3 FGM: elaboration by tape casting and SHS. Journal of the European Ceramic Society, 21(13), 2353-2360.

[32] A. Shahrjerdi, F. Mustapha, M. Bayat, S. M. Sapuan, D. L. A. Majid (2011). Fabrication of functionally graded hydroxyapatite-titanium by applying optimal sintering procedure and powder metallurgy. International Journal of Physical Sciences, 6(9), 2258-2267.

[33] Y. Watanabe, N. Yamanaka, Y. Fukui (1998). Control of composition gradient in a metal-ceramic functionally graded material manufactured by the centrifugal method. Composites Part A: Applied Science and Manufacturing, 29(5-6), 595-601.

[34] T. Katayama, S. Sukenaga, N. Saito, H. Kagata, K. Nakashima (2011). Fabrication of Al2O3-W functionally graded materials by slip casting method. In 3rd International Congress on Ceramics, ICC 2011, IOP Conference Series: Materials Science and Engineering, Osaka; Japan.

[35] J.G. Yeo, Y.G. Jung, S.C. Choi (1998). Design and microstructure of ZrO2/SUS316 functionally graded materials by tape casting. Mater. Lett, 37 (6) 304–311.

[36] R.M. Mahamood, E.T. Akinlabi, M. Shukla, S. Pityana (2014). Evolutionary additive manufacturing: an overview. Lasers in Engineering 27, 161–178.

[37] A. Saiyathibrahim, M. S. S. Nazirudeen, P. Dhanapala (2015). Processing techniques of functionally graded materials—a review. In International Conference on Systems, Science, Control, Communication, Engineering and Technology 1, 98-105.

[38] Y. Lian, X. Liu, Z. Xu, J. Song, Y. Yu (2013). Preparation and properties of CVD-W coated W/Cu FGM mock-ups. Fusion Engineering and Design, 88(9-10), 1694-1698.

[39] J. F. Groves, H. N. G. Wadley (1997). Functionally graded materials synthesis via low vacuum directed vapor deposition. Composites Part B: Engineering, 28(1-2), 57-69.

[40] I. M. El-Galy, B. I. Saleh, M. H. Ahmed (2019). Functionally graded materials classifications and development trends from industrial point of view. SN Applied Sciences, 1(11), 1-23.

[41] A. Kawasaki, R. Watanabe (1997). Concept and P/M fabrication of functionally gradient materials. Ceramics international, 23(1), 73-83.

[42] Y. Watanabe, H. Sato, E. Miura-Fujiwara (2015). Functionally graded metallic biomaterials. In Advances in Metallic Biomaterials, 181-209. Springer, Berlin, Heidelberg.

[43] A. Gupta, M. Talha (2015). Recent development in modeling and analysis of functionally graded materials and structures. Progress in Aerospace Sciences, 79, 1–14.

[44] R. M. Mahamood (2018). Introduction to Laser Metal Deposition Process. In Laser Metal Deposition Process of Metals, Alloys, and Composite Materials, 1-9. Springer, Cham.

[45] G. H. Loh, E. Pei, D. Harrison, M. D. Monzón (2018). An overview of functionally graded additive manufacturing. Additive Manufacturing, 23, 34-44.

[46] A. Miteva, A. Bouzekova-Penkova (2021). Some aerospace applications of functionally graded materials. DOI: https://doi.org/10.3897/arb.v33.e14.

[47] L. Marin (2005). Numerical solution of the Cauchy problem for steady-state heat transfer in two dimensional functionally graded materials. Int. J. Solids Struct, 42(15), 4338-4351.

[48] G. Udupa, S. Shrikantha Rao, K.V. Gangadharan (2012). Future applications of carbon nanotube reinforced functionally graded composite materials. In IEEE-International Conference On Advances in Engineering, Science and Management (ICAESM -2012).

[49] S. Matsuo, F. Watari, N. Ohata (2001). Fabrication of a functionally graded dental composite resin post and core by laser lithography and finite element analysis of its stress relaxation effect on tooth root. Dental materials journal, 20(4), 257-274.

[50] F. Watari, A. Yokoyama, M. Omori, T. Hirai, H. Kondo, M. Uo, T. Kawasaki (2004). Biocompatibility of materials and development to functionally graded implant for bio-medical application. Composites Science and Technology, 64(6), 893-908.

[51] A. Sadollah, A. Bahreininejad, H. Eskandar, M. Hamdi (2013). Optimum material gradient for functionally graded dental implant using particle swarm optimization. In Advanced Materials Research. Trans Tech Publications Ltd. Vol. 647, 30-36.

[52] W. W. Chen, A. M. Rajendran, B. Song, X. Nie (2007). Dynamic fracture of ceramics in armor applications. Journal of the American Ceramic Society, 90(4), 1005-1018.

[53] M. Niino, K. Kisara, M. Mori (2005). Feasibility study of FGM technology in space solar power systems (SSPS). In Materials Science Forum, 492, 163-170. Trans Tech Publications Ltd.

[54] E. Müller, Č. Drašar, J. Schilz, W.A. Kaysser (2003). Functionally graded materials for sensor and energy applications. Materials Science and Engineering: Part A, 362(1), 17–39.

[55] R. M. Mahamood, E. T. Akinlabi (2017). Types of functionally graded materials and their areas of application. In Functionally graded materials, 9-21. Springer, Cham.

[56] P.M. Pandey, S. Rathee, M. Srivastava, P.K. Jain (2021). Functionally Graded Materials (FGMs): Fabrication, Properties, Applications, and Advancements (1st ed.). CRC Press.

[57] M. Herrmann, W. Sobek (2017). Functionally graded concrete: Numerical design methods and experimental tests of mass-optimized structural components. Structural Concrete, 18(1), 54-66.

[58] J. H. Kim, G. H. Paulino (2003). An accurate scheme for mixed-mode fracture analysis of functionally graded materials using the interaction integral and micromechanics models. International Journal for Numerical Methods in Engineering, 58(10), 1457-1497.

[59] A. R. Nemati, M. J. Mahmoodabadi (2020). Effect of micromechanical models on stability of functionally graded conical panels resting on Winkler–Pasternak foundation in various thermal environments. Archive of Applied Mechanics, 90(5), 883-915.

[60] W. Voigt (1889). Ueber die Beziehung zwischen den beiden Elasticitätsconstanten isotroper Körper. Annalen der physik, 274(12), 573-587.

[61] A. Reuss (1929). Berechnung der fließgrenze von mischkristallen auf grund der plastizitätsbedingung für einkristalle. ZAMM-Journal of Applied Mathematics and Mechanics/Zeitschrift für Angewandte Mathematik und Mechanik, 9(1), 49-58.

[62] Z. Hashin (1960). The elastic moduli of heterogeneous materials. HARVARD UNIV CAMBRIDGE MA.

[63] Z. Hashin, S. Shtrikman (1963). A variational approach to the theory of the elastic behavior of multiphase materials. Journal of the Mechanics and Physics of Solids, 11(2), 127-140.

[64] T. Mori, K. Tanaka (1973). Average stress in matrix and average elastic energy of materials with misfitting inclusions. Acta metallurgica, 21(5), 571-574.

[65] R. Hill (1965). A self-consistent mechanics of composite materials. Journal of the Mechanics and Physics of Solids, 13(4), 213-222.

[66] R. M. Christensen, K. Lo (1979). Solutions for effective shear properties in three phase sphere and cylinder models. Journal of the Mechanics and Physics of Solids, 27(4), 315-330.

[67] K. Wakashima, H. Tsukamoto (1991). Mean-field micromechanics model and its application to the analysis of thermomechanical behavior of composite materials. Materials Science and Engineering: A, 146(1-2), 291-316.

[68] J. C. Halpin (1969). Effects of Environmental Factors on Composite Materials. Air Force Materials Lab Wright-Patterson AFB OH.

[69] I. Tamura (1973). Strength and ductility of Fe-Ni-C alloys composed of austenite and martensite with various strength. In Proceedings of the third international conference on strength of metals and alloys, 1, 611-615. Cambridge, Institute of Metals.

[70] M. M. Gasik (1998). Micromechanical modelling of functionally graded materials. Computational Materials Science, 13(1-3), 42-55.

[71] J. R. Zuiker (1995). Functionally graded materials: choice of micromechanics model and limitations in property variation. Composites Engineering, 5(7), 807-819.

[72] T. Reiter, G. J. Dvorak (1998). Micromechanical modeling of functionally graded materials. In IUTAM Symposium on Transformation Problems in Composite and Active Materials (pp. 173-184). Springer, Dordrecht.

[73] B. Klusemann, B. J. T. M. Svendsen (2010). Homogenization methods for multi-phase elastic composites: Comparisons and benchmarks. Technische Mechanik-European Journal of Engineering Mechanics, 30(4), 374-386.

[74] B. Karami, D. Shahsavari, M. Janghorban, L. Li (2019). Influence of homogenization schemes on vibration of functionally graded curved microbeams. Composite Structures, 216, 67-79.

[75] Y. Benveniste (1987). A new approach to the application of Mori-Tanaka's theory in composite materials. Mechanics of materials, 6(2), 147-157.

[76] K. Wakashima, T. Hirano, M. Niino (1990). Functionally Gradient Materials(Fgm) Architecture: A New Type of Ceramic-Metal Assemblage Designed for Hot Structural Components.

[77] S. Suresh, A. Mortensen (1998). Fundamentals of functionally graded materials. 1sted. London: IOM Communications.

[78] S. H. Chi, Y. L. Chung (2006). Mechanical behavior of functionally graded material plates under transverse load—Part I: Analysis. International Journal of Solids and Structures, 43(13), 3657-3674.

[79] S. H. Chi, Y. L.Chung (2002). Cracking in sigmoid functionally graded coating. J Mech, 18(2002), 41-53.

[80] J. H. Kim, G. H. Paulino (2002). Finite element evaluation of mixed mode stress intensity factors in functionally graded materials. International Journal for Numerical Methods in Engineering, 53(8), 1903-1935.

[81] C. Zhang, A. Savaidis, G. Savaidis, H. Zhu (2003). Transient dynamic analysis of a cracked functionally graded material by a BIEM. Computational materials science, 26, 167-174.

[82] F. Delale, F. Erdogan (1983). The crack problem for a nonhomogeneous plane. ASME Journal of Applied Mechanics 50, 609–614.

[83] E. H. Love (2013). A treatise on the mathematical theory of elasticity. Cambridge university press.

[84] G. Kirchhoff (1850). Über das Gleichgewicht und die Bewegung einer elastischen Scheibe. Journal für die reine und angewandte Mathematik (Crelles Journal), 1850(40), 51-88.

[85] J. N. Reddy (2003). Mechanics of laminated composite plates and shells: theory and analysis. CRC press.

[86] J. N. Reddy (2006). Theory and analysis of elastic plates and shells. CRC press.

[87] E. Reissner (1945). The effect of transverse shear deformation on the bending of elastic plates.

[88] R. Mindlin (1951). Influence of rotary inertia and shear on flexural motions of isotropic. elastic plates. J. of Appl. Mech, 18(1), 31-38.

[89] R. Khandan, S. Noroozi, P. Sewell, J. Vinney (2012). The development of laminated composite plate theories: a review. Journal of Materials Science, 47(16), 5901-5910.

[90] Y.-Y. Yu (1959). Simple thickness-shear modes of vibration of infinite sandwich plates. ASME Journal of Applied Mechanics, 26, 679–681.

[91] T. S. Chow (1971). On the propagation of flexural waves in an orthotropic laminated plate and its response to an impulsive load. Journal of Composite Materials, 5(3), 306-319.

[92] J.M. Whitney (1973). Shear correction factors for orthotropic laminates under shear load. ASME Journal of Applied Mechanics, 40, 302–304.

[93] J. M. Whitney (1972). Stress analysis of thick laminated composite and sandwich plates. Journal of Composite materials, 6(3), 426-440.

[94] A. K. Noor, J. M. Peters (1989). A posteriori estimates for the shear correction factors in multi-layered composite cylinders. Journal of engineering mechanics, 115(6), 1225-1244.

[95] A. K. Noor, W. S. Burton, J. M. Peters (1990). Predictor-corrector procedures for stress and free vibration analyses of multilayered composite plates and shells. Computer Methods in Applied Mechanics and Engineering, 82(1-3), 341-363.

[96] T. K. Nguyen, K. Sab, G. Bonnet (2006). A Reissner-Mindlin Plate Model for Functionally Graded Materials. In III European Conference on Computational Mechanics (pp. 564-564). Springer, Dordrecht.

[97] E. Efraim, M. Eisenberger (2007). Exact vibration analysis of variable thickness thick annular isotropic and FGM plates. Journal of Sound and Vibration, 299(4-5), 720-738.

[98] T. K. Nguyen, K. Sab, G. Bonnet (2007). Shear correction factors for functionally graded plates. Mechanics of Advanced Materials and Structures, 14(8), 567-575.

[99] T. K. Nguyen, K. Sab, G. Bonnet (2008). First-order shear deformation plate models for functionally graded materials. Composite Structures, 83(1), 25-36.

[100] S. Hosseini-Hashemi, H. R. D. Taher, H. Akhavan, M. Omidi (2010). Free vibration of functionally graded rectangular plates using first-order shear deformation plate theory. Applied Mathematical Modelling, 34(5), 1276-1291.

[101] E. Reissner (1963). On the derivation of boundary conditions for plate theory. Proceedings of the Royal Society of London. Series A. Mathematical and Physical Sciences, 276(1365), 178-186.

[102] K. H. Lo, R. M. Christensen, E. M. Wu (1977). A High-Order Theory of Plate Deformation, Part-1: Homogeneous Plates. ASME Journal of Applied Mechanics, 44, 663–668.

[103] K. H. Lo, R. M. Christensen, E. M. Wu (1977). A High-Order Theory of Plate Deformation, Part-2: Laminated Plates. ASME Journal of Applied Mechanics, 44, 669–676.

[104] M. Levinson (1980). An accurate, simple theory of the statics and dynamics of elastic plates. Mechanics Research Communications, 7(6), 343-350.

[105] M. V. V. Murthy (1981). An Improved Transverse Shear Deformation Theory for Laminated Anisotropic plates. NASA Tech. Paper 1903, 1–37.

[106] J. N. Reddy (1984a). A Simple Higher Order Theory for Laminated Composite Plates. ASME Journal of Applied Mechanics, 51, 745–752.

[107] T. A. R. U. N. Kant, K. Swaminathan (2002). Analytical solutions for the static analysis of laminated composite and sandwich plates based on a higher order refined theory. Composite structures, 56(4), 329-344.

[108] Y. M. Ghugal, R. P. Shimpi (2002). A review of refined shear deformation theories of isotropic and anisotropic laminated plates. Journal of Reinforced Plastics and Composites, 21(9), 775-813.

[109] J. M. Whitney, C. T. Sun (1973). A higher order theory for extensional motion of laminated composites. Journal of Sound and Vibration, 30(1), 85-97.

[110] M. Touratier (1991). An efficient standard plate theory. International journal of engineering science, 29(8), 901-916.

[111] K. P. Soldatos (1992). A transverse shear deformation theory for homogeneous monoclinic plates. Acta Mechanica, 94(3), 195-220.

[112] M. Karama, K. S. Afaq, S. Mistou (2003). Mechanical behaviour of laminated composite beam by the new multi-layered laminated composite structures model with transverse shear stress continuity. International Journal of solids and structures, 40(6), 1525-1546.

[113] Shimpi, R. P. (2002). Refined plate theory and its variants. AIAA journal, 40(1), 137-146.

[114] H. T. Thai, S. E. Kim (2013). A simple quasi-3D sinusoidal shear deformation theory for functionally graded plates. Composite Structures, 99, 172-180.

[115] J. N. Reddy, Z. Q. Cheng (2001). Three-dimensional thermomechanical deformations of functionally graded rectangular plates. European Journal of Mechanics-A/Solids, 20(5), 841-855.

[116] S. S. Vel, R. C. Batra (2002). Exact solution for thermoelastic deformations of functionally graded thick rectangular plates. AIAA journal, 40(7), 1421-1433.

[117] E. Pan (2003). Exact solution for functionally graded anisotropic elastic composite laminates. Journal of Composite Materials, 37(21), 1903-1920.

[118] N. J. Pagano (1970). Exact solutions for rectangular bidirectional composites and sandwich plates. Journal of composite materials, 4(1), 20-34.

[119] I. Elishakoff, C. Gentilini (2005). Three-dimensional flexure of rectangular plates made of functionally graded materials. ASME J Appl Mech 72, 788–791

[120] M. Kashtalyan (2004). Three-dimensional elasticity solution for bending of functionally graded rectangular plates. European Journal of Mechanics-A/Solids, 23(5), 853-864.

[121] B. Woodward, M. Kashtalyan (2011). Three-dimensional elasticity solution for bending of transversely isotropic functionally graded plates. European Journal of Mechanics-A/Solids, 30(5), 705-718.

[122] M. Kashtalyan, M. Menshykova (2009). Three-dimensional elasticity solution for sandwich panels with a functionally graded core. Composite structures, 87(1), 36-43.

[123] B. Woodward, M. Kashtalyan (2011). 3D elasticity analysis of sandwich panels with graded core under distributed and concentrated loadings. International journal of mechanical sciences, 53(10), 872-885.

[124] M. Gholami, A. Hassani, S. S. Mousavi, R. A. Alashti (2019). Bending analysis of anisotropic functionally graded plates based on three-dimensional elasticity. European Journal of Computational Mechanics, 1-25.

[125] S. H. Chi, Y. L. Chung (2006). Mechanical behavior of functionally graded material plates under transverse load—Part II: Numerical results. International Journal of Solids and Structures, 43(13), 3675-3691.

[126] M. Amirpour, R. Das, E. I. S. Flores (2017). Bending analysis of thin functionally graded plate under in-plane stiffness variations. Applied Mathematical Modelling, 44, 481-496.

[127] G. N. Praveen, J. N. Reddy (1998). Nonlinear transient thermoelastic analysis of functionally graded ceramic-metal plates. International journal of solids and structures, 35(33), 4457-4476.

[128] L. Della Croce, P. Venini (2004). Finite elements for functionally graded Reissner–Mindlin plates. Computer Methods in Applied Mechanics and Engineering, 193(9-11), 705-725.

[129] M. K. Singha, T. Prakash, M. Ganapathi (2011). Finite element analysis of functionally graded plates under transverse load. Finite elements in Analysis and Design, 47(4), 453-460.

[130] H. T. Thai, D. H. Choi (2013). A simple first-order shear deformation theory for the bending and free vibration analysis of functionally graded plates. Composite Structures, 101, 332-340.

[131] H. T. Thai, T. K. Nguyen, T. P. Vo, J. Lee (2014). Analysis of functionally graded sandwich plates using a new first-order shear deformation theory. European Journal of Mechanics-A/Solids, 45, 211-225.

[132] J. L. Mantari, E. V. Granados (2015). A refined FSDT for the static analysis of functionally graded sandwich plates. Thin-Walled Structures, 90, 150-158.

[133] H. Bellifa, K. H. Benrahou, L. Hadji, M. S. A. Houari, A. Tounsi (2016). Bending and free vibration analysis of functionally graded plates using a simple shear deformation theory and the concept the neutral surface position. Journal of the Brazilian Society of Mechanical Sciences and Engineering, 38(1), 265-275.

[134] S. Srividhya, K. Basant, R. K. Gupta, A. Rajagopal, J. Reddy (2018). Influence of the homogenization scheme on the bending response of functionally graded plates. Acta Mechanica, 229(10), 4071-4089.

[135] K. K. Joshi, V. R. Kar (2020). Bending analysis of bi-dimensional functionally graded plate using FEA. Materials Today: Proceedings, 26, 1766-1770.

[136] J. Reddy (2000). Analysis of functionally graded plates. International Journal for numerical methods in engineering, 47(1-3), 663-684.

[137] A. J. M. Ferreira, R. C. Batra, C. M. C. Roque, L. F. Qian, P. A. L. S. Martins (2005). Static analysis of functionally graded plates using third-order shear deformation theory and a meshless method. Composite structures, 69(4), 449-457.

[138] A. R. Saidi, M. Bodaghi, S. R. Atashipour (2012). Levy-type solution for bending-stretching of thick functionally graded rectangular plates based on third-order shear deformation theory. Mechanics of Advanced Materials and Structures, 19(8), 577-589.

[139] M. G. Taj, A. Chakrabarti, A. H. Sheikh (2013). Analysis of functionally graded plates using higher order shear deformation theory. Applied Mathematical Modelling, 37(18-19), 8484-8494.

[140] T. Q. Bui, T. Van Do, L. H. T. Ton, D. H. Doan, S. Tanaka, D. T. Pham, ... & S. Hirose (2016). On the high temperature mechanical behaviors analysis of heated functionally graded plates using FEM and a new third-order shear deformation plate theory. Composites Part B: Engineering, 92, 218-241.

[141] A. M. Zenkour (2005). A comprehensive analysis of functionally graded sandwich plates: Part 1—Deflection and stresses. International journal of solids and structures, 42(18-19), 5224-5242.

[142] A. M. Zenkour (2006). Generalized shear deformation theory for bending analysis of functionally graded plates. Applied Mathematical Modelling, 30(1), 67-84.

[143] A. M. Zenkour, N. A. Alghamdi (2008). Thermoelastic bending analysis of functionally graded sandwich plates. Journal of materials science, 43(8), 2574-2589.

[144] A. M. Zenkour, N. A. Alghamdi (2010). Bending analysis of functionally graded sandwich plates under the effect of mechanical and thermal loads. Mechanics of Advanced Materials and Structures, 17(6), 419-432.

[145] A. M. Zenkour (2012). Exact relationships between classical and sinusoidal theories for FGM plates. Mechanics of Advanced Materials and Structures, 19(7), 551-567.

[146] A. Mahi, A. Tounsi (2015). A new hyperbolic shear deformation theory for bending and free vibration analysis of isotropic, functionally graded, sandwich and laminated composite plates. Applied Mathematical Modelling, 39(9), 2489-2508.

[147] J. L. Mantari, A. S. Oktem, C. G. Soares (2012). Bending response of functionally graded plates by using a new higher order shear deformation theory. Composite Structures, 94(2), 714-723.

[148] J. L. Mantari, C. G. Soares (2012). Bending analysis of thick exponentially graded plates using a new trigonometric higher order shear deformation theory. Composite Structures, 94(6), 1991-2000.

[149] J. L. Mantari, C. G. Soares (2013). Finite element formulation of a generalized higher order shear deformation theory for advanced composite plates. Composite Structures, 96, 545-553.

[150] J. L. Mantari, C. G. Soares (2014). Static response of advanced composite plates by a new non-polynomial higher-order shear deformation theory. International Journal of Mechanical Sciences, 78, 60-71.

[151] J. L. Mantari, E. M. Bonilla, C. G. Soares (2014). A new tangential-exponential higher order shear deformation theory for advanced composite plates. Composites Part B: Engineering, 60, 319-328.

[152] J. L. Mantari, I. A. Ramos, E. Carrera, M. Petrolo (2016). Static analysis of functionally graded plates using new non-polynomial displacement fields via Carrera Unified Formulation. Composites Part B: Engineering, 89, 127-142.

[153] E. Carrera (1995). A class of two dimensional theories for multilayered plates analysis, Atti Acc. Sci. Torino, 19, 20.

[154] Y. Belkhodja, D. Ouinas, F. Z. Zaoui, H. Fekirini (2020). An exponential-trigonometric higher order shear deformation theory (HSDT) for bending, free vibration, and buckling analysis of functionally graded materials (FGMs) plates. Advanced Composites Letters, 29, 0963693519875739.

[155] H. Matsunaga (2009). Stress analysis of functionally graded plates subjected to thermal and mechanical loadings. Composite Structures, 87(4), 344-357.

[156] M. Talha, B. Singh (2010). Static response and free vibration analysis of FGM plates using higher order shear deformation theory. Applied mathematical modelling, 34(12), 3991-4011.

[157] S. Natarajan, G. Manickam (2012). Bending and vibration of functionally graded material sandwich plates using an accurate theory. Finite Elements in Analysis and Design, 57, 32-42.

[158] T. M. Tu, T. H. Quoc, N. V. Long (2017). Bending analysis of functionally graded plates using new eight-unknown higher order shear deformation theory. Struct. Eng. Mech, 62(3), 311-324.

[159] I. Mechab, H. A. Atmane, A. Tounsi, H. A. Belhadj, E. A. A. Bedia (2010). A two variable refined plate theory for the bending analysis of functionally graded plates. Acta Mechanica Sinica, 26(6), 941-949.

[160] H. H. Abdelaziz, H. A. Atmane, I. Mechab, L. Boumia, A. Tounsi, A. B. El Abbas (2011). Static analysis of functionally graded sandwich plates using an efficient and simple refined theory. Chinese journal of aeronautics, 24(4), 434-448.

[161] R. P. Shimpi, H. G. Patel (2006). A two variable refined plate theory for orthotropic plate analysis. International Journal of Solids and Structures, 43(22-23), 6783-6799.

[162] I. Mechab, B. Mechab, S. Benaissa (2013). Static and dynamic analysis of functionally graded plates using four-variable refined plate theory by the new function. Composites Part B: Engineering, 45(1), 748-757.

[163] H. T. Thai, D. H. Choi (2013). Finite element formulation of various four unknown shear deformation theories for functionally graded plates. Finite Elements in Analysis and Design, 75, 50-61.

[164] H. T. Thai, S. E. Kim (2013). A simple higher-order shear deformation theory for bending and free vibration analysis of functionally graded plates. Composite Structures, 96, 165-173.

[165] D. Li, Z. Deng, G. Chen, H. Xiao, L. Zhu (2017). Thermomechanical bending analysis of sandwich plates with both functionally graded face sheets and functionally graded core. Composite Structures, 169, 29-41.

[166] A. Farzam, B. Hassani (2019). A new efficient shear deformation theory for FG plates with in-plane and through-thickness stiffness variations using isogeometric approach. Mechanics of Advanced Materials and Structures, 26(6), 512-525.

[167] E. Carrera, S. Brischetto, M. Cinefra, M. Soave (2011). Effects of thickness stretching in functionally graded plates and shells. Composites Part B: Engineering, 42(2), 123-133.

[168] J. L. Mantari, C. G. Soares (2012). Generalized hybrid quasi-3D shear deformation theory for the static analysis of advanced composite plates. Composite Structures, 94(8), 2561-2575.

[169] A. M. A. Neves, A. J. M. Ferreira, E. Carrera, C. M. C. Roque, M. Cinefra, R. M. N. Jorge, C. M. M. Soares (2012). A quasi-3D sinusoidal shear deformation theory for the static and free vibration analysis of functionally graded plates. Composites Part B: Engineering, 43(2), 711-725.

[170] A. M. A. Neves, A. J. M. Ferreira, E. Carrera, M. Cinefra, C. M. C. Roque, R. M. N. Jorge, C. M. Soares (2012). A quasi-3D hyperbolic shear deformation theory for the static and free vibration analysis of functionally graded plates. Composite Structures, 94(5), 1814-1825.

[171] A. M. A. Neves, A. J. M. Ferreira, E. Carrera, M. Cinefra, C. M. C. Roque, R. M. N. Jorge, C. M. Soares (2013). Static, free vibration and buckling analysis of isotropic and sandwich functionally graded plates using a quasi-3D higher-order shear deformation theory and a meshless technique. Composites Part B: Engineering, 44(1), 657-674.

[172] H. T. Thai, S. E. Kim (2013). A simple quasi-3D sinusoidal shear deformation theory for functionally graded plates. Composite Structures, 99, 172-180.

[173] A. Bessaim, M. S. Houari, A. Tounsi, S. R. Mahmoud, E. A. A. Bedia (2013). A new higher-order shear and normal deformation theory for the static and free vibration analysis of sandwich plates with functionally graded isotropic face sheets. Journal of Sandwich Structures & Materials, 15(6), 671-703.

[174] A. M. Zenkour (2013). A simple four-unknown refined theory for bending analysis of functionally graded plates. Applied Mathematical Modelling, 37(20-21), 9041-9051.

[175] A. M. Zenkour (2013). Bending analysis of functionally graded sandwich plates using a simple four-unknown shear and normal deformations theory. Journal of Sandwich Structures & Materials, 15(6), 629-656.

[176] M. S. A. Houari, A. Tounsi, O. A. Bég (2013). Thermoelastic bending analysis of functionally graded sandwich plates using a new higher order shear and normal deformation theory. International journal of mechanical sciences, 76, 102-111.

[177] Z. Belabed, M. S. A. Houari, A. Tounsi, S. R. Mahmoud, O. A. Bég (2014). An efficient and simple higher order shear and normal deformation theory for functionally graded material (FGM) plates. Composites Part B: Engineering, 60, 274-283.

[178] H. Hebali, A. Tounsi, M. S. A. Houari, A. Bessaim, E. A. A. Bedia (2014). New quasi-3D hyperbolic shear deformation theory for the static and free vibration analysis of functionally graded plates. Journal of Engineering Mechanics, 140(2), 374-383.

[179] M. Amirpour, R. Das, E. S. Flores (2016). Analytical solutions for elastic deformation of functionally graded thick plates with in-plane stiffness variation using higher order shear deformation theory. Composites Part B: Engineering, 94, 109-121.

[180] A. M. Zenkour, R. A. Alghanmi (2018). Bending of functionally graded plates via a refined quasi-3D shear and normal deformation theory. Curved and Layered Structures, 5(1), 190-200.

[181] M. Khiloun, A. A. Bousahla, A. Kaci, A. Bessaim, A. Tounsi, S. R. Mahmoud (2020). Analytical modeling of bending and vibration of thick advanced composite plates using a four-variable quasi 3D HSDT. Engineering with Computers, 36(3), 807-821.

[182] S. S. Vel, R. C. Batra (2004). Three-dimensional exact solution for the vibration of functionally graded rectangular plates. Journal of Sound and Vibration, 272(3-5), 703-730.

[183] B. Uymaz, M. Aydogdu (2007). Three-dimensional vibration analyses of functionally graded plates under various boundary conditions. Journal of Reinforced Plastics and Composites, 26(18), 1847-1863.

[184] Q. Li, V. P. Iu, K. P. Kou (2008). Three-dimensional vibration analysis of functionally graded material sandwich plates. Journal of Sound and Vibration, 311(1-2), 498-515.

[185] K. S. K. Reddy, T. Kant (2014). Three-dimensional elasticity solution for free vibrations of exponentially graded plates. Journal of Engineering Mechanics, 140(7), 04014047.

[186] G. Jin, Z. Su, S. Shi, T. Ye, S. Gao (2014). Three-dimensional exact solution for the free vibration of arbitrarily thick functionally graded rectangular plates with general boundary conditions. Composite Structures, 108, 565-577.

[187] A. Singh, P. Kumari (2020). Three-Dimensional free vibration analysis of composite FGM rectangular plates with in-plane heterogeneity: An EKM solution. International Journal of Mechanical Sciences, 180, 105711.

[188] S. Abrate (2008). Functionally graded plates behave like homogeneous plates. Composites part B: engineering, 39(1), 151-158.

[189] D. G. Zhang, Y. H. Zhou (2008). A theoretical analysis of FGM thin plates based on physical neutral surface. Computational Materials Science, 44(2), 716-720.

[190] D. Y. Liu, C. Y. Wang, W. Q. Chen (2010). Free vibration of FGM plates with in-plane material inhomogeneity. Composite Structures, 92(5), 1047-1051.

[191] S. Yin, T. Yu, P. Liu (2013). Free vibration analyses of FGM thin plates by isogeometric analysis based on classical plate theory and physical neutral surface. Adv Mech Eng.

[192] I. Ramu, S. C. Mohanty (2014). Modal analysis of functionally graded material plates using finite element method. Procedia Materials Science, 6, 460-467.

[193] M. A. R. Loja, J. I. Barbosa (2020). In-plane functionally graded plates: A study on the free vibration and dynamic instability behaviors. Composite Structures, 237, 111905.

[194] R. C. Batra, J. Jin (2005). Natural frequencies of a functionally graded anisotropic rectangular plate. Journal of Sound and Vibration, 282(1-2), 509-516.

[195] X. Zhao, Y. Y. Lee, K. M. Liew (2009). Free vibration analysis of functionally graded plates using the element-free kp-Ritz method. Journal of sound and Vibration, 319(3-5), 918-939.

[196] J. L. Mantari, E. V. Granados (2015). Dynamic analysis of functionally graded plates using a novel FSDT. Composites Part B: Engineering, 75, 148-155.

[197] G. M. S. Bernardo, F. R. Damásio, T. A. N. Silva, M. A. R. Loja (2016). A study on the structural behavior of FGM plates static and free vibrations analyses. Composite Structures, 136, 124-138.

[198] S. Abrate (2006). Free vibration, buckling, and static deflections of functionally graded plates. Composites Science and Technology, 66(14), 2383-2394.

[199] A. J. M. Ferreira, R. C. Batra, C. M. C. Roque, L. F. Qian, R. M. N. Jorge (2006). Natural frequencies of functionally graded plates by a meshless method. Composite Structures, 75(1-4), 593-600.

[200] J. Kim, J. N. Reddy (2013). Analytical solutions for bending, vibration, and buckling of FGM plates using a couple stress-based third-order theory. Composite Structures, 103, 86-98.

[201] A. M. Zenkour (2005). On vibration of functionally graded plates according to a refined trigonometric plate theory. International Journal of Structural Stability and Dynamics, 5(02), 279-297.

[202] H. Matsunaga (2008). Free vibration and stability of functionally graded plates according to a 2-D higher-order deformation theory. Composite structures, 82(4), 499-512.

[203] S. Xiang, Y. X. Jin, Z. Y. Bi, S. X. Jiang, M. S. Yang (2011). A n-order shear deformation theory for free vibration of functionally graded and composite sandwich plates. Composite Structures, 93(11), 2826-2832.

[204] D. K. Jha, T. Kant, R. K. Singh (2012). Higher order shear and normal deformation theory for natural frequency of functionally graded rectangular plates. Nuclear Engineering and Design, 250, 8-13.

[205] S. A. Sheikholeslami, A. R. Saidi (2013). Vibration analysis of functionally graded rectangular plates resting on elastic foundation using higher-order shear and normal deformable plate theory. Composite Structures, 106, 350-361.

[206] R. C. Batra, S. Vidoli (2002). Higher-order piezoelectric plate theory derived from a three-dimensional variational principle. AIAA journal, 40(1), 91-104.

[207] J. L. Mantari, E. V. Granados, C. G. Soares (2014). Vibrational analysis of advanced composite plates resting on elastic foundation. Composites Part B: Engineering, 66, 407-419.

[208] A. Gupta, M. Talha, V. K. Chaudhari (2016). Natural frequency of functionally graded plates resting on elastic foundation using finite element method. Procedia Technology, 23, 163-170.

[209] A. Mahmoudi, R. Bachir-Bouiadjra, S. Benyoucef, A. Tounsi (2017). Influence de la porosité sur la vibration libre des plaques FGM sur fondation élastique. Nature & Technology, (17).

[210] F. Z. Zaoui, D. Ouinas, A. Tounsi (2019). New 2D and quasi-3D shear deformation theories for free vibration of functionally graded plates on elastic foundations. Composites Part B: Engineering, 159, 231-247.

[211] L. Hadji, H. A. Atmane, A. Tounsi, I. Mechab, E. A. Adda Bedia (2011). Free vibration of functionally graded sandwich plates using four-variable refined plate theory. Applied Mathematics and Mechanics, 32(7), 925-942.

[212] A. Benachour, H. D. Tahar, H. A. Atmane, A. Tounsi, M. S. Ahmed (2011). A four variable refined plate theory for free vibrations of functionally graded plates with arbitrary gradient. Composites Part B: Engineering, 42(6), 1386-1394.

[213] H. T. Thai, T. Park, D. H. Choi (2013). An efficient shear deformation theory for vibration of functionally graded plates. Archive of Applied Mechanics, 83(1), 137-149.

[214] R. Benferhat, T. H. Daouadji, M. S. Mansour (2016). Free vibration analysis of FG plates resting on an elastic foundation and based on the neutral surface concept using higher-order shear deformation theory. Comptes Rendus Mecanique, 344(9), 631-641.

[215] Y. Xue, G. Jin, H. Ding, M. Chen (2018). Free vibration analysis of in-plane functionally graded plates using a refined plate theory and isogeometric approach. Composite Structures, 192, 193-205.

[216] M. Slimane, B. Samir, B. Hakima, H. M. Adda (2019). Free vibration analysis of functionally graded plates FG with porosities. International Journal of Engineering Research & Technology (IJERT), 8(03).

[217] S. S. Tabatabaei, A. M. Fattahi (2020). A finite element method for modal analysis of FGM plates. Mechanics Based Design of Structures and Machines, 1-12.

[218] V. Birman (1995). Stability of functionally graded hybrid composite plates. Composites Engineering, 5(7), 913-921.

[219] E. Feldman, J. Aboudi (1997). Buckling analysis of functionally graded plates subjected to uniaxial loading. Composite Structures, 38(1-4), 29-36.

[220] R. Javaheri, M. R. Eslami (2002). Buckling of functionally graded plates under in-plane compressive loading. ZAMM-Journal of Applied Mathematics and Mechanics/Zeitschrift für Angewandte Mathematik und Mechanik: Applied Mathematics and Mechanics, 82(4), 277-283.

[221] R. Javaheri, M. Eslami (2002). Thermal buckling of functionally graded plates. AIAA journal, 40(1), 162-169.

[222] B. S. Shariat, R. Javaheri, M. R. Eslami (2005). Buckling of imperfect functionally graded plates under in-plane compressive loading. Thin-walled structures, 43(7), 1020-1036.

[223] B. S. Shariat, M. R. Eslami (2006). Thermal buckling of imperfect functionally graded plates. International journal of solids and structures, 43(14-15), 4082-4096.

[224] M. Mahdavian (2009). Buckling analysis of simply-supported functionally graded rectangular plates under non-uniform in-plane compressive loading.

[225] M. Mohammadi, A. R. Saidi, E. Jomehzadeh (2010). Levy solution for buckling analysis of functionally graded rectangular plates. Applied Composite Materials, 17(2), 81-93.

[226] I. Ramu, S. C. Mohanty (2014). Buckling analysis of rectangular functionally graded material plates under uniaxial and biaxial compression load. Procedia Engineering, 86, 748-757.

[227] C. A. N. Nihat, N. KURGAN, A. H. A. HASSAN (2020). Buckling Analysis of Functionally Graded Plates Using Finite Element Analysis. International Journal of Engineering and Applied Sciences, 12(1), 43-56.

[228] W. Lanhe (2004). Thermal buckling of a simply supported moderately thick rectangular FGM plate. Composite Structures, 64(2), 211-218.

[229] X. Zhao, Y. Y. Lee, K. M. Liew (2009). Mechanical and thermal buckling analysis of functionally graded plates. Composite Structures, 90(2), 161-171.

[230] H. Yaghoobi, P. Yaghoobi (2013). Buckling analysis of sandwich plates with FGM face sheets resting on elastic foundation with various boundary conditions: an analytical approach. Meccanica, 48(8), 2019-2035.

[231] Y. H. Lee, S. I. Bae, J. H. Kim (2016). Thermal buckling behavior of functionally graded plates based on neutral surface. Composite Structures, 137, 208-214.

[232] A. Shahbaztabar, K. Arteshyar (2019). Buckling analysis of functionally graded plates partially resting on elastic foundation using the differential quadrature element method. Acta Mechanica Sinica, 35(1), 174-189.

[233] B. S. Shariat, M. R. Eslami (2007). Buckling of thick functionally graded plates under mechanical and thermal loads. Composite Structures, 78(3), 433-439.

[234] H. Foroughi, M. Azhari (2014). Mechanical buckling and free vibration of thick functionally graded plates resting on elastic foundation using the higher order B-spline finite strip method. Meccanica, 49(4), 981-993.

[235] S. Yin, T. Yu, T. Q. Bui, X. Zheng, S. Tanaka (2016). In-plane material inhomogeneity of functionally graded plates: A higher-order shear deformation plate isogeometric analysis. Composites Part B: Engineering, 106, 273-284.

[236] T. Van Do, D. K. Nguyen, N. D. Duc, D. H. Doan, T. Q. Bui (2017). Analysis of bi-directional functionally graded plates by FEM and a new third-order shear deformation plate theory. Thin-Walled Structures, 119, 687-699.

[237] J. S. Moita, A. L. Araújo, V. F. Correia, C. M. M. Soares, J. Herskovits (2018). Buckling and nonlinear response of functionally graded plates under thermo-mechanical loading. Composite Structures, 202, 719-730.

[238] A. M. Zenkour (2005). A comprehensive analysis of functionally graded sandwich plates: Part 2—Buckling and free vibration. International Journal of Solids and Structures, 42(18-19), 5243-5258.

[239] A. M. Zenkour, D. S. Mashat (2010). Thermal buckling analysis of ceramic-metal functionally graded plates. Natural Science, 2(09), 968.

[240] A. M. Zenkour, M. Sobhy (2010). Thermal buckling of various types of FGM sandwich plates. Composite Structures, 93(1), 93-102.

[241] M. Bodaghi, A. R. Saidi (2010). Levy-type solution for buckling analysis of thick functionally graded rectangular plates based on the higher-order shear deformation plate theory. Applied Mathematical Modelling, 34(11), 3659-3673.

[242] A. M. A. Neves, A. J. M. Ferreira, E. Carrera, M. Cinefra, R. M. N. Jorge, C. M. M. Soares (2012). Buckling analysis of sandwich plates with functionally graded skins using

a new quasi-3D hyperbolic sine shear deformation theory and collocation with radial basis functions. ZAMM-Journal of Applied Mathematics and Mechanics/Zeitschrift für Angewandte Mathematik und Mechanik, 92(9), 749-766.

[243] B. S. Reddy, J. S. Kumar, C. E. Reddy, K. Reddy (2013). Buckling analysis of functionally graded material plates using higher order shear deformation theory. Journal of composites, 2013.

[244] T. I. Thinh, T. M. Tu, T. H. Quoc, N. V. Long (2016). Vibration and buckling analysis of functionally graded plates using new eight-unknown higher order shear deformation theory. Latin American Journal of Solids and Structures, 13(3), 456-477.

[245] V. N. Van Do, C. H. Lee (2017). Thermal buckling analyses of FGM sandwich plates using the improved radial point interpolation mesh-free method. Composite Structures, 177, 171-186.

[246] A. M. Zenkour, M. H. Aljadani (2018). Mechanical buckling of functionally graded plates using a refined higher-order shear and normal deformation plate theory. Advances in aircraft and spacecraft science, 5(6), 615.

[247] Z. Nouri, S. Sarrami-Foroushani, F. Azhari, M. Azhari (2020). Application of Carrera unified formulation in conjunction with finite strip method in static and stability analysis of functionally graded plates. Mechanics of Advanced Materials and Structures, 1-17.

[248] A. Tati (2021). Finite element analysis of thermal and mechanical buckling behavior of functionally graded plates. Archive of Applied Mechanics, 91(11), 4571-4587.

[249] M. Farrokh, M. Afzali, E. Carrera (2021). Mechanical and thermal buckling loads of rectangular FG plates by using higher-order unified formulation. Mechanics of Advanced Materials and Structures, 28(6), 608-617.

[250] N. El Meiche, A. Tounsi, N. Ziane, I. Mechab (2011). A new hyperbolic shear deformation theory for buckling and vibration of functionally graded sandwich plate. International Journal of Mechanical Sciences, 53(4), 237-247.

[251] A. Fekrar, N. El Meiche, A. Bessaim, A. Tounsi, E. A. Adda Bedia (2012). Buckling analysis of functionally graded hybrid composite plates using a new four variable refined plate theory. Steel and Composite Structures, 13(1), 91-107.

[252] H. T. Thai, D. H. Choi (2012). An efficient and simple refined theory for buckling analysis of functionally graded plates. Applied Mathematical Modelling, 36(3), 1008-1022.

[253] M. Bateni, Y. Kiani, M. R. Eslami (2013). A comprehensive study on stability of FGM plates. International Journal of Mechanical Sciences, 75, 134-144.

[254] C. H. Thai, A. M. Zenkour, M. A. Wahab, H. Nguyen-Xuan (2016). A simple four-unknown shear and normal deformations theory for functionally graded isotropic and sandwich plates based on isogeometric analysis. Composite Structures, 139, 77-95.

[255] A. Tati, S. Bouadjadja, Y. Bada (2019). Free vibration of thermally stressed angle-ply laminated composite using first-order shear deformation theory model with assumed natural shear strain. Journal of The Institution of Engineers (India): Series C, 100(6), 937-947.

[256] A. Tati. (2021). A five unknowns high order shear deformation finite element model for functionally graded plates bending behavior analysis. Journal of the Brazilian Society of Mechanical Sciences and Engineering, 43(1), 1-14.

[257] E. N. Dvorkin, K. J. Bathe (1984). A continuum mechanics based four-node shell element for general non-linear analysis. Engineering computations.

[258] H. C. Huang, E. Hinton (1984). A nine node Lagrangian Mindlin plate element with enhanced shear interpolation. Engineering computations, 1(4), 369-379.

[259] S. J. Lee, H. R. Kim (2013). FE analysis of laminated composite plates using a higher order shear deformation theory with assumed strains. Latin American Journal of Solids and Structures, 10(3), 523-547.

[260] R. P. Shimpi, H. Arya, N. K. Naik (2003). A higher order displacement model for the plate analysis. Journal of reinforced plastics and composites, 22(18), 1667-1688.

[261] A. K. Soh, S. Cen, Y. Q. Long, Z. F. Long (2001). A new twelve DOF quadrilateral element for analysis of thick and thin plates. European Journal of Mechanics-A/Solids, 20(2), 299-326.

[262] A. Boucheta (2019) Application de la théorie raffinée à quatre variables pour l'étude du comportement des structures FGM. Thèse de Doctorat. Université de Tahri-Mohamed-Béchar.

[263] T. K. Nguyen, T. P. Vo, H. T. Thai (2014). Vibration and buckling analysis of functionally graded sandwich plates with improved transverse shear stiffness based on the first-order shear deformation theory. Proceedings of the Institution of Mechanical Engineers, Part C: Journal of Mechanical Engineering Science, 228(12), 2110-2131.

[264] S. Hosseini-Hashemi, M. O. H. A. M. M. A. D. Fadaee, S. R. Atashipour (2011). A new exact analytical approach for free vibration of Reissner–Mindlin functionally graded rectangular plates. International Journal of Mechanical Sciences, 53(1), 11-22.

[265] R. Saha, P. R. Maiti (2012). Buckling of simply supported FGM plates under uniaxial load. International Journal of Civil and Structural Engineering, 2(4), 1035.